



HAL
open science

Dispersions of nanomagnets in ionic liquids for thermoelectric applications

Jesse Riedl

► **To cite this version:**

Jesse Riedl. Dispersions of nanomagnets in ionic liquids for thermoelectric applications. Theoretical and/or physical chemistry. Sorbonne Université, 2020. English. NNT : 2020SORUS468 . tel-04002091

HAL Id: tel-04002091

<https://theses.hal.science/tel-04002091>

Submitted on 23 Feb 2023

HAL is a multi-disciplinary open access archive for the deposit and dissemination of scientific research documents, whether they are published or not. The documents may come from teaching and research institutions in France or abroad, or from public or private research centers.

L'archive ouverte pluridisciplinaire **HAL**, est destinée au dépôt et à la diffusion de documents scientifiques de niveau recherche, publiés ou non, émanant des établissements d'enseignement et de recherche français ou étrangers, des laboratoires publics ou privés.



Thèse de doctorat

Pour l'obtention du grade de

Docteur de Sorbonne Université

École doctorale de Chimie Physique et Chimie Analytique de Paris Centre (ED 388)

Dispersions of nanomagnets in ionic liquids for thermoelectric applications

Présentée par : Jesse Cornelius RIEDL

Directrice de thèse : Véronique Peyre

Présentée et soutenue publiquement le *25 septembre 2020* devant un jury composé de :

Markus VALTINER, professeur (TU WIEN) *Rapporteur*

Ben ERNE, professeur associé (Utrecht University) *Rapporteur*

Sophie CASSAIGNON, professeur (Sorbonne Université) *Examinatrice*

Véronique PEYRE, maître de conférences (Sorbonne Université) *Directrice de thèse*

“Übung macht den Meister”

“Actions speak louder than words”

“Le mieux est l’ennemi du bien.”

“Barriga vazia não tem alegria.”

“Nunca es demasiado.”

“学习学习再学习”

Acknowledgements

These three years were very fruitful both on the work and private side. I learned a lot and met so many amazing people. I want to thank all of them for this very nice time!

First, I want to thank Markus Valtiner and Ben Ern  to having accepted to referee this work and Sophie Cassaignon to examine it. I hope you will enjoy the work and that it has a benefit for your own research. My gratitude goes to my two supervisors Emmanuelle Dubois and V ronique Peyre who were always there for me when I needed them and at the same time gave me enough space to develop my own ideas. They taught me a lot from how to use programs like IGOR, over developing new sample holders, cells etc., how to organise to spend nice nights and weekends at Synchrotrons or neutron reactors up to the analysis of experiments and the writing of reports and articles. All this was always very pleasant, I cannot thank both enough!

I also want to show my gratitude to Gilles, Guillaume, Mitraddeep, Thiago, R gine, who worked in close contact with me especially but not only regarding the thermodiffusion measurements. The many discussions were very important to develop new ideas and ways to further improve the properties of the ionic liquid-based nanoparticle dispersions.

Thanks to Fabrice Cousin all the SAS measurements were possible which came to a total of several hundred of samples over the three years. I want to thank him for the very pleasant work together whether it was at the weekend at the neutron reactor, during a conference on a boat dinner, in front of his flat in one of the many hand-overs of the studied samples.

Thanks to the MAGENTA project partners. The most time was spent with the partners at CEA, which include Blanca, Kakoli, Michel, Saco, with whom I had many fruitful discussions and a nice time during x-ray reflectivity runs at the synchrotron Soleil together with our local partners Alexandro and Jean Daillant. This study was accompanied by QCM measurements Ivan Lucas, Ozlem Sel, and Hubert Perrot.

I also want to thank all the other MAGENTA project partners for the interesting discussions during the meetings which dealt a big scope from the simulations of ionic liquid properties, over measured properties also together with our produced nanoparticle dispersions, to the dissipation for example of a video clip over the project.

I thank both interns Gabriel and Souhaila who did a great work and helped to advance the understanding of the colloidal stability and thermodiffusion measurements.

I thank Amandine Anfry for DLS and Karl-Fischer measurements, Aude Michel for FAAS measurements, Arnaud H lary for the design of the coupled DLS-SANS measurement setup at

LLB (Laboratoire Léon Brillouin), Pierre Burckel for the ICP-MS measurements performed at the IPGP, and Sandra Casale for the TEM images taken at the IMPC (Institut des Matériaux de Paris-Centre).

I thank the doctoral school represented by Koonavadee, Alexa Courty and Loic Journal.

I am very happy for the great opportunities to prepare my professional future with a great help by Paule Biaudet, Anne HERVE-MINVIELLE, Mickaël LE GUEN. Thanks a lot for your great work!

I want to thank all the colleagues of the PHENIX laboratory for the great ambience that was omnipresent at the laboratory. A lot became friends and I am happy to continue time with you after finishing the PhD.

Parts of this work (ICP-MS measurements in chapter 5) were supported by the IPGP multidisciplinary program PARI, and by Paris-IdF region SESAME Grant no. 12015908.

This work has been mainly supported by the European Union Horizon 2020 research and innovation program under the grant number 731976 (MAGENTA).

Lastly, I want to thank my family and friends who always supported me and will continue to do so.

Big thanks go to all of you!

Abstract

Thermoelectricity (TE) allows for the conversion of heat to electricity providing one possible methodology for the recycling of low-grade waste heat. Despite improvements, present thermoelectric solid materials have several limitations. Therefore, investigations of complex liquids (e.g. ionic liquids or nanofluids) have been proposed in recent years. This work presents the elaboration of novel ionic-liquid based magnetic complex fluids for such applications. Ionic liquids are a broad class of liquids, that consist solely of ions, and can be liquid at room temperature, with many properties ideal for thermoelectric materials. In addition, recent studies on aqueous nanoparticle dispersions have demonstrated that the addition of magnetic nanoparticles (nanomagnets) can influence the thermoelectric coefficient and enhance the liquid's thermoelectric efficiency. It is here thus proposed to combine the two avenues by using dispersions of nanomagnets in ionic liquids for thermoelectric applications. In former studies, using ethylammonium nitrate (EAN) as ionic liquid, it was shown that colloidal stability was controlled by the solid-liquid interface. This finding was here extended to a broad range of ionic liquids with different sets of cations and anions, defining general trends and principles for colloidal stability in ionic liquids at room temperature. To obtain ionic liquid-based colloids, it is necessary to control the surface charge of the nanoparticles, the nature of charged surface groups and molecules producing this superficial charge, the nature of the counterions compensating this charge, and the route of transfer from water (the synthesis medium for the nanoparticles) to the ionic liquid. In a second step colloidal stability was studied in the temperature range of target thermoelectric devices (20-200°C) for different counterions and nanoparticle concentrations. Even if the temperature stability of ionic liquids is one of their advantages over molecular liquids such a temperature study has not been addressed yet. Indeed, some of the dispersions keep their stability up to 200°C. In this case, thermodiffusion, a property closely related to thermoelectricity, was measured. Optical microscopy, transmission electron microscopy (TEM), magnetic measurements, FAAS and ICP-MS were performed at room temperature whereas Dynamic Light Scattering (DLS), forced Rayleigh scattering (FRS) and small angle x-ray/neutron scattering (SAXS/SANS) together with thermogravimetric analysis (TGA) were used to analyse the ionic liquid-based nanoparticle dispersion behaviour with temperature.

Keywords : IONIC LIQUID, COLLOID, FERROFLUID, NANOPARTICLE, IRON OXIDE, STABILITY, INTERFACE

Résumé

La thermoélectricité (TE) permet la conversion de la chaleur en électricité, fournissant une méthode possible pour le recyclage de la chaleur fatale. Malgré les améliorations, les matériaux solides thermoélectriques actuels présentent plusieurs limitations. Par conséquent, des études sur des liquides complexes (par exemple des liquides ioniques ou des nanofluides) ont été proposées ces dernières années. Ce travail présente l'élaboration de nouveaux fluides complexes magnétiques à base de liquides ioniques pour de telles applications. Les liquides ioniques sont une large classe de liquides, constitués uniquement d'ions, et peuvent être liquides à température ambiante, avec de nombreuses propriétés très intéressantes pour les matériaux thermoélectriques. En outre, des études récentes sur les dispersions aqueuses de nanoparticules ont démontré que l'ajout de nanoparticules magnétiques (nanomagnets) peut influencer le coefficient thermoélectrique et améliorer l'efficacité thermoélectrique du liquide. Il est ainsi proposé ici de combiner les deux voies en utilisant des dispersions de nano-aimants dans des liquides ioniques pour des applications thermoélectriques. Dans des études antérieures, utilisant du nitrate d'éthylammonium (NEA) comme liquide ionique, il a été montré que la stabilité colloïdale était contrôlée par l'interface solide-liquide. Cette découverte a été étendue ici à une large gamme de liquides ioniques avec différents ensembles de cations et d'anions, définissant les tendances générales et les principes de stabilité colloïdale dans les liquides ioniques à température ambiante. Pour obtenir des colloïdes à base de liquide ioniques, il est nécessaire de contrôler la charge de surface des nanoparticules, la nature des groupes de surface chargés et des molécules produisant cette charge superficielle, la nature des contre-ions compensant cette charge, et la voie de transfert depuis le milieu de synthèse des nanoparticules (ici l'eau) vers le liquide ionique. Dans une deuxième étape, la stabilité colloïdale a été étudiée dans la gamme de température des dispositifs thermoélectriques cibles (20-200°C) pour différents contre-ions et concentrations de nanoparticules. Même si la stabilité en température des liquides ioniques est l'un de leurs avantages par rapport aux liquides moléculaires, l'étude en température des dispersions colloïdales dans les liquides ioniques a été très peu abordée. Pour cette étude, la thermodiffusion, propriété étroitement liée à la thermoélectricité, a été mesurée. La microscopie optique, la microscopie électronique à transmission (MET), les mesures magnétiques, FAAS et ICP-MS ont été effectuées à température ambiante tandis que la diffusion dynamique de la lumière (DLS), la diffusion forcée de Rayleigh (FRS) et la diffusion des rayons X / neutrons aux petits angles (SAXS / SANS) ainsi qu'une analyse thermogravimétrique (TGA) ont été utilisées pour analyser le comportement avec la température de dispersion des

nanoparticules à base de liquide ioniques. Les analyses montrent que certaines des dispersions conservent leur stabilité jusqu'à 200°C.

Mots clefs : LIQUIDE IONIQUE, COLLOIDE, FERROFLUIDE, NANOPARTICULE, OXIDE DE FER, STABILITE, INTERFACE

Contents

List of Tables	v
List of Figures	vi
Abbreviations	x
Introduction	1
1 Background	5
1.1 Colloids	5
1.2 Ionic liquids	6
1.2.1 Properties	7
1.2.2 Surface behaviour	8
1.3 Ionic liquid-based colloids	10
2 Materials and methods	12
2.1 Materials	12
2.2 Dispersions of maghemite nanoparticles	14
2.2.1 Synthesis of maghemite nanoparticles	14
2.2.2 Dispersion of nanoparticles in molecular solvents	15
2.2.2.1 Positive nanoparticles	15
2.2.2.2 Citrate coated nanoparticles	16
2.2.2.3 Polymer coated nanoparticles	17
2.2.2.4 Transfer from water to another molecular solvent	17
2.2.3 Routes of transfer towards ionic liquids	17
2.2.4 Concentrated ionic liquid-based ferrofluids	18
2.3 Characterisation techniques	18
2.3.1 Dynamic light scattering (DLS)	19
2.3.2 Flame atomic absorption spectroscopy (FAAS)	20

2.3.3	Forced Rayleigh scattering (FRS)	21
2.3.4	Inductively coupled plasma - mass spectrometry	21
2.3.5	Karl Fischer titration	22
2.3.6	Magnetisation measurements	22
2.3.7	Small angle X-ray/neutron scattering (SAXS/SANS)	23
2.3.8	Transmission electron microscopy (TEM)	25
2.3.9	Thermogravimetric analysis (TGA)	26
3	Elucidating the key parameters of colloidal dispersions of oxide nanoparticles in ionic liquids at room temperature	28
3.1	Introduction	28
3.2	Article: “colloidal dispersions of oxide nanoparticles in ionic liquids: elucidating the key parameters”	29
3.3	Conclusion	49
4	Colloidal and thermal stabilities of oxide nanoparticle dispersions in EMIM TFSI stabilised with sulfonate based imidazolium ions	51
4.1	Introduction	51
4.2	Article: “colloidal and thermal stabilities of oxide nanoparticle dispersions in EMIM TFSI stabilised with sulfonate based imidazolium ions”	52
4.3	Conclusion	68
5	Zwitterion-stabilised iron oxide nanoparticles in the ionic liquid EMIM TFSI: role of steric repulsion on colloidal stability up to 200°C	69
5.1	Introduction	69
5.2	Preparation of the nanoparticle dispersions	71
5.3	Results and discussion	72
5.3.1	First results at room temperature	72
5.3.2	Influence of temperature on colloidal stability	74
5.3.3	Discussion	77
5.4	Conclusion	79
6	Thermodiffusion in Molecular Solvents	81
6.1	Introduction	81

6.2	Article: “Inversion of thermodiffusive properties of ionic colloidal dispersions in water-DMSO mixtures probed by forced Rayleigh scattering”	82
6.3	Conclusion	99
7	Thermodiffusion in an ionic liquid and effect of magnetic fields	100
7.1	Introduction	100
7.2	Article: “Thermodiffusion anisotropy under magnetic field in ionic liquid-based ferrofluids”	101
7.3	Conclusion	113
	Conclusions and Perspectives	115
	Bibliography	II
	Appendix	XI

List of Tables

5.1	ICP-MS measurements for nanoparticle dispersions in EMIM TFSI and EMIM FSI with PAC _x MIM [±] Br ⁻ counterions. The corresponding uncoloured water rich phase after the phase transfer to the ionic liquid was removed with a pipette before freeze-drying for all samples, except if marked with* and is also analysed. n.m.= could not be measured yet.	72
5.2	SAXS and SANS SLD values for the calculated curves in Figure 5.7.	79
7.1	Overview of colloidal stability at the micrometre scale observed with optical microscopy. Different surface modifications of the nanoparticles and several ionic liquids are analysed.	XII

List of Figures

1.1	Representation of three types of ionic liquids: aprotic, protic, and zwitterionic. Taken from [1]	7
1.2	Scheme of layering of ionic liquids at a surface depending on the ratio $\kappa_{ion} = \sigma/\Theta_{ion}^{max} $. Example of a negatively charged surface); blue: anion of the ionic liquid, red: cation of the ionic liquid, green: additional cation; See text for information.	9
1.3	Free energy of the interaction between two nanocrystals in a molten salt obtained by MD simulations. Taken from ref [2]	11
2.1	Structure of studied ionic liquids. The influence of the anion is analysed with the same cation EMIM and the vice-versa for the same anion TFSI.	14
2.2	Scheme of the surface state of maghemite nanoparticles at different pH values. Graph reproduced from reference [3].	16
2.3	Scheme of the transfer of the nanoparticle dispersions from a molecular solvent (shown here as H ₂ O) to an ionic liquid (IL).	18
2.4	Illustration of the multi-scale analysis employed in this work.	19
2.5	Scheme of the used FRS setup and induced thermodiffusion for a thermophobic system. The cell is about 8 mm × 30 mm.	22
2.6	SAXS cell development during this work. 1) commercial polyimide capillaries, 2) self-made cells based on polyimide spacer, 3) borosilicate cells.	23
2.7	SANS cells developed for high temperature measurements up to 200°C for nanoparticle volume fractions 1) $\phi_{NP} < 3$ vol%, 2) $3 \text{ vol}\% < \phi_{NP} < 10$ vol%, and 3) $\phi_{NP} > 10$ vol%. Each cell is about 2 cm in diameter.	24
2.8	SAXS intensities obtained for the initial ferrofluid with different nanoparticle concentration ϕ_{NP} and the deduced form factor.	25

2.9	Example of structure factors for attractive ($S(Q \rightarrow 0) > 1$) and repulsive ($S(Q \rightarrow 0) < 1$) nanoparticle dispersions obtained by small angle scattering. Inset; absolute scattered intensities (divided by ϕ_{NP}) with different nanoparticle concentration ϕ_{NP} for a repulsive system.	26
2.10	Example TGA curve indicating how T_{start} and T_{onset} are determined. Taken from ref. [4]	27
3.1	Schemes of the interface for different surface charge densities σ and counterion sizes (example of a positively charged nanoparticle); dark blue: initial anionic counterion of the particle, light blue: anion of the ionic liquid, orange: cation of the ionic liquid; b) the counterion size is too small to form a dense monolayer on the surface. The first layer containing counterions, and ions of the IL is poorly organised and cannot act as a protection for aggregation. a) The surface is too densely charges, which attracts many anions that globally compensate this charge. There is no motor for the formation of a second organised protective layer. e) The charge is too low to attract anions and induce the formation of (sufficient) anionic/ cationic protective layers. d) The counterions are too large to fit onto the surface. Some extra counterions disrupt the organisation of the following cation layer. c) the good match: counterions size perfectly fit the surface size density and lead to overscreening and a new anionic surface, which in turn induces the formation of a cationic layer and so on. the presence of these alternate layers prevents the close approach of the particles and hence produces colloidal stability.	50
5.1	Structures of the analysed counterions and ionic liquid. C_x represents the length of the alkyl chain length (=number of CH_2) connecting the phosphonate with the imidazolium group and is analysed here for 4,6, and 12. $\text{PAC}_4\text{MIM}^\pm$ is the equivalent to SBMIM^\pm with a phosphonate instead of a sulfonate group.	70
5.2	TEM images of nanoparticle dispersions in EMIM TFSI with $\text{PAC}_x\text{MIM}^\pm \text{Br}^-$ counterions for a) and d) $x=4$, b) and e) $x=6$, and c) and f) $x=12$. For the dispersions displayed in a)-c) the supernatants were removed before freeze-drying and in d)-f) they were kept.	74

5.3	SAXS absolute scattered intensities (normalised by the nanoparticle volume fraction $\Phi_{NP} \approx 1$ vol% for all nanoparticle dispersions) as a function of the scattering vector Q for nanoparticle dispersions in EMIM TFSI. a) nanoparticle dispersions with and without removing the uncoloured water rich phase after the phase transfer to the ionic liquid with a pipette before freeze-drying are analysed with $\text{PAC}_6\text{MIM}^\pm \text{Br}^-$ and $\text{PAC}_{12}\text{MIM}^\pm \text{Br}^-$ counterions. b) nanoparticle dispersions before and after heating to 200°C are given for $\text{PAC}_x\text{MIM}^\pm$ (with $x=4, 6,$ and 12) Br^- counterions. A curve for nanoparticle dispersions with $\text{SBMIM}^\pm \text{TfO}^-$ counterions are given as a reference.	75
5.4	SANS absolute scattered intensities (normalised by the nanoparticle volume fraction Φ_{NP}) at different temperatures (27°C (\circ), 70°C (\square), 135°C (\triangle), and 200°C (∇) and back at 27°C (\diamond)) as a function of the scattering vector Q for nanoparticle dispersions in EMIM TFSI. The uncoloured water rich phase after the phase transfer to the ionic liquid was not removed with a pipette before freeze-drying, meaning that all introduced ions are in the samples. Nanoparticle dispersions with $\text{PAC}_6\text{MIM}^\pm \text{Br}^-$ counterions at $\phi_{NP}=0.85$ vol% (in red) and with $\text{PAC}_{12}\text{MIM}^\pm \text{Br}^-$ counterions at $\phi_{NP}=0.84$ vol% (in black) are shown. The inset shows the corresponding apparent hydrodynamic diameter obtained by DLS measurements.	76
5.5	Correlation functions G_1 obtained from DLS measurements for nanoparticle dispersions with PAC_xMIM ($x=4, 6$ and 12) Br^- counterions at $\phi_{NP} \approx 1$ and 0.1 vol%.	76
5.6	Schemes of the nanoparticle (NP) ionic liquid (IL) interface for an imaginable case for a) $\text{PAC}_4\text{MIM}^\pm \text{Br}^-$ counterions in analogy to the scheme for $\text{SBMIM}^\pm \text{TfO}^-$ counterions shown in Figure 8b) of chapter 4, b) $\text{PAC}_6\text{MIM}^\pm \text{Br}^-$ counterions and c) $\text{PAC}_{12}\text{MIM}^\pm \text{Br}^-$ counterions. They are shown for a high surface charge density $\sigma \approx 25 \mu\text{C}/\text{cm}^2$ illustrated by several "+" on the nanoparticle surface. The ions are represented as ellipsoids, the zwitterion $\text{PAC}_x\text{MIM}^\pm$ in green, the cation EMIM^+ in yellow, and the anions TFSI^- and Br^- in light and dark blue, respectively.	78
5.7	Calculated SAXS and SANS scattered intensities for nanoparticles with $d=7$ nm and $\sigma=0.25$ at $\phi_{NP} 1$ vol% for a layer thickness of $\text{PAC}_x\text{MIM}^\pm$ corresponding to half their stretched size.	80

6.1 Scheme for electrostatically stabilised nanoparticle dispersions with ClO_4^- counterions behaving thermophilic in water and thermophobic in DMSO. Taken from [5] 99

Abbreviations

AFM	atomic force microscopy
BAM	N-Trimethyl-N- butylammonium
BF ₄	tetrafluoroborate
BMIM	1-butyl-3-methylimidazolium
BMPyrr	1-Butyl-1- methylpyrrolidinium
Cit	citrate
DEME	N,N-Diethyl- N-methyl-N-(2-methoxyethyl) ammonium
DEP	diethyl phosphate
DLS	dynamic light scattering
C _r (r=2,4,6,7,8)	ethyl, butyl, hexyl, heptyl, octyl
EAN	ethylammonium nitrate
EMIM	1-ethyl-3-methylimidazolium
EP	ethylphosphonate
EtSO ₄	ethyl sulphate
FAAS	flame atomic absorption spectroscopy
FSI	bis(fluorosulfonyl) imide
FRS	forced Rayleigh scattering
HEIM	1-Ethyl-3-H-imidazolium
HSMIM	1-(4-Sulfobutyl)-3- methylimidazolium
IL	ionic liquid
ICP	inductively coupled plasma
NP	nanoparticle
MS	mass spectrometry
MD	molecular dynamics
OctylMIM	1-octyl-3-methylimidazolium

OHEMIM	1-(2-hydroxyethyl)-3-methylimidazolium
OHPMIM	1-(3-Propanol)-3- methylimidazolium
PF ₆	hexafluorophosphate
PAA ⁻	poly acrylate
PAC ₄ MIM [±]	1-Methyl-3-(butylphosphonate)imidazolium zwitterion
PAC ₆ MIM [±]	1-Methyl-3-(hexylphosphonate)imidazolium zwitterion
PAC ₁₂ MIM [±]	1-Methyl-3-(dodecylphosphonate)imidazolium zwitterion
PAMMA ⁻	poly acrylate-co-maleate
PZC	point of zero charge
SANS	small angle neutron scattering
SAS	small angle scattering
SAXS	small angle x-ray scattering
SCN	thiocyanate
SFA	surface force apparatus
SMIM [±] = SMIM [±]	butylsulfonate methylimidazolium zwitterion
TBA ⁻	tetrabutylammonium
TEM	transmission electron microscopy
TFSI	bis(trifluoromethane)sulfonimide
TfO	trifluoromethane-sulfonate

Introduction

The global energy consumption is rising at a steady pace. Much of this consumed energy is wasted as heat at all levels of human activity. For example, thermal losses represent 20 to 50% of the total energy consumption of different industrial sectors. If a small fraction of this waste heat could be converted into more usable energy, for example in the form of electricity, it would save huge amounts of energy consumption. This conversion is described by the thermoelectric (TE) effect which is the direct conversion of a temperature difference into an electric voltage. Currently, the thermoelectric materials with the highest performances are based on nanostructured solids that however only deliver small powers, they are generally composed of toxic and rare materials and they are rather expensive to produce.

Within this context the European project MAGENTA (MAGnetic nanoparticle based liquid ENergy materials for Thermoelectric device Applications) proposes to develop non-toxic, versatile, and economical thermoelectric materials. The originality of the project is based on the thermoelectric conversion capacity of liquids, which have promising thermoelectric properties. [6] The proposed liquids are ionic liquids which are liquids only composed of ions. In addition to their interesting properties, it has been shown that the presence of magnetic nanoparticles (nanomagnets) could have a beneficial effect for the target TE applications. [7,8] The aim is to develop fundamental knowledge on new (magneto-)thermoelectric phenomena in these liquid materials by seeking optimal conditions for waste-heat recovery.

In order to accomplish these goals, ten partners were part of the MAGENTA project. The tasks to be undertaken included experimental work such as preparation of optimised materials, measurements of the relevant properties such as thermodiffusion and thermoelectricity production, theoretical work (simulations) for a better understanding of the properties, and elaboration of prototypes of thermoelectrical cells. All tasks were related to the others by multiple inputs and feedbacks.

The main part of this PhD work was to formulate, understand and optimise stable magnetic nanoparticle dispersions in chosen ionic liquids in a broad range of temperatures (dealt with in chapters 3 to 5) in order for the project partners to analyse their thermoelectric and ther-

modiffusion properties. Facing the countless possible choices for the ionic liquids and the poorly developed colloidal models to disperse nanoparticles therein, it was desirable to elucidate general parameters needed to obtain stable dispersions in a broad range of ionic liquids. This knowledge could then readily be employed to prepare stable nanoparticle dispersions in new proposed ionic liquids.

A second important part of this PhD work (developed in chapters 6 and 7) was the characterisation of thermodiffusion in the previously obtained dispersions. Thermodiffusion describes the diffusion of nanoparticles in a temperature gradient, a property highly related to the generation of thermoelectricity. These thermodiffusion measurements were performed within the PHENIX lab, in a close collaboration between the physics and chemists teams. Indeed, the constant laboratory - internal cooperation and dialog was crucial for the development of the ionic liquid-based nanoparticle dispersions.

This manuscript first describes in chapter 1 the background knowledge necessary to understand the theory of nanoparticle dispersions in general and the state of the art of colloidal stability in ionic liquids.

Chapter 2 describes how the nanoparticles are synthesised and how their surfaces are modified to disperse them in ionic liquids. The analysed parameters include the nanoparticle surface charge, the nature of the surface groups and molecules producing this surface charge, the nature of the ions that compensate this surface charge (= counterions), and the route of transfer from water (the synthesis medium for the nanoparticles) to the ionic liquid. In addition, this chapter describes the characterisation techniques that are used to analyse the colloidal, magnetic, thermal, and thermodiffusive properties as well as the chemical composition of the nanoparticle dispersions.

The following chapters 3 to 7 are presented as articles that are already published or that will be submitted soon after missing measurements are completed that were not possible yet due to the COVID-19 lock-down.

Elucidating the key parameters to obtain colloidally stable dispersions in a broad range of ionic liquids at room temperature is the focus of chapter 3. This was analysed in zero magnetic field and under field varying the nanoparticle - ionic liquid interface and in particular the nanoparticle counterions.

Chapter 4 explores this interface for two promising counterions (based on a sulfonate zwitterion) in detail to understand their role on the colloidal stability. This is analysed in the well studied ionic liquid ethyl-methyl-imidazolium bistriflimide (EMIM TFSI) which is promising for the

targeted thermoelectric applications. The best compositions (nature and amount of the nanoparticle surface charge as well as of the counterions) are then used to study dispersions with different nanoparticle concentrations ϕ_{NP} and in a broad range of temperatures (20 to 200°C), all in regard for their potential use for thermoelectric applications.

The findings of chapter 4 led to start the systematic study of a new family of counterions, still based on a zwitterion, but with a phosphonate part that is explored in chapter 5. The possible tuning of the chemical structure of these counterions enables more detailed analysis of the interface thanks to steric effects.

Chapter 6 deals with the first physical properties of dispersions through the characterisation of thermodiffusion. Prior to experiments in ionic liquids, it was necessary to give a proof of concept and to optimize the setup for systems easier to handle, molecular solvents, at room temperature. The influence of the solvent (dimethyl sulfoxide (DMSO) and water) on the thermodiffusive properties of the nanoparticle dispersions is analysed.

In chapter 7 the developments of the thermodiffusion measurement setup during the MAGENTA project and explored in chapter 6 are used to analyse the thermodiffusive properties of one of the most promising ionic liquid-based nanoparticle dispersions which were studied in chapter 4 regarding their colloidal and thermal stabilities. The thermodiffusion is analysed at an elevated nanoparticle concentration ϕ_{NP} and with varying magnetic fields and temperatures.

Background

Contents

1.1 Colloids	5
1.2 Ionic liquids	6
1.2.1 Properties	7
1.2.2 Surface behaviour	8
1.3 Ionic liquid-based colloids	10

This chapter describes the background knowledge and literature findings necessary to understand the theory of the nanoparticle dispersions in ionic liquids developed during this PhD work. First, colloids in molecular solvents are described, followed by a description of ionic liquids and their behaviour next to surfaces. In a last step, findings in the literature concerning ionic liquid-based colloids are presented.

1.1 | Colloids

Although the aim of this work is to disperse magnetic nanoparticles in ionic liquids, the first step is the synthesis of these nanomagnets in water and therefore the basics of colloidal dispersions in molecular solvents are required.

DLVO theory [9] (named after Boris Derjaguin and Lev Landau, Evert Verwey and Theodoor Overbeek) describes colloidal stability in weak electrolytes by the interplay of repulsive electrostatic Coulomb interactions and attractive van der Waals interactions between the colloidal particles. Well dispersed nanoparticle dispersions are obtained if the repulsive interactions are

bigger than the attractive ones. Note that another possible stabilisation mechanism is due to steric repulsion. The strength of the van der Waals interactions is determined by the shape and size of the colloidal particles as well as by the chemical composition of the system. The repulsive electrostatic interaction between two charged surfaces decays exponentially with their separation and with a decay length called Debye length, which is given by

$$\kappa^{-1} = \sqrt{\frac{\epsilon k_B T}{2nq^2}} \quad (1.1)$$

with the dielectric constant ϵ of the medium ($\epsilon =$ vacuum permittivity $\epsilon_0 \times$ relative permittivity ϵ_r), the Boltzmann constant k_B , the temperature T , the ion charge q , and the number density of ions n .

Repulsive interactions can hence be controlled by the temperature, the choice of the solvent (e.g. $\epsilon_r=80$ for water and $\epsilon_r=46$ for dimethyl sulfoxide (DMSO)), the nature of the ions (valency) and the ion concentration (addition of salts, acids and bases).

Ferrofluids are a class of colloids consisting of magnetic monodomain nanoparticles with a diameter around 10 nm, stable in the long term, having usual properties of a liquid but behaving as a liquid paramagnet. It means that they move as a whole in the direction of the highest magnetic field while retaining their liquid properties in a uniform magnetic field H . [10, 11] These characteristics make them interesting for a number of technological applications, including sealing, damping, hydrodynamic bearings, loudspeakers, and sensors, biomedical diagnosis and therapy, targeted drug delivery, microfluidics, and optical materials. [10–22] Combining this with the properties of ionic liquids opens the possibility for new applications, for example at low pressures as well as at high temperatures and voltages. [23]

1.2 | Ionic liquids

Ionic liquids are a class of liquids that solely consist of ions, with melting points below 100°C. [24] Molten salts are their analogues with a melting temperature above 100°C. In the class of ionic liquids, a high number have melting points below room temperature and they are therefore called room-temperature ionic liquids. They have such a low melting temperature compared to conventional salts thanks to diminished electrostatic attraction between ions due to the larger size of the ions, weakening the interaction between the ions. In addition, most ionic liquids are composed of at least one unsymmetrical ion, having long side groups which

introduce a large number of degrees of freedom which further decrease their melting point by hindering crystallographic organisation. One possible classification considers aprotic, protic, and zwitterionic ionic liquids, shown in Figure 1.1. As shown in the figure, it is the cations that make

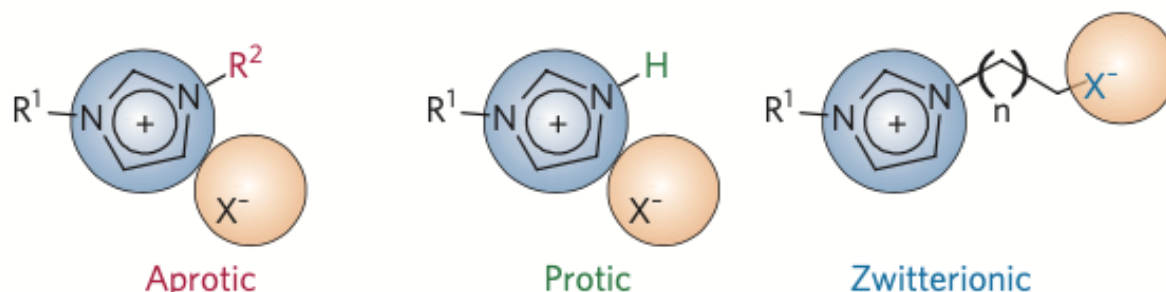


Figure 1.1 – Representation of three types of ionic liquids: aprotic, protic, and zwitterionic. Taken from [1]

the difference for the different types. Shown here is one of the most prominent cation type, which is with an imidazolium core. Other cores based on aromatic heterocycles are pyrrolidinium and pyridinium. Other possibilities include ammonium and phosphonium cores. Aprotic and protic ionic liquids are usually similar in structure, however with one of side chains (R^2) replaced with a hydrogen atom. Protic ionic liquids are simpler to synthesise than aprotic ionic liquids as they can be produced by a proton transfer reaction from a Brønsted acid to a Brønsted base, leading to a lower production cost, however they generally show lower thermal and electrochemical stabilities. [25] The third class is zwitterionic which consists of two oppositely charges separated by a alkyl chain. The choice of the cation changes the ionic liquid type, but the choice of the anion has a bigger effect on their properties. [26–31] Some of prominent anions in ionic liquids are bistriflimide, triflate, tetrafluoroborate, and acetate. One example for the huge effect of the choice of the anion on the ionic liquid properties is the different thermal stabilities of the two ionic liquids ethyl-methyl-imidazolium (EMIM) bistriflimide and EMIM acetate, changing from one of the best thermal stabilities reported for ionic liquids with the anion bistriflimide to one of the lowest with the anion acetate. [26]

1.2.1 | Properties

Ionic liquids have a variety of properties interesting for a huge amount of different application fields which include high liquidus temperature range, low vapour pressures, high thermal and electrochemical stabilities, modest conductivities, and their abilities to dissolve many chemical species. One of the most promising are energy related applications [1, 6, 32–34] which the

MAGENTA project is exploring. However, ionic liquids also have some properties hindering their industrial use. For instance, most ionic liquids have elevated viscosities compared to molecular solvents which leads to poor mass transport properties limiting their performance in energy applications. [6, 32]. The viscosity reduces exponentially with temperature, making this property less important at elevated temperature. Hence, their use at elevated temperatures is very promising for applications.

1.2.2 | Surface behaviour

The structure of ionic liquids close to solid surfaces has been the topic of a huge amount of research. The structure of these liquid interfaces has been studied by surface force experiments [35, 36] atomic force microscopy [37–40], scattering experiments [41, 42] quartz crystal microbalance [43] and molecular dynamics simulations [29, 44–46].

It has been found that the charge at solid surfaces is screened differently in ionic liquids compared to conventional electrolytes. At uncharged surfaces the distribution of the cations and anions of the ionic liquid is distributed equally. However, increasing the surface charge density σ leads to an enrichment of oppositely charged ions (= counterions) in the first layer close to the interface, even leading to overscreening, while the next layer contains more ions with the same charge as the surface (= co-ions). This structure is illustrated in Figure 1.2a) and is called a multilayer structure. This alternation with enrichment of co- and counterions can extend over a few layers. Further increase of the surface charge leads to a monolayer of counterions, shown in 1.2b), that completely compensate the surface charge, followed by a bulk ionic liquid structure above this layer. 1.2c) shows the case for even higher surface charges which is described by a crowding over several layers of counterions at the surface, first described by Bazant *et al.* [47]. The observed structures of ionic liquids close to solid surfaces has been described using various different approaches. One description, which is used in this PhD work is provided by Ivaništšev *et al.* [45, 46, 48]. This approach defines the transitions regarding the surface charge at which a first monolayer of counterions is formed on the surface. The interface structure is controlled by the ratio κ_{ion} of the solid's surface charge density σ to Θ_{ion}^{max} which is the charge density of a densely packed monolayer of counterions. [46] This quantity Θ_{ion}^{max} solely depends on the structure and geometry of the counterion, it is independent of the nature of the surface. A multilayered structure of ions is formed close to the solid surface if the ratio $\kappa_{ion} = |\sigma/\Theta_{ion}^{max}|$ is close to 0.5 (1.2a)). [45, 46] The transitions above were described for changing surface charge densities σ . However, a change of the ion size (Θ_{ion}^{max}) also influences the ratio κ_{ion} . Taking

the example for small ions, the smaller the ion the more ions can fit in a monolayer and Θ_{ion}^{max} increases, hence the ratio κ_{ion} decreases. Consequently, a higher σ value is needed to obtain a ratio $\kappa_{ion} \approx 0.5$.

Introducing additional ions different from the ionic liquid with a high surface affinity can change the interface structure. [38,39] Schemes of the interface for additional ions are depicted in Figure 1.2 for examples with d) half the size, e) the same size and f) double the size of the ionic liquid ions are depicted. Starting from a ratio $\kappa_{ion}=0.5$, the introduction of additional ions changes the ratio to $\kappa_{ion}=0.4$ and 1 for half the size, and double the size of the ionic liquid, respectively. Smaller ions therefore change the interface less than bigger ions.

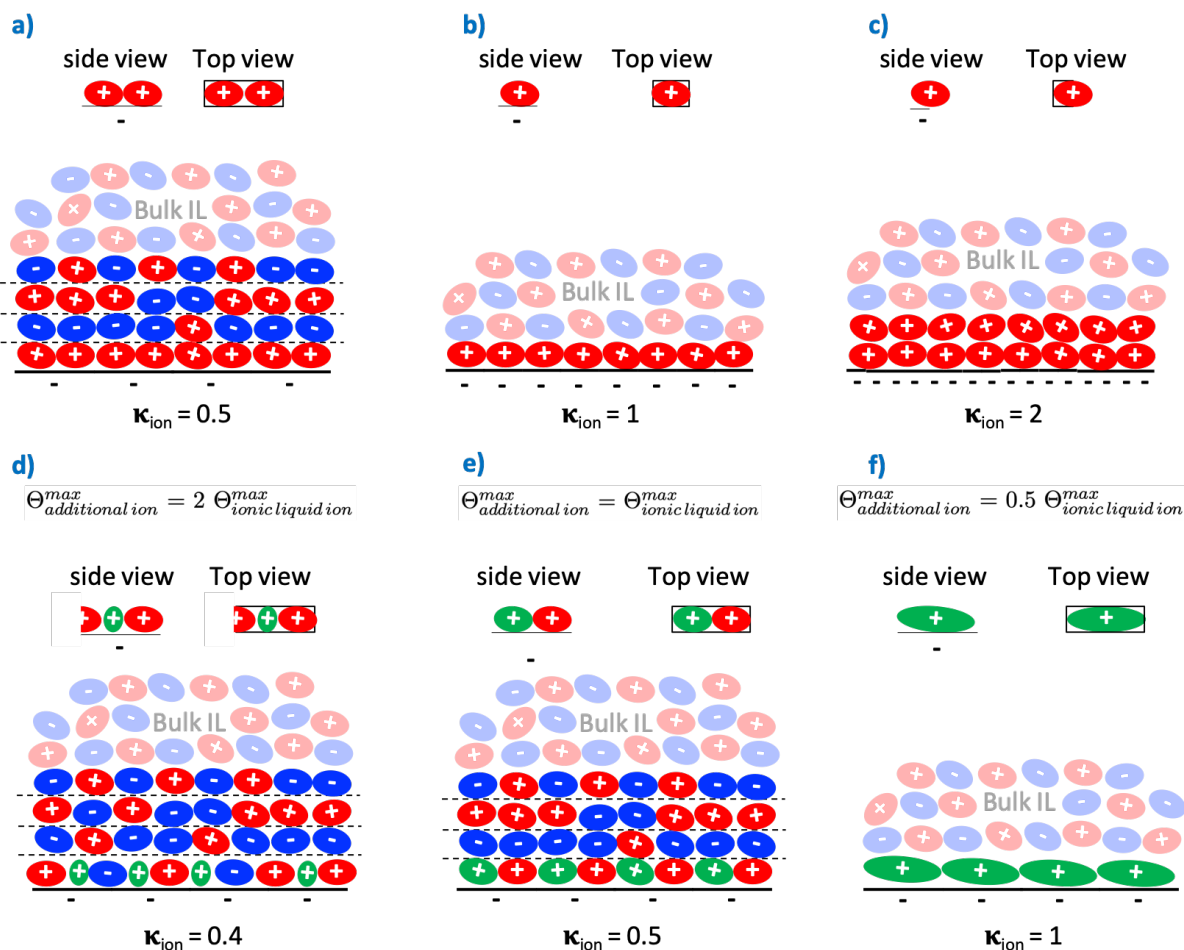


Figure 1.2 – Scheme of layering of ionic liquids at a surface depending on the ratio ratio $\kappa_{ion} = |\sigma/\Theta_{ion}^{max}|$. Example of a negatively charged surface); blue: anion of the ionic liquid, red: cation of the ionic liquid, green: additional cation; See text for information.

In addition, water can influence the nanostructure at the interface. [40] The effect is very different for protic and aprotic ions and depends strongly on the affinity for water.

1.3 | Ionic liquid-based colloids

The ionic liquids analysed here have a total bulk ion concentrations between 3 and 7 mol/L. Applying the concepts described in chapter 1.1 for electrostatically stabilised nanoparticles in molecular solvents, Debye lengths in the order of 0.1 nm are obtained which is smaller than the size of individual ionic liquid ions. Additionally, DLVO theory is based on some assumptions that are not valid in ionic liquids, e.g. point charges. Hence, this concept is not adapted for ionic liquids.

In the past, various strategies were used to produce nanoparticle dispersions in ionic liquids. However, these experimental approaches were mostly empirical since colloidal models to describe nanoparticles therein are still poorly developed and no predictions are possible to date. [49]

Possible stabilisation strategies are grafting of polymers to the surface of nanoparticles (steric repulsion) [50–53] inducing ion layering of the ionic liquid around bare nanoparticles (e.g. oxides coated with hydroxyl species), and coating nanoparticles with surfactants having groups that imitate groups of the ionic liquid or with small organic ligands. [2, 23, 50, 54, 54–56, 56, 57, 57–65]. However, despite the differences of the vast group of ionic liquids, studies were mainly focused on a small number of ionic liquids. This leads to the question whether the results for each system are specific or if these results are transportable to other systems. Only one group provided an overall picture about colloidal stability, however, mainly in molten salts [2, 54]. They showed by molecular dynamics (MD) simulations [2] and X-ray pair distribution analysis [54] of nanoparticle dispersions in molten salts that the ion layering on the nanoparticle surface leads to repulsive (oscillatory) forces that can outrank the attractive Van der Waals forces between the nanoparticles and therefore lead to colloidal stability, shown in Figure 1.3.

As explained in chapter 1.2.2 the multilayer structure on flat charged surfaces is dependent on the ratio $\kappa_{ion} = |\sigma / \Theta_{ion}^{max}|$. Supposing this model developed for flat surfaces can be also employed for curved interfaces such as nanoparticles, the same formalism can be used. The ratio can be adjusted by changing the surface charge density σ of the nanoparticles and by the choice of the solvent ions from the ionic liquid. The nanoparticle surface charge density can be changed depending on their material and possible coatings. For instance, the limits for citrate coated iron oxide nanoparticles are between 0 and 32 $\mu\text{C}/\text{cm}^2$. [3] Otherwise, Θ_{ion}^{max} can be changed by changing the ionic liquids itself (cation and anion) as well as by the addition of additional ions, thereby changing the ratio κ_{ion} . Various works evidenced that these additional ions influence the colloidal stability. [51, 56, 57, 61, 66]

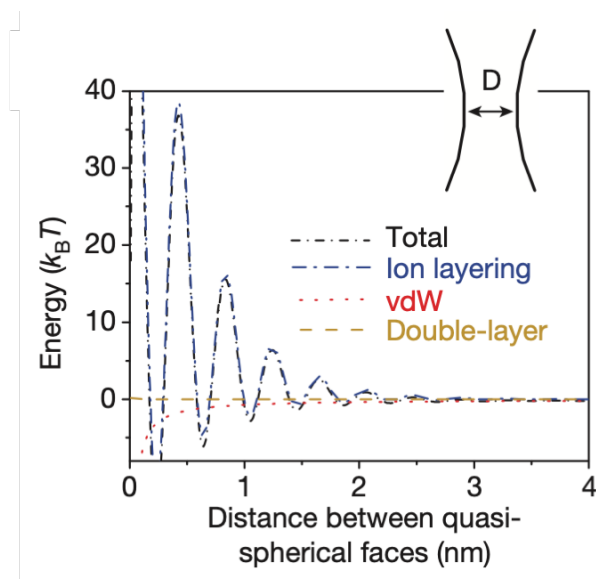


Figure 1.3 – Free energy of the interaction between two nanocrystals in a molten salt obtained by MD simulations. Taken from ref [2]

What needs to be remembered

Ionic liquids form a huge class of liquids with interesting and tunable properties. Combining their properties with nanoparticles can combine the advantages of both. However, an overall understanding to prepare and describe colloidal nanoparticle dispersions therein does not exist yet. Hence, it would be desirable to elucidate general parameters needed to obtain stable dispersions in a broad range of ionic liquids. This knowledge could then readily be employed to prepare stable nanoparticle dispersions in any ionic liquids.

Materials and methods

Contents

2.1	Materials	12
2.2	Dispersions of maghemite nanoparticles	14
2.2.1	Synthesis of maghemite nanoparticles	14
2.2.2	Dispersion of nanoparticles in molecular solvents	15
2.2.3	Routes of transfer towards ionic liquids	17
2.2.4	Concentrated ionic liquid-based ferrofluids	18
2.3	Characterisation techniques	18
2.3.1	Dynamic light scattering (DLS)	19
2.3.2	Flame atomic absorption spectroscopy (FAAS)	20
2.3.3	Forced Rayleigh scattering (FRS)	21
2.3.4	Inductively coupled plasma - mass spectrometry	21
2.3.5	Karl Fischer titration	22
2.3.6	Magnetisation measurements	22
2.3.7	Small angle X-ray/neutron scattering (SAXS/SANS)	23
2.3.8	Transmission electron microscopy (TEM)	25
2.3.9	Thermogravimetric analysis (TGA)	26

2.1 | Materials

All used materials are described here, hence, the materials sections in the articles can be skipped in further reading. The following materials were used without further purification:

1-Bromobutane (C_4H_9Br , purity 99%, Acros Organics); 1-Methyl-3-(butylphosphonic acid) imidazolium bromide ($C_8H_{16}BrN_2O_3P$, purity $\geq 95\%$, Sikémia); 1-Methyl-3-(hexylphosphonic acid) imidazolium bromide ($C_{10}H_{20}BrN_2O_3P$, purity $\geq 97\%$, Sikémia); 1-Methyl-3-(dodecylphosphonic acid)imidazolium bromide ($C_{16}H_{32}BrN_2O_3P$, purity $\geq 98\%$, Sikémia); (1,3-Propanediaminium-N,N,N,N',N'-pentamethyl-N'-dodecylphosphonic acid) dichloride ($C_{20}H_{47}Cl_2N_2O_3P$, purity $\geq 97\%$, Sikémia); 1-Methylimidazole ($C_4H_6N_2$, purity 99%, Acros Organics); 1-(4-Sulfobutyl)-3-methylimidazolium bistriflimide (HSBMIM TFSI, purity 98%, SOLVIONIC); 1-(4-Sulfobutyl)-3-methylimidazolium triflate (HSBMIM TfO, purity 98%, SOLVIONIC); 1-(4-Sulfobutyl)-3-methylimidazolium (SBMIM $^{\pm}$, purity 98%, SOLVIONIC); acetone (technical, VWR); ammonia solution (20%, VWR); citric acid ($H_3Cit \times H_2O$, purity $> 99\%$, NORMAPUR); diethyl ether (purity 99.8%, AnalaR Normapur); dimethyl sulfoxide (DMSO, technical, VWR); $HClO_4$ (65 wt% in water, VWR); hydrochloric acid (HCl , 37% water solution, AnalaR Normapur); iron(II) chloride ($FeCl_2 \times 4H_2O$, AnalaR Normapur, VWR); iron(III) chloride ($FeCl_3 \times 6H_2O$, Prolabo); iron(III) nitrate ($Fe(NO_3)_3 \times 9H_2O$, technical, VWR); Lithium Hydroxide ($LiOH \times H_2O$, purity $> 99\%$, Fluka BioChemika); Nitric acid (HNO_3 , 69.5% water solution, Carlo Erba); Poly (acrylic acid sodium salt) (PAA Na, average $M_w = 2100$ g/mol, SIGMA-ALDRICH); triflic acid (HTfO, 49.2 wt% in water, purity 99%, SOLVIONIC); triflimidic acid (HTFSI, purity 95%, Fluorochem); Poly (acrylic acid) (PAA, average $M_w = 2000$ g/mol, 63wt%, Acros Organics); Poly (Acrylic co-Maleic Acid) solution (PAAMA, average $M_w = 3000$ g/mol, 50 wt% in H_2O , SIGMA-ALDRICH); Sodium hydroxide (NaOH pellets, 98%, Acros Organics); Tetrabutylammonium hydroxide 30-hydrate ($TBAOH \times 30H_2O$, purity $> 99\%$, SIGMA-ALDRICH).

Figure 2.1 shows the structure of the studied ionic liquids.

Following the procedure of reference [67], BMIM Br was prepared by an alkylation of 1-bromobutane and 1-methylimidazole. Its anion was exchanged with OH with an AMBERLITETM IRN78 resin. The resin was prepared by alternating additions of NaOH (1M) and HCl (1M) in order to have a number of moles twice as big as the capacity of the resin and with intermediate washing with ultra-pure water till a pH between 5.5 and 7 was reached. BMIM Br was added and the pH was checked after one hour of stirring. A small quantity was mixed with Ag (NO_3) to test if Br^- ions were remaining, which is easy to detect as a formation of a pale yellow precipitate would be observed in this case.

Potable water is transformed to ultra-pure water (Type 1, resistivity of $\simeq 18$ M Ω cm) using a MILLIPORE DIRECT-Q system.

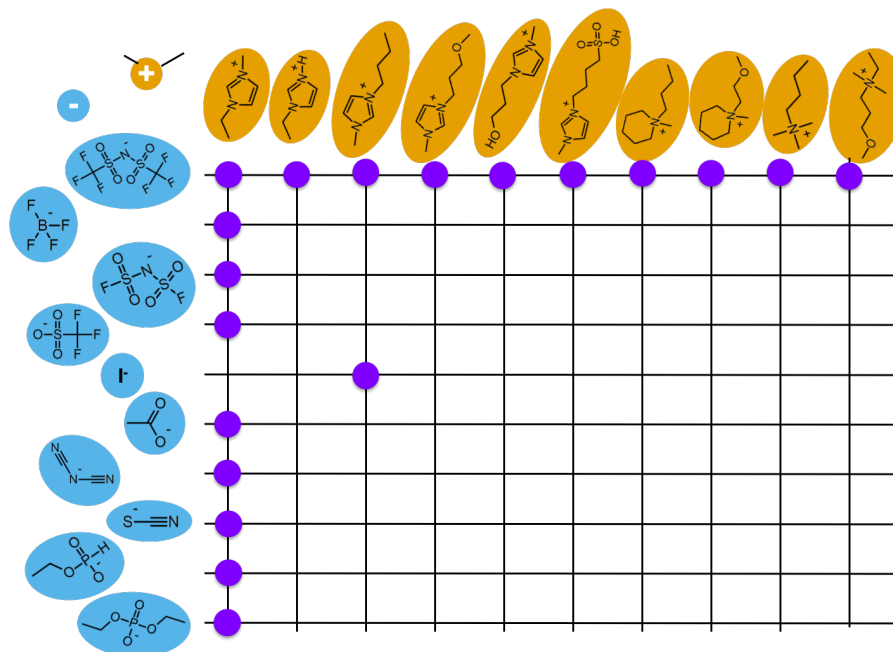


Figure 2.1 – Structure of studied ionic liquids. The influence of the anion is analysed with the same cation EMIM and the vice-versa for the same anion TFSI.

2.2 | Dispersions of maghemite nanoparticles

The synthesis of maghemite ($\gamma\text{-Fe}_2\text{O}_3$) nanoparticles in water and their dispersions in ionic liquids is described in detail in this chapter.

2.2.1 | Synthesis of maghemite nanoparticles

Iron oxides belong to the easiest oxide nanoparticles to produce. In addition, the synthesis in water is simpler and cheaper than in ionic liquids. Hence, a synthesis method of maghemite ($\gamma\text{-Fe}_2\text{O}_3$) nanoparticles in water was chosen that produces several grams of nanoparticles in one synthesis and that can be up-scaled, making it interesting for applications. [68] Acidic aqueous solutions of FeCl_3 and FeCl_2 were mixed in a stoichiometric ratio of 2:1 leading to precipitation of magnetite (Fe_3O_4) in a strongly alkaline medium after addition of ammonia. [68] These spinel type nanoparticles are sensitive to oxidation reactions in the presence of oxygen and to acid attack and therefore tend to evolve in acidic medium. [69] Hence, magnetite was chemically oxidised to maghemite at 80°C with $\text{Fe}(\text{NO}_3)_3$ leading to long-term stable maghemite nanoparticles. Subsequent washing with ether and acetone was followed with the final step of dispersion of the nanoparticles in aqueous nitric acid solution at a pH between 1.5 and 2. X-ray diffraction shows that maghemite nanoparticles are produced in this process. [11, 57] Size-sorting

based on phase separation induced by an added electrolyte was then performed to reduce the nanoparticle's polydispersity. [70] A medium size (around 9 nm) was chosen as a compromise between high magnetisation and low van der Waals interactions between the nanoparticles, both increasing with the nanoparticle size. High magnetisation is desired for thermodiffusion and thermoelectric applications, however, too big particles are difficult to be dispersed due to increasing attractive van der Waals interactions. The same batch of these size-sorted nanoparticles was used for all experiments in this work and is called "initial ferrofluid" in the following.

2.2.2 | Dispersion of nanoparticles in molecular solvents

The nanoparticle surface was then changed in water before their transfer to ionic liquids (sometimes with an intermediate transfer to dimethyl sulfoxide (DMSO)) changing the pH value. Figure 2.2 illustrates how oxide surfaces can be changed adapting the pH. [71] At low pH values, positive nanoparticles with OH_2^+ groups are obtained. At $\text{pH} \approx 7$, being the point of zero charge (PZC) of maghemite, uncharged nanoparticles have OH groups on their surface. High pH values lead to negative nanoparticles with O^- groups on the surface. Three different surface modifications are detailed in the following sections.

2.2.2.1 | Positive nanoparticles

Aqueous sodium hydroxide solution (1M) was added to the initial ferrofluid to reach the point of zero charge (PZC) of maghemite. The supernatant could then be removed from the magnetically sedimented nanoparticles. The concentration of free NO_3^- was reduced below 10^{-6} M, washing the nanoparticles several times with ultra-pure water. An aqueous acid solution is added at this step to redisperse the nanoparticles in a colloidal state. The particles are thus positively charged, their counterion being the conjugated base of the added acid. Various acids were used, in order to precisely analyse the influence of the nature of the counterion, represented as blue circles in Figure 2.2. The tested acids included 1-Methyl-3-(butylphosphonic acid) imidazolium bromide (HPAC₄MIM Br), 1-Methyl-3-(dodecylphosphonic acid) imidazolium bromide (HPAC₁₂MIM Br), 1-Methyl-3-(hexylphosphonic acid) imidazolium bromide (HPAC₆MIM Br), (1,3-Propanediaminium- pentamethyl-dodecylphosphonic acid) dichloride (HPAC2Ch Cl₂), 1-(4-Sulfobutyl)-3-methylimidazolium bistriflimide (HSBMIM TFSI), 1-(4-Sulfobutyl)-3-methylimidazolium triflate (HSBMIM TfO), benzenesulfonic acid ($\text{C}_6\text{H}_5\text{SO}_3\text{H}$), perchloric acid (HClO_4), triflic acid (HTfO), and triflimidic acid (HTFSI). The pH was reduced

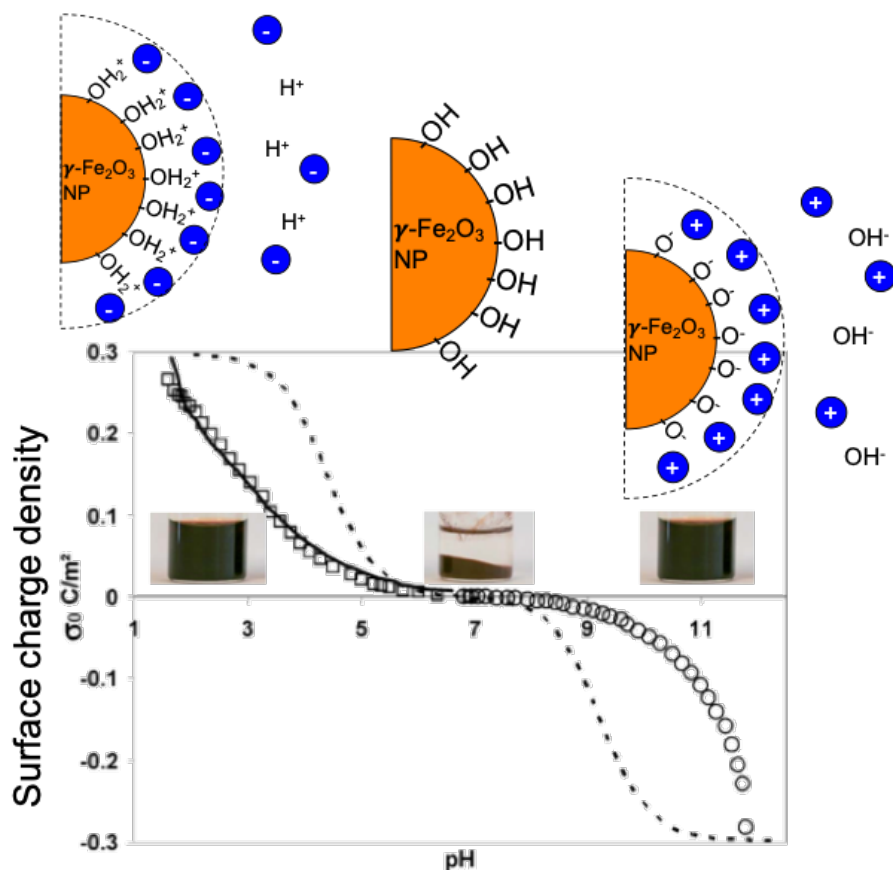


Figure 2.2 – Scheme of the surface state of maghemite nanoparticles at different pH values. Graph reproduced from reference [3].

to ≈ 1.5 -2 thus increasing the nanoparticle surface charge density σ to $\approx 30 \mu\text{C}/\text{cm}^2$, assuming a similar behaviour for different counterions [3]. In chapter 4 nanoparticle dispersions with additional pH values (up to 5) corresponding to lower surface charge densities σ (down to $4 \mu\text{C}/\text{cm}^2$) are prepared in order to analyse the effect of the surface charge density σ on the colloidal stability.

2.2.2.2 | Citrate coated nanoparticles

Citric acid was added in excess to the initial ferrofluid which led to agglomerated nanoparticles. Several washing steps with aqueous citric acid solution (0.01 M) were performed to remove the initial nitrate ions and to obtain a free citric acid concentration of approximately 0.01 M. A base (1 M) of the type $x\text{OH}$, with $x = \text{Li}, \text{Na}$, tetrabutyl ammonium (TBA) or 1-butyl-3-methyl imidazolium (BMIM) was added until a $\text{pH} \approx 7$ was obtained, which led to stable colloids. The negatively charged citrate coated nanoparticles compensate their charge with the cations x of the added base.

2.2.2.3 | Polymer coated nanoparticles

Concentrated aqueous nitric acid (68%) was added to aqueous poly(acrylic acid sodium salt) (PAA Na) solution (1 wt%) until flocculation at a pH of ≈ 2 was obtained. The initial ferrofluid was added, leading to flocculation. After a minute of magnetic stirring, the nanoparticles were magnetically sedimented and the supernatant was removed. Adding ammonia solution dispersed the nanoparticles at pH ≈ 7 , with NH_4 as the counterion. The remaining free polymer and ions were removed by dialysis with 10-12 kDa membranes. The same steps were used for poly(acrylic co-maleic acid) (PAAMA) except for the addition of nitric acid at the start, the PAAMA solution being already at pH ≈ 2 . The counterions for both polymer coated nanoparticles could then be changed, adding nitric acid (1M) until a pH approximately 2 occurs, several washing steps with ultra-pure water, and consequent addition of BMIMOH (0.02M) and TBAOH (1M) to disperse the nanoparticles at pH ≈ 7 or addition of aqueous ethylamine solution (≈ 5 -10 wt%) to disperse the nanoparticles at pH ≈ 9 . In a last step, a dialysis with 10-12 kDa membranes removed the remaining free ions.

2.2.2.4 | Transfer from water to another molecular solvent

Dimethyl sulfoxide (DMSO) is miscible with all tested ionic liquids, which is not the case for water. Hence, some of the modified nanoparticles were transferred from water to DMSO to test the influence of the way of transfer from the molecular solvent towards the ionic liquid. This was achieved by dialysis with 10-12 kDa membranes. Only the solvent molecules and the ions were exchanged as the nanoparticles were bigger than the pores in the membrane. A water concentration below 10^{-2} vol% is obtained, changing the outside DMSO solution with the adapted free ion concentration several times.

2.2.3 | Routes of transfer towards ionic liquids

These modified systems were added to the ionic liquids in adapted proportions to obtain nanoparticle dispersions with a volume fraction $\phi_{NP} \approx 1$ vol% in the ionic liquids after removing the initial molecular solvent in a freeze-dryer (Figure 2.3). The vapour pressure of ionic liquids is several magnitudes lower than that of water and DMSO, hence, the low pressure in the freeze-dryer ($p \approx 0.02$ mbar) removes the molecular solvent. All systems were kept at least 10 hours in these conditions in order to evaporate a maximum of initial solvent. The amount of evaporating ionic liquid in these conditions is not measurable with the used balances (detection

limit = 0.1 mg). One aim of this work is to analyse the effect of temperature on the systems and hence the freeze-drying method was chosen because the samples do not need to be heated for it. Other techniques including heating (e.g. evaporation at higher temperatures) were not chosen as they would bias the results as the sample would have been heated to a higher temperature already before the measurements.

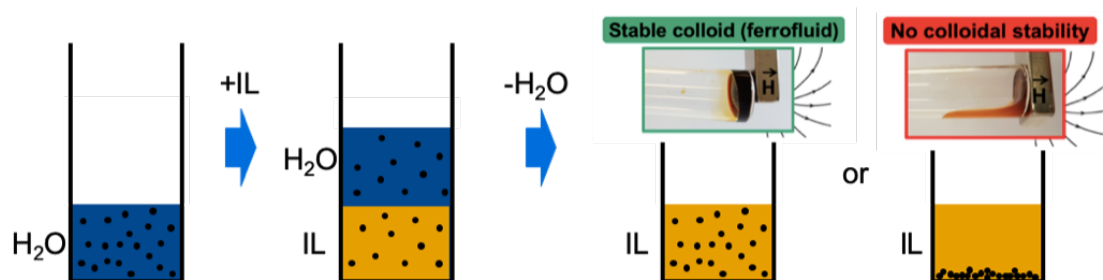


Figure 2.3 – Scheme of the transfer of the nanoparticle dispersions from a molecular solvent (shown here as H_2O) to an ionic liquid (IL).

2.2.4 | Concentrated ionic liquid-based ferrofluids

Two ionic liquid-based ferrofluids, one with $\text{SBMIM}^{\pm} \text{TFSI}^{-}$ counterions in EMIM TFSI and another with $\text{PAC}_6\text{MIM}^{\pm} \text{Br}^{-}$ counterions in EMIM FSI were centrifuged using an Optima 70 ultracentrifuge and a type 100 Ti fixed-angle rotor from the company Beckman Coulter, USA. The samples were centrifuged at 30 000 to 55 000 rpm (equals 55 000 to 243 000g) for one to two days at 19 °C. Separating the supernatant led to concentrated samples with nanoparticle volume fractions $\phi_{NP} \approx 5\text{-}20 \text{ vol } \%$ which were diluted with their supernatants to appropriate concentrations, if necessary.

2.3 | Characterisation techniques

Several techniques were used to analyse nanoparticle dispersions in molecular solvents and in ionic liquids in respect to their colloidal, magnetic, thermal, and thermodiffusive properties as well as their chemical composition. Figure 2.4 illustrates the multi-length-scale analysis approach applied to analyse the ionic liquid-based nanoparticle dispersions and over time. Visual observation on the mm-scale was performed first. Suspensions with big aggregates appear turbid and brownish due to visible light scattering and well dispersed maghemite nanoparticles appear dark red to black depending on the nanoparticle volume fractions. In a next step, visually stable

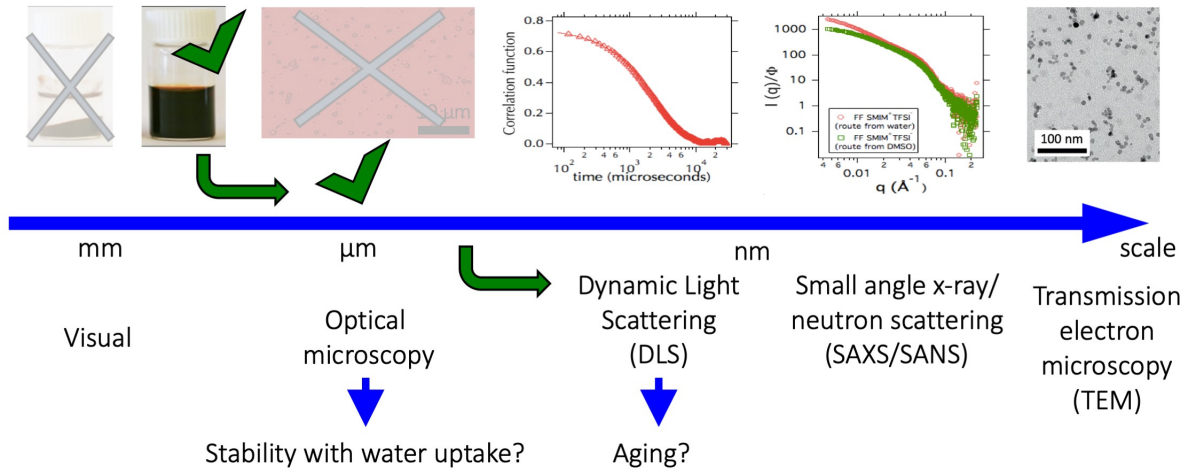


Figure 2.4 – Illustration of the multi-scale analysis employed in this work.

nanoparticle dispersions were analysed with optical microscopy on the presence of agglomerates on the μm -scale. Note that the stability with water uptake could be analysed with this technique. If no agglomerates were observed, the sample was analysed by dynamic light scattering (DLS), which was available at the PHENIX laboratory and its easy access permitted to study the sample ageing. If the apparent diameter extracted from DLS was lower than 100 nm, forced Rayleigh scattering (FRS) and small-angle X-ray scattering (SAXS) measurements were performed. The most promising nanoparticle dispersions were then analysed with small angle neutron scattering (SANS) and transmission electron microscopy (TEM).

2.3.1 | Dynamic light scattering (DLS)

Dynamic light scattering (DLS) measurements were performed using a Vasco, VascoFlex or VascoKin DLS Particle Analyzer from Cordouan Technologies to study translational diffusion properties of the nanoparticle dispersions for nanoparticle volume fractions ϕ_{NP} ranging from 0.1 vol% to 12.5 vol%. The laser of the devices is operating at a wavelength $\lambda=656$ nm. The sample was introduced in the Vasco particle analyser and an around 200 μm thin film was analysed in backscattering mode at 135° . For the VascoFlex and VascoKin particle analysers, the sample is analysed in any transparent container external to the machine, also in backscattering mode but at 170° . The corresponding wavevectors can be determined with equation 2.1.

$$q = \frac{4\pi n_0}{\lambda} \sin(\theta/2) \quad (2.1)$$

with n_0 the refractive index ranging for the analysed liquids between 1.33 (for water) and 1.57 (for 1-Butyl-3-Methyl Imidazolium iodide (BMIM I)) leading to a range of $Q=2.3 \times 10^{-3}$ and $2.8 \times 10^{-3} \text{ \AA}^{-1}$ for the Vasco DLS Particle Analyzer and $Q=2.5 \times 10^{-3}$ and $3.0 \times 10^{-3} \text{ \AA}^{-1}$ for the VascoFlex and VascoKin DLS Particle Analyzer. These conditions prevent both the effects of light absorption by the colloidal suspension and multiple scattering, even in strongly absorbing media. [72] In the case of the Vasco and VascoFlex DLS Particle Analyzers, field autocorrelation curves with a precise baseline at long times were obtained optimising parameters such as the sampling time, the number of channels, and the incident laser power. For the VascoKin DLS Particle Analyzer the only adjustable parameter is the incident laser power and autocorrelation curves are obtained for a much higher time range up to some seconds. The measured intensity correlation function $G(t)$ was transformed into the field autocorrelation function $G_1(t)$ using the expression 2.2:

$$G_1(t) = [G(t)]^{1/2} - offset \quad (2.2)$$

For both machines the so obtained curves are normalised with their maximum and were analysed with a stretched exponential function, $e^{-(t/\tau)^\beta}$ with a distribution of relaxation times described by a decay time τ and a stretching exponent β . The nanoparticle translation time τ was probed. It corresponds to the translational diffusion coefficient $D_t = (\tau Q^2)^{-1}$, which, in non-interacting conditions, is related to the intensity-averaged hydrodynamic diameter d_H using Stokes-Einstein's equation:

$$D_t = \frac{k_B T}{6\pi\eta \frac{d_H}{2}} \quad (2.3)$$

with the Boltzmann constant k_B , the temperature T , and the solvent shear-viscosity η .

Note that the solvent viscosity of the ionic liquid-based nanoparticle dispersions depends on the water traces and on the other additives. [73] In addition, reflection of the sample holders can introduce errors in external DLS measurements with the VascoFlex and VascoKin DLS Particle Analyzer. Therefore, the diffusion coefficient and the apparent hydrodynamic diameter d_H determined from DLS can have bigger errors depending on how well the sample is known and the technique controlled.

2.3.2 | Flame atomic absorption spectroscopy (FAAS)

The nanoparticle dispersions were dissolved in some drops of aqueous concentrated hydrochloric acid solution (37%) and then diluted with aqueous nitric acid solution (2%) till the desired

iron concentration was obtained which was determined by flame atomic absorption measurements (FAAS) with an Analyst 100 spectrometer from PerkinElmer. The volume fractions ϕ_{NP} were determined from the total iron concentration in the sample, considering the masses of the dilution steps and with the density for the liquids and maghemite (5.07 g cm^{-3}) and its molar weight (159.7 g mol^{-1}). [74]

2.3.3 | Forced Rayleigh scattering (FRS)

The working principle of forced Rayleigh scattering (FRS) is well described in chapters 6 and 7. Briefly, the irradiation of a high power lamp (6285 - 500W - Hg Arc Lamp - Spectra Physics) focused on the sample after passing through a grid, induces a thermal grating $\Delta T = T_1 - T_2$ with a period Λ between 88 and 145 μm due to the strong optical absorption of maghemite nanoparticles, illustrated in Figure 2.5 with illuminated and dark zones. The Soret effect induces a concentration grating $\Delta\phi = \phi_1 - \phi_2$ in the nanoparticle dispersion due to thermodiffusion of the nanoparticles, shown here for a thermophobic system (=the nanoparticles move towards cold regions, Soret coefficient $S_T > 0$). Both gratings ($\Delta\phi$ and ΔT) which can be separated due to their different time scales, are probed by the first order diffraction of a He-Ne laser beam detected in a photomultiplier (PM). Sample cells were developed in order to analyse ionic liquid-based colloids avoiding their contact with the atmosphere and one example is shown in the figure. They consist of a polyimide spacer (between 25 and 125 μm thickness) placed between two glass plates with the adapted dimensions for the FRS sample holder. The outside was sealed with an epoxy glue except for two entrances. The cell was then filled with the sample in inert atmosphere and sealed with Araldite[®] Rapid two component fast cure epoxy adhesive. The entrances and the possible sample filling in the cell was chosen in a S form in order to limit the contact of the analysed sample spot in the middle with the impurities coming from the entrances (e.g. glue). Only $\approx 5 \mu\text{L}$ are needed to fill a 25 μm cell which meant that almost every sample could be measured even when only small quantities were available.

The temperature of the FRS cells can be controlled between 20°C and 190°C and magnetic fields can be adjusted with two sets of permanent magnets up to 100 kA/m by variation of their distance to the sample.

2.3.4 | Inductively coupled plasma - mass spectrometry

The dilution of nanoparticle dispersions were prepared as for FAAS and the concentration of brome, iron and phosphore were determined with inductively coupled plasma - mass spectrometry

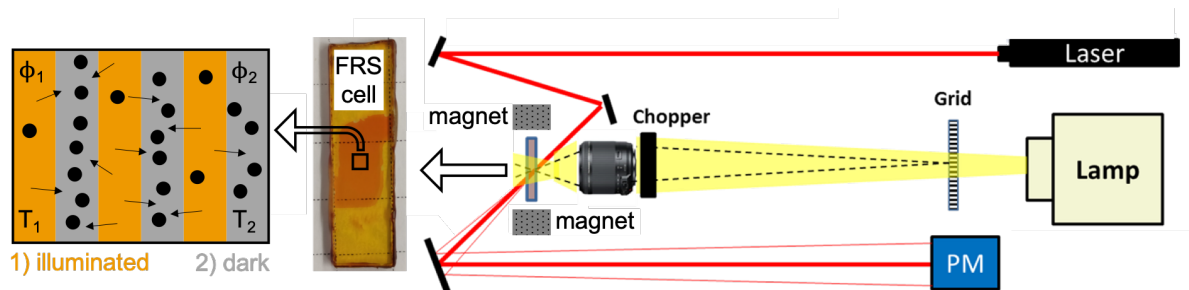


Figure 2.5 – Scheme of the used FRS setup and induced thermodiffusion for a thermophobic system. The cell is about $8 \text{ mm} \times 30 \text{ mm}$.

at IPGP (Institut de Physique du Globe de Paris). The nanoparticle volume fractions ϕ_{NP} were determined as for FAAS.

2.3.5 | Karl Fischer titration

Trace amounts of water were determined in the ionic liquids with Karl Fischer coulometric titration using a Schott TitroLine KF Trace titration unit. Water amounts can be quantified due to the oxidation reaction of sulfur dioxide with iodine which consumes water. Three measurements of each ionic liquid were performed with at least 0.1 mL or a multiple of 0.1 mL for each 1000 ppm of expected water. The results for the initial water content in some analysed ionic liquids are shown in Table S-1 of chapter 3

2.3.6 | Magnetisation measurements

Room temperature magnetisation measurements were performed using a home-made vibrating sample magnetometer (VSM) with magnetic fields up to $H=700\text{kA/m}$. A voltage proportional to the magnetisation M of the material is generated in the measuring coil when the vibrating sample is magnetised. The first Langevin's equation describes the mean orientation of a magnetic moment under a magnetic field H for monodisperse nanoparticles with a saturation magnetisation m_s and a diameter d . The saturation magnetisation m_s , d_o and σ are determined introducing a lognormal size distribution [11] with a median diameter d_o and a polydispersity σ in the fits. Ionic liquid-based ferrofluids were measured in sealed commercial polyimide capillaries with a diameter of approximately 1 mm as the available sample volume was not sufficient for the most of the samples.

2.3.7 | Small angle X-ray/neutron scattering (SAXS/SANS)

SAXS experiments were carried out with a laboratory XEUSS 2.0 (W)SAXS in the laboratoire Léon Brillouin, CEA, Saclay, France. The beam energy was fixed at 8 keV and the wavelength was $\lambda=1.54 \text{ \AA}$. The sample to detector distance was 3 m to yield an accessible Q-range of $0.004 \text{ \AA}^{-1} - 0.2 \text{ \AA}^{-1}$. Figure 2.6 illustrates the development of the used SAXS cells during this work. First, commercial polyimide capillaries ($\approx 1 \text{ mm}$ thick) were used, leading to poor transmissions in the order of 0.1% due to X-ray absorption by the iron atoms and the ionic liquids. In a second step, cells on the basis of 25-125 μm polyimide spacer sheets were developed to reduce the thickness, which however varied a lot between the cells and sealing was not always working well. Finally, 0.1 mm thick (and 1 mm wide) borosilicate capillaries from Vitrocom[®] gave the best compromise between absorption and diffused signal and sealing with Araldite[®] Rapid two component fast cure epoxy adhesive led to well sealed capillaries that could be reused even after several months. Still, the interior thickness error is $\pm 10\%$ and the wall thickness of 0.07 mm has an error of $\pm 20\%$. Hence, determination of absolute intensities was difficult and the high Q region ($> 0.1 \text{ \AA}^{-1}$) was rather noisy. Consequently, SANS measurements were used to adjust the SAXS curves to absolute intensities together with the nanoparticle volume fraction ϕ_{NP} .

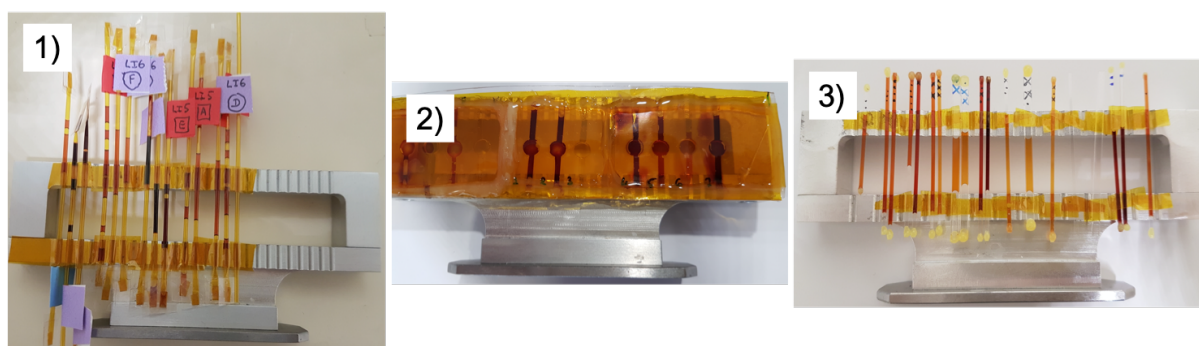


Figure 2.6 – SAXS cell development during this work. 1) commercial polyimide capillaries, 2) self-made cells based on polyimide spacer, 3) borosilicate cells.

SANS experiments were performed on the PAXY spectrometer at the LLB facility (CEA Saclay, France). Three different configurations were used in the three SANS allocated beam times during this work (1st beam time: neutron wavelength $\lambda=6 \text{ \AA}$, sample to detector distance $d=1\text{m}$; $\lambda=6 \text{ \AA}$, $d=3 \text{ m}$ and $\lambda=8.5 \text{ \AA}$, $d=5 \text{ m}$; 2nd: $\lambda=5 \text{ \AA}$, $d=1\text{m}$; $\lambda=5 \text{ \AA}$, $d=3 \text{ m}$ and $\lambda=8.5 \text{ \AA}$, $d=5 \text{ m}$; 3rd: $\lambda=4 \text{ \AA}$, $d=1\text{m}$; $\lambda=5 \text{ \AA}$, $d=3 \text{ m}$ and $\lambda=8.5 \text{ \AA}$, $d=5 \text{ m}$) leading to an accessible Q-range of 0.004 \AA^{-1} to 0.2 \AA^{-1} . Samples based on molecular solvents were measured in commercial quartz

cells with 1 mm inner thickness. Ionic liquid-based colloids were also measured in quartz cells but in self-made cells, shown in Figure 2.7 with ≈ 1 mm thick teflon spacer for nanoparticle volume fractions $\phi_{NP} < 3$ vol%, with 0.25 mm thick mica spacer for $3 \text{ vol}\% < \phi_{NP} < 10 \text{ vol}\%$, and with 0.125 mm thick polyimide spacer for higher ϕ_{NP} values. The spacers were glued together with the quartz windows and sealed with epoxy glue except for at least one hole on the top to evacuate gases that may form during the heating process. For both thinner cells a second opening was necessary to fill the cells (with the help of capillary forces) which was sealed with Araldite[®] Rapid two component fast cure epoxy adhesive after the cell was filled. This adhesive was used as it hardens at room temperature and is stable up to 200°C in the time of the measurements. For the case of ionic liquid-based ferrofluids, all cells were filled in inert atmosphere and placed in an oven filled with inert gas at around 0.5 bar, see Figure S3 in chapter 4.2. SANS measurements were performed at 27°C, 70°C, 135°C, 200°C and back to 27°C.

Standard correction procedures [75] were performed for both SAXS and SANS measurements

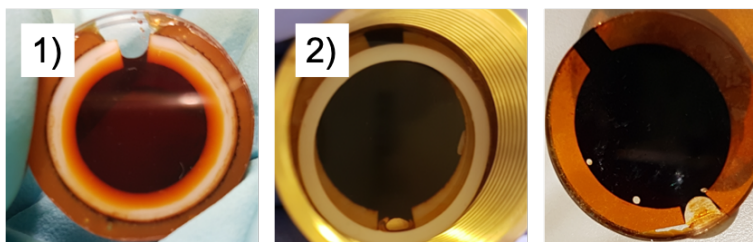


Figure 2.7 – SANS cells developed for high temperature measurements up to 200°C for nanoparticle volume fractions 1) $\phi_{NP} < 3$ vol%, 2) $3 \text{ vol}\% < \phi_{NP} < 10 \text{ vol}\%$, and 3) $\phi_{NP} > 10 \text{ vol}\%$. Each cell is about 2 cm in diameter.

using the Paset software (available free of charge at <http://didier.lairez.fr/>) to determine the absolute intensity expressed as (2.4):

$$I(q) = (\Delta\rho)^2 \phi_{NP} V_{NP} P(q) S(q, \phi) \quad (2.4)$$

with $\Delta\rho$ the difference of scattering length densities (SLD) between the nanoparticles and the solvent ($(\Delta\rho)^2$ being the contrast), the nanoparticle volume fraction ϕ_{NP} , the nanoparticle volume V_{NP} , the nanoparticle form factor $P(q)$ and their structure factor $S(q, \phi_{NP})$. The form factor $P(q)$ of the nanoparticles was determined from a set of dilutions of the initial ferrofluid at nanoparticle concentrations $\phi_{NP} = 0.1, 0.3$ and $1 \text{ vol}\%$ for SAXS measurements and $\phi_{NP} = 0.33, 0.66$ and $1 \text{ vol}\%$ for SANS measurements (keeping the free electrolyte concentration constant). These concentrations are chosen as a compromise between low particle interactions and a high

enough signal to noise ratio in reasonable times. $I(q)/((\Delta\rho)^2\phi_{NP})$ is plotted as a function of ϕ_{NP} for all wavevectors q and the form factor $P(q)$ is obtained with a linear extrapolation to the single particle contribution at $\phi_{NP} = 0$ vol% where $S(q, \phi_{NP} = 0) = 1$, shown in Figure 2.8 as an example for SAXS.

Figure 2.9 shows an example of scattered intensities obtained by small angle scattering for

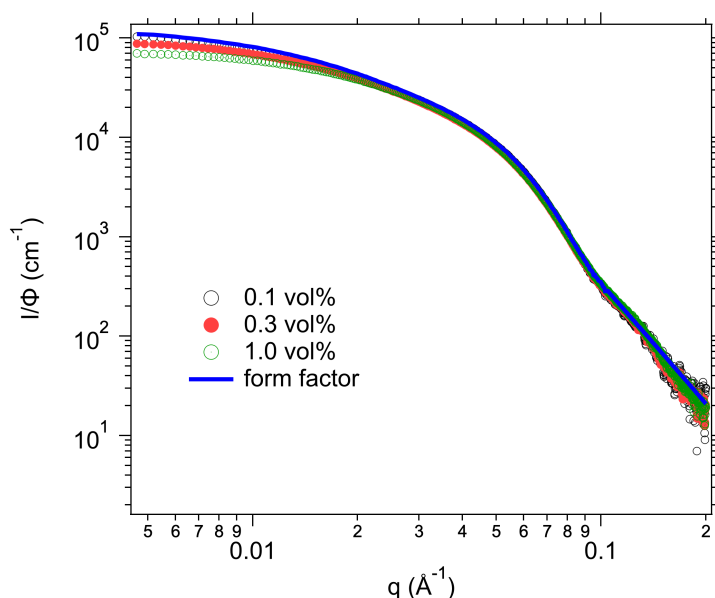


Figure 2.8 – SAXS intensities obtained for the initial ferrofluid with different nanoparticle concentration ϕ_{NP} and the deduced form factor.

nanoparticle dispersions with different nanoparticle concentration ϕ_{NP} in the inset. Different information about the nanoparticle dispersions like their surface, shape, size and compressibility (interparticle interactions) can be obtained depending on the spatial length scale in real space ($2\pi/q$) indicated in the graph. Structure factors for attractive ($S(Q \rightarrow 0) > 1$) and repulsive ($S(Q \rightarrow 0) < 1$) nanoparticle dispersions are also shown in the graph.

2.3.8 | Transmission electron microscopy (TEM)

Transmission electron microscopy (TEM) is used to show the crystalline structure of the maghemite nanoparticles and their dispersion state. The observation of nanoparticles dispersed in the ionic liquid is possible due to the low vapor pressure of ionic liquids that do almost not evaporate (in the time of the measurement) even in ultra-high-vacuum which is needed for TEM measurements. [49,50,53,64] However, complementary other techniques should be used as well as the preparation of the sample for the TEM measurements can change the sample properties (e.g. interparticle interactions). First, the sample needs to be diluted (here for a sample with around 1

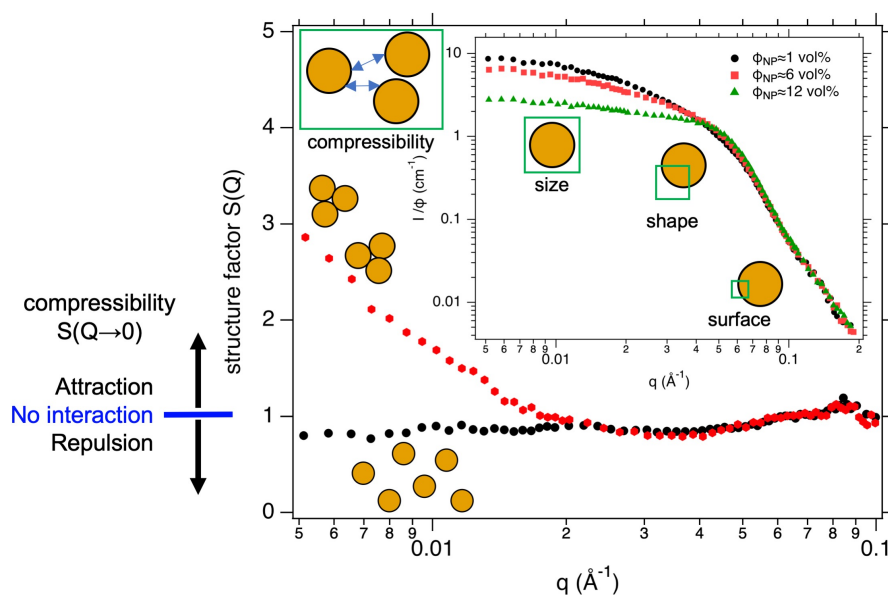


Figure 2.9 – Example of structure factors for attractive ($S(Q \rightarrow 0) > 1$) and repulsive ($S(Q \rightarrow 0) < 1$) nanoparticle dispersions obtained by small angle scattering. Inset; absolute scattered intensities (divided by ϕ_{NP}) with different nanoparticle concentration ϕ_{NP} for a repulsive system.

vol% by a factor 100 with pure ionic liquid) which can change the equilibrium of condensed and free counterions and thus affect the colloidal state. Second, during the deposition on the TEM grid, the sample is exposed to humidity of the air. As small amounts of water can affect the ionic liquid-solid interface, this can also affect the colloidal stability. [40] Third, in TEM measurements only a small volume of the sample is analysed. In general around 500-1000 nanoparticles are analysed which is several magnitudes smaller than for other techniques used here (e.g. SAS and DLS).

2.3.9 | Thermogravimetric analysis (TGA)

Ramped and isothermal temperature thermogravimetric analysis (TGA) were performed with a TGA 550 from TA Instruments. Around 10-20 mg sample (with a mass precision $\pm 0.1 \mu\text{g}$) were measured in platinum pans and with a nitrogen gas flow of 40 mL/min. Short-term temperature stabilities were conducted with a heating rate of $10^\circ\text{C}/\text{min}$ from room temperature up to 600°C and T_{start} and T_{onset} can be determined as indicated in Figure 2.10. Long-term temperature stabilities were measured in isothermal mode for several hours at the specified isothermal temperature with a heating rate of $20^\circ\text{C}/\text{min}$ from room temperature up to this temperature.

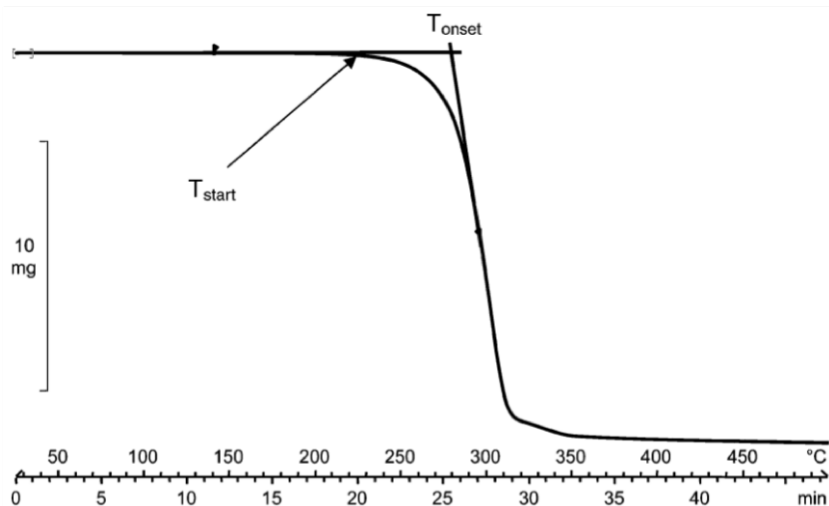


Figure 2.10 – Example TGA curve indicating how T_{start} and T_{onset} are determined. Taken from ref. [4]

What needs to be remembered

It is always favourable to use several techniques at once that complement each other making the results more trustworthy. Due to developments of measurement setups during this work (e.g. cells for FRS, VSM, SAXS, and SANS), it is now possible to perform most of the techniques (SAXS, DLS, FRS and TEM) with less than 20 μL in total. This allows to obtain information on colloidal and thermal stabilities with a very low consumption of the sample.

Elucidating the key parameters of colloidal dispersions of oxide nanoparticles in ionic liquids at room temperature

Contents

3.1	Introduction	28
3.2	Article: “colloidal dispersions of oxide nanoparticles in ionic liquids: elucidating the key parameters”	29
3.3	Conclusion	49

3.1 | Introduction

Contrary to other works in literature that usually focus on a single or small number of systems, this chapter explores the broad principles of colloidal stability of nanoparticles in a variety of ionic liquids through the systematic study of a number of different systems. Starting from the same batch of nanoparticles, several surface modifications are performed in order to tune the nanoparticle - ionic liquid interface and dispersions in various representative ionic liquids are analysed. The aim is to determine the key parameters in order to obtain long-term colloidal stability at room temperature. Moreover, the magnetic properties of the obtained nanoparticle dispersions are analysed to determine if they are ferrofluids and therefore suitable

for applications with magnetic fields.

3.2 | Article: “colloidal dispersions of oxide nanoparticles in ionic liquids: elucidating the key parameters”

Cite this: *Nanoscale Adv.*, 2020, 2, 1560

Colloidal dispersions of oxide nanoparticles in ionic liquids: elucidating the key parameters†

J. C. Riedl,^a M. A. Akhavan Kazemi,^a F. Cousin,^b E. Dubois,^{*a} S. Fantini,^c S. Lois,^c R. Perzynski^a and V. Peyre^{*a}

The combination of ionic liquid and nanoparticle properties is highly appealing for a number of applications. However, thus far there has been limited systematic exploration of colloidal stabilisation in these solvents, which provides an initial direction towards their employment. Here, we present a new and comprehensive study of the key parameters affecting the colloidal stability in dispersions of oxide nanoparticles in ionic liquids. Twelve diverse and representative ionic liquids are used to disperse iron oxide nanoparticles. The liquid interface of these nanoparticles has been carefully tuned in a molecular solvent before transferring into an ionic liquid, without passing through the powder state. Multiscale-characterisation is applied, on both the micro and the nano scale, incorporating both small angle X-ray scattering and dynamic light scattering. The results show the surface charge of the nanoparticles to be a crucial parameter, controlling the layering of the surrounding ionic liquid, and hence producing repulsion allowing efficient counterbalancing of the attractive interactions. For intermediate charges the strength of the repulsion depends on the specific system causing varying levels of aggregation or even none at all. Several samples consist of sufficiently repulsive systems leading to single dispersed nanoparticles, stable in the long term. Thanks to the magnetic properties of the chosen iron oxide nanoparticles, true ferrofluids are produced, appropriate for applications using magnetic fields. The strength and breadth of the observed trends suggests that the key parameters identified here can be generalised to most ionic liquids.

Received 5th September 2019
Accepted 15th January 2020

DOI: 10.1039/c9na00564a

rsc.li/nanoscale-advances

1 Introduction

Ionic liquids (ILs) have a variety of properties making them interesting for several fields of applications. For instance, their ability to dissolve many chemical species is used for synthesis and catalytic applications.¹ Their high thermal stabilities together with their low vapor pressures are useful for seals and bearings.² Their additional modest conductivities and high electrochemical stabilities make them interesting for thermoelectric applications.^{3–5} Adding nanoparticles (NPs) to ionic liquids can further improve the system's properties.⁶ The addition of charged nanoparticles, for example, can improve the thermoelectric properties compared to the use of a solvent alone.^{7,8} Increasing the electrical conductivity of colloidal dispersions provides new possibilities, for example, complex electrolytes for electrochemical devices.⁶

In the past, several approaches were used to stabilise nanoparticles in ionic liquids. One way is grafting of polymers to the surface of nanoparticles. If the ionic liquid is a good solvent for the polymer, the polymer swells in the solvent and causes steric repulsion. Stable colloids of this type were reported in EAN,^{9,10} EMIM X (X = AcO,⁹ EtSO₄¹¹), BMIM PF₆,¹² and OctylMIM TFSI.¹² These acronyms and the following are listed in the Abbreviations section.

Another way to achieve stabilisation is based on ion layering of the ionic liquid around the nanoparticles. Molecular dynamics (MD) simulations performed by Zhang *et al.*¹³ were used to calculate the free energy of the interaction between two nanocrystals in a molten salt. Molten salts are the equivalent of ionic liquids based on inorganic species, with a melting temperature above 100 °C. Their simulations showed that the decay length and the amplitude of the force induced by the oscillatory layering of ions are greater than those of van der Waals forces. This leads to colloidal stability. The layering close to the surface was recently experimentally determined by the same group using X-ray pair distribution analysis of nanoparticles in molten salts.¹⁴ This layering at the interface was used to explain colloidal stability for three types of nanoparticle surfaces: bare (*i.e.* oxides coated with hydroxyl species), coated with small organic ligands, and coated with surfactants having groups that imitate the groups of the ionic liquids. Bare nanoparticles have been reported to form

^aSorbonne Université, Laboratoire PHENIX, 4 place Jussieu, case 51, 75005, Paris, France. E-mail: emmanuelle.dubois@sorbonne-universite.fr; veronique.peyre@sorbonne-universite.fr

^bLaboratoire Léon Brillouin, UMR 12, CNRS-CEA, CEA-Saclay, 91191, Gif-sur-Yvette, France

^cSolvionic SA, 195 route d'Espagne, BP1169, 31036 Toulouse Cedex 1, France

† Electronic supplementary information (ESI) available. See DOI: 10.1039/c9na00564a



stable colloids in EMIM X (X = AcO,⁹ BF₄,¹⁵ SCN,⁹ EtSO₄¹³), BMIM X (X = BF₄,¹³⁻¹⁶ Cl,^{13,14} Br,¹⁴ I^{13,14}), OHEMIM TFSI,¹⁵ and DEME TFSI.¹⁵ However, the surface charge is usually not mentioned. Stable colloids with nanoparticles coated with small organic ligands have been reported in trihexyl(tetradecyl)phosphonium bis(2,4,4-trimethylpentyl)phosphinate¹³ and EAN.^{17,18} Surfactants having groups that imitate the groups of the ionic liquids are used to stabilise nanoparticles in EMIM TFSI,¹⁹ BMIM X (X = TFSI,²⁰ BF₄²¹), and C_rMIM X (r = 6, 7, 8 and X = TFSI;² r = 2, 4, 6 and X = BF₄²²).

However, ionic liquids with their numerous combinations²³ of anions and cations are very different from molecular solvents and the stability of ionic liquid-based colloidal solutions has been neither perfectly understood nor predictable to date.²⁴ Despite the enormous variety of ionic liquids, studies were in general focused on a small number of ionic liquids. This raises the question of whether the results for each system are a specific case and whether these findings are applicable to other systems. Only one group provided an overall picture about colloidal stability, however, mainly in molten salts.^{13,14} Ueno *et al.*¹⁵ studied the stability of hydrophilic silica particles in 11 ionic liquids, which produced some well dispersed systems according to rheological measurements. The stability was attributed to specific interactions between the surface-bound OH and one of the ions of the ionic liquid.

To the best of our knowledge, no overall experimental study exists on the colloidal stability of nanoparticles in room temperature ionic liquids, with a well described or controlled nanoparticle-ionic liquid interface, yet. Especially in systems with charged nanoparticles, counter-ions are almost never mentioned, although they are essential as they balance the charge in the initial solvent before transferring the nanoparticles to the ionic liquid. However, Mamusa *et al.*^{17,18} and Guibert *et al.*¹⁰ proved that the nature of these counter-ions influences the colloidal stability in the ionic liquid despite their low concentration compared to the ions from the ionic liquid. In addition, Nordström *et al.* observed an increased stability range of fumed silica particles due to the addition of Li⁺ ions.²⁵ These observations are in accordance with studies analysing the nanostructure at the interface between ionic liquids and chargeable surfaces like gold²⁶ and graphite.²⁷ In all the experiments the interfacial structure was modified when small quantities of Li⁺ or Cl⁻ ions were added and the surface potential was changed.

This work examines routes to properly disperse oxide nanoparticles, in this case (magnetic) iron oxides, in a large variety of ionic liquids, carefully controlling the solid-liquid interface, in order to give an overall picture of stability in ionic liquid-based colloids. The aim is to determine key parameters for colloidal stability, emphasising the role of: (i) the nature of the cations and anions of the ionic liquid, (ii) the nature of the nanoparticles' surface, (iii) the counter-ions, and (iv) the method of transfer of the nanoparticles to the ionic liquid. The characterisation methods of optical microscopy, transmission electron microscopy (TEM), Dynamic Light Scattering (DLS), small angle X-ray/neutron scattering (SAXS/SANS) and magnetic measurements are used in order to determine if these systems

are suitable for applications. Moreover, the colloidal dispersion stability is examined over time and under a magnetic field.

2 Experiments

2.1 Materials

The products purchased and used as received are listed in Section S-1.1 of the ESI† except for the ionic liquids, which are listed in Fig. 1.

2.2 The selected ionic liquids

Ionic liquids are chosen in order to test several families of cations and anions, stable at temperatures equal to or higher than 200 °C, Fig. 1. In one series of seven ionic liquids the cation is varied keeping the anion the same, in this case TFSI. Cations based on imidazolium, pyrrolidinium and ammonium are tested as well as the influence of the substituents on the imidazolium core. In the other series of six ionic liquids the cation was kept the same (EMIM) and the anion was varied (anions including fluorinated,

Abbreviation	IUPAC Name	Structure: Cation	Structure: Anion
BAM TFSI	N-Trimethyl-N-butylammonium bistriflimide		
BMPyrr TFSI	1-Butyl-1-methylpyrrolidinium bistriflimide		
HSMIM TFSI	1-(4-Sulfobutyl)-3-methylimidazolium bistriflimide		
OHPMIM TFSI	1-(3-Propanol)-3-methylimidazolium bistriflimide		
BMIM TFSI	1-Butyl-3-methylimidazolium bistriflimide		
HEIM TFSI	1-Ethyl-3-H-imidazolium bistriflimide		
EMIM TFSI	1-Ethyl-3-methylimidazolium bistriflimide		
EMIM FSI	1-Ethyl-3-methylimidazolium bis(fluorosulfonyl)imide		
EMIM TfO	1-Ethyl-3-methylimidazolium trifluoromethanesulfonate		
EMIM AcO	1-Ethyl-3-methylimidazolium acetate		
EMIM EP	1-Ethyl-3-methylimidazolium ethylphosphonate		
EMIM DEP	1-Ethyl-3-methylimidazolium diethyl phosphate		

Fig. 1 Ionic liquids studied (properties in Table S-1, ESI†).



carboxylic and phosphorus groups). Their properties (water content, water uptake, density, viscosity, refractive index, and miscibility with water) are shown in Table S-1 of the ESI.† All ionic liquids were supplied by SOLVIONIC.

2.3 Dispersion of nanoparticles in molecular solvents

In view of applications, the synthesis of nanoparticles in water is much cheaper and simpler than in ionic liquids. In addition, among oxides, iron oxides are easy to produce as nanometric particles. This is why maghemite iron oxide is chosen as it is formed at room temperature in water. In this work, the same batch of maghemite ($\gamma\text{-Fe}_2\text{O}_3$) nanoparticles is used for all experiments. It is prepared by co-precipitation in water of Fe^{II} and Fe^{III} solutions.²⁸ The detailed synthesis is described in Section S-1.2 of the ESI.† Fig. 2 shows a TEM image (a) and a HRTEM image (b) of these particles. Their diameter is obtained from a log-normal fit of the size distribution, shown in (c), with a median diameter of 8.7 nm and a polydispersity index $\sigma = 0.3$.

After the synthesis in water, the pH of the dispersion is around 2 and the nanoparticles bear a positive surface charge compensated by nitrate counter-ions. In the second step, their interface (ligand and counter-ion) is modified (still in water) and they can be transferred to DMSO²⁹ in order to elucidate the importance of the initial molecular solvent (water or DMSO). In these molecular solvents, the sign of the charge of the oxide surface can be changed by varying the pH with acids or bases, leading to a positive or a negative surface, respectively. In addition, the nature of the surface charge can be modified. For more details see Section S-1.3 of the ESI.†

Here, three types of nanoparticle surfaces are studied to test the function of the surface: bare nanoparticles with hydroxyl groups on the surface (that can be protonated or deprotonated), particles coated with citrate molecules and nanoparticles coated with a polymer (poly acrylate or poly(acrylate-co-maleate)). Besides the sign of the structural charge and the nature of the charged group producing it, a third significant parameter is the nature of the counter-ions of the nanoparticles which

compensate the charge. Li^+ , Na^+ , NH_4^+ , TBA^+ , and BMIM^+ are used for anionic particles and nitrate (NO_3^-), perchlorate (ClO_4^-), benzenesulfonate ($\text{C}_6\text{H}_6\text{O}_3\text{S}^-$), TFSI^- , and $\text{SMIM}^{+/-}$ are used for cationic ones. Among these, $\text{SMIM}^{+/-}$ TFSI^- is the deprotonated form of the ionic liquid HSMIM TFSI . Indeed, the sulfonate group is a strong acid in water, and thus the cation HSMIM^+ dissociates to form the zwitterion $\text{SMIM}^{+/-}$ and the resulting entity $\text{SMIM}^{+/-}$ TFSI^- is anionic. In water or DMSO, as the structural charge of the nanoparticles is large (around 2 elementary charges per nm^2), condensation of a large number of the counter-ions on the surface occurs. This defines the effective charge of the moving nanoobjects in the liquid and therefore of the dispersed oxide nanoparticles together with the condensed counter-ions. These condensed ions are crucial as their presence in the moving objects can completely modify the properties of the nanoparticles, for instance their thermodiffusion.³⁰ Finally, the amount of free electrolyte can be changed in order to modulate the range of the electrostatic repulsive interaction in molecular solvents. This parameter will not be explored here.

The volume fraction of nanoparticles in the initial molecular solvent Φ_{NP} is 1 vol%, except for most of the nanoparticles coated with polymers, for which $\Phi_{\text{NP}} = 0.1$ vol%.

2.4 Routes of transfer towards ionic liquids

In order to avoid any irreversible aggregation, which is likely to occur in the dry state, the particles are kept solvated in water or DMSO all through the nanoparticle surface modifications. The dispersions are mixed with a similar volume of the ionic liquids. DMSO is miscible with all the tested ionic liquids unlike water which is immiscible with some of them (tested in 50 : 50 mixtures, Table S-1, ESI.†). In the last step, the molecular solvent is removed by freeze-drying. Ionic liquids do not evaporate in this process due to their low vapor pressure. Fig. 3 shows pictures of the samples before and after freeze-drying for different typical situations. Dispersions in ionic liquids can be obtained from initially flocculated systems in water (brown colour, case a). When two phases exist after addition of the ionic liquid, phase transfer towards the ionic liquid rich phase can

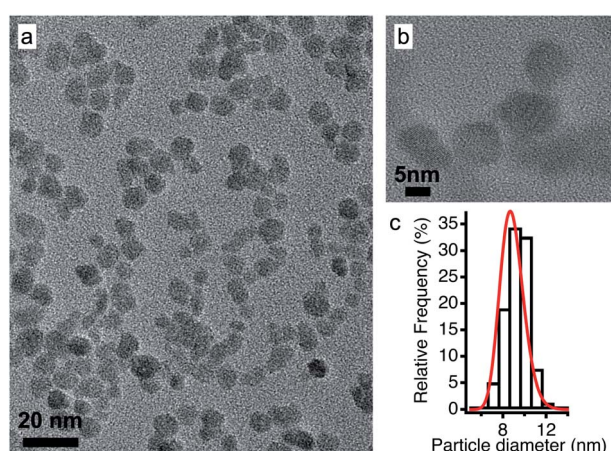


Fig. 2 (a) TEM and (b) HRTEM images of the maghemite nanoparticles and (c) their size distribution fitted using a log-normal distribution.

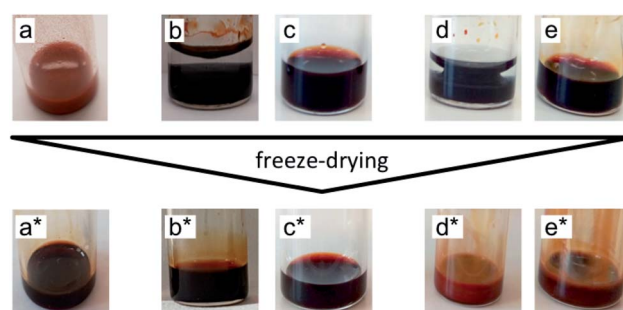


Fig. 3 Pictures of the samples before and after freeze-drying for possible transfer routes including at least one stable phase during the process. (a) An unstable sample becomes stable after freeze-drying (a*); stable (b) two-phase and (c) one-phase samples remain stable after freeze-drying (b* and c*); stable (d) two-phase and (e) one-phase samples become unstable after freeze-drying (d* and e*).



occur. This phase is always the bottom one as ionic liquids' densities are higher than the ones of water and DMSO (Table S-1, ESI†). Nanoparticles can disperse in this bottom phase (cases b and d), which may not be the case in the ionic liquid after freeze-drying (case d*). When the initial solvent and the ionic liquid are miscible, the nanoparticles can be dispersed in this mixture (cases c and e). However, this does not preclude the result after freeze-drying (case e*). Indeed, a flocculated initial sample can also be flocculated in the ionic liquid after freeze-drying. In conclusion, the initial state of aggregation in the molecular solvent (they are known to be reversible flocs here) and in the intermediate state in the mixture cannot be used to forecast the final state in the ionic liquid.

2.5 Analyses of the sample

The ionic liquid-based colloids are analysed on several spatial length scales and over time. Visual observation is performed on the mm-scale. Maghemite absorbs visible light in the blue and green wavelengths. Unstable suspensions appear turbid and brownish due to visible light scattering (Fig. 3a, d* and e*). Regarding the other samples in Fig. 3, stable dispersions appear dark red saturating to black with increasing nanoparticle volume fractions. If the sample looks stable, optical microscopy is performed in order to detect agglomerates on the micrometre scale. If none are observed, the sample is analysed by DLS. If the apparent diameter extracted from DLS is lower than 100 nm, SAXS and SANS measurements are performed. The viscosity of the final dispersions is difficult to determine accurately as it is highly dependent on the water traces²³ and on the other additives in the dispersions. Therefore, the diffusion coefficient and the apparent diameter determined by DLS are not always accurate (Section S-1.4.4, ESI†). Thus, small angle scattering (SAS, with neutrons (SANS) or with X-rays (SAXS)) is used to study the nanostructure and DLS is restricted to study the sample ageing (properly kept in a dry atmosphere), as the comparison between signals over time is reliable. Note that SAS is preferred to *in situ* TEM, which could be possible as ionic liquids do not evaporate,^{9,12,21,24} because it averages the whole sample and gives more precise information, especially on interparticle interactions. A laboratory SAXS instrument is used ($\lambda = 1.54 \text{ \AA}$ and Q -range $0.004\text{--}0.2 \text{ \AA}^{-1}$). However, the samples strongly absorb X-rays due to the ionic liquid itself and due to the iron atoms. Thus, either the transmission is low when using classical capillaries (around 1 mm thick) or the thickness is not accurate when reducing the thickness under 100 microns with home-made cells. As a consequence, absolute intensity cannot be determined and the high Q region ($>0.1 \text{ \AA}^{-1}$) is highly noisy. Therefore, SANS is used to determine the absolute intensity, to explore the high Q region and to check that X-rays do not damage the samples. The results prove that these SAXS measurements are reliable in the small Q range (Fig. S-1a, ESI†). The form factor $P(Q)$ of the nanoparticles is determined from several measurements at a low nanoparticle concentration in water and this curve is used for all samples in ionic liquids to determine structural factors $S(Q)$ using $S(Q) = I(Q)/(\Phi_{\text{NP}} \times \text{contrast} \times P(Q))$.

The value of $S(Q \rightarrow 0)$ therefore compares the studied dispersion to a “reference” dispersion of individual nanoparticles without interparticle interaction. The difference can be due either to interparticle interaction or to a change of the scattering objects (for example formation of small aggregates). Evolution of the size or shape of the nanoparticles after transfer to the IL can be discarded from the scattered intensity at a large Q . As normalized intensities in water and the ionic liquid are similar, the nanoparticles are the same (shown by the SANS data in Fig. S-1b, ESI†). If the scattering objects are still individual nanoparticles:

$$S(Q \rightarrow 0) = \chi = \frac{kT}{V_{\text{NP}}} \frac{\partial \Phi_{\text{NP}}}{\partial \Pi} \quad (1)$$

where Π is the osmotic pressure and V_{NP} is the volume of the nanoparticle. At a low volume fraction Φ_{NP} , Π can be developed and χ can be derived:

$$\Pi = \frac{\Phi_{\text{NP}} kT}{V_{\text{NP}}} (1 + A_2 \Phi_{\text{NP}}) \quad \text{and} \quad \chi \approx \frac{1}{1 + 2A_2 \Phi_{\text{NP}}} \quad (2)$$

A_2 is the second virial coefficient. For individual nanoparticles, $A_2 > 0$ corresponds to repulsive interparticle interaction with $\chi < 1$, whereas $A_2 < 0$ corresponds to attractive interparticle interaction with $S(Q \rightarrow 0) = \chi > 1$. For such individual nanoparticles, it has been shown that stable dispersions of similar maghemite nanoparticles were obtained up to A_2 around -20 which corresponds to $\chi \approx 1.7$ at $\Phi_{\text{NP}} = 1 \text{ vol\%}$ (and $\chi \approx 1.04$ at $\Phi_{\text{NP}} = 0.1 \text{ vol\%}$).³¹ Higher values of $S(Q \rightarrow 0)$ indicate that some aggregation occurs and it measures the number of particles per aggregate.³² These aggregates can be stable over time or not, depending on the interactions between them. Hereafter, we will focus on the values of $S(Q \rightarrow 0)$ to analyse the differences between the samples.

The colloidal stability of the dispersions is also analysed under a magnetic field, which increases the attractive component of the interparticle interaction and is a good indication of the efficiency of the stabilisation (a field up to $716 \text{ kA m}^{-1} = 9000 \text{ Oe}$ is applied). The iron concentration is determined by flame atomic absorption spectroscopy (FAAS) in order to obtain the nanoparticle volume fraction. The technical details and the implementation of the techniques are detailed in Section S-1.4 of the ESI†.

3 Results and discussion

The first systematic observation is the impossibility of transferring uncharged nanoparticles whatever the tested ionic liquid (first column in Fig. 4). The nanoparticles thus need to have a charge in the initial molecular solvent, a condition which is necessary but not sufficient. Several other parameters have a decisive impact as shown in Fig. 4. These parameters are the nature of the initial counter-ions, the nature of the nanoparticle surface, the nature of the ionic liquid and the route of transfer (this latter parameter is not shown here but is shown in Table S-2 of the ESI†).



surface charge →	0 $\mu\text{C}/\text{cm}^2$	16-32 $\mu\text{C}/\text{cm}^2$					200-300 $\mu\text{C}/\text{cm}^2$ *				
	OH	OH_2^+		Citrate ⁻			PAA ⁻			PAAMA ⁻	
concentration →	1 vol%	1 vol%		1 vol%			0.1 vol%			0.1 vol%	1 vol%
counter-ions →	None	NO_3^- , ClO_4^- , $\text{C}_6\text{H}_5\text{O}_3\text{S}^-$, TFSI ⁻	SMIM ^{+/-} , TFSI ⁻	Li^+ , Na^+	TBA ⁺	BMIM ⁺	NH_4^+	TBA ⁺	BMIM ⁺	NH_4^+	TBA ⁺
ionic liquids ↓	None										
BAMTFSI	no	no	yes	no	yes	no	no*	no*	no*	no*	
BMPyrrTFSI	no	no	yes	no	yes	no	no*	no*	no*	no*	
HSMIMTFSI	no	no	no	no	no	no	yes	yes	yes	yes	no
OHPMIMTFSI	no	no	yes	no	yes	no	no*	no*	no*	no*	
BMIMTFSI	no	no	yes	no	yes	yes	no*	no*	no*	no*	
HEIMTFSI	no	no	no	no	yes	yes	no*	no*	no*	no*	
EMIMTFSI	no	no	yes	no	no	no	no*	no*	no*	no*	
EMIMFSI			yes								
EMIMtFO			yes								
EMIMAcO	no	no	no/yes			no	yes			yes	yes
EMIMEP	no	no	no/yes			no	yes				yes
EMIMDEP	no	no	no			no	yes				no

Fig. 4 Stability observed by eye and optical microscopy. "Yes" means that at least one route produces dispersions with no aggregates on the micron scale. "No/yes" means that the sample stabilised over time. "No" means that dispersions with aggregates on the micron scale or bigger are obtained. Groups on the surface: OH: neutral hydroxyl ending groups on the nanoparticles at the point of zero charge of the nanoparticles; OH_2^+ : hydroxyl protonated ending groups on the nanoparticles; citrate⁻: citrate coated nanoparticles; PAA⁻ and PAAMA⁻: polymer coated nanoparticles (poly acrylate and poly(acrylate-co-maleate), respectively); SMIM^{+/-} TFSI⁻: butylsulfonate methylimidazolium bistriflimide (SMIM^{+/-} being a zwitterion); NO_3^- : nitrate; ClO_4^- : perchlorate; $\text{C}_6\text{H}_5\text{O}_3\text{S}^-$: benzenesulfonate; TFSI⁻: bistriflimide; TBA⁺: tetrabutylammonium; BMIM⁺: butylmethylimidazolium; NH_4^+ : ammonium.* In the case of a collapsed polyelectrolyte. If the polymer is not collapsed, part of the charge is on the surface of the oxide and part in the solvent, which is a different and more complicated situation. See the text for more information.

Fig. 4 gives the first assessment of the stability by visual observation using optical microscopy, usually confirmed by DLS. In the second step SAXS measurements of homogeneous samples allow analysis of the nanostructure of the dispersions. The measured scattered intensity is reproducible while performing several measurements on one sample or on different samples prepared in the same way. The $S(Q \rightarrow 0)$ values (given in Table S-2, ESI[†]) range between 0.6 (repulsive interaction) and 4.8 (presence of aggregates of approximately 5 nanoparticles). This means that the scattering objects range from individual particles to small aggregates of a few nanoparticles depending on the exact composition.

3.1 Routes of transfer towards ionic liquids

The molecular solvent of the initial dispersion is not always miscible with the final ionic liquid. Therefore, two very different routes of transfer exist: (i) in the case of immiscibility, there is a phase transfer of the particles between the molecular solvent and the ionic liquid; (ii) in the case of miscibility, the system passes through an intermediate state where the nanoparticles are in a 50 : 50 solvent/ionic liquid mixture, that is, a concentrated salt solution. Here water and DMSO were used as the initial solvents, since water is not miscible with all ionic liquids (Table S-1, ESI[†]) but DMSO is. In most cases, there is no visual difference between these two routes for the resulting dispersion in the ionic liquid. The stability observed by microscopy is the

same in most cases for both initial molecular solvents (water or DMSO). However, SAXS shows differences on the nanoscale. Fig. 5 shows one example of SAXS measurements for nanoparticles dispersed in HEIM TFSI with the same citrate coating and TBA⁺ counter-ions but initially dispersed in water or in DMSO before the transfer to the same ionic liquid. The normalized intensity shows differences at small wavevectors $q < 0.05 \text{ \AA}^{-1}$ indicating differences in the nanostructure. The sample transferred from DMSO scatters more at small q . $S(Q \rightarrow 0)$ in this case is 5 although $S(Q \rightarrow 0) = 0.8$ for the sample transferred from water. The interaction is thus repulsive in this latter sample although it is attractive with the formation of small aggregates when transferred from DMSO. This difference will be commented on later.

3.2 Nature of the counter-ions

The first idea concerning counter-ions is to closely adapt them to the ionic liquid, choosing one ion of the ionic liquid as the counter-ion. Looking closer at the cases, it can be shown that in most cases this doesn't lead to colloidal stability.

Positive nanoparticles with hydroxyl ligands in the initial solvent cannot be dispersed in any ionic liquid shown in Fig. 4 using the counter-ions nitrate, perchlorate, benzenesulfonate or TFSI⁻, even in ionic liquids containing TFSI⁻ as the anion. However, if the anionic entity SMIM^{+/-} TFSI⁻ is used as the counter-ion, these particles can be dispersed in more than half



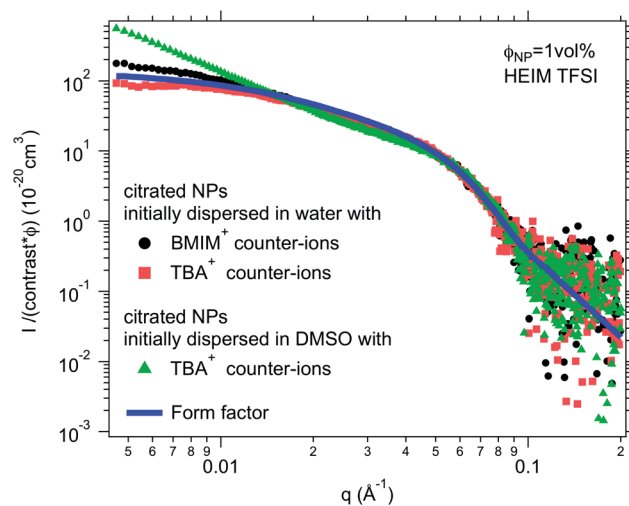


Fig. 5 SAXS absolute scattered intensities (normalized by the nanoparticle volume fraction $\phi_{\text{NP}} \approx 1$ vol% and their contrast with the solvent) for dispersions of citrated maghemite nanoparticles in HEIM TFSI with different counter-ions (BMIM⁺ and TBA⁺) and as a comparison with the same counter-ion TBA⁺ for samples once initially dispersed in water and once in DMSO before transfer to the same ionic liquid HEIM TFSI.

of the tested ionic liquids. Moreover, interestingly, they cannot be dispersed in the ionic liquid HSMIM TFSI, which is based on the same species, and they cannot be systematically dispersed in ionic liquids based on imidazolium cations. In contrast, they can be dispersed in ammonium based ionic liquids (BAM TFSI and BMPyrr TFSI). Keeping the same anion, in this case TFSI, the stability mainly depends on the side chains of the cation, while keeping the same cation, in this case EMIM, the stability depends on the nature of the anion. For example, samples based on ionic liquids with anions containing fluorinated groups (TFSI⁻, FSI⁻, and TfO⁻) yield micron-scale stable dispersions which is not systematically true for samples based on ionic liquids with anions containing phosphorus groups (EP⁻ and DEP⁻).

For negatively charged nanoparticles in the initial solvent (*i.e.* coated with citrate or with a polyelectrolyte), the counter-ions do not play a major role if the charge is a result of short negative polymers based on carboxylic groups. In contrast, their role is crucial if the carboxylic groups come from a small ligand (here citrate). Sodium and lithium initial counter-ions never enable dispersion in contrast to tetrabutyl ammonium (TBA⁺) and BMIM⁺, which lead to nanoparticle dispersions in some ionic liquids. Here again the side groups of the ionic liquid cation (methyl, butyl...) have more influence than the nature of its charged core (imidazolium, pyrrolidinium or ammonium). On the nanoscale however, additional differences between counter-ions are observed that cannot be detected with a microscope. Both TBA⁺ and BMIM⁺ lead to dispersions in HEIM TFSI for similar routes of transfer from water; however, interparticle interactions are weakly repulsive with TBA⁺ and weakly attractive with BMIM⁺ (Fig. 5). For nanoparticles coated with short polymers in HSMIM TFSI, interactions are also

weakly repulsive with TBA⁺ while small aggregates are formed with NH₄⁺ or BMIM⁺ (Fig. 6).

3.3 Nanoparticle surface: organisation and charge

Although similar carboxylic groups produce the nanoparticles' charge for polyacrylate-based polymers and small citrate ligands, the nanoparticles cannot be dispersed in the same ionic liquids with these two coatings. Polymer coated nanoparticles are in particular the only ones tested here which can be dispersed in HSMIM TFSI.

In water, these short polymers (around 20 monomers) are strongly adsorbed to the nanoparticles by around ten monomers, the other monomers being free, acting as "hairs".³³ Being charged, these "hairs" enable a much higher nanoparticle electric charge to be reached, more than ten times higher than that with citrate ligands. Therefore, these polymers provide stabilisation which is both electrostatic and steric in water.

In the ionic liquid, the charged polymers can still behave as "hairs" around the nanoparticle or collapse on the surface depending on its solubility in the ionic liquid. A steric contribution to the interparticle interaction can exist and/or some contribution resulting from induced organisation due to the charges. This has been seen in EAN where dispersions have been obtained with similar nanoparticles when coated with polyacrylate or with a corresponding polyacrylic uncharged polymer.¹⁰

Here, the solubility of the polymer PAA⁻ with NH₄⁺ counter-ions (see Section S-1.3.3 of the ESI† for the experimental details) correlates with the stability reported in Fig. 4 except in HSMIM TFSI. In this latter ionic liquid, the polymer solubilizes after exposure of the ionic liquid to air, which introduces a small percentage of water. As the nanoparticles are originally dispersed in water, some water can remain close to their

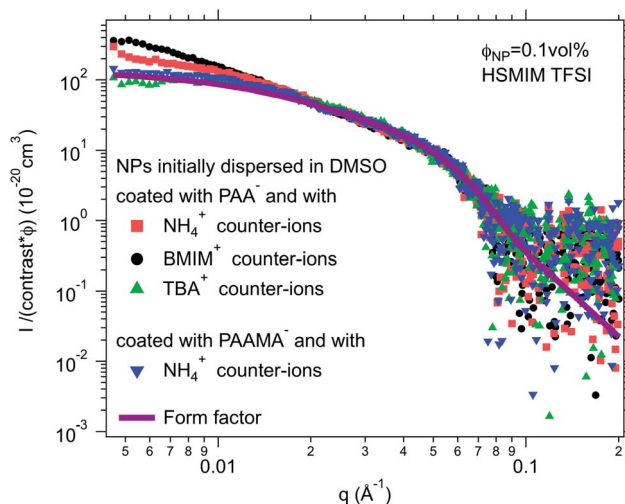


Fig. 6 SAXS absolute scattered intensities (normalized by the nanoparticle volume fraction $\phi_{\text{NP}} \approx 0.1$ vol% and their contrast with the solvent) for dispersions of polymer coated maghemite nanoparticles in HSMIM TFSI with different counter-ions for PAA⁻ and as a comparison with the same counter-ion NH₄⁺ for PAA⁻ and PAAMA⁻ coated nanoparticles.



interface after the transfer to the ionic liquid despite the freeze-drying process, which explains the dispersion of the nanoparticles in HSMIM TFSI despite the insolubility of the polymer in the dry HSMIM TFSI.

In the first situation, *i.e.* the polymer is soluble in the ionic liquid (EMIM X with X = AcO, EP, DEP), dispersions can be obtained; however small aggregates are nearly always present (Table S-2, ESI[†]). The steric contribution to repulsion brought about by the polymer is thus lower than the highest repulsion that can be obtained without polymers, which is not intuitive. An influence of the nature of the counter-ions nevertheless still exists.

In the second situation, *i.e.* the polymer is not soluble in the ionic liquid, the polymer is collapsed on the nanoparticle, and thus a much smaller steric contribution to repulsion is expected. Despite a large apparent charge, the nanoparticles are not dispersed whatever the nature of the counter-ions. This can originate from a rougher surface or from the higher density of charge due to the polymer (around $32 \mu\text{C cm}^{-2}$ for citrate and $400 \mu\text{C cm}^{-2}$ for polyacrylate³³). This high value can influence the structuring of the ionic liquid at the surface^{34–36} and could be the origin for the difference in colloidal stability between nanoparticles coated with small citrate ligands or larger polymers containing the same carboxylate groups. This will be discussed in more detail later.

3.4 Discussion: which are the key parameters?

The presented results confirm the major role of the solid–liquid interface, through the charge of the nanoparticles and the nature of the molecules close to the surface, in order to produce a repulsive contribution to the interaction able to counterbalance the attractive van der Waals (plus in this case also magnetic dipolar) interaction leading to a stable colloidal dispersion in ionic liquids. This generalizes the previous findings in one particular ionic liquid, EAN.¹⁸ The role of the transfer route and of the nature of the charges is also highlighted here. Moreover, the experiments evidence that, whatever the ionic liquid, a combination can be found in order to obtain colloidal dispersions. What is hidden behind these observations?

Layering of ionic liquids on flat surfaces has been evidenced for a long time using several experimental techniques^{37–39} and numerical simulations.^{36,40–43} It depends on the nature of the surface, on its charge, on the amount of water and on the ionic liquid. This layering is assumed to be at the origin of the colloidal stability in ionic liquids if the number of ionic layers is sufficient. Very recently evidenced on nanoparticles in molten salts, which are cousins of ionic liquids melting at higher temperature, and in BMIM I, the organisation of the ions close to the solid has been studied by X-ray PDF analysis.¹⁴ This is supported by previous¹³ and new¹⁴ numerical simulations. These authors correlate the colloidal stability with the affinity of the molten salt for the nanoparticle surface. Their nanoparticles are based on various materials and dispersed in the molten salts after removing the initial ligands present in the original organic solvent used for synthesis, without an additional control of the

nanoparticle surface. Here in contrast, we focus on nanoparticles all made from the same material with fine tuning of their surface.

Here the nanoparticle surface is modified in the initial step of the preparation in the molecular solvent, where nanoparticles are charged, this charge being compensated in their neighbourhood by an equal number of counter-ions. The charge on the iron oxide nanoparticles is the structural charge Z_{NP} . As it is large here (around 1–2 charges per nm^2 , Z_{NP} around 250–500 for bare and citrate coated nanoparticles and even more for the polymer coated ones[‡]), a large portion of the counter-ions is condensed on the nanoparticles, resulting in a smaller effective charge at the surface of this layer of bound counter-ions. This effective charge in the molecular solvent is compensated by the free counter-ions which are around the nanoparticles in the diffuse layer. An electrolyte composed of the counter-ions and an ion of opposite charge, *i.e.* a co-ion, is present in the initial colloidal dispersions in molecular solvents, with concentrations usually lower than 0.1 mol L^{-1} .

While transferring these nano-objects from the initial molecular solvent towards the ionic liquid, the electrolyte mentioned above is diluted in a much larger concentration of ions of the ionic liquid. Concerning the counter-ions of the nanoparticles, many situations can occur: the initial condensed counter-ions of the nanoparticles can stay around the nanoparticles or they can be exchanged with ions from the ionic liquid. Any intermediate situation can also be encountered. Therefore, the effective charge at the surface of the first layer of bound counter-ions may differ in the ionic liquid compared to the initial value in the molecular solvent.

Considering the spatial distribution of ions, on a random basis, the initial free counter-ions of the nanoparticles should be distributed over the whole volume, and the initial condensed counter-ions could be replaced by the ions of the same charge from the ionic liquid. However, it was observed in EAN that some of the condensed initial counter-ions of sodium and lithium stayed close to the nanoparticle, explaining the difference in the nanostructure in the corresponding dispersions in EAN.¹⁸ In the present experiments, the influence of counter-ions (Fig. 4–6) also proves that at least some of them stay close to the interface. They generate a particular ionic liquid organisation, and therefore modify the interparticle interactions, the nanostructure and the stability. This influence of the counter-ions can be due to their affinity with cations, anions and the nanoparticles' surface, to their interaction with water, and to their size compared to that of the cations and anions of the ionic liquid. For example, Na^+ and Li^+ are small compared to the cations and anions of the scanned ionic liquids, which can strongly influence (destroy or improve) any spatially oscillating structural organisation of ionic liquid ions around the nanoparticles. Similar localisations of species at the interface can be deduced from the experiments of Zhang *et al.*: they managed to disperse nanoparticles in an ionic liquid where these

[‡] If the polymer is not collapsed, part of the charge is on the surface of the oxide and part in the solvent, which is a different and more complicated situation. See the text for more information.



nanoparticles were flocculated by adding a small amount of another ionic liquid which allowed their dispersion.¹³ Localisation of lithium ions added as LiBF_4 in BMIMBF_4 on fumed silica particles has also been reported from spectroscopic measurements.²⁵ Finally, experiments analysing the nanostructure of ionic liquids at the surface of chargeable flat surfaces like gold²⁶ and graphite²⁷ show that the interfacial structure is modified when small quantities of Li^+ or Cl^- ions are added and if the surface potential and the resulting density of charge are changed. The influence of the initial counter-ions thus comes from their possible localisation at the solid-liquid interface, which also depends on the nanoparticles' surface charge and on the details of the different molecules at the interface.

It is not only the counter-ions that are important but also the value of the nanoparticles' structural charge Z_{NP} on their surface, through its density σ . Indeed, the surface structures vary with the superficial surface charge densities σ , as evidenced by molecular dynamics simulations^{36,40,42,43} and experiments, for example, on flat conductive surfaces^{38,43,44} changing the electric potential applied on the solid electrode. Looking deeper into the details of the phenomena obtained from simulations,⁴² the structure close to a flat charged surface strongly depends on the surface charge density σ and on the nature of the ion of opposite charge in the IL. For this counter-ion, they define $\Theta_{\text{ion}}^{\text{max}}$, the

maximal density of the counter-ions that can be accumulated in the first layer of pure counter-ions close to the charged solid surface. Values of $\Theta_{\text{ion}}^{\text{max}}$ were calculated by means of molecular dynamics simulations⁴⁵ for several representative ions, not considering the influence of co-ions (the same sign of charge as the surface). The values for the ones used here are $\sim 45 \mu\text{C cm}^{-2}$ for BMIM^+ , $\sim 30 \mu\text{C cm}^{-2}$ for TBA^+ , and $\sim -50 \mu\text{C cm}^{-2}$ for TFSI^- . $|\Theta_{\text{ion}}^{\text{max}}|$ is bigger for smaller ions as more ions can fit in the same area. For example, the value for BF_4^- is $\sim -100 \mu\text{C cm}^{-2}$ and such high absolute values are expected here for the alkaline cations sodium and lithium and for the anions nitrate and perchlorate.

On an uncharged surface, where $\sigma/\Theta_{\text{ion}}^{\text{max}} = 0$, the ionic liquid is seen to organise in the plane of the surface but not perpendicular to it. The first layer close to the surface contains cations and anions. An increase in the charge, while $|\sigma/\Theta_{\text{ion}}^{\text{max}}| < 1$, can be compensated by counter-ions in the first layer. Each counter-ion occupies less space than the area per surface charge available. Therefore, the amount of counter-ions in the first layer can be larger than the surface charge. This organisation is sometimes called overscreening in the literature.⁴⁶ If the first layer is not fully filled with counter-ions, then co-ions will complete the layer.²⁷ In the direction perpendicular to the surface, layers are formed with an oscillatory/multilayer structure of counter- and co-ions and with a maximal number of layers around $|\sigma/\Theta_{\text{ion}}^{\text{max}}| =$

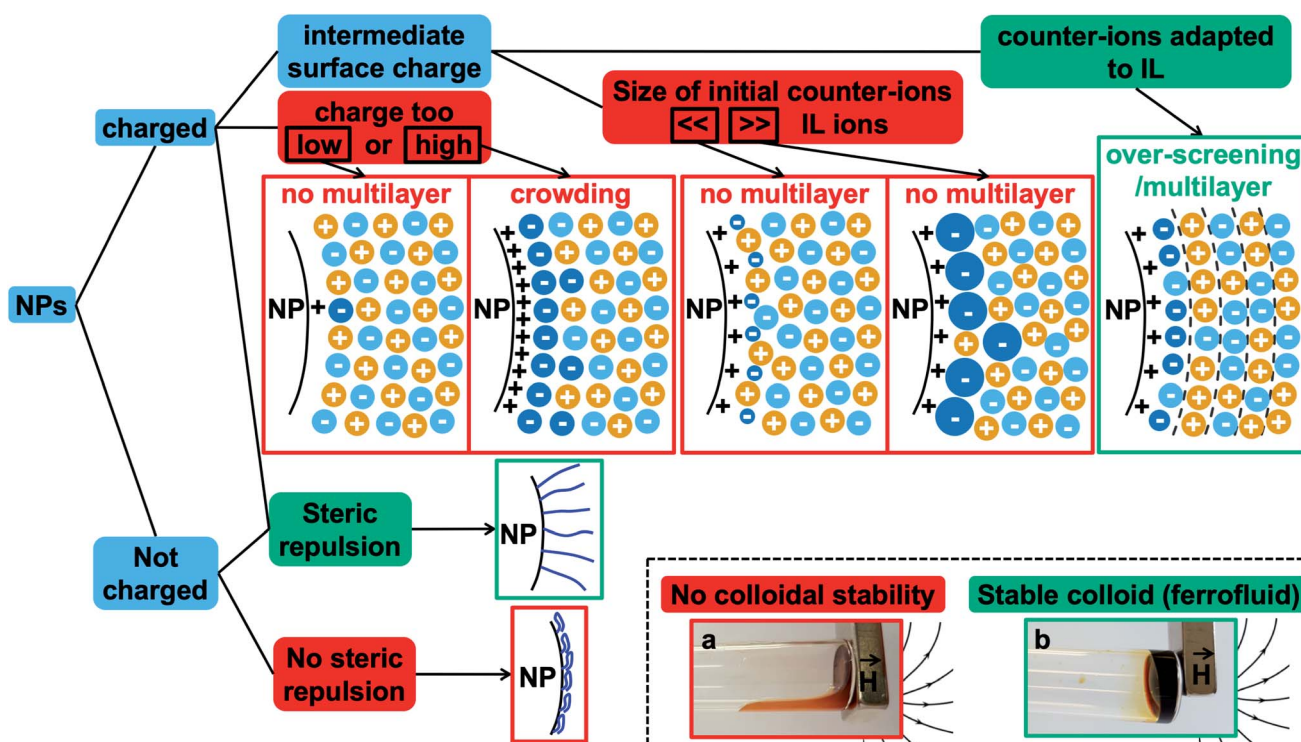


Fig. 7 Summary of the different possibilities at the interface of the nanoparticles, charged or not, in an ionic liquid. This indicates the main parameters to tune in order to obtain stable ionic liquid-based colloids. Red boxes: conditions leading to unstable systems. Green boxes: conditions leading to stable dispersions. The diagrams show possible organisations close to the charged solid interface in the case of a positive structural charge of the nanoparticle: the dark blue ions are the initial counter-ions of the nanoparticles, the light blue ions are the counter-ions from the ionic liquid, and the yellow ions are the co-ions of the ionic liquid. The photos show the two situations: on the right of the tube, the magnet traps the liquid when a stable colloidal suspension is obtained as the nanoparticles move with the liquid (b). In contrast, the magnet only traps the nanoparticles when colloidal stability is not reached and the solvent flows at the bottom of the tube (a).



0.5. If $|\sigma| = |\Theta_{\text{ion}}^{\text{max}}|$, a monolayer of counter-ions is formed, which compensates for the surface charge. The ionic liquid structure after this first layer is bulk-like. If $|\sigma/\Theta_{\text{ion}}^{\text{max}}| > 1$, crowding (sometimes called a monotonic structure) occurs, first described by Bazant *et al.*⁴⁶ This means that counter-ions accumulate in more than one layer close to the charged surface because this charge is very high and because the bulky counter-ions cannot compensate for this charge with one dense layer of pure counter-ions. Crowding was observed experimentally by an X-ray reflectivity study⁴⁷ in an ionic liquid containing bistriflimide (TFSI) starting from a surface charge density of $\sim 50 \mu\text{C cm}^{-2}$ which is in agreement with the simulated value for $\Theta_{\text{ion}}^{\text{max}}$.

On the basis of all these elements, some of the different possibilities of organisation close to the surface are shown in Fig. 7 in the case of ideal nanoparticles, showing in particular overscreening leading to a multilayer structure or crowding. Additional counter-ions different from the ones of the ionic liquid are considered as they are present in our experiments (they are the initial counter-ions of the particles, localised close to the nanoparticle surface in the ionic liquid). This means that an effective $\Theta_{\text{ion}}^{\text{max}}$ for a mixed layer of two kinds of counter-ions needs to be defined, which can hugely modify the layering close to the solid compared to a layer with one type of counter-ion. Real nanoparticles are rougher, which will influence the structuring of the ionic liquids compared to a flat surface.^{34–36} Also, the curved surface can influence the layering; however $|\sigma/\Theta_{\text{ion}}^{\text{max}}|$ should remain an important parameter.

Fig. 7 also summarises what these observations tell us about the colloidal stability observed in this study. Firstly, if the nanoparticle has no structural charge prior to the transfer to the ionic liquid, no dispersion will form in any ionic liquid, as we observe here. Indeed, there is no impetus from which an ordered multilayer structure can arise. When this structure is not present there is no phenomenon that can produce any repulsive effect between nanoparticles, and therefore the dispersed nanoparticles are observed to coagulate and sediment.

Secondly, when the surface charge density of the nanoparticle is in the range 16 to 32 $\mu\text{C cm}^{-2}$ (hydroxyl or citrate coated nanoparticles), $|\sigma/\Theta_{\text{ion}}^{\text{max}}|$ remains between 0 and 1 producing layering of the ionic liquid influenced by the nature of the counter-ion. Looking for an example in the case of citrate coated nanoparticles in BMIM TFSI (Fig. 4), both TBA⁺ and BMIM⁺ initial counter-ions facilitate dispersion of the nanoparticles. Differences between the two samples nevertheless appear in the analysis of interactions (Table S-2, ESI[†]). However, if the initial counter-ions are Li⁺ or Na⁺, which stay at the interface in the ionic liquid, the effective $|\sigma/\Theta_{\text{ion}}^{\text{max}}|$ is lower due to their small size and the structuring induced is not sufficient, which is consistent with the impossibility of stabilising the nanoparticles. Li⁺ or Na⁺ always destroys the stability here (Fig. 4). However, the use of Li⁺ or Na⁺ as initial counter-ions can lead to colloidal stability in the ionic liquid EAN^{17,18} whose cation and anion sizes are smaller than those of the ones tested here. Therefore, the $\sigma/\Theta_{\text{ion}}^{\text{max}}$ ratio is closer to the optimum of 0.5 and a multilayer structure can be formed that leads to colloidal stability. Moreover, Na⁺ led to better colloidal stability than Li⁺

and EA⁺ as the size matching with the EAN ions is better and therefore the $\sigma/\Theta_{\text{ion}}^{\text{max}}$ ratio is closer to the optimum of 0.5 for Na⁺. In contrast, the ratio is smaller for Li⁺ and bigger for EA⁺ leading to fewer multilayers and therefore worse/no colloidal stability.

Thirdly, if the charge is much larger (200–300 $\mu\text{C cm}^{-2}$, for collapsed polyelectrolytes), $|\sigma/\Theta_{\text{ion}}^{\text{max}}| > 1$, which corresponds to the crowding regime. This does not allow the stabilisation of the nanoparticles in the IL, whatever the counter-ion, which confirms that layering of the ionic liquid close to the solid surface is essential.

However, for a given structural charge of the nanoparticles, our results also highlight the influence of both the anions and the cations of the ionic liquid, *i.e.* not only of the counter-ions but also of the co-ions (referring to the charge of the solid surface). Indeed, for example, for positive surfaces obtained with SMIM^{+/-} species condensed on the nanoparticles' surface, taking similar TFSI⁻ ionic liquid anions constituting the layer close to SMIM^{+/-}, the dispersion state depends on the nature of the cation (Fig. 4). However, the structural surface charge density does not govern the organization on its own either. Here, for similar σ values (positive or negative nanoparticles with citrate), with counter-ions of similar $\Theta_{\text{ion}}^{\text{max}}$ (TFSI⁻ and BMIM⁺), a dispersion is obtained for negative nanoparticles with BMIM⁺ counter-ions while no dispersion is obtained for positive nanoparticles with TFSI⁻ counter-ions. This is probably due to a variation of $\sigma/\Theta_{\text{ion}}^{\text{max}}$, which in fact depends on all the species: the sign of the superficial solid charge, nature of this charge, and nature of the co-ions. Indeed, for a given surface, the extent of the layering depends on the cation/anion couple.³⁵ The ratio $\sigma/\Theta_{\text{ion}}^{\text{max}}$ will thus depend on the substituents of the cations (size of the alkyl chains, for example, here HEIM TFSI and EMIM TFSI are not equivalent for dispersing the same nanoparticles) and also on the different interactions (for example, changing the ethyl group for an alcohol as in POMI TFSI, able to form hydrogen bonds). This is why these groups appear more important than the nature of the positive group in the cation. There is also a strong influence of the nature of the anion for a given cation (here EMIM). Indeed, the shape of the anion can modulate the accessibility of the negative charge and thus the interactions with neighbouring species, thus $\sigma/\Theta_{\text{ion}}^{\text{max}}$. This is consistent with their huge influence on many properties, for example water uptake (Table S-1 in ESI[†]), conductivities,⁴⁸ or Seebeck coefficients.⁴⁹

Consequently, the strength of the interparticle repulsion is governed not only by the value of the surface charge of the nanoparticles but also by the size and nature of the counter-ions, which either come from the ionic liquids or are different ions introduced on purpose as they can localise at the interface and produce a different organisation of the ions. However, it is not only the ions of opposite sign to that of the surface, *i.e.* the counter-ions, that are important. The co-ions of the same sign are also crucial as the structure results from the coupling of anions and cations.

Finally, a supplementary parameter, frequently hidden, should be mentioned. Indeed, the remaining water, which is always present in ionic liquids despite careful drying, can hugely



modify interfaces if it localises there; therefore it can strongly influence the behaviour. In the present case, water is the initial solvent used for maghemite synthesis and some water can remain after the transfer of the nanoparticles to DMSO and to the ionic liquids. This water content can solvate the oxide surface groups or the counter-ions, if it remains close to the interface. Its influence is moreover very clear looking at the effect of water uptake (by simply keeping the samples in contact with air). It can destabilise some samples in a few seconds (for example all samples based on citrate coated nanoparticles) or can have no impact after several months (for example for bare nanoparticles with SMIM^{+/−} TFSI[−] counter-ions in EMIM TFSI, the sample shown in Fig. 8a, red squares, and Fig. 8b, red squares and blue triangles).

The role of water in the structure has been directly evidenced from surface force apparatus (SFA) measurements on mica with EMIM TFSI.³⁹ The structuring of the ionic liquid close to the mica increased when water was added. This was attributed to a modification of the interface by the solvation of K⁺ counter-ions by water which resulted in an increase of the effective charge of the mica surface. In contrast, for EMIM TFSI on carbon, no difference was detected for the interfacial structure up to water contents of around 3 wt% for surface potentials compatible with AFM measurements.²⁷

As a result, no systematic behaviour can be predicted for water as it will depend on its mechanism of action in each system, and therefore on the details of the solid–liquid interface. However, the remaining water or solvent, in this case DMSO, can explain the influence of the route of transfer as the amount and nature of the remaining molecules at the interface can also change the layering and thus the nanostructure. Finally, it should be kept in mind that such remaining molecules of solvent should be considered a tuning parameter as they can either destroy or improve the colloidal stability.

Lastly, recent studies have evidenced the existence of a long-range repulsive force between two mica surfaces of the same charge in ionic liquids.^{50–53} This contribution may also play a role in the colloidal stability in ionic liquids.

4 Towards applications

Ionic liquid-based colloids will only be suitable for application if they remain stable during use over a long term. DLS measurements repeated several months apart give information on the long-term evolution of the sample. DLS shows that in all the tested ionic liquids at least one set of parameters leads to a long-term stable sample. It is not only samples with $\chi < 1$ (repulsive interparticle interaction) that are stable over months but also samples for which $1 < S(Q \rightarrow 0) < 3.5$, that is, slightly attractive or with small aggregates. Among these samples stable in the long term, 3 are chosen to illustrate the following situations of interparticle interactions: $S(Q \rightarrow 0) = \chi < 1$, $S(Q \rightarrow 0) = \chi \approx 1$ or $S(Q \rightarrow 0) > 1$ (Fig. 8). At the volume fraction of the experiments, the characteristic time deduced from the DLS correlation curve can be converted to an effective size considering the viscosity of the solvent. However, as already mentioned, the viscosities are not precisely known and the sizes are considered orders of magnitude. The values obtained are nevertheless compatible with the other information on the nanoparticle size from SAXS (Section S-1.4.4, ESI†). Therefore, the shifts shown in Fig. 8 are mainly due to the different viscosities of the solvents. In each solvent, the curves measured months apart overlap for the selected samples, and hence these samples are long-term stable.

The strength of the stability can also be assessed thanks to the magnetic properties of the NPs. An applied magnetic field H induces anisotropic interparticle interaction due to the orientation of the magnetic dipoles of the nanoparticles in the applied field, attractive on average. The maximum value of H for which stability is maintained gives an indication of the strength of the repulsive interaction. This is tested by analysing the

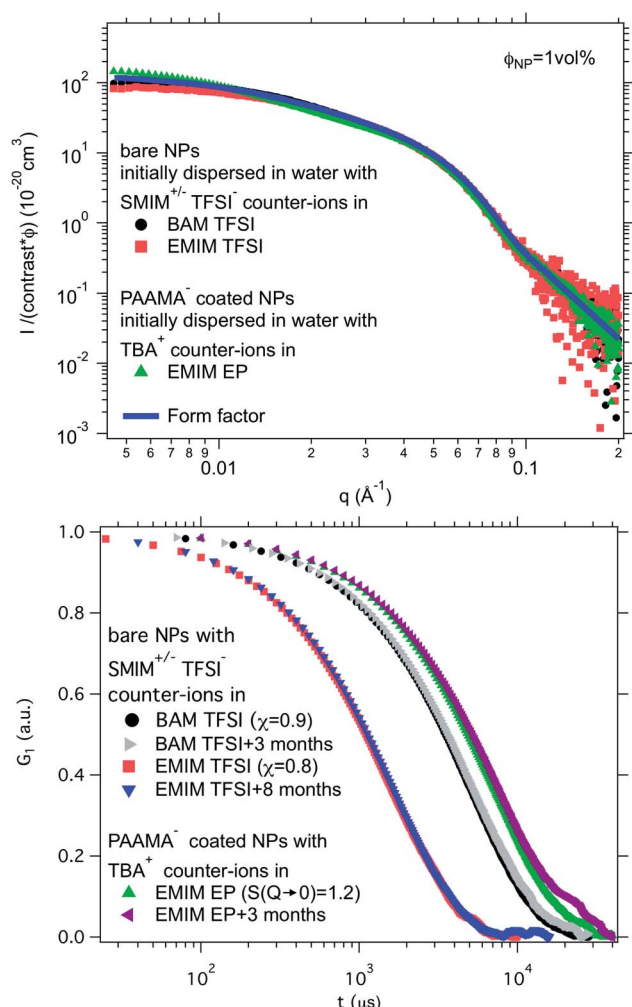


Fig. 8 Top: Absolute scattered intensities (normalised by the nanoparticle volume fraction $\phi_{\text{NP}} \approx 1 \text{ vol}\%$ and their contrast with the solvent) obtained from SAXS. Bottom: Normalised auto-correlation function G_1 from DLS after preparation and after several months. The shift between the samples is due to their different viscosities at 25 °C. Nanoparticles in BAM TFSI ($\eta = 113 \text{ cP}$ ²³) and EMIM TFSI ($\eta = 34 \text{ cP}$ ²³) have OH₂⁺ on their surface and SMIM^{+/−} TFSI[−] as counter-ions; the nanoparticles in EMIM EP ($\eta = 241 \text{ cP}$ ²³) are coated with poly(acrylate-co-maleate)[−] and have TBA⁺ as counter-ions.



scattering pattern of a laser beam passing through the sample under the field. The dispersion is stable if no diffraction is observed. If a diffraction line perpendicular to the field direction is obtained,⁵⁴ it means that a second magnetic phase or big aggregates elongated along the applied field are induced. Here several samples are stable up to an applied magnetic field of 716 kA m^{-1} including the three samples shown in Fig. 8. These results confirm that a strong repulsion between particles exists.

As the samples are stable under the field, magnetisation curves can be measured. The normalised data are plotted as a function of the applied field (Fig. 9) for two samples in ionic liquids (one case of slightly attractive interparticle interaction and one case of repulsive interaction) and compared with the original sample in water. The similarity of the three curves shows that all NPs are transferred to the ionic liquid, retaining their magnetic properties. Note that this also confirms that the chemical composition of the NPs is stable over time and that their size distribution is maintained.

Consequently, colloidal dispersions stable in the long run have been produced. Due to the magnetic properties of the NPs, they moreover fulfill the definition of magnetic fluids (or ferrofluids).^{55,56} A ferrofluid is a colloidal dispersion of magnetic particles which are magnetic monodomains with a diameter around 10 nm, stable in the long term. It has the usual properties of a liquid but behaves like a liquid paramagnet. It moves as a whole in the direction of the highest magnetic field and retains its liquid properties in a uniform magnetic field H . These characteristics make it an interesting liquid for a number of applications, including, for example, sealing, damping and hydrodynamic bearings. Combining this with the properties of ionic liquids leads to the possibility of new applications in high

temperature environments, at low pressures and at high voltages, for instance.²

5 Conclusion

A set of 12 ionic liquids changing either the cation for a given anion or the anion for a given cation is used to disperse iron oxide nanoparticles. In order to identify the key parameters to obtain stable colloidal dispersions, the oxide nanoparticle interface is carefully tuned in a molecular solvent before transferring towards an ionic liquid, without passing through the powder state.

Fig. 7 shows a scheme of the main parameters. Two very different situations occur depending on the charge of the nanoparticles. Uncharged nanoparticles without coatings cannot be directly dispersed in these ionic liquids. However, introducing steric repulsion from adsorbed polymers or other molecules can produce stable colloidal dispersions, a stabilisation method which was not analysed here. In contrast, bare charged nanoparticles can be dispersed thanks to a spatially oscillating multilayer structure formed by the cations and anions of the ionic liquid, which can overcome the attractive contributions to the interparticle interaction. The efficiency of the repulsion depends on the surface occupied by one nanoparticle's counter-ion compared to the area occupied by one superficial charge on the bare nanoparticle. The ratio needs to be between zero and one to create a layering between the solid surface and the bulk ionic liquid. The diagrams in Fig. 7 show that the structural surface charge should not be too low (no layering of the ionic liquid) or too high (crowding of the ionic liquid) in order to induce an appropriate layering of the ions around the nanoparticle.

Another important key parameter is the nature of the nanoparticles' counter-ions initially introduced (they may differ from the ones of the ionic liquid), because of their possible localisation at the solid-liquid charged interface. They modify the layers close to the interface, and thus the dispersion state. As changing the bare charge density of the solid oxide surface is not always experimentally easy, varying these localised counterions enables solids and ionic liquids to become compatible.

A coating of charged polymers on the nanoparticles was used to increase the structural surface charge of the nanoparticles and to add a steric contribution to the repulsion. Although stable dispersions can be obtained when the polymer produces a steric repulsive contribution, surprisingly the repulsion is weaker than the one induced by the organisation of ionic liquids on the bare charged nanoparticle surface.

It is not only the nature of the counter-ions that hugely influences the layering at the interface but also the nature of the co-ions and all other species that can locate at the interface like amounts of residual water. This repulsion produced by the layering depends on the geometry and on the nature of the chemical groups of all the species. Therefore, tiny modifications can switch the balance of interaction from repulsive to attractive, and thus switch the structure from individually dispersed nanoparticles to small aggregates.

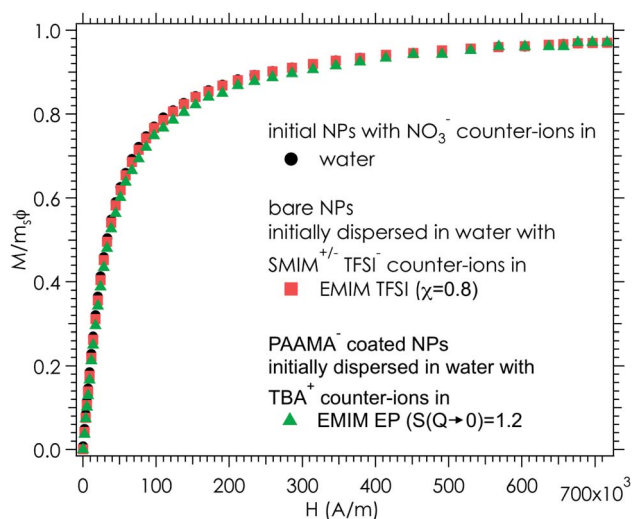


Fig. 9 Magnetization divided by the volume fraction of nanoparticles (1.53 ± 0.03 vol% in water, 0.96 ± 0.03 vol% in EMIM TFSI and 1.00 ± 0.03 vol% in EMIM EP) and the saturation magnetization ($m_s(\text{water}) = 278 \pm 17 \text{ kA m}^{-1}$, $m_s(\text{EMIM TFSI}) = 292 \pm 18 \text{ kA m}^{-1}$ and $m_s(\text{EMIM EP}) = 278 \pm 17 \text{ kA m}^{-1}$) as a function of the applied magnetic field H . The error bars are around 6%, due to an uncertainty of 0.03% for the concentration determination by FAAS and an uncertainty of 2% for the volume of the ferrofluid in the magnetic measurements.



This study thus identifies the key parameters and suggests that conditions allowing long-term colloidal dispersion can be found in the vast majority of ionic liquids despite their diversity. Indeed, stable colloidal dispersions were produced here whatever the ionic liquid for a particular composition set. However, the exact combination of species which will provide stability for a given ionic liquid cannot be foreseen yet.

Summarising the interesting sample properties for applications, the colloidal dispersions obtained are stable in the long run, and they fulfill the characteristics of ferrofluids, thanks to the magnetic properties of the chosen nanoparticles, retaining their stability under a magnetic field, and they have an increased electrical conductivity compared to the usual molecular solvents, leading to new opportunities.

In the future, it would be interesting to investigate mixtures of ionic liquids and molecular solvents to better understand the role of uncharged molecules. The behaviour at higher temperatures, which is an interesting specific property of ionic liquids, would also be important to explore.

Conflicts of interest

There are no conflicts of interest to declare.

Abbreviations

AcO	Acetate
BF ₄	Tetrafluoroborate
BMIM	1-Butyl-3-methylimidazolium
DEME	<i>N,N</i> -Diethyl- <i>N</i> -methyl- <i>N</i> -(2-methoxyethyl) ammonium
Cr (<i>r</i> = 2, 4, 6, 7, 8)	Ethyl, butyl, hexyl, heptyl, octyl
EAN	Ethylammonium nitrate
EMIM	1-Ethyl-3-methylimidazolium
EtSO ₄	Ethyl sulphate
OctylMIM	1-Octyl-3-methylimidazolium
OHEMIM	1-(2-Hydroxyethyl)-3-methylimidazolium
PF ₆	Hexafluorophosphate
SCN	Thiocyanate
TFSI	Bis(trifluoromethane)sulfonimide

Acknowledgements

The authors thank Amandine Anfray for DLS measurements, Aude Michel for FAAS measurements and Juliette Sirieix-Plénet for the synthesis of BMIM Br. This work was supported by the European Union Horizon 2020 research and innovation program under grant number 731976 (MAGENTA).

References

- 1 T. Welton, *Chem. Rev.*, 1999, **99**, 2071–2084.
- 2 L. Mestrom, J. J. M. Lenders, R. de Groot, T. Hooghoudt, N. A. J. M. Sommerdijk and M. V. Artigas, *Nanotechnology*, 2015, **26**, 285602.

- 3 M. Bonetti, S. Nakamae, B. T. Huang, T. J. Salez, C. Wiertel-Gasquet and M. Roger, *J. Chem. Phys.*, 2015, **142**, 244708.
- 4 E. Laux, S. Uhl, L. Jeandupeux, P. P. López, P. Sanglard, E. Vanoli, R. Marti and H. Keppner, *J. Electron. Mater.*, 2018, 1–5.
- 5 M. Dupont, D. MacFarlane and J. Pringle, *Chem. Commun.*, 2017, **53**, 6288–6302.
- 6 Z. He and P. Alexandridis, *Adv. Colloid Interface Sci.*, 2017, **244**, 54–70.
- 7 B. T. Huang, M. Roger, M. Bonetti, T. J. Salez, C. Wiertel-Gasquet, E. Dubois, R. Cabreira Gomes, G. Demouchy, G. Mériguet, V. Peyre, M. Kouyaté, C. L. Filomeno, J. Depuyrot, F. A. Tourinho, R. Perzynski and S. Nakamae, *J. Chem. Phys.*, 2015, **143**, 054902.
- 8 T. J. Salez, B. T. Huang, M. Rietjens, M. Bonetti, C. Wiertel-Gasquet, M. Roger, C. L. Filomeno, E. Dubois, R. Perzynski and S. Nakamae, *Phys. Chem. Chem. Phys.*, 2017, **19**, 9409–9416.
- 9 N. Jain, X. Zhang, B. S. Hawkett and G. G. Warr, *ACS Appl. Mater. Interfaces*, 2011, **3**, 662–667.
- 10 C. Guibert, V. Dupuis, J. Fresnais and V. Peyre, *J. Colloid Interface Sci.*, 2015, **454**, 105–111.
- 11 L. Rodríguez-Arco, M. T. López-López, F. González-Caballero and J. D. Durán, *J. Colloid Interface Sci.*, 2011, **357**, 252–254.
- 12 K. Ueno, A. Inaba, M. Kondo and M. Watanabe, *Langmuir*, 2008, **24**, 5253–5259.
- 13 H. Zhang, K. Dasbiswas, N. B. Ludwig, G. Han, B. Lee, S. Vaikuntanathan and D. V. Talapin, *Nature*, 2017, **542**, 328–331.
- 14 V. Kamysbayev, V. Srivastava, N. B. Ludwig, O. J. Borkiewicz, H. Zhang, J. Ilavsky, B. Lee, K. W. Chapman, S. Vaikuntanathan and D. V. Talapin, *ACS Nano*, 2019, **13**, 5760–5770.
- 15 K. Ueno, S. Imaizumi, K. Hata and M. Watanabe, *Langmuir*, 2009, **25**, 825–831.
- 16 F. C. C. Oliveira, L. M. Rossi, R. F. Jardim and J. C. Rubim, *J. Phys. Chem. C*, 2009, **113**, 8566–8572.
- 17 M. Mamusa, J. Sirieix-Plénet, F. Cousin, E. Dubois and V. Peyre, *Soft Matter*, 2014, **10**, 1097.
- 18 M. Mamusa, J. Sirieix-Plénet, F. Cousin, R. Perzynski, E. Dubois and V. Peyre, *J. Phys.: Condens. Matter*, 2014, **26**, 284113.
- 19 R. Bhandary, J. G. Alauzun, P. Hesemann, A. Stocco, M. In and P. H. Mutin, *Soft Matter*, 2017, **13**, 8023–8026.
- 20 A. M. M. S. Medeiros, A. L. Parize, V. M. Oliveira, B. A. Neto, A. F. Bakuzis, M. H. Sousa, L. M. Rossi and J. C. Rubim, *ACS Appl. Mater. Interfaces*, 2012, **4**, 5458–5465.
- 21 J. Gao, R. S. Ndong, M. B. Shiflett and N. J. Wagner, *ACS Nano*, 2015, **9**, 3243–3253.
- 22 X. Shi, W. Huang and X. Wang, *Lubr. Sci.*, 2018, **30**, 73–82.
- 23 K. Padaszyński and U. Domańska, *J. Chem. Inf. Model.*, 2014, **54**, 1311–1324.
- 24 Z. He and P. Alexandridis, *Phys. Chem. Chem. Phys.*, 2015, **17**, 18238–18261.
- 25 J. Nordström, L. Aguilera and A. Matic, *Langmuir*, 2012, **28**, 4080–4085.



- 26 R. Hayes, N. Borisenko, B. Corr, G. B. Webber, F. Endres and R. Atkin, *Chem. Commun.*, 2012, **48**, 10246.
- 27 A. Elbourne, S. McDonald, K. Voïchovsky, F. Endres, G. G. Warr and R. Atkin, *ACS Nano*, 2015, **9**, 7608–7620.
- 28 R. Massart, *IEEE Trans. Magn.*, 1981, **17**, 1247–1248.
- 29 C. L. Filomeno, M. Kouyaté, V. Peyre, G. Demouchy, A. F. C. Campos, R. Perzynski, F. A. Tourinho and E. Dubois, *J. Phys. Chem. C*, 2017, **121**, 5539–5550.
- 30 M. Kouyaté, C. L. Filomeno, G. Demouchy, G. Mériguet, S. Nakamae, V. Peyre, M. Roger, A. Cēbers, J. Depeyrot, E. Dubois and R. Perzynski, *Phys. Chem. Chem. Phys.*, 2019, **21**, 1895–1903.
- 31 E. Dubois, R. Perzynski, F. Boué and V. Cabuil, *Langmuir*, 2000, **16**, 5617–5625.
- 32 B. Frka-Petesic, E. Dubois, L. Almasy, V. Dupuis, F. Cousin and R. Perzynski, *Magneto hydrodynamics*, 2013, **49**, 328–338.
- 33 J. Fresnais, M. Yan, J. Courtois, T. Bostelmann, A. Bée and J.-F. Berret, *J. Colloid Interface Sci.*, 2013, **395**, 24–30.
- 34 A. Sheehan, L. A. Jurado, S. N. Ramakrishna, A. Arcifa, A. Rossi, N. D. Spencer and R. M. Espinosa-Marzal, *Nanoscale*, 2016, **8**, 4094–4106.
- 35 R. Hayes, G. G. Warr and R. Atkin, *Phys. Chem. Chem. Phys.*, 2010, **12**, 1709.
- 36 M. V. Fedorov and A. A. Kornyshev, *Chem. Rev.*, 2014, **114**, 2978–3036.
- 37 M. Mezger, H. Schroder, H. Reichert, S. Schramm, J. S. Okasinski, S. Schoder, V. Honkimaki, M. Deutsch, B. M. Ocko, J. Ralston, M. Rohwerder, M. Stratmann and H. Dosch, *Science*, 2008, **322**, 424–428.
- 38 R. Hayes, N. Borisenko, M. K. Tam, P. C. Howlett, F. Endres and R. Atkin, *J. Phys. Chem. C*, 2011, **115**, 6855–6863.
- 39 H.-W. Cheng, P. Stock, B. Moeremans, T. Baimpos, X. Banquy, F. U. Renner and M. Valtiner, *Adv. Mater. Interfaces*, 2015, 1500159.
- 40 J. Vatamanu, O. Borodin and G. D. Smith, *J. Am. Chem. Soc.*, 2010, **132**, 14825–14833.
- 41 C. Merlet, B. Rotenberg, P. A. Madden and M. Salanne, *Phys. Chem. Chem. Phys.*, 2013, **15**, 15781.
- 42 V. Ivaništšev, S. O'Connor and M. Fedorov, *Electrochem. Commun.*, 2014, **48**, 61–64.
- 43 S. W. Coles, A. M. Smith, M. V. Fedorov, F. Hausen and S. Perkin, *Faraday Discuss.*, 2018, **206**, 427–442.
- 44 J.-W. Yan, Z.-Q. Tian and B.-W. Mao, *Curr. Opin. Electrochem.*, 2017, **4**, 105–111.
- 45 S. A. Kislenko, Y. O. Moroz, K. Karu, V. B. Ivaništšev and M. V. Fedorov, *Russ. J. Phys. Chem. A*, 2018, **92**, 999–1005.
- 46 M. Z. Bazant, B. D. Storey and A. A. Kornyshev, *Phys. Rev. Lett.*, 2011, **106**, 046102.
- 47 M. Chu, M. Miller and P. Dutta, *ACS Cent. Sci.*, 2016, **2**, 175–180.
- 48 S. Zhang, N. Sun, X. He, X. Lu and X. Zhang, *J. Phys. Chem. Ref. Data*, 2006, **35**, 1475–1517.
- 49 A. Sosnowska, M. Barycki, A. Gajewicz, M. Bobrowski, S. Freza, P. Skurski, S. Uhl, E. Laux, T. Journot, L. Jeandupeux, H. Keppner and T. Puzyn, *ChemPhysChem*, 2016, **17**, 1591–1600.
- 50 M. A. Gebbie, A. M. Smith, H. A. Dobbs, A. A. Lee, G. G. Warr, X. Banquy, M. Valtiner, M. W. Rutland, J. N. Israelachvili, S. Perkin and R. Atkin, *Chem. Commun.*, 2017, **53**, 1214–1224.
- 51 A. A. Lee, C. S. Perez-Martinez, A. M. Smith and S. Perkin, *Phys. Rev. Lett.*, 2017, **119**, 026002.
- 52 M. A. Gebbie, H. A. Dobbs, M. Valtiner and J. N. Israelachvili, *Proc. Natl. Acad. Sci. U. S. A.*, 2015, **112**, 7432–7437.
- 53 P. Gaddam and W. Ducker, *Langmuir*, 2019, **35**, 5719–5727.
- 54 J.-C. Bacri, R. Perzynski, D. Salin, V. Cabuil and R. Massart, *J. Magn. Magn. Mater.*, 1990, **85**, 27–32.
- 55 *Magnetic Fluids and Applications Handbook*, ed. B. Berkovski, Begell House Inc. Publ., New York, 1996.
- 56 R. Rosensweig, *Ferrohydrodynamics*, 2014.



Colloidal dispersions of oxide nanoparticles in ionic liquids: elucidating the key parameters

J. C. Riedl¹, M. A. Akhavan Kazemi¹, F. Cousin², E. Dubois^{1,*}, S. Fantini³, S. Lois³, R. Perzynski¹, and V. Peyre^{1,*}

¹Sorbonne Université, Laboratoire PHENIX, 4 place Jussieu, case 51, 75005, Paris, France

²Laboratoire Léon Brillouin, UMR CNRS 12, CE Saclay, Gif sur Yvette, France

³Solvionic SA, 195 route d'Espagne, BP1169, 31036 Toulouse Cedex 1, France.

*emmanuelle.dubois@sorbonne-universite.fr, veronique.peyre@sorbonne-universite.fr

+these authors contributed equally to this work

SUPPLEMENTARY INFORMATION

S-1 Experimental section

S-1.1 Materials

The following materials were used without further purification:

Citric acid ($\text{H}_3\text{Cit}\cdot\text{H}_2\text{O}$, purity > 99%, NORMAPUR); Poly (acrylic acid sodium salt) (PAA Na, average $M_w = 2100$ g/mol, SIGMA-ALDRICH); Poly (acrylic acid) (PAA, average $M_w = 2000$ g/mol, 63wt%, Acros Organics); Poly (Acrylic co-Maleic Acid) solution (PAAMA, average $M_w = 3000$ g/mol, 50 wt% in H_2O , SIGMA-ALDRICH); ammonia solution (20%, VWR), sodium hydroxide (NaOH pellets, 98%, Acros Organics); dimethyl sulfoxide (DMSO, technical, VWR); Tetrabutylammonium hydroxide 30-hydrate ($\text{TBAOH}\cdot 30\text{H}_2\text{O}$, purity > 99%, SIGMA-ALDRICH); HClO_4 (65 wt% in water, VWR); hydrochloric acid (HCl, 37% water solution, AnalaR Normapur); iron(II) chloride ($\text{FeCl}_2\cdot 4\text{H}_2\text{O}$, AnalaR Normapur, VWR); iron(III) chloride ($\text{FeCl}_3\cdot 6\text{H}_2\text{O}$, Prolabo); iron(III) nitrate ($\text{Fe}(\text{NO}_3)_3\cdot 9\text{H}_2\text{O}$, technical, VWR); acetone (technical, VWR); diethyl ether (purity 99.8%, AnalaR Normapur); Nitric acid (HNO_3 , 69.5% water solution, Carlo Erba); Lithium Hydroxide ($\text{LiOH}\cdot\text{H}_2\text{O}$, purity > 99%, Fluka BioChemika); HTFSI (purity 95%, Fluorochem); 1-Methylimidazole ($\text{C}_4\text{H}_6\text{N}_2$, purity 99%, Acros Organics); 1-Bromobutane ($\text{C}_4\text{H}_9\text{Br}$, purity 99%, Acros Organics).

BMIMOH was prepared from BMIMBr exchanging the anion using an AMBERLITE™ IRN78 resin. The resin was prepared by the following steps: 1) NaOH (1M) was added 2) washing 3) HCl (1M) was added 4) washing 5) NaOH (1M) was added 6) washing; the washing was done with ultra-pure water until the pH was between 5.5 and 7 and the number of moles of base and acid was twice as big as the capacity of the resin. Then, BMIMBr was added and after one hour of stirring the pH was checked and a small quantity was mixed with Ag (NO_3) to test if only BMIMOH was remaining. BMIMBr was prepared by the alkylation of 1-Methylimidazole and 1-Bromobutane following the procedure of reference¹.

Ultra-pure water (Type 1, resistivity of ≈ 18 M Ω cm) is produced from potable water by means of a MILLIPORE DIRECT-Q system before use.

S-1.2 Synthesis of magnetic nanoparticles in water

Acidic solutions of FeCl_2 and FeCl_3 were mixed in a stoichiometric ratio and magnetite (Fe_3O_4) precipitated in a strongly alkaline medium.⁵ These spinel type nanoparticles evolve in acidic medium due to their sensitivity to acid attack and oxidation reactions in the presence of oxygen.⁶ Therefore, chemical oxidation of magnetite to maghemite at 80°C ($\gamma\text{-Fe}_2\text{O}_3$) was performed with $\text{Fe}(\text{NO}_3)_3$. This leads to long-term stable (for years) maghemite nanoparticles even in strongly acidic medium. In a final step, after subsequently washing the NPs with acetone and ether, they were dispersed in an aqueous nitric acid solution the pH of which lies between 1.5 and 2. This is called below the "initial ferrofluid". This standard process produces nanoparticles of maghemite, as checked by X-Ray diffraction.^{7,8}

S-1.3 Dispersion of the colloidal dispersions in molecular solvent

Several kinds of nanoparticle differing by their surface have been produced in molecular solvents before their transfer to ionic liquids: bare nanoparticles with hydroxyl groups on the surface, citrate coated and polymer-coated nanoparticles. Their

Table S-1. Physical and chemical properties of studied ionic liquids measured at 25°C at PHENIX laboratory*, at SOLVIONIC** or taken from literature. The miscibility of the ionic liquids with water is given for 50:50 mixtures.

short name	CAS	initial water content* in ppm	water uptake in 15min/24h* in wt%	Density in g/cm ³	viscosity in mPa s	refractive index*	miscible with water*
BAM TFSI	25827 3-75-5	563±70	<0.1/0.4	1.41 ²	113 ³	1.409	no
BMPyrr TFSI	223437-11-4	397±50	0.2/0.5	1.39**	81 ³	1.424	no
HSMIM TFSI	909390-59-6	11714±1464	0.1/5.8	1.58*	1711** (22°C)	1.450	yes
OHPMIM TFSI	-	470±59	<0.1/1.3	1.54 ²	109 ³	1.437	no
BMIM TFSI	174899-83-3	573±72	0.1/0.5	1.44 ⁴	88 ³	1.427	no
HEIM TFSI	-	1231±154	<0.1/1.5	1.57 ²	54 ³	1.423	no
EMIM TFSI	174899-82-2	83±10	<0.1/0.6	1.52 ²	34 ³	1.424	no
EMIM FSI	235789-75-0	48±6	0.1/0.8	1.39 ²	17 ³	1.449	no
EMIM TfO	145022-44-2	324±41	<0.1/3.1	1.38 ²	48 ³	1.434	no
EMIM AcO	143314-17-4	2067±258	0.1/5.1	1.10 ²	127 ³	1.501	yes
EMIM EP	-	72±28	0.2/4.5	1.13 ²	241 ³	1.485	yes
EMIM DEP	848641-69-0	2145±268	0.2/4.6	1.14**	401 ³	1.470	yes

preparation is detailed in the following sections.

S-1.3.1 Bare nanoparticles with hydroxyl groups

1M NaOH aqueous solution was added to 1 vol% of initial ferrofluid in water (prepared as described above, with nitric acid, pH around 1.5) till the point of zero charge (PZC) of maghemite was reached at pH \approx 7. The nanoparticles were magnetically precipitated and the supernatant was removed. The particles were washed several times with ultra-pure water until the free NO₃⁻ concentration was reduced below 10⁻⁶ M. At the PZC these uncharged bare nanoparticles have hydroxyl groups on their surface. To test the influence of the nature of the counter-ion, several different aqueous acids were added, including perchloric acid (HClO₄), benzenesulfonic acid (C₆H₅SO₃H), bistriflimide (HTFSI), and aqueous 1-(4-sulfobutyl)-3-methyl imidazolium bistriflimide (HSMIM TFSI) solution. For each case the pH was reduced to \approx 1.5, leading to stable colloids except for the addition of SMIM^{+/-} TFSI⁻ solution which led to flocculated nanoparticles in water.

S-1.3.2 Citrate coated particles

The addition of citric acid to 1 vol% of initial ferrofluid in water led to sedimented nanoparticles. They were washed several times with a 10⁻² M aqueous citric acid solution with the help of magnetic induced sedimentation and removal of the supernatant to obtain a free citric acid concentration of \approx 10⁻² M. A 1 M base of the type XOH, with X = Li, Na, tetrabutyl ammonium (TBA) or 1-butyl-3-methyl imidazolium (BMIM), was added till a pH \approx 7 was reached, leading to a stable colloid in all cases. The negatively charged citrate coated nanoparticles balance their charge with the cations X of the added base.

S-1.3.3 Polymer coated particles

68% concentrated nitric acid was added to 100 mL of 1 wt% aqueous Poly (Acrylic Acid Sodium salt) solution till a pH of \approx 2 was reached. 50 ml of 1 vol% aqueous initial acid ferrofluid with NO₃⁻ counter ions was added. After 1 minute of magnetic stirring the nanoparticles were magnetically precipitated and the supernatant was removed. Ammonia solution was added to disperse the nanoparticles at pH \approx 7. In a last step the remaining free ions and polymer is removed by dialysis with 10-12 kDa membranes. The counter-ion is then NH₄⁺. The same steps were applied for Poly (Acrylic co-Maleic Acid) (PAAMA) except the addition of nitric acid in the beginning as the PAAMA solution was already at pH \approx 2. The counter ions were changed by the following steps. First, nitric acid (1M) was added till a pH \approx 2 was reached and the precipitated particles were washed several times. Second, BMIMOH (0.02M) or TBAOH (1M) was added to disperse the nanoparticles at pH \approx 7. In a last step the remaining free ions are removed by dialysis with 10-12 kDa membranes.

The solubility of poly (acrylic acid) was tested in the 12 ionic liquids in order to connect the colloidal stability of PAA⁻ coated NPs with the solubility of the polymer in the ionic liquids. Therefore, ammonia solution was added to poly (acrylic acid) with 16wt% PAANA and 47wt% PAAH till the ratio of H⁺ and NH₄⁺ was 1:1 and the pH was close to 7 to exchange H⁺ with NH₄⁺. NH₄⁺ was one of the counter-ions that lead to colloidal stability in some of the ionic liquids. The solution was freeze-dried and heated at 120°C while pumping for 3 hours to remove the water. Around 0.01 mol of the polymer powder per litre of ionic liquid was added. After one day of magnetic stirring the polymer was dissolved in EMIM X (X= AcO, EP, and DEP). The other samples were brought into contact with the moisture of the air and after another week, the polymer was dissolved only in HSMIM TFSI. This can be due to the large water uptake of this ionic liquid, here around 13wt% after 1 week.

S-1.3.4 Transfer from water to DMSO

In contrast to water, dimethyl sulfoxide (DMSO) is miscible with all tested ionic liquids. Therefore, all these different systems were transferred from water to DMSO in order to test the influence of the way of transfer from the molecular solvent towards the ionic liquids. A dialysis step was used, with 10-12 kDa membranes. As the nanoparticles were bigger than the holes in the membrane, only the solvent molecules and the ions were exchanged. The outside DMSO solution with the adapted free ion concentration is changed several times until the water concentration is lower than 10^{-2} vol%. In a last step the different systems were added to the ionic liquid in adapted proportions to obtain, after removing DMSO by freeze-drying, a final colloid with a volume fraction of ≈ 0.01 .

Table S-2. Structure factor at low Q , $S(Q \rightarrow 0)$, of ionic liquid-based colloids from SAXS (see text for details). * In the case of collapsed polyelectrolyte. If the polymer is not collapsed, part of the charge is on the surface of the oxide and part in the solvent, which is a different and more complicated situation. See main text for more information. "yes/no" means that the sample destabilised before the SAXS measurements. "no" means that dispersions with aggregates on the micron scale or bigger are obtained and ** means that there are no aggregates on the micron scale but there was not enough sample left to perform the SAXS measurement. OH_2^+ : hydroxyl protonated ending groups on the nanoparticles; citrate $^-$: citrate coated nanoparticles; PAA $^-$ and PAAMA $^-$: polymer coated nanoparticles (poly acrylate and poly(acrylate-co-maleate), respectively); SMIM $^{+/-}$ TFSI $^-$: butylsulfonate methylimidazolium bistriflimide (SMIM $^{+/-}$ being a zwitterion); TBA $^+$: tetrabutylammonium; BMIM $^+$: butylmethylimidazolium; NH_4^+ : ammonium.

		16-32 $\mu\text{C}/\text{cm}^2$			200-300 $\mu\text{C}/\text{cm}^2$ *				
		OH_2^+	Citrate $^-$		PAA $^-$			PAAMA $^-$	
surface charge \rightarrow		1 vol%	1 vol%		0.1 vol%			0.1 vol% 1 vol%	
surface \rightarrow									
concentration \rightarrow									
counter-ions \rightarrow									
ionic liquids		SMIM $^{+/-}$ -TFSI $^-$	TBA $^+$	BMIM $^+$	NH_4^+	TBA $^+$	BMIM $^+$	NH_4^+	TBA $^+$
initial solvent									
BAMTFSI	H ₂ O	0.9	0.8	no	no*		no*	no*	
	DMSO	1.3	1.5		no*	no*	no*	no*	
BMPyrrTFSI	H ₂ O	2.8	1.4	no	no*		no*	no*	
	DMSO	1.8	1.7		no*	no*	no*	no*	
HSMIMTFSI	H ₂ O	no	no	no	no		no	2.5	no
	DMSO	no	no		2.6	0.9	3.1	1.1	
OHPMIMTFSI	H ₂ O	2.0	no	no	no*		no*	no*	
	DMSO	no	1.9		no*	no*	no*	no*	
BMIMTFSI	H ₂ O	2.8	0.7	yes/no	no*		no*	no*	
	DMSO	1.6	1.7		no*	no*	no*	no*	
HEIMTFSI	H ₂ O	no	0.8	1.5	no*		no*	no*	
	DMSO	no	4.8		no*	no*	no*	no*	
EMIMTFSI	H ₂ O	0.7	no	no	no*		no*	no*	
	DMSO	0.9	no		no*	no*	no*	no*	
EMIMFSI	H ₂ O	1.6							
EMIMTfO	H ₂ O	1.2							
EMIMAcO	H ₂ O	yes/no		no	**			2.0	1.8
	DMSO								
EMIMEP	H ₂ O	1.0		no	1.9				1.2
EMIMDEP	H ₂ O	no		no	2.6				no
	DMSO								

S-1.4 Techniques

S-1.4.1 Flame Atomic Absorption Spectroscopy (FAAS)

The maghemite-based ferrofluids were dissolved in a concentrated hydrochloric acid solution and their total iron concentration were determined by flame atomic absorption measurements (FAAS) with an Analyst 100 spectrometer from PerkinElmer. The volume fractions ϕ were determined from the total iron concentration in the sample. Taking the molar weight (159.7 g mol^{-1}) and density (5.07 g cm^{-3}) of maghemite,⁹ the volume fraction of NPs can be calculated as: $\phi \text{ (vol\%)} = [\text{Fe}](\text{mol L}^{-1}) * 1.577$.

Table S-3. Magnetisation measurements for the three studied ferrofluids. The error bars for the saturation magnetisation m_s are calculated with an uncertainty of 0.0003 on the volume fraction calculation from the concentration determination by FAAS and 2% for the volume of the ferrofluid in the magnetic measurements.

sample	m_s in kA/m	diameter d_o in nm	polydispersity index σ
NPs with OH_2^+ on their surface and NO_3^- as counter-ions in water	278 ± 17	9.1	0.23
NPs with OH_2^+ on their surface and $\text{SMIM}^{+/-} \text{TFSI}^-$ as counter-ions in EMIM TFSI	292 ± 18	8.9	0.23
Poly acrylate ⁻ coated NPs with TBA^+ counter-ions in EMIM EP	278 ± 17	9.0	0.25

S-1.4.2 Magnetisation

Room temperature magnetisation measurements were performed on the initial aqueous ferrofluid and two ionic liquid-based ferrofluids using a home-made Vibrating Sample Magnetometer (VSM) up to $H=700\text{kA/m}$. When magnetised, the vibrating sample generates in the measuring coil a voltage at the same frequency proportional to the magnetisation M of the material. The magnetisation is described by the first Langevin's equation, which describes the mean orientation of the magnetic moment under a field H for mono-disperse nanoparticles with a diameter d and a saturation magnetisation m_s . Introducing a lognormal size distribution with a median diameter d_o and a polydispersity σ in the fits, the saturation magnetisation m_s is determined as well as d_o and σ . The characteristics corresponding to the samples presented in figure 6 of the main text are given in table S-3.

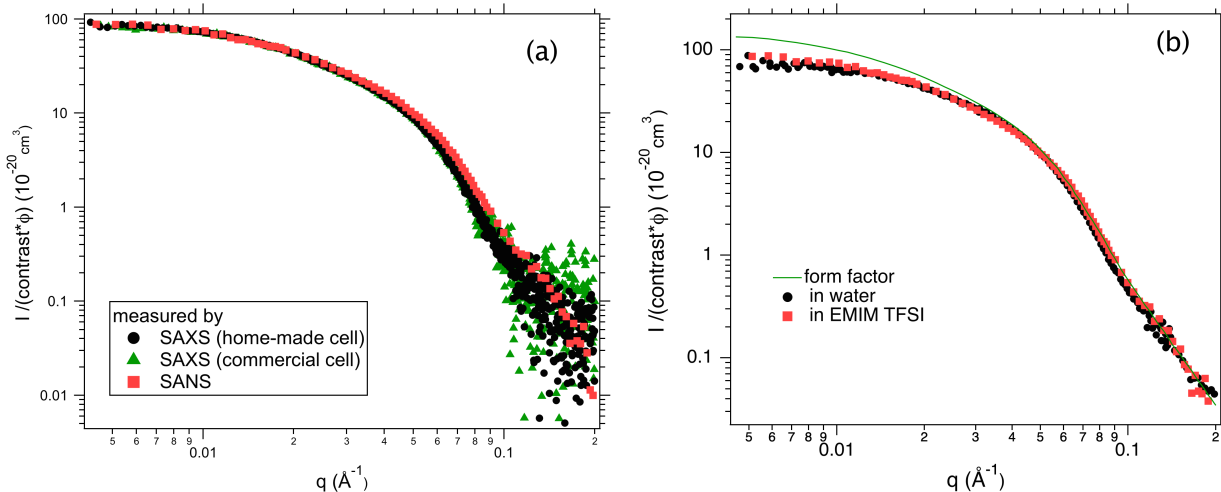


Figure S-1. Absolute scattered intensities (normalized by the NP volume fraction ϕ , here around 1%, and their contrast with the solvent): (a) for dispersions of $\text{SMIM}^{+/-} \text{TFSI}$ coated maghemite NPs in EMIM TFSI. Two SAXS measurements, once in a home-made cell and once in a classical capillary, are compared to the SANS measurement (this latter providing the absolute level on the Y axis). (b) for the nanoparticles in the initial sample in water and after transfer to the ionic liquid, here as an example the case of EMIM TFSI (same data as (a)), using SANS. The form factor of the nanoparticles is also plotted.

S-1.4.3 Small Angle X-ray and neutron Scattering (SAXS and SANS)

SAXS experiments were carried out with a laboratory XEUSS 2.0 (W)SAXS. The beam energy was fixed at 8 keV and the wavelength at $\lambda=1.54 \text{ \AA}$. The sample to detector distance was 3m to yield an accessible Q -range of 0.004 \AA^{-1} - 0.2 \AA^{-1} . The form factor $P(Q)$ of the NPs is determined from a set of dilute samples at NP concentrations of 0.1, 0.3 and 1 vol% in water (keeping the free electrolyte concentration constant) extrapolating the scattering intensities to the single particle contribution at $\phi=0 \text{ vol\%}$. This form factor was used for all the samples in ionic liquids to determine the apparent structure factors $S(Q)$ from the experimental scattered intensity $I(Q)$ using equation 1 from the main paper. The value $S(Q \rightarrow 0)$ is related to the interparticle interactions and the values are given in table S-2. If the particles are individually dispersed, $S(Q \rightarrow 0)$ is the osmotic compressibility χ . A system is attractive if $\chi > 1$ and repulsive for $\chi < 1$. High values of $S(Q \rightarrow 0)$ indicate the formation of aggregates.

However, as explained in the main text of the paper, the samples strongly absorb X-rays due to the ionic liquids and to iron. Therefore, either the transmission was very low when using classical calibrated polyimide capillaries (thickness 1.5mm) or

the thickness was not accurate when reducing the thickness with home-made cells (thickness < 0.1 μm). As a consequence, absolute intensity cannot be determined and the high Q region (> 0.2 \AA^{-1}) is highly noisy (see Fig. S-1a).

Therefore SANS were performed on the PAXY spectrometer at the LLB facility (CEA Saclay, France). Three different configurations were used (neutron wavelength $\lambda=6\text{\AA}$, sample to detector distance $d=1\text{m}$; $\lambda=6\text{\AA}$, $d=3\text{ m}$ and $\lambda=8.5\text{\AA}$, $d=5\text{ m}$) leading to an accessible Q-range of 0.004 \AA^{-1} to 0.2 \AA^{-1} . Samples were measured in quartz cells with 1 mm inner thickness. Standard correction procedures were performed¹⁰ using the Pasinet software (available free of charge at <http://didier.lairez.fr/>) in order to determine the absolute intensity (cm^{-1}). The SAXS curves rescaled on the SANS measurement in figure S-1a prove that these SAXS measurements are reliable in the small Q range.

Figure S-1-b shows SANS measurements of colloidal dispersions of the same NPs in water and in an ionic liquid (namely EMIM TFSI). The high Q region where the scattered intensity can be identified to the form factor of the NPs (Q above 0.06 \AA^{-1}) is properly measured by SANS (by opposition to SAXS in Fig. S-1-a). We then conclude that the nanoparticles keep their shape and their size distribution after transfer from water to the ionic liquid. This conclusion is valid for all dispersions measured by SANS.

S-1.4.4 Dynamic Light Scattering (DLS)

Light scattering measurements were performed using a Vasco DLS Particle Analyzer from Cordouan Technologies to study translational diffusion properties of water-based and IL-based dispersions for volume fractions ϕ ranging from 0.1 vol% to 1.53 vol%. The laser of the device is operating at a wavelength $\lambda=656\text{ nm}$. An around 200 μm thin film is analysed in backscattering mode at 135 $^\circ$ (i.e. $Q=2.3*10^{-3}\text{ \AA}^{-1}$ in water). These conditions prevent both the effects of light absorption by the colloidal suspension and multiple scattering even in strongly absorbing media.¹¹ Field autocorrelation curves with a precise baseline at long times were obtained by optimizing parameters such as the incident laser power, the sampling time and the number of channels. The measured intensity correlation function $G(t)$ was transformed into $G_1(t)$ using the expression:

$$G_1(t) = [G(t)]^{1/2} - offset \quad (1)$$

The normalized intensity auto correlation functions $G_1(t)$ were analysed with a stretched exponential function, $e^{-(t/\tau)^\beta}$ with a distribution of relaxation times described by a decay time τ and a stretching exponent β . The nanoparticle translation time τ is probed. It corresponds to the translational diffusion coefficient $D_t = (\langle \tau \rangle Q^2)^{-1}$, which, in non-interacting conditions, is related to the hydrodynamic radius R_H using Stokes-Einstein's equation:

$$D_t = \frac{k_B T}{6\pi\eta R_H} \quad (2)$$

where k_B is the Boltzmann constant, T the absolute temperature, η the solvent shear-viscosity (0.89*10⁻³ Pa s for water; see η in table S-1) for ionic liquids; the values are given for T=25 $^\circ\text{C}$ at which all experiments were performed.

The values for the determined hydro-dynamical diameter d_H of the samples depicted in figure 7b) of the main paper are given in table S-4. The reference hydro-dynamical diameter d_H of the initial sample in water is 13.4 nm for 1 vol% NP concentration. The stretching exponent β is close to 1 for all measurements meaning that there exists only one population of particle size. For NPs with hydroxyl protonated groups on their surface and SMIM^{+/-} TFSI⁻ as counter-ions the zwitterion concentration is around 2%. This could increase the viscosity of the sample whereas the samples viscosity would be decreased by a higher water content. A plausible order of magnitude of an eventual amount of molecular solvent remaining after freeze-drying is the amount of water taken by the ionic liquid alone after 24 hours at air. Assuming that both contributions influence linearly the viscosity, an average hydro-dynamical diameter d_H can be calculated with equation 2 and an error bar is estimated.

Table S-4. Values for DLS results for the three ferrofluids depicted in figure 7b of the main paper. The error bars for the hydro-dynamical diameter d_H are calculated with a linear contribution of the additive's viscosity to the viscosity value of the pure ionic liquid as explained in the text and an uncertainty of 0.0005 for the refractive index. The second measurement was done after 3 months except for EMIMTFSI (8 months).

sample	d_H (1 st measure) in nm	d_H (2 nd measure) in nm
NPs with OH ₂ ⁺ on their surface and SMIM ^{+/-} TFSI ⁻ as counter-ions in BAM TFSI	9.8±1.1	10.2±1.2
NPs with OH ₂ ⁺ on their surface and SMIM ^{+/-} TFSI ⁻ as counter-ions in EMIM TFSI	9.6±3.1	9.6±3.1
Poly acrylate ⁻ coated NPs with TBA ⁺ counter-ions in EMIM EP	9.1±0.3	9.8±0.3

References

1. Sirieix-Plénet, J., Gaillon, L. & Letellier, P. Behaviour of a binary solvent mixture constituted by an amphiphilic ionic liquid, 1-decyl-3-methylimidazolium bromide and water. *Talanta* **63**, 979–986, DOI: [10.1016/j.talanta.2004.01.001](https://doi.org/10.1016/j.talanta.2004.01.001) (2004).
2. Dong, Q. *et al.* ILThermo: A Free-Access Web Database for Thermodynamic Properties of Ionic Liquids †. *J. Chem. Eng. Data* **52**, 1151–1159, DOI: [10.1021/je700171f](https://doi.org/10.1021/je700171f) (2007).
3. Padaszyński, K. & Domańska, U. Viscosity of Ionic Liquids: An Extensive Database and a New Group Contribution Model Based on a Feed-Forward Artificial Neural Network. *J. Chem. Inf. Model.* **54**, 1311–1324, DOI: [10.1021/ci500206u](https://doi.org/10.1021/ci500206u) (2014).
4. Currás, M. R., Husson, P., Pádua, A. A. H., Costa Gomes, M. F. & García, J. High-Pressure Densities of 2,2,2-Trifluoroethanol + Ionic Liquid Mixtures Useful for Possible Applications in Absorption Cycles. *Ind. & Eng. Chem. Res.* **53**, 10791–10802, DOI: [10.1021/ie5008568](https://doi.org/10.1021/ie5008568) (2014).
5. Massart, R. Preparation of aqueous magnetic liquids in alkaline and acidic media. *IEEE transactions on magnetics* **17**, 1247–1248 (1981).
6. Jolivet, J.-P. & Tronc, E. Interfacial electron transfer in colloidal spinel iron oxide. Conversion of Fe₃O₄-Fe₂O₃ in aqueous medium. *J. Colloid Interface Sci.* **125**, 688–701, DOI: [10.1016/0021-9797\(88\)90036-7](https://doi.org/10.1016/0021-9797(88)90036-7) (1988).
7. Mamusa, M. *et al.* Microstructure of colloidal dispersions in the ionic liquid ethylammonium nitrate: influence of the nature of the nanoparticles' counterion. *J. Physics: Condens. Matter* **26**, 284113, DOI: [10.1088/0953-8984/26/28/284113](https://doi.org/10.1088/0953-8984/26/28/284113) (2014).
8. Berkovski, B. (ed.) *Magnetic Fluids and Applications Handbook* (Begell House Inc. Publ. New York, 1996).
9. Schwertmann, U. & Cornell, R. M. *Iron oxides in the laboratory* (John Wiley & Sons, 2008).
10. Brûlet, A., Lairez, D., Lapp, A. & Cotton, J.-P. Improvement of data treatment in small-angle neutron scattering. *J. Appl. Crystallogr.* **40**, 165–177, DOI: [10.1107/S0021889806051442](https://doi.org/10.1107/S0021889806051442) (2007).
11. Frot, D., Patin, P., Woodley, B. & Pinier, F. Détecteur d'Intensité Lumineuse Diffusée par des Films de Milieux Colloïdaux. *Eur. Pat. Off. 0-654-661-A1* (1994).

3.3 | Conclusion

The article in this chapter presents a novel and comprehensive approach to predict and understand the stabilisation mechanisms of nanoparticle dispersions in ionic liquids. The results show that the control of the solid-liquid interface is the key to obtain stable colloidal dispersions not only for ethylammonium nitrate (EAN) [56, 57, 60, 61] but it seems to be universal for ionic liquids in general. Long-term stable colloids at room temperature can be obtained despite differences in the nanostructure for repulsive but also for attractive interparticle interactions (here for $S(Q \rightarrow 0) < 3.5$).

As a summary of the main findings, Figure 3.1 illustrates the effect of two key parameters: the surface charge density σ and the counterion size. If both fit ($\kappa_{ion} = |\sigma/\Theta_{ion}^{max}| \approx 0.5$), over-screening of counterions can lead to a multilayer structure of alternating oppositely charged ion layers leading to repulsion between the nanoparticles. Additional parameters are the nature of the charged surface groups and molecules producing this superficial charge, the nature of the counterions compensating this charge, and the route of transfer.

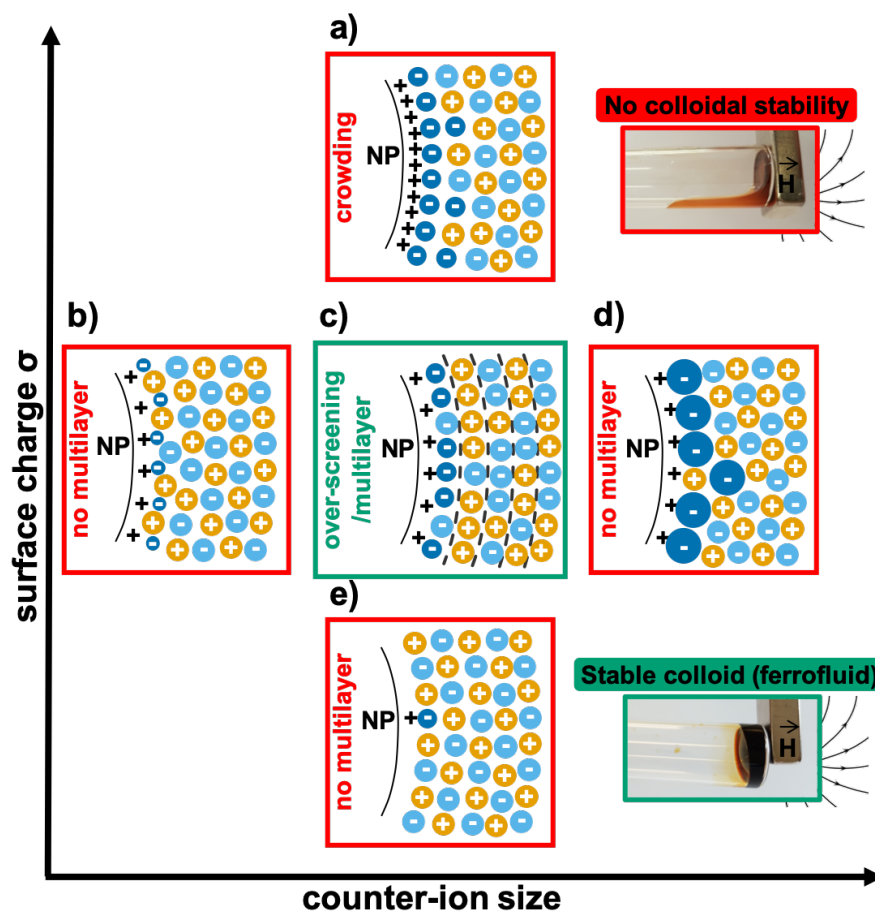


Figure 3.1 – Schemes of the interface for different surface charge densities σ and counterion sizes (example of a positively charged nanoparticle); dark blue: initial anionic counterion of the particle, light blue: anion of the ionic liquid, orange: cation of the ionic liquid; b) the counterion size is too small to form a dense monolayer on the surface. The first layer containing counterions, and ions of the IL is poorly organised and cannot act as a protection for aggregation. a) The surface is too densely charged, which attracts many anions that globally compensate this charge. There is no motor for the formation of a second organised protective layer. e) The charge is too low to attract anions and induce the formation of (sufficient) anionic/ cationic protective layers. d) The counterions are too large to fit onto the surface. Some extra counterions disrupt the organisation of the following cation layer. c) the good match: counterions size perfectly fit the surface size density and lead to overscreening and a new anionic surface, which in turn induces the formation of a cationic layer and so on. the presence of these alternate layers prevents the close approach of the particles and hence produces colloidal stability.

Colloidal and thermal stabilities of oxide nanoparticle dispersions in EMIM TFSI stabilised with sulfonate based imidazolium ions

Contents

4.1	Introduction	51
4.2	Article: “colloidal and thermal stabilities of oxide nanoparticle dispersions in EMIM TFSI stabilised with sulfonate based imidazolium ions”	52
4.3	Conclusion	68

4.1 | Introduction

After obtaining a broader understanding in a wide range of ionic liquids with various interfaces, this chapter focuses on positive nanoparticles with $\text{SBMIM}^{\pm} \text{TFSI}^{-}/\text{TfO}^{-}$ counterions in EMIM TFSI. Nanoparticles with these counterions can be dispersed in the vast majority of the ionic liquids analysed in the previous chapter. Indeed, nanoparticle dispersions with these counterions in EMIM TFSI led to the most promising sample, being repulsive, long-term colloidal stable at room temperature and under magnetic fields (up to 716 kA/m). Such dispersions hence form a true ferrofluid. This chapter explores this system more in detail in order to determine the effect of both the SBMIM^{\pm} and $\text{TFSI}^{-}/\text{TfO}^{-}$ counterions separately. Additionally, the system with

the optimal concentrations of SBMIM[±] and TFSI⁻ counterions is analysed in a broad range of temperatures (up to 200°C) and with different nanoparticle concentrations. The aim is to better define the nanoparticle ionic liquid interface and to determine suitability for high temperature applications.

This chapter is presented as a preprint of an article that was to be submitted this spring. Unfortunately, due to the COVID-19 break, some planned TGA experiments, necessary to completely ascertain the results, had to be postponed to next autumn. The conclusions presented here, within the PhD work are however sound and will be published as soon as possible.

4.2 | Article: “colloidal and thermal stabilities of oxide nanoparticle dispersions in EMIM TFSI stabilised with sulfonate based imidazolium ions”

Cite this: DOI: 00.0000/xxxxxxxxxx

Colloidal and thermal stabilities of iron oxide nanoparticle dispersions in EMIM TFSI stabilised with sulfonate based imidazolium ions[†]J. C. Riedl,^a M. Sarkar,^a T. Fiuza,^{a,b} F. Cousin,^c E. Dubois,^{*,a} G. Mériquet,^a R. Perzynski,^a V. Peyre^aReceived Date
Accepted Date

DOI: 00.0000/xxxxxxxxxx

The use of ionic liquid-based colloids at elevated temperatures is one of their most promising fields of application. Long-term colloidal and thermal stability needs to be guaranteed at the application conditions in order to employ their practical use. Therefore, first the influence of the surface charge density as well as the nature and concentration of counterions on colloidal stability is analysed in oxide nanoparticle dispersions in EMIM TFSI stabilised with sulfonate based imidazolium ions. An optimal surface charge density as well as amount and nature of counterions is obtained. In a second step, thermal stabilities of these nanoparticle dispersions are analysed on the short and long term up to 200°C combining dynamic light scattering (DLS), small angle X-ray/neutron scattering (SAXS/SANS) and thermogravimetric analysis (TGA). Long-term stable ionic liquid-based colloidal dispersions of iron oxide nanoparticles in EMIM TFSI can be obtained at least up to 200°C and nanoparticle concentrations of 12 vol% ($\approx 30\text{wt}\%$).

1 Introduction

Ionic liquids (ILs) have a variety of properties such as high electrochemical and thermal stabilities, low vapour pressures, their abilities to dissolve many chemical species, and modest conductivities making them interesting for several fields of applications. Some examples are found in synthesis and catalysis processes¹, seals and bearings², as well as energy related applications^{3,4} such as batteries, super-capacitors and thermoelectric applications^{5–7}. However, ionic liquids also have some properties hindering their industrial employment in some fields. For example they generally show elevated viscosities compared to molecular solvents which is connected to poor mass transport properties limiting the performance in energy applications.^{3,7} However, the viscosity reduces significantly when the ionic liquids are heated up whereby this disadvantage (almost) vanishes. Therefore, the use of ionic liquids at elevated temperatures is extremely interesting for applications. In addition, the performance of electrochemical de-

vices is improved with increasing temperature. A way to further improve the system's properties at low and higher temperatures can be the addition of nanoparticles to ionic liquids.⁸ The addition of charged nanoparticles to electrolytes of electrochemical devices can, for instance, improve the thermoelectric properties compared to the solvent alone.^{9,10}

Several approaches can stabilise nanoparticle dispersions in ionic liquids, ion layering of the ionic liquid around the nanoparticle being one possibility.^{11–16} It leads to repulsive (oscillatory) forces that can outrank the attractive Van der Waals forces between the nanoparticles and therefore colloidal stability is obtained. This was shown by molecular dynamics (MD) simulations¹¹ and X-ray pair distribution analysis¹² of nanoparticle dispersions in molten salts^{*} and some ionic liquids.

MD simulations of ionic liquids on flat surfaces show that this ion layering at the interface is controlled by the ratio $\kappa_{ion} = |\sigma / \Theta_{ion}^{max}|$ with σ being the solid's surface charge density and Θ_{ion}^{max} being the maximum charge density of a densely packed counterion[†] monolayer.¹⁷ A multilayered structure of ions is formed close to the solid surface if the ratio $\kappa_{ion} = |\sigma / \Theta_{ion}^{max}|$ is close to 0.5.^{17,18} The ion size thereby influences the threshold value Θ_{ion}^{max} for the formation of a monolayer. Taking the example for small ions, the smaller the ion the more ions can fit in a mono-

^a Sorbonne Université, Laboratoire PHENIX, 4 place Jussieu, case 51, 75005, Paris, France.^b Inst. de Física, Complex Fluid Group, Universidade de Brasília, Brasília, Brazil^c Laboratoire Léon Brillouin, UMR 12 CNRS-CEA, CEA-Saclay, 91191, Gif-sur-Yvette, France.^d Département de Physique - Univ. Cergy-Pontoise, 33 bd du port 95011 Cergy-Pontoise, France.^{*} Corresponding author: emmanuelle.dubois@sorbonne-universite.fr[†] Electronic Supplementary Information (ESI) available: [details of any supplementary information available should be included here]. See DOI: 00.0000/00000000.^{*} analogue of ionic liquids with a melting temperature above 100°C[†] ions of opposite charge compared to the surface

layer and Θ_{ion}^{max} increases. Consequently, a higher surface charge density σ is needed to obtain a ratio $\kappa_{ion} \approx 0.5$. However, the range of variation of the surface charge density σ of nanoparticles is limited. It depends on the material as well as on the coating of the nanoparticles. For instance, the limits for citrate coated iron oxide nanoparticles are between 0 and $32 \mu\text{C}/\text{cm}^2$.¹⁹ On the other hand, the counterions can be changed in the system, either by the choice of the ionic liquid itself or by additional ions. Several works analysing ionic-liquid based colloids evidenced that these additional ions influence the colloidal stability despite their low concentration compared to the ions from the ionic liquid.^{14,15,20–22} Furthermore, nanostructure changes are observed in interface studies between ionic liquids and chargeable surfaces like graphite²³ and gold²⁴ when adding additional small ions like Li^+ or Cl^- . These ions (even at low concentrations) have an influence as they can locate at the interface.

In this work, first the colloidal stability of nanoparticle dispersions in the ionic liquid EMIM TFSI is analysed changing the surface charge density as well as the nature and concentration of counterions. Choosing a system where it is possible, the optimal surface charge density as well as the amount and nature of counterions is obtained for charged (magnetic) iron oxide based systems using optical microscopy, dynamic light scattering (DLS) and small angle X-ray scattering (SAXS) measurements. The two best compositions are then analysed by transmission electron microscopy (TEM).

The use of ionic liquids at elevated temperatures is extremely interesting for applications and to be suitable, the ionic liquid-based systems need to be long-term stable in these application conditions. Some ionic liquids are only decomposed at 400°C and higher temperatures when analysed in the short term, EMIM TFSI having one of the highest values and is therefore chosen as the ionic liquid here.²⁵ However, their long-term temperature stability can be up to a factor two lower.^{26,27} Thus, long-term analysis is necessary to determine suitability for applications. Therefore, the second part of this work examines the long-term stability of colloids in optimal room temperature conditions found in the first part. They are analysed up to 200°C for hours combining dynamic light scattering (DLS), small angle X-ray/neutron scattering (SAXS/SANS) as well as thermogravimetric analysis (TGA) supported by DLS measurements over days.

2 Materials and Methods

2.1 Preparation of ionic liquid-based colloids

The products were purchased and used as received. They are listed in the ESI†. The same batch of maghemite ($\gamma\text{-Fe}_2\text{O}_3$) nanoparticles was used for all experiments. The synthesis^{28,29} and the sample characteristics are described in detail in ref.¹⁶. Briefly, sodium hydroxide solution was added to the initial acid ferrofluid stabilised with nitrate counterions till the point of zero charge was reached at $\text{pH} \approx 7$. The free ions were washed off several times with ultra-pure water. The particles can be charged by protonation of the oxide surface with four different strong acids to form hydroxyl groups: triflimidic acid (HTFSI), triflic acid (HTfO), 1-(4-Sulfobutyl)-3-methylimidazolium bistriflimide

(HSBMIM TFSI), and 1-(4-Sulfobutyl)-3-methylimidazolium triflate (HSBMIM TfO). The charge increases while decreasing the pH and it is compensated by the deprotonated form of these four acids, shown in Figure 1. Note that the acids HSBMIM TFSI and HSBMIM TfO are composed of two entities: the protonated cation HSBMIM⁺ and the anion TFSI⁻ or TfO⁻. The deprotonated form is thus composed of the zwitterion SBMIM[±] and the anion. In HSBMIM TFSI and HSBMIM TfO, the ratio of SBMIM[±] and TFSI⁻ or TfO⁻ can be varied by adding first HTFSI or HTfO and then SBMIM[±] (which is a powder).

All the initial aqueous dispersions were mixed with a similar volume of the ionic liquid EMIM TFSI (see Figure 1) and the water was removed by freeze-drying. The resulting nanoparticle volume fraction Φ_{NP} in the ionic liquid of around 1vol% and the concentration of the initial counterions was hence kept.

The system with HSBMIM TFSI was centrifuged using an Optima 70 ultracentrifuge and a type 100 Ti fixed-angle rotor from the company Beckman Coulter, USA. The samples were centrifuged at 55 000 rpm (243 000g) for 24 hours at 19°C . Separating the clear supernatant led to concentrated samples with nanoparticle volume fractions $\phi \approx 10\text{-}20\text{vol}\%$ which were diluted with their supernatant to appropriate concentrations.

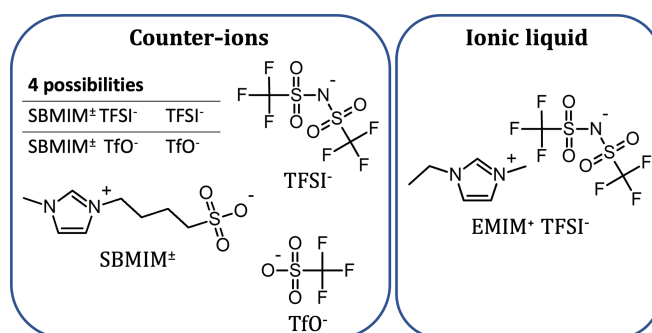


Fig. 1 Structures of the ions 1-(4-butylsulfonate)-3-methylimidazolium (SBMIM[±]), triflate (TfO⁻), bistriflimide (TFSI⁻), and 1-ethyl-3-methylimidazolium (EMIM⁺).

2.2 Analyses of the sample

The ionic liquid-based colloids were analysed by optical microscopy in order to detect agglomerates on the micrometre scale. They could also be analysed by transmission electron microscopy (TEM) using a JEOL-100 CX TEM. A droplet of the ionic liquid-based ferrofluids (diluted to around 0.01vol% with pure ionic liquid) was deposited on a carbon-coated copper grid and the back-side of the grid was swiped over a paper to remove as much liquid as possible. However, the analysis with TEM needs to be complemented with other techniques as the preparation of the sample for the TEM measurements can affect the sample (e.g. interparticle interactions) due to dilution, exposure to humidity of the air and small analysed volumes (compared to the other techniques employed here). If no major agglomeration is observed in optical microscopy, the samples were analysed by dynamic light scattering (DLS). Light scattering measurements were performed using Vasco, VascoFlex or VascoKin DLS Particle Analyzers from Cor-

douan Technologies to study translational diffusion properties of the ionic liquid-based colloids. Note that the viscosity of the ionic liquid-based colloids is difficult to know accurately as it depends on water traces³⁰ and on the other additives in the dispersions. However, performed together with other techniques, DLS can give complementary information and the properties of the samples can be analysed in the long-term.

Light scattering was coupled with small angle neutron scattering (SANS) up to 200°C for hours. The setup and the details of the experiments performed on the PAXY spectrometer at the LLB facility (CEA Saclay, France) are described in detail in the ESI †. Three different configurations were used leading to an accessible Q-range of 0.005 Å⁻¹ to 0.2 Å⁻¹.

SAXS experiments were carried out with a laboratory XEUSS 2.0 (W)SAXS. The beam energy was fixed at 8 keV and the wavelength at $\lambda=1.54$ Å. The sample to detector distance was 3 m to yield an accessible Q-range of 0.005 Å⁻¹-0.2 Å⁻¹. The samples absorb X-rays due to the ionic liquid EMIM TFSI and due to the iron atoms. Therefore thin capillaries were needed and the best compromise between absorption and diffused signal was obtained with 0.1 mm thick borosilicate capillaries from Vitrocom®. However, the wall thickness of 0.07 mm has an error of $\pm 20\%$ and the interior thickness error is $\pm 10\%$. As a consequence, absolute intensity could hardly be determined and the high Q region (> 0.1 Å⁻¹) was rather noisy. As a conclusion, the nanoparticle volume fraction together with the SANS measurements were used to adjust the SAXS curves to absolute intensities.

The SAXS and SANS form factor $P(Q)$ of the nanoparticles were obtained from several measurements at low nanoparticle volume fractions in water and these form factors were used to determine structure factors $S(Q)$ from $S(Q) = \frac{I(Q)}{\Delta\rho^2 V \Phi_{NP} P(Q)}$. The value of $S(Q \rightarrow 0)$ therefore compares the studied dispersions to a "reference" dispersion of individual nanoparticles without interparticle interaction. The difference can be due to interparticle interaction or to a change of the scattering objects (for example formation of small aggregates).

Static and ramped temperature thermogravimetric analysis (TGA) were performed with a TGA 550 from TA Instruments. All samples (about 10-20 mg with the mass precision ± 0.1 μg) were measured in platinum pans and with a nitrogen gas flow of 40 mL/min. Short-term temperature stabilities were conducted with a heating rate of 10°C/min from room temperature up to 600°C. Long-term temperature stabilities were measured at isothermal mode for several hours at the specified isothermal temperature with a heating rate of 20°C/min from room temperature up to this temperature.

The nanoparticle volume fractions were deduced from the iron concentration determined by flame atomic absorption spectroscopy (FAAS) taking a density of 4.87 g/cm³³¹.

The technical details and the implementation of the techniques are detailed in the ESI of ref¹⁶.

3 Results and discussion

3.1 Decoupled analysis of the optimal counterion concentrations

In a recent publication¹⁶ it was demonstrated that colloiddally long-term stable dispersions of oxide nanoparticles in EMIM TFSI can be prepared composed of positive nanoparticles with SBMIM[±] TFSI⁻ assumed to be at the solid liquid interface. Here, the role of both counterions (the zwitterion SBMIM[±] and the anion TFSI⁻) is analysed in a decoupled way. In addition, SBMIM[±] TFSI⁻ is replaced by SBMIM[±] TfO⁻ in order to look at the influence of the anion, TfO⁻ being smaller than TFSI⁻, its charge coming from a different chemical group.

For this purpose, in a first step the surface charge density is changed in water thanks to pH. Adding HTFSI or HTfO to the neutral nanoparticles at the point of zero charge, the particles become positive with TFSI⁻ or TfO⁻ counterions, the charge increasing while pH decreases. The concentration of HTFSI and HTfO was adapted to reach pH values between 5 and 1.3 which convert to concentrations between 0.0035 and 0.075 mol/L. For the studied iron oxide nanoparticles and similar counterions, this converts to a surface charge between around 4 and 30 $\mu\text{C}/\text{cm}^2$.¹⁹ Note that lowering the pH too much can lead to dissolving of the particles. Therefore the minimum pH was set to pH=1.3 (equivalent of around 30 $\mu\text{C}/\text{cm}^2$) to prevent particle dissolution.

Adding the zwitterion SBMIM[±] to these samples allows to introduce the second counterion independently so that the ratio of SBMIM[±] to TFSI⁻ or TfO⁻ can be adjusted.

After transfer to the ionic liquid the samples are analysed by DLS measurements and the deduced apparent hydrodynamic diameter d_H are depicted in Figure 2. Note that the process can be performed in one step by simply adding HSBMIM TFSI or HSBMIM TfO, leading to a ratio SBMIM[±]/ TFSI⁻ or TfO⁻ equals one. These cases are shown as blue cones.

Several observations can be made.

- 1) Nanoparticles with TFSI⁻ or TfO⁻ counterions alone are flocculated systems whatever the surface charge densities analysed here (around 4 to 30 $\mu\text{C}/\text{cm}^2$).
- 2) Adding SBMIM[±] to these systems can stabilise the nanoparticles if the concentration of TFSI⁻ or TfO⁻ counterions (the surface charge density) is high enough which means that SBMIM[±] localises at least partly at the solid liquid interface.
- 3) In these colloiddally stable systems, a higher surface charge density leads to a lower apparent hydrodynamic diameter d_H for the same SBMIM[±] concentration for both TfO⁻ or TFSI⁻ added ions.
- 4) In addition, the nature of the first ions introduced (TfO⁻ or TFSI⁻) can influence the apparent hydrodynamic diameter d_H for the same counterion concentrations (surface charge density). For example for a surface charge density of 14 $\mu\text{C}/\text{cm}^2$ (0.014 mol/L TfO⁻ or TFSI⁻ introduced with the added acid) and a SBMIM[±] concentration of around 0.07 mol/l the apparent hydrodynamic diameter for nanoparticle dispersions containing TfO⁻ is ≈ 60 nm, although it is bigger than 100 nm for dispersions with TFSI⁻.
- 5) The apparent hydrodynamic diameter d_H is influenced by the added zwitterion SBMIM[±] concentration. Starting from aggre-

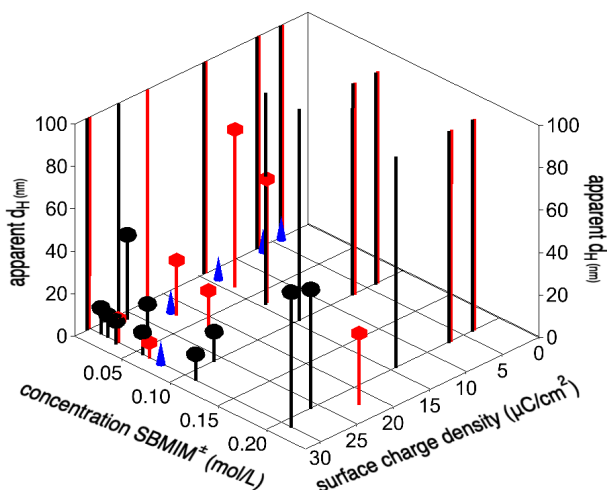


Fig. 2 DLS measurements for nanoparticle dispersions in EMIM TFSI with TfO⁻ and SBMIM[±] TfO⁻ counterions (red boxes) as well as TFSI⁻ and SBMIM[±] TFSI⁻ counterions (black spheres). The corresponding ion structures are depicted in Figure 1. The surface charge density is introduced by the addition of HTFSI or HTfO to the nanoparticles. See text for more information. If only the drop line is visible it means that the apparent hydrodynamic diameter d_H is higher than 100 nm.

gated systems with only TFSI⁻ or TfO⁻ counterions, the addition of SBMIM[±] first decreases the apparent hydrodynamic diameter d_H , which increases again at higher SBMIM[±] concentrations. The lowest apparent hydrodynamic diameter d_H are observed at the maximum surface charge density $\sigma \approx 30 \mu\text{C}/\text{cm}^2$ which corresponds to a counterion concentration of 0.075 mol/L. A 1:1 ratio of SBMIM[±] to TFSI⁻ or TfO⁻ ions introduced leads to (one of) the lowest apparent hydrodynamic diameter d_H and can be added in one step in the form of HSBMIM TFSI or HSBMIM TfO. This makes the process easier and faster and it is thus used for further experiments as it is also more interesting for applications. According to the results presented above, the nanoparticles have thus SBMIM[±] TFSI⁻ or SBMIM[±] TfO⁻ counterions, in these two kinds of dispersions.

3.2 Room temperature colloidal stabilities

Among the nanoparticle dispersions with the lowest apparent hydrodynamic diameter d_H analysed in section 3.1 the most interesting for applications (easiest to prepare) are analysed with transmission electron microscopy (TEM) and the images are depicted in Figure 3. They show for both nanoparticles with SBMIM[±] TFSI⁻ and SBMIM[±] TfO⁻ counterions that the shape of the nanoparticles is not changed compared to the initial sample in water (TEM picture given in ref¹⁶). Figure 3 shows that the nanoparticles with SBMIM[±] TFSI⁻ counterions are well dispersed in EMIM TFSI. The particles with SBMIM[±] TfO⁻ counterions are rather well dispersed as well, however, some small and loose aggregates are observed whose nanoparticles don't seem to stick together.

Figure 4 shows SANS measurements for bare nanoparticles dispersed in EMIM TFSI with SBMIM[±] TFSI⁻ and SBMIM[±]

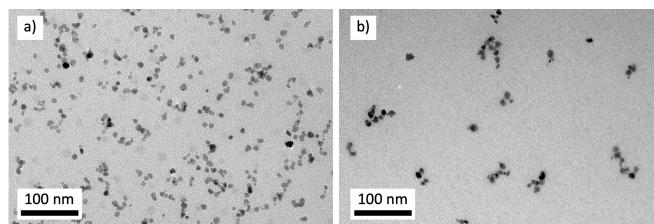


Fig. 3 TEM images of nanoparticles dispersed in the ionic liquid EMIM TFSI with a) SBMIM[±] TFSI⁻ and b) SBMIM[±] TfO⁻ counterions. The ion structures are depicted in Figure 1. Both samples were diluted to a nanoparticle volume fraction $\phi_{NP} \approx 0.01 \text{ vol}\%$ with pure EMIM TFSI before the deposition of the ionic liquid-based colloid on the TEM grid.

TfO⁻ counterions. The structure factors $S(Q)$ of the samples are depicted which are defined by the ratio between their scattered intensity $I_{\text{sample}}(Q)$ and the scattered intensity of the sample's form factor $I_{\text{form factor}}(Q)$ which is equivalent to a sample without interparticle interaction. Interparticle interactions can be deduced from the value of the structure factor $S(Q)$ extrapolated to $Q=0 \text{ \AA}^{-1}$. If $S(Q \rightarrow 0)$ is bigger or smaller than 1, the system is attractive or repulsive, respectively. The values for $S(Q \rightarrow 0)$ are given in the inset of Figure 4 as a function of the temperature and in Figure 5 as a function of the nanoparticle volume fraction ϕ_{NP} . Figure 5 shows the values of $S(Q \rightarrow 0)$ determined from SANS and SAXS measurements for the same sample batch. From both SAXS and SANS it can be deduced that the global interparticle interactions of the system with SBMIM[±] TfO⁻ counterions is attractive ($S(Q \rightarrow 0) > 1$) and that of the system with SBMIM[±] TFSI⁻ counterions is repulsive ($S(Q \rightarrow 0) < 1$). This shows that not only the zwitterion SBMIM[±] stabilises the nanoparticles but that introducing the additional counterions TfO⁻ or TFSI⁻ also plays a role in the nanostructure at the nanoparticle interface. This means that they need to be situated at the interface (at least in parts) to influence the nanoparticle interactions.

Apparent hydrodynamic diameter d_H deduced from DLS measurements for the nanoparticles with SBMIM[±] TFSI⁻ counterions is approximately 12 nm (as for the initial water samples,¹⁶) which proves that no aggregates are present. On the other hand, the sample with SBMIM[±] TfO⁻ counterions shows an average apparent hydrodynamic diameter $d_H \approx 25 \text{ nm}$, which suggests that small aggregates are present in the order of a few particles per aggregate.

Summarizing, the results obtained with small angle scattering, DLS and TEM at room temperature match well. The sample with SBMIM[±] TFSI⁻ counterions is well dispersed in the TEM image (Figure 3) and the system's interparticle interactions are repulsive. In addition, the low apparent hydrodynamic diameter proves that no aggregates are present in this sample. The sample with SBMIM[±] TfO⁻ counterions is also colloidal stable, however, it shows some small loose aggregates in the TEM image, is slightly attractive deduced from SANS and SAXS measurements which is confirmed by a higher average apparent hydrodynamic diameter $d_H \approx 25 \text{ nm}$ representing around a few particles per aggregate. Besides their differences both samples are long-term stable at least for one year as shown by SAXS

measurements (Figure S2 of the ESI†).

The concentration of attractive ionic liquid-based colloids

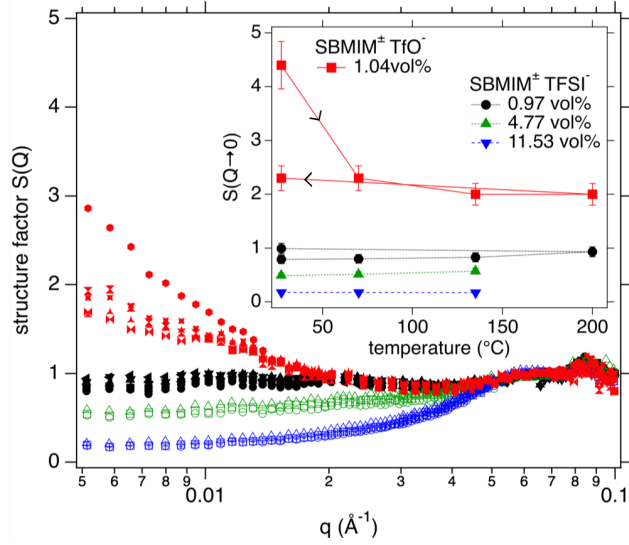


Fig. 4 Structure factors $S(Q)$ at different temperatures (27°C (\circ), 70°C (\square), 135°C (\triangle), and 200°C (∇) and back at 27°C (\diamond) obtained by small angle neutron scattering (SANS) as a function of the scattering vector Q for nanoparticle dispersions in EMIM TFSI. One sample with SBMIM $^\pm$ TfO $^-$ counterions at $\phi_{NP}=1.04$ vol% (in red) and three samples with SBMIM $^\pm$ TFSI $^-$ counterions at $\phi_{NP}=0.97$, 4.77 or 11.53 vol% (in black, green, and blue, respectively) are shown. The ion structures are depicted in Figure 1. The inset gives the values for $S(Q\rightarrow 0)$ as a function of temperature. The lines are shown for an optical guideline. Note that both concentrated sample cells leaked at 200°C . Therefore, no further SANS measurements could be obtained (SAXS and DLS could be performed with the remaining sample, the latter being plotted in Figure 5)

can lead to phase separation shown for citrated iron oxide nanoparticles with sodium counterions.³² Hence, here only the nanoparticle system with SBMIM $^\pm$ TFSI $^-$ counterions is concentrated as it is repulsive. The interparticle interactions of the sample system as a function of the nanoparticle volume fraction ϕ_{NP} is analysed by SAXS and SANS measurements. The deduced values of $S(Q\rightarrow 0)$ are shown in Figure 5 and equal osmotic compressibilities χ for a repulsive system. For individual dispersed particles, χ relates to the osmotic pressure Π .

$$S(Q \rightarrow 0) = \chi(\phi_{NP}) = \frac{kT}{V_{NP}} \frac{\partial \Phi_{NP}}{\partial \Pi} \quad (1)$$

with V_{NP} the volume of the nanoparticles. At a low volume fraction Φ_{NP} , the second order virial development of Π relates $\chi(\Phi_{NP})$ with the second order virial coefficient A_2 by: $\chi(\phi_{NP})=(1+2A_2\Phi_{NP})^{-1}$. Note that $K_T = 2A_2$ quantifies the two-bodies interparticle interaction in the dispersion. The osmotic compressibility $\chi(\phi_{NP})$ decreases with increasing nanoparticle volume fraction Φ_{NP} and therefore the two-bodies interparticle interaction in the dispersion K_T is positive and the interparticle interaction is repulsive. In this case, the Carnahan-Starling expression for effective hard spheres^{33,34} can be used to analyse the compressibility χ up to large volume fractions as in references^{21,35-40}. In this model an effective volume fraction Φ_{eff}

accounts for a decrease of the interparticle interaction through a characteristic length κ^{-1} which is the analogue of the Debye screening length of interparticle electrostatic repulsion in standard polar solvents. Equation (2) describes the compressibility

$$\chi(\Phi_{NP}) = \chi_{CS}(\Phi_{eff}) = \frac{(1 - \Phi_{eff})^4}{1 + 4\Phi_{eff} + 4\Phi_{eff}^2 - 4\Phi_{eff}^3 + \Phi_{eff}^4} \quad (2)$$

with

$$\Phi_{eff} = \Phi \frac{d_{eff}^3}{d_{NP}^3} = \Phi \left(1 + \frac{2\kappa^{-1}}{d_{NP}}\right)^3 \quad \text{and} \quad d_{eff} = d_{NP} + 2\kappa^{-1} \quad (3)$$

and the two-bodies interparticle interaction K_T is then

$$K_T = 2A_2 = 8 \frac{\Phi_{eff}}{\Phi}. \quad (4)$$

The experimental data of the compressibility is fitted in Figure 5 with the Equations (2) and (3). The best fit is obtained for a fitting parameter $\kappa^{-1} \approx 1.0$ nm taking $d_{NP}=8.7$ nm. The associated repulsive interparticle interaction range is 3-5 κ^{-1} , hence 3-5 nm. The two-bodies interparticle interaction K_T is then $K_T=15.6\pm 1.0$ ($A_2=7.8\pm 0.5$) which is almost the double of the hard sphere value $K_T^{HS}=8$ ($A_2^{HS}=4$)³³ and of the values obtained for citrate coated oxide nanoparticles in ethylammonium nitrate with sodium counterions ($A_2=4.6$).^{15,21}

3.3 Thermal stabilities

The long-term stability of samples needs to be guaranteed on a large range of temperatures to be suitable for applications. Therefore, the two best systems already studied in the previous section are analysed at high temperatures. These systems are nanoparticles with SBMIM $^\pm$ TfO $^-$ counterions ($\phi=1.04$ vol%) and nanoparticles with SBMIM $^\pm$ TFSI $^-$ counterions ($\phi=0.97$ vol%, 4.77 vol%, and 11.53 vol%). Several techniques are coupled on different length scales.

Let us begin with the in-situ measurements of SANS and DLS up to 200°C . Given the limited SANS time, few temperatures were chosen (27°C , 70°C , 135°C , 200°C , and back at 27°C). For each step, DLS was performed after heating and enables checking that equilibrium is reached before measuring SANS. This is possible as the viscosity varies with temperature which influences the correlation function. Hence, stability of the correlation function means that the viscosity and temperature is stable. DLS performed after SANS tells us whether some change occurred. One T step lasts around two hours, the whole cycle from 27°C back to 27°C around 10 hours.

The structure factors are plotted in Figure 4 and the DLS is presented as an apparent d_H in the inset of Figure 5 at 27°C before and after the heating cycle up to 200°C . Note that SAXS before and after heating has also been performed (Figure 5) to complement the analysis.

Looking first at the two samples at $\phi \approx 1$ vol% with different counterions shows a weak evolution at high temperature (Figure 4 and its inset showing $S(Q\rightarrow 0)$). Indeed, the strong decrease of intensity for nanoparticles with SBMIM $^\pm$ TfO $^-$ coun-

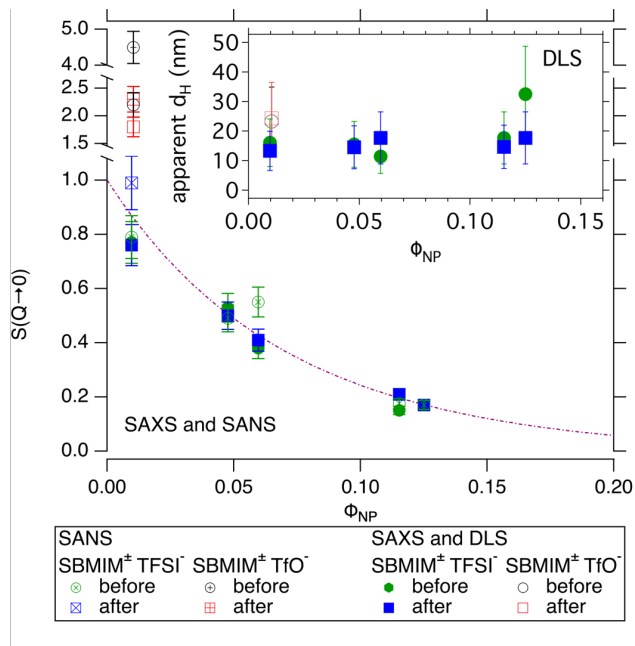


Fig. 5 $S(Q \rightarrow 0)$ deduced from SAXS and SANS measurements at room temperature for SBMIM[±] TFSI⁻ counterions before and after heating the sample for several hours up to 200°C are depicted as a function of the nanoparticle volume fraction ϕ_{NP} . The full line corresponds to the fit of the data with Equations (2) and (3) using $\phi_{eff}/\phi = 1.82$ (two-bodies interparticle interaction $K_T = 15.6 \pm 1.0$ and second virial coefficient $A_2 = 7.8 \pm 0.5$). The inset shows apparent hydrodynamic diameter d_H at room temperature before and after heating the samples for several hours up to 200°C as a function of the nanoparticle volume fraction ϕ_{NP} for both SBMIM[±] TFSI⁻ and SBMIM[±] TfO⁻ counterions. The ion structures are depicted in Figure 1.

terions between 27°C and 70°C appears as an accident. The corresponding SAXS measurement at room temperature gives $S(Q \rightarrow 0) = 2.2 \pm 0.2$, which matches with the SANS after the cycle. Moreover, the DLS is similar before and after heating. This accident can be due to some pollution (water, solvent,...) that is removed reversibly while heating. Leaving aside this point, the values of $S(Q \rightarrow 0)$ show that for these nanoparticles with SBMIM[±] TfO⁻ counterions, the same small aggregates/weak attractions remain whatever the temperature. Both the repulsive and the attractive sample appear stable on the time scale of the experiment.

For the nanoparticles with SBMIM[±] TFSI⁻ counterions, the interaction remains weakly repulsive whatever the temperature. However, due to a small increase of $S(Q \rightarrow 0)$ from 0.83 ± 0.08 to 0.98 ± 0.10 after heating, a long-term experiment was performed. The sample was heated several days at three temperatures up to 170°C under vacuum and its state was checked with a DLS measurement at room temperature after each plateau. The results are summarised in Figure 6. The apparent hydrodynamic diameter is $d_H = 12 \pm 2$ nm showing that the sample is long-term stable at high temperature, here during 18 days. Analysing now the behaviour of the concentrated samples based on nanoparticles with SBMIM[±] TFSI⁻ counterions, the results are quite similar. Note however that both concentrated sample cells leaked at 200°C,

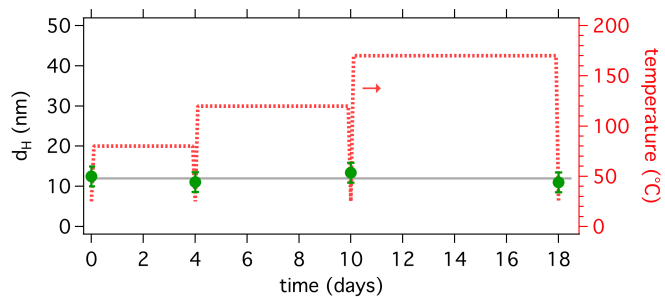


Fig. 6 DLS measurements for the iron oxide nanoparticle dispersion with SBMIM[±] TFSI⁻ counterions at a nanoparticle volume fraction $\phi_{NP} = 0.97$ vol% shown in Figure 4 and 5. The sample was heated in a low vacuum of ≈ 10 mbar in an open bottle at the indicated temperatures for days. Note that the maximum temperature of the heating device is 170°C. DLS measurements were performed at room temperature which gives extra information about temperature cycling.

therefore no SANS could be performed. SAXS and DLS after heating were nevertheless measured with the remaining sample. Such a leak also appeared with dilute samples ($\phi_{NP} \approx 1$ vol%) during the tests of the cell and was solved by adapting the nature of the ring spacer (and the nature of the materials). It appeared as a mixture of wetting phenomena and bubbling/degassing at high temperature, which was not occurring in the same way depending on the nature of the materials used to build the cell. This result shows however that these wetting phenomena and bubbling/degassing grow with ϕ_{NP} .

At high temperature, the structure factors are close to those at room temperature and the compressibilities ($S(Q \rightarrow 0)$, Figure 5) after heating are also quite similar (Figure 4). The apparent d_H differ before and after heating for the concentrated samples (Figure 5, inset), however, with different trends. This is probably due to an underestimated error bar on these values. Indeed, more concentrated samples are more difficult to measure and some pollution introduced by the cell or during the transfer to the oven may change the viscosity (water, solvent,...).

All these elements converge towards a good stability of these concentrated sample at high temperature, keeping the same nanostructure and interaction.

These analysis have been complemented by TGA, which brings an indirect and global information while heating and elucidates the maximum application temperatures of the samples in the short and long term. The weight losses and derivative weights of ramped TGA measurements up to 600°C are depicted in Figure 7 for ionic liquids without and with nanoparticles. Several values can be given for the thermal degradation, with T_{onset} and T_{start} being among the most popular.^{27,41} T_{onset} is defined by the intersection of the linear extrapolation of the weight loss at decomposition to the baseline weight, either from the beginning of the experiment or after a drying step.⁴¹ This value gives higher decomposition temperatures than T_{start} that is the temperature at which the sample starts to lose weight. It is here defined for a derivative mass loss of $1.67 \times 10^{-2} \%$ /°C which represents a weight loss of 10%/1h (for a heating rate of 10°C/min) and is indicated in the graph. We will focus here on T_{start} values as this

gives closer values to long-term applications.

Table 1 gives the results for the ferrofluids with a nanoparticle volume fraction $\phi_{NP} \approx 1$ vol%, $T_{start} = 303 \pm 10^\circ\text{C}$ for both $\text{SBMIM}^\pm \text{TFSI}^-$ and $\text{SBMIM}^\pm \text{TfO}^-$ counterions although T_{onset} for $\text{SBMIM}^\pm \text{TFSI}^-$ is around 20°C smaller than for the sample with $\text{SBMIM}^\pm \text{TfO}^-$ counterions.

These curves can be compared to the data for pure EMIM TFSI. The literature values give T_{onset} in the range of 410 and 450°C and $T_{start} \approx 320^\circ\text{C}$,^{26,42,43} values higher than for the ferrofluids analysed here. However, the ferrofluids may contain some water around the nanoparticles which would correspond to 0.15 - 0.3 vol% if one or two water layers were present at the interface. EMIM TFSI left at air thus containing 0.5 wt% has been measured. It gives $T_{onset} = 386 \pm 10^\circ\text{C}$ and $T_{start} = 322 \pm 10^\circ\text{C}$, lower than dry EMIM TFSI, however, higher than for the ferrofluids. The small difference between the nanoparticle dispersions could also be explained by the TfO^- ions in the case of $\text{SBMIM}^\pm \text{TfO}^-$ counterions. However, EMIM TfO in literature ($T_{onset} = 348^\circ\text{C}$;⁴⁴) and here with absorbed water (≈ 1.5 wt%) is less stable than EMIM TFSI. Another element is however present in the ferrofluids: SBMIM $^\pm$ with an amount of around 2.5 wt% for $\phi \approx 1$ vol%. Hence, dry EMIM TFSI with this amount of HSBMIM TFSI is analysed and gives $T_{onset} = 401^\circ\text{C}$ and $T_{start} = 295 \pm 10^\circ\text{C}$, a little smaller than pure dry EMIM TFSI.

The sample with an elevated nanoparticle volume fraction ($\phi_{NP} = 4.77$ vol%) gives $T_{start} = 283 \pm 10^\circ\text{C}$, 20°C lower than for both nanoparticle dispersions at around 1 vol% nanoparticles. Indeed, more concentrated ferrofluids contain more SBMIM $^\pm$.

Note that partial evaporation of the sample also leads to a weight loss although the sample is not decomposed. EMIM TFSI for example is considered relatively volatile compared to other ionic liquids and its partial pressure at 200°C is 0.02 Pa (calculated with the values of ref⁴⁴). This will be discussed in detail in the following section.

In addition, long term thermal stabilities are analysed in isothermal mode. Figure S5 of the ESI † shows that the weight loss for the ionic liquid EMIM TfO is smaller than 0.1% after 10 hours at 200°C (+ 3 hours at 160°C and 180°C each).

3.4 Discussion

The colloidal stability of the analysed iron oxide nanoparticle dispersions is first discussed in general and then in regard of thermal stability.

A structuring of ions at the solid-liquid interface is proven to be the reason for colloidal stability in ionic liquids and molten salts.^{11,12} Simulations of ionic liquids on flat surfaces show that this ion layering at the interface is controlled by the ratio $\kappa_{ion} = |\sigma / \Theta_{ion}^{max}|$ with σ being the solid's surface charge density and Θ_{ion}^{max} being the maximum charge density of a densely packed counterion monolayer.¹⁷ A multilayered structure of positive and negative ions is formed close to the solid surface if the ratio κ_{ion} is close to 0.5 .^{17,18} Although a curvature of the nanoparticle surface and surface roughness influence the situation it is helpful for a discussion.

Experimentally, both σ and Θ_{ion}^{max} can be varied for the studied

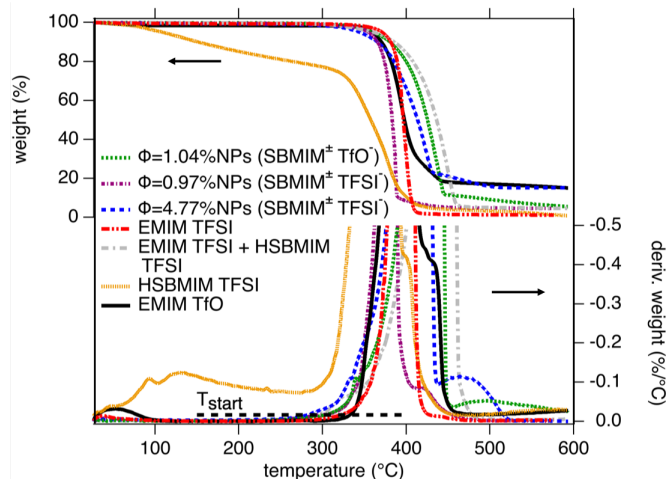


Fig. 7 Ramped thermogravimetric analysis (TGA) measurements for nanoparticle dispersions in EMIM TFSI are depicted with a nanoparticle volume fraction $\phi_{NP} = 1.04$ vol% with $\text{SBMIM}^\pm \text{TfO}^-$ counterions as well as $\phi_{NP} = 0.97$ vol% and a concentrated sample with $\phi_{NP} = 4.77$ vol% nanoparticles with $\text{SBMIM}^\pm \text{TFSI}^-$. Wet EMIM TFSI and wet EMIM TfO as well as dry HSBMIM TFSI and dry EMIM TFSI containing 2.5 wt% HSBMIM TFSI are also depicted, 2.5 wt% HSBMIM TFSI being the amount in nanoparticle dispersions with around 1 vol% nanoparticles. T_{start} is here defined for a derivative mass loss of $1.67 \times 10^{-2} \%$ /°C representing a weight loss of $10\%/1\text{h}$ and is indicated in the graph.

systems, Θ_{ion}^{max} through the nature of the ions and σ through the pH of the surrounding medium. Assuming a similar behaviour for the nanoparticle charge for different counterions¹⁹, σ is here tuned between 4 and $30 \mu\text{C}/\text{cm}^2$.

The Θ_{ion}^{max} values of the analysed ions are $|\Theta_{EMIM}^{max}| \approx 45 \mu\text{C}/\text{cm}^2$,¹⁸ $|\Theta_{TFSI}^{max}| \approx 50 \mu\text{C}/\text{cm}^2$,⁴⁸ $|\Theta_{TfO}^{max}| \approx 100 \mu\text{C}/\text{cm}^2$ assuming that it is around half the size of the TFSI^- anion, and $|\Theta_{SBMIM}^{max}| \approx 35 \mu\text{C}/\text{cm}^2$ considering that SBMIM $^\pm$ is a BMIM $^+$ cation with an extra sulfonate group leading to a slightly smaller Θ_{ion}^{max} value.

What can we learn from the results described above? Figure 8 shows two imaginable schemes of the nanoparticle (NP) ionic liquid (IL) interface for the case of $\text{SBMIM}^\pm \text{TFSI}^-$ and $\text{SBMIM}^\pm \text{TfO}^-$ counterions.

- The zwitterions SBMIM $^\pm$ must locate at the solid-liquid interface as colloidal stability can only be achieved in their presence.
- For the maximal surface charge density σ (here $\approx 30 \mu\text{C}/\text{cm}^2$), the ratio $\kappa_{ion} = |\sigma / \Theta_{ion}^{max}|$ for the zwitterion SBMIM $^\pm$ is close to 1 meaning that a structure close to a monolayer would be formed on the nanoparticle surface. As SBMIM $^\pm$ is a zwitterion this would not change the sign and value of the positive nanoparticle surface charge. The zwitterion SBMIM $^\pm$ could hence increase the distance of an ion layering to the nanoparticle surface leading to a bigger repulsion between the nanoparticles.
- With the negative sulfonate group close to the positive nanoparticle surface, the imidazolium end shows away from the nanoparticle surface, providing a positive charge on the top of the SBMIM $^\pm$ layer, which can induce organisation. For this maximal surface charge, stable dispersions are obtained on a large range of SBMIM $^\pm$ concentrations (0.01 - 0.12 mol/L). Note that 0.01 mol/L

Table 1 Critical temperatures (T_{start} and T_{onset}) deduced from ramped thermogravimetric analysis (TGA) measurements. T_{start} gives the temperature at which the sample starts to loose weight, here defined for a derivative weight loss of $1.67 \times 10^{-2} \%$ /°C. T_{onset} is defined by the linear extrapolation of the weight loss at decomposition to the baseline at zero weight loss. All temperatures are given in °C and the error is $\pm 10^\circ\text{C}$. * losses due to evaporation are removed; ⁱ for ionic liquid containing water.

	measured			literature			
	T_{start}	T_{onset}	weight loss after 10h at 200°C	T_{start}	T_{onset}	$T_{0.01/10h}$ or $T_{0.02/10h}$	$T_{max,0.01/year}$
$\phi_{NP}=1.04 \text{ vol}\%$ SBMIM [±] TfO ⁻	303	393		-	-		
$\phi_{NP}=0.97 \text{ vol}\%$ SBMIM [±] TFSI ⁻	303	374		-	-		
$\phi_{NP}=4.77 \text{ vol}\%$ SBMIM [±] TFSI ⁻	283	377		-	-		
EMIM TfO	333 ⁱ	373 ⁱ	<0.1%		348 ⁴⁴		185 ⁴⁴ *
EMIM TFSI	322 ⁱ	386 ⁱ	<0.1% ⁴⁵	320 ²⁶	410-450 ^{26,42,43}	222 ²⁶ or 252 ⁴⁵	286 ⁴⁴ *
EMIM TFSI + 2.5 wt% HSBMIM TFSI	295	401		-	-		
HSBMIM TFSI	30	305					
HSBMIM HSO ₄					327 ⁴⁶		
HSPMIM TfO					288 ⁴⁷		

corresponds to around half a monolayer of SBMIM[±] assuming all these zwitterions located at the nanoparticle interface, and that several hours of stirring are necessary to reach dispersions. This time decreases to a few seconds for higher concentration. The negative charge of the next layer can be the sulfonate of the SBMIM[±] or TfO⁻ or TFSI⁻ depending on the composition. As the properties of the two systems, with either SBMIM[±] TFSI⁻ or SBMIM[±] TfO⁻, differ (SANS/SAXS, DLS, TEM), this suggests that the TfO⁻ ions localise at least in parts close to the solid-liquid interface (shown in Figure 8b).

At the maximum surface charge density σ , the ratio $\kappa_{ion} \approx 0.3$ in the case of introduced TfO⁻ anions and $\kappa_{ion} \approx 0.6$ in the case of TFSI⁻ anions (with the values of ref^{18,48}). The latter being closer to 0.5, this could explain the better colloidal stability seen in the experiments for this system, leading to 3-4 more ion layers.^{17,18} Considering the size of the ions, this matches well with the value obtained for associated repulsive interparticle interaction in the range of 3-5 nm. The slightly lower colloidal stability of nanoparticle dispersions with SBMIM[±] TfO⁻ counterions could also be explained by a disturbance of the SBMIM[±] monolayer. Both SBMIM[±] and TfO⁻ contain a sulfonate group having an affinity for oxide surfaces.^{49,50} A localisation of some TfO⁻ ions would therefore disturb the monolayer of SBMIM[±] zwitterions due to their size difference and hence the multilayer structure formed behind, explaining the difference observed in the colloidal stability.

Looking now at lower surface charge densities σ , the apparent d_H increases while the charge decreases until unstable systems are obtained. This is consistent with the decrease of the ratio $\kappa_{ion} = |\sigma / \Theta_{ion}^{max}|$ far below 0.5, thus a decrease of the number of organised layers. However, one would expect a better stability with SBMIM[±] TFSI⁻ than for SBMIM[±] TfO⁻ counterions according to a bigger κ_{ion} value and closer to a value of 0.5. This result also indicates that TfO⁻ anions are close to the solid-ionic liquid

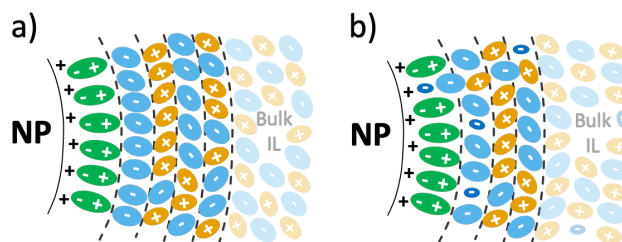


Fig. 8 Schemes of the nanoparticle (NP) ionic liquid (IL) interface for an imaginable case for a) SBMIM[±] TFSI⁻ counterions and b) SBMIM[±] TfO⁻ counterions. They are shown for a high surface charge density $\sigma \approx 30 \mu\text{C}/\text{cm}^2$ illustrated by several "+" on the nanoparticle surface. The ions are represented as ellipsoids, the zwitterion SBMIM[±] in green, the cation EMIM⁺ in yellow, and the anions TFSI⁻ and TfO⁻ in light and dark blue, respectively. Here $\kappa_{SBMIM^\pm} = |\sigma / \Theta_{SBMIM^\pm}^{max}| \approx 1$ leading to a layer (or more) of SBMIM[±] zwitterions acting as a steric component not changing the absolute charge. After the SBMIM[±] zwitterion layer (possibly disturbed by TfO⁻ counterions), a multilayer of the ionic liquid ions EMIM⁺ and TFSI⁻ (and possibly TfO⁻ or SBMIM[±] ions) is shown which is obtained due to overscreening of the surface charge at a ratio of $\kappa_{ion} = |\sigma / \Theta_{ion}^{max}| \approx 0.5$. After some layers (around 3-4) the bulk ionic liquid structure is recovered, shown here with transparent ions (for more details see text).

interface, maybe even in the first layer of the SBMIM[±], modifying the organisation, producing dispersions of small aggregates instead of individual nanoparticles.

Let us look now at the thermal stability, starting with the definition of used criteria for thermal stability. Many studies use TGA, and provide T_{onset} , sometimes T_{start} , both corresponding to short-term behaviour under gas flow. On the long term, several criteria have been defined, one example being 1% weight loss in 10 hours $T_{0.01/10h}$ ²⁶ and another being the maximum operation temperature for an annual decomposition of 1% $T_{max,0.01/year}$ ^{44,51}, a value extrapolated from isothermal measurements on much shorter du-

ration than 1 year. All these values are available here only for EMIM TFSI (see Table 1) and show that T_{start} and T_{onset} are much larger than $T_{0.01/10h}$ or $T_{max,0.01/year}$. Nevertheless, it is important to point out that evaporation can occur and is usually not taken into account (except for $T_{max,0.01/year}$ in table 1), so that the loss of mass measured is a mixture of evaporation and degradation. Let us consider the case of EMIM TFSI. At 200°C, its vapour pressure is 0.02 Pa (from ref⁴⁴), however a high amount of gas passes in TGA. In 10 hour isothermal measurement, 24 L of gas pass on 30 micro litres (around 20 mg) of sample, thus $8 \times 10^5 \text{ m}_{gas}^3 \text{ m}^{-3} \text{ ionicliquid h}^{-1}$. If the gas saturated immediately (which is far from being the case) this would lead to complete evaporation of EMIM TFSI in around 1 minute which explains why evaporation can be observed in some ionic liquids if the carrier gas absorbs at least a bit. Note that for EMIM TfO, the vapour pressure is 0.002 Pa, 10 times lower.

It means that the degradation is usually overestimated from TGA measurements. Therefore at our maximal temperature of analysis for the ferrofluids here, EMIM TFSI can be considered as long-term stable, with no degradation and only evaporation. Another difficulty comes from the additives present in the ferrofluid, not only constituted of iron oxide and EMIM TFSI. SBMIM[±] and HSBMIM are present as well as TfO⁻ anions in one of the samples. Such mixtures have never been studied and the only available data concern pure ionic liquids. HSBMIM TFSI was not studied, however some ionic liquids with other anions have been tested like HSBMIM HSO₄⁴⁶ and HSPMIM TfO⁴⁷, the latter cation having one carbon separation less between the imidazolium and sulfonate functionalities. The average of their T_{onset} values compared to the experimental result here for HSBMIM TFSI are similar, however, the latter seeming to evaporate already near room temperature. ‡ In ionic liquids, the possible mechanisms of degradation have been explored. Chen *et al.*⁵² analysed the temperature stability by TGA-MS of EMIM TFSI and found in their experiments that above 350°C first TFSI decomposes to more nucleophilic groups, such as F, CF₃ and NH₂ that mainly attack the ethyl group of the cation EMIM by elimination and nucleophilic substitution mechanisms. The same is observed for BMIM TfO that also decomposes to methylimidazolium (MIM) and HCF₃.⁵³ Ethyl imidazols are the first species that are detected followed by methyl imidazoles. SO₂ is also detected for TFSI and as well for TfO based ionic liquids. Nakurte *et al.*⁵⁴ analysed the decomposition mechanisms of different zwitterions dissolved in water, one being close to the zwitterion SBMIM[±] analysed here but with a propyl instead of a butyl side chain. ESI-MS for the compound shows protonation as the most probable. As observed in a lot of other studies for ionic liquids^{26,27,52} it is the longer

side chain of the imidazolium ring that is cleaved in the highest amount (here 60%) generating propane sulfonate and methyl-imidazolium. The second most probable mechanism is the elimination of sulfurous acid leaving methyl-propylene-imidazolium (10%).

From literature, it appears that the thermal stability of ionic liquids is governed by nucleophilic anion attack of the cation. Thermal stability is therefore higher for lower nucleophilicity (= higher lewis basicity).²⁷ As lewis bases (for the anion) lower the degradation temperature, it is assumed that lewis acids (for the cation) do as well. Hence, the (H)SBMIM could be causing the formation of neutral molecules that evaporate after.

From the measurements performed here on the components of the ferrofluids and on the ferrofluids, looking at T_{start} and T_{onset} , the colloidal dispersions appear less stable than pure EMIM TFSI (T shifted by 20-60°C) which seems to originate from HSBMIM. However the stability is kept at 200°C on the scale of hours from the SANS, SAXS, DLS experiments and TGA shows limits for short-term temperature stability of around 280 to 300°C.

4 Conclusions

This work examines charged (magnetic) iron oxide based colloidal systems varying the (i) the surface charge of the nanoparticles (ii) counterions and their concentration (iii) the particle volume fraction and (iv) their temperature stability.

Information could be obtained on the nanoparticle ionic liquid interface. The results indirectly prove that the zwitterions SBMIM[±] locate at the solid-liquid interface as colloidal stability can only be achieved in their presence and elevated nanoparticle surface charge introduced by HTFSI or HTfO.

Despite the difference in nanostructure between the nanoparticle dispersions (well dispersed and repulsive interparticle interactions with SBMIM[±] TFSI⁻ counterions or slightly attractive and having some small loose aggregates with SBMIM[±] TfO⁻ counterions) both systems are colloidally stable according to all the techniques (small angle scattering (SANS and SAXS), dynamic light scattering (DLS) and transmission electron microscopy (TEM)) also in the long term at least for one year. In addition, their colloidal stability is kept up to 200°C which is also the case for higher nanoparticle concentrations up to 12 vol% (only tested for the well dispersed and repulsive interparticle interactions with SBMIM[±] TFSI⁻ counterions). Hence, these long term stable ferrofluids are suited for the use in applications.

Conflicts of interest

There are no conflicts of interest to declare.

Acknowledgements

We thank Amandine Anfray for DLS measurements, Aude Michel for FAAS measurements, Arnaud H elary for the design of the coupled DLS-SANS measurement setup at LLB (Laboratoire L eon Brillouin), and Sandra Casale for the TEM images taken at the IMPC (Institut des Mat eriaux de Paris-Centre). This work has been supported by the European Union Horizon 2020 research and innovation program under the grant number 731976 (MAGENTA).

‡ The measurements of HSBMIM TFSI by TGA (see Figure 7) shows a 25% loss of mass before the degradation, not reported in literature for the other sulfonate containing liquids mentioned. This result is not consistent with the data on the ionic liquid received. In particular, the water is determined by Solvionic in an oven at 120°C until the mass is stable, which is not the case here. The measurement needs to be checked in case this is a technical problem or a mistake however this was not possible due to the COVID-19 crisis as the laboratory was closed. After the lock-down, the TGA device did not restart due to a technical problem, not yet solved.

Notes and references

- 1 T. Welton, *Chemical Reviews*, 1999, **99**, 2071–2084.
- 2 L. Mestrom, J. J. M. Lenders, R. de Groot, T. Hooghoudt, N. A. J. M. Sommerdijk and M. V. Artigas, *Nanotechnology*, 2015, **26**, 285602.
- 3 D. R. MacFarlane, N. Tachikawa, M. Forsyth, J. M. Pringle, P. C. Howlett, G. D. Elliott, J. H. Davis, M. Watanabe, P. Simon and C. A. Angell, *Energy Environ. Sci.*, 2014, **7**, 232–250.
- 4 M. Armand, F. Endres, D. R. MacFarlane, H. Ohno and B. Scrosati, *Materials For Sustainable Energy: A Collection of Peer-Reviewed Research and Review Articles from Nature Publishing Group*, World Scientific, 2011, pp. 129–137.
- 5 M. Bonetti, S. Nakamae, B. T. Huang, T. J. Salez, C. Wiertel-Gasquet and M. Roger, *The Journal of Chemical Physics*, 2015, **142**, 244708.
- 6 E. Laux, S. Uhl, L. Jeandupeux, P. P. López, P. Sanglard, E. Vanoli, R. Marti and H. Keppner, *Journal of Electronic Materials*, 2018, 1–5.
- 7 M. Dupont, D. MacFarlane and J. Pringle, *Chem. Commun.*, 2017, **53**, 6288–6302.
- 8 Z. He and P. Alexandridis, *Advances in Colloid and Interface Science*, 2017, **244**, 54–70.
- 9 B. T. Huang, M. Roger, M. Bonetti, T. J. Salez, C. Wiertel-Gasquet, E. Dubois, R. Cabreira Gomes, G. Demouchy, G. Mériduet, V. Peyre, M. Kouyaté, C. L. Filomeno, J. Depeyrot, F. A. Tourinho, R. Perzynski and S. Nakamae, *The Journal of Chemical Physics*, 2015, **143**, 054902.
- 10 T. J. Salez, B. T. Huang, M. Rietjens, M. Bonetti, C. Wiertel-Gasquet, M. Roger, C. L. Filomeno, E. Dubois, R. Perzynski and S. Nakamae, *Physical Chemistry Chemical Physics*, 2017, **19**, 9409–9416.
- 11 H. Zhang, K. Dasbiswas, N. B. Ludwig, G. Han, B. Lee, S. Vaikuntanathan and D. V. Talapin, *Nature*, 2017, **542**, 328–331.
- 12 V. Kamysbayev, V. Srivastava, N. B. Ludwig, O. J. Borkiewicz, H. Zhang, J. Ilavsky, B. Lee, K. W. Chapman, S. Vaikuntanathan and D. V. Talapin, *ACS Nano*, 2019, **13**, 5760–5770.
- 13 F. C. C. Oliveira, L. M. Rossi, R. F. Jardim and J. C. Rubim, *The Journal of Physical Chemistry C*, 2009, **113**, 8566–8572.
- 14 M. Mamusa, J. Sirieix-Plénet, F. Cousin, E. Dubois and V. Peyre, *Soft Matter*, 2014, **10**, 1097.
- 15 M. Mamusa, J. Sirieix-Plénet, F. Cousin, R. Perzynski, E. Dubois and V. Peyre, *Journal of Physics: Condensed Matter*, 2014, **26**, 284113.
- 16 J. C. Riedl, M. A. Akhavan Kazemi, F. Cousin, E. Dubois, S. Fantini, S. Lois, R. Perzynski and V. Peyre, *Nanoscale Advances*, 2020, **2**, 1560–1572.
- 17 V. Ivaništšev, S. O'Connor and M. Fedorov, *Electrochemistry Communications*, 2014, **48**, 61–64.
- 18 V. Ivanistsev and M. V. Fedorov, *Interface magazine*, 2014, **23**, 65–69.
- 19 I. T. Lucas, S. Durand-Vidal, E. Dubois, J. Chevalet and P. Turq, *J. Phys. Chem. C*, 2007, **111**, 18568–18576.
- 20 C. Guibert, V. Dupuis, J. Fresnais and V. Peyre, *Journal of Colloid and Interface Science*, 2015, **454**, 105–111.
- 21 K. Bhattacharya, M. Sarkar, T. J. Salez, S. Nakamae, G. Demouchy, F. Cousin, E. Dubois, L. Michot, R. Perzynski and V. Peyre, *ChemEngineering*, 2020, **4**, 5.
- 22 J. Nordström, L. Aguilera and A. Matic, *Langmuir*, 2012, **28**, 4080–4085.
- 23 A. Elbourne, S. McDonald, K. Voichovsky, F. Endres, G. G. Warr and R. Atkin, *ACS Nano*, 2015, **9**, 7608–7620.
- 24 R. Hayes, N. Borisenko, B. Corr, G. B. Webber, F. Endres and R. Atkin, *Chemical Communications*, 2012, **48**, 10246.
- 25 S. Werner, M. Haumann and P. Wasserscheid, *ANNUAL REVIEW OF CHEMICAL AND BIOMOLECULAR ENGINEERING, VOL 1, ANNUAL REVIEWS*, 4139 EL CAMINO WAY, PO BOX 10139, PALO ALTO, CA 94303-0897 USA, 2010, vol. 1, pp. 203–230.
- 26 Y. Cao and T. Mu, *Ind. Eng. Chem. Res.*, 2014, **53**, 8651–8664.
- 27 C. Maton, N. D. Vos and C. V. Stevens, *Chemical Society Reviews*, 2013, **42**, 5963–5977.
- 28 R. Massart, *IEEE transactions on magnetics*, 1981, **17**, 1247–1248.
- 29 J.-P. Jolivet and E. Tronc, *Journal of Colloid and Interface Science*, 1988, **125**, 688–701.
- 30 K. Padaszyński and U. Domańska, *Journal of Chemical Information and Modeling*, 2014, **54**, 1311–1324.
- 31 U. Schwertmann and R. M. Cornell, *Iron Oxides in the Laboratory: Preparation and Characterization*, John Wiley & Sons, 2008.
- 32 M. Mamusa, J. Sirieix-Plénet, R. Perzynski, F. Cousin, E. Dubois and V. Peyre, *Faraday Discussions*, 2015, **181**, 193–209.
- 33 N. F. Carnahan and K. E. Starling, *The Journal of Chemical Physics*, 1970, **53**, 600–603.
- 34 J. A. Barker and D. Henderson, *The Journal of Chemical Physics*, 1967, **47**, 4714–4721.
- 35 M. Sarkar, J. C. Riedl, G. Demouchy, F. Gélébart, G. Mériduet, V. Peyre, E. Dubois and R. Perzynski, *Eur. Phys. J. E*, 2019, **42**, 72.
- 36 M. Kouyaté, C. L. Filomeno, G. Demouchy, G. Mériduet, S. Nakamae, V. Peyre, M. Roger, A. Cēbers, J. Depeyrot, E. Dubois and R. Perzynski, *Physical Chemistry Chemical Physics*, 2019, **21**, 1895–1903.
- 37 E. Wandersman, A. Cēbers, E. Dubois, G. Mériduet, A. Robert and R. Perzynski, *Soft Matter*, 2013, **9**, 11480.
- 38 C. L. Filomeno, M. Kouyaté, V. Peyre, G. Demouchy, A. F. C. Campos, R. Perzynski, F. A. Tourinho and E. Dubois, *The Journal of Physical Chemistry C*, 2017, **121**, 5539–5550.
- 39 C. Lopes Filomeno, M. Kouyaté, F. Cousin, G. Demouchy, E. Dubois, L. Michot, G. Mériduet, R. Perzynski, V. Peyre, J. Sirieix-Plénet and F. Tourinho, *Journal of Magnetism and Magnetic Materials*, 2017, **431**, 2–7.
- 40 R. Cabreira Gomes, A. Ferreira da Silva, M. Kouyaté, G. Demouchy, G. Mériduet, R. Aquino, E. Dubois, S. Nakamae,

- M. Roger, J. Depeyrot and R. Perzynski, *Phys. Chem. Chem. Phys.*, 2018, **20**, 16402–16413.
- 41 C. P. Fredlake, J. M. Crosthwaite, D. G. Hert, S. N. V. K. Aki and J. F. Brennecke, *J. Chem. Eng. Data*, 2004, **49**, 954–964.
- 42 W. H. Awad, J. W. Gilman, M. Nyden, R. H. Harris, T. E. Sutto, J. Callahan, P. C. Trulove, H. C. DeLong and D. M. Fox, *Thermochimica Acta*, 2004, **409**, 3–11.
- 43 H. L. Ngo, K. LeCompte, L. Hargens and A. B. McEwen, *Thermochimica Acta*, 2000, **357-358**, 97–102.
- 44 F. Heym, B. J. M. Etzold, C. Kern and A. Jess, *Green Chem.*, 2011, **13**, 1453.
- 45 M. Villanueva, A. Coronas, J. García and J. Salgado, *Ind. Eng. Chem. Res.*, 2013, **52**, 15718–15727.
- 46 J. Gui, H. Ban, X. Cong, X. Zhang, Z. Hu and Z. Sun, *Journal of Molecular Catalysis A: Chemical*, 2005, **225**, 27–31.
- 47 A. S. Amarasekara and O. S. Owereh, *J Therm Anal Calorim*, 2011, **103**, 1027–1030.
- 48 S. A. Kislenko, Y. O. Moroz, K. Karu, V. B. Ivaništšev and M. V. Fedorov, *Russian Journal of Physical Chemistry A*, 2018, **92**, 999–1005.
- 49 X. Lu, S. Deng, B. Wang, J. Huang, Y. Wang and G. Yu, *Journal of Colloid and Interface Science*, 2016, **474**, 199–205.
- 50 E. Potapova, R. Jolsterå, A. Holmgren and M. Grahn, *Journal of Surfactants and Detergents*, 2014, **17**, 1027–1034.
- 51 A. Seeberger, A.-K. Andresen and A. Jess, *Phys. Chem. Chem. Phys.*, 2009, **11**, 9375.
- 52 Y. Chen, Y. Cao, Y. Shi, Z. Xue and T. Mu, *Ind. Eng. Chem. Res.*, 2012, **51**, 7418–7427.
- 53 H. Ohtani, S. Ishimura and M. Kumai, *Anal. Sci.*, 2008, **24**, 1335–1340.
- 54 I. Nakurte, P. Mekss, K. Klavins, A. Zicmanis, G. Vavilina and S. Dubrovina, *Eur J Mass Spectrom (Chichester)*, 2009, **15**, 471–478.

Colloidal and thermal stabilities of iron oxide nanoparticle dispersions in EMIM TFSI stabilised with sulfonate based imidazolium ions

J. C. Riedl¹, M. Sarkar¹, T. Fiuza^{1,2}, F. Cousin³, E. Dubois^{1,*}, G. Mériquet¹, R. Perzynski¹, and V. Peyre^{1,*}

¹Sorbonne Université, Laboratoire PHENIX, 4 place Jussieu, case 51, 75005, Paris, France

²Inst. de Fisica, Complex Fluid Group, Universidade de Brasília, Brasília, Brazil

³Laboratoire Léon Brillouin, UMR CNRS 12, CE Saclay, Gif sur Yvette, France

*emmanuelle.dubois@sorbonne-universite.fr, veronique.peyre@sorbonne-universite.fr

SUPPLEMENTARY INFORMATION

S1 Materials

The following materials were used without further purification:

Sodium hydroxide (NaOH pellets, 98%, Acros Organics); hydrochloric acid (HCl, 37% water solution, AnalaR Normapur); iron(II) chloride ($\text{FeCl}_2 \cdot 4\text{H}_2\text{O}$, AnalaR Normapur, VWR); iron(III) chloride ($\text{FeCl}_3 \cdot 6\text{H}_2\text{O}$, Prolabo); iron(III) nitrate ($\text{Fe}(\text{NO}_3)_3 \cdot 9\text{H}_2\text{O}$, technical, VWR); triflimidic acid (HTFSI, purity 95%, Fluorochem); triflic acid (HTfO, 49.2 wt% in water, purity 99%, SOLVIONIC); 1-(4-Sulfobutyl)-3-methylimidazolium bistriflimide (HSBMIM TFSI, purity 98%, SOLVIONIC); 1-(4-Sulfobutyl)-3-methylimidazolium triflate (HSBMIM TfO, purity 98%, SOLVIONIC); 1-(4-Sulfobutyl)-3-methylimidazolium (SBMIM[±], purity 98%, SOLVIONIC).

S2 Colloidal Stabilities

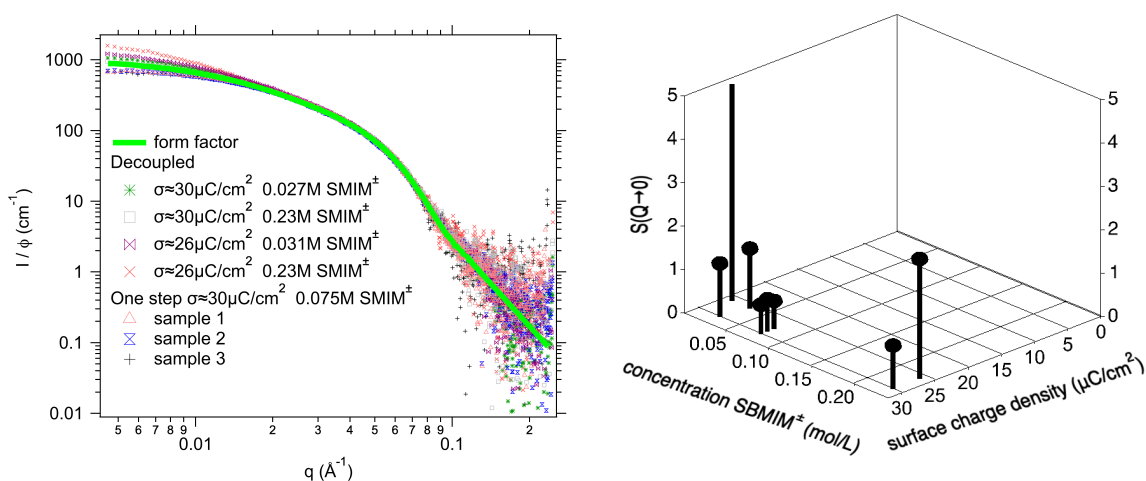


Figure S1. a) Absolute scattered intensities (normalized by the nanoparticle volume fraction $\Phi_{\text{NP}} \approx 0.5\text{-}1\text{vol}\%$ and their contrast with the solvent) obtained by SAXS for nanoparticle dispersions in EMIM TFSI with SBMIM[±] TFSI⁻ counterions in different ratios and concentrations. b) The corresponding $S(Q \rightarrow 0)$ values.

Additional results for decoupled analysis of the optimal counterion concentrations are presented. In the case of first introducing HTFSI and in a second step SBMIM[±] a transfer of an H to the latter zwitterion would lead to the ionic liquid

HSBMIM TFSI, having a high viscosity (≈ 1700 cP at 25 °C). Note that the apparent hydrodynamic diameter d_H in a DLS measurement is deduced from the diffusion coefficient D using the Stokes-Einstein relation.

$$D = \frac{k_B T}{6\pi\eta \frac{d_H}{2}} \quad (1)$$

with the Boltzmann constant k_B , the absolute temperature T , and the solvent shear-viscosity η . In the calculation of the apparent hydrodynamic diameter d_H only the viscosity of EMIM TFSI is considered. Hence, an increase of the solvent viscosity in a mixture with HSBMIM TFSI would lead to an overestimated apparent hydrodynamic diameter. A maximum error can be estimated assuming all HTFSI introduced in a first step would combine with SBMIM $^{\pm}$ to form HSBMIM TFSI. This represents around 2% in concentration and assuming a linear influence on the viscosity this would almost double the viscosity. Hence, the apparent hydrodynamic diameter d_H would be half the size. However, it is unlikely that all HTFSI introduced in the beginning would be free as the particles were stabilised with it.

SAXS measurements on selected nanoparticle dispersions with SBMIM $^{\pm}$ TFSI $^-$ counterions were performed in order to analyse if the increase of D_H is due to the increase of viscosity or a change of the nanostructure (e.g. formation of aggregates or/and change of interparticle interactions). The results in shown in Figure S1 show the same behaviour as in the DLS measurements, however less pronounced. This suggests that it is mainly the nanostructure that changes, however, together with an additional influence of the viscosity with increasing SBMIM $^{\pm}$ concentration.

Figure S2 shows that the colloidal stability of both nanoparticle dispersions with SBMIM $^{\pm}$ TFSI $^-$ counterions and SBMIM $^{\pm}$ TfO $^-$ counterions is kept for a year despite their difference in interparticle interaction. This was also the case when kept in open bottles without control of the atmosphere.

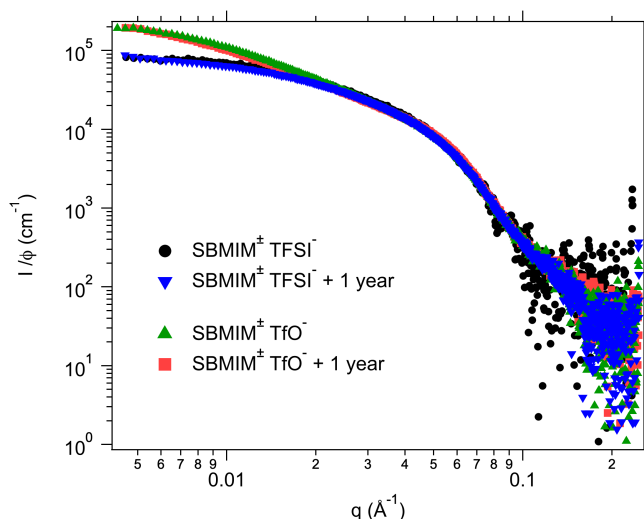


Figure S2. Absolute scattered intensities (normalized by the nanoparticle volume fraction $\Phi_{NP} \approx 1$ vol%) obtained by SAXS for dispersions of nanoparticles in EMIM TFSI with SBMIM $^{+/-}$ TFSI $^-$ and SBMIM $^{+/-}$ TfO $^-$ counter-ions measured more than one year apart. During this time the sample was stored at ambient temperature and the sample with SBMIM $^{+/-}$ TFSI $^-$ was additionally in contact with (the moisture of) air.

S3 Thermal Stabilities

S3.1 Coupled SANS and DLS measurements

DLS and SANS measurements were coupled at temperatures up to 200°C. Figure S3 shows the setup of the experiments performed at PAXY, LLB. A furnace was fixed on a controlled rotating table to ensure a reproducible position for all samples. The oven was filled with nitrogen gas to work under inert atmosphere. A self-designed support for a DLS laser remote source (from Cordouan Vascoflex or VascoKin) was fixed on the rotating table, Figure 3d. Figure S3 e) shows the DLS remote laser source fixed on the support after turning the table by 45° and with a laser protection for security. As DLS measurements are fast (around 2 min for ionic liquid-based colloids analysed here) the samples were analysed during temperature changes to monitor temperature variations inside the sample. After obtaining a constant temperature, i.e., a constant DLS signal, the DLS remote laser was removed. The table was turned back to the initial position and the SANS measurement was performed. These steps

were repeated at 27°C, 70°C, 135°C, 200°C and back to 27°C. As only classical spherical quartz/spacer/quartz sandwich could fit in this furnace and no change of the furnace was possible, adapted cells were developed, Figure S3a, making it possible to heat liquid samples in the furnace. The cells are based on a Teflon spacer glued on quartz with a hole on the top to evacuate gases that may form during the heating process. Figure S3b shows a filled cell and in c) the cell was placed in the oven. During three neutron runs, three configurations were used that slightly differed.

1st run) neutron wavelength $\lambda=6 \text{ \AA}$, sample to detector distance $d=1\text{m}$; $\lambda=6 \text{ \AA}$, $d=3 \text{ m}$ and $\lambda=8.5 \text{ \AA}$, $d=5 \text{ m}$

2nd run) $\lambda=5 \text{ \AA}$, $d=1\text{m}$; $\lambda=5 \text{ \AA}$, $d=3 \text{ m}$ and $\lambda=8.5 \text{ \AA}$, $d=5 \text{ m}$

3rd run) $\lambda=4 \text{ \AA}$, $d=1\text{m}$; $\lambda=5 \text{ \AA}$, $d=3 \text{ m}$ and $\lambda=8.5 \text{ \AA}$, $d=5 \text{ m}$

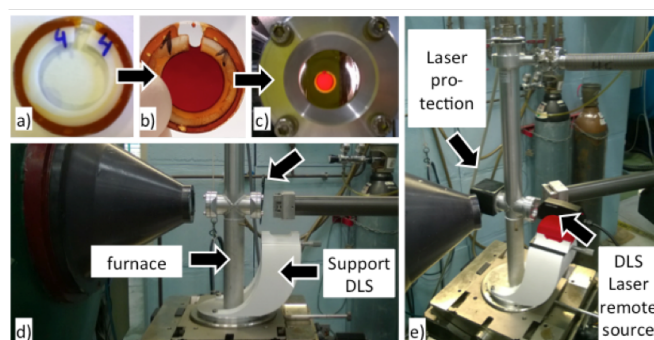


Figure S3. Scheme of the coupled SANS and DLS measurement setup at the PAXY spectrometer. a) Circular quartz/spacer/quartz sandwich with a hole on the top to evacuate gases that may form during the heating process at elevated temperatures. In b) this cell is filled with a sample and in c) it is in the furnace. D) Shows the configuration for SANS measurements and e) for DLS measurements.

DLS enables checking that equilibrium is reached before measuring SANS. This is possible as the viscosity varies with temperature which influences the correlation function. Hence, stability of the correlation function means that the viscosity and temperature is stable. DLS performed after SANS tells us whether some change occurred. In addition, agglomeration could be detected if curves drift to longer correlation lengths and hence time could be saved by skipping SANS measurements. Figure S4 shows an example for nanoparticle dispersions with SBMIM[±] TFSI⁻ counterions in EMIM TFSI and it is visible that the change of the correlation functions $G_1(t)$ is due to a viscosity change as the two correlation functions before and after heating to 200°C superimpose (ignoring a measurement problem due to vibrations leading to oscillations in the signal).

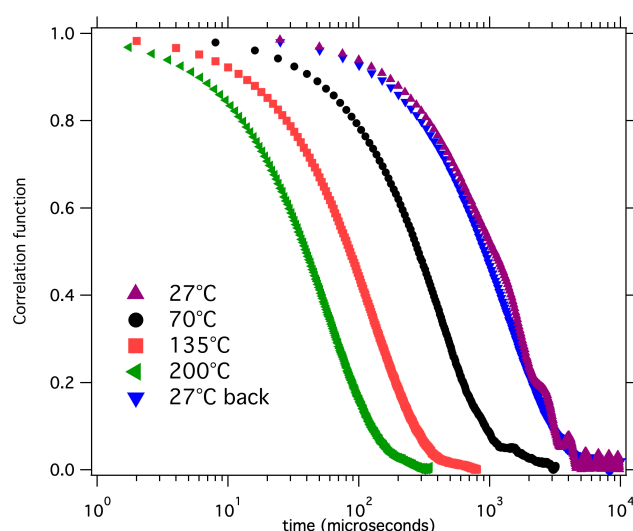


Figure S4. Dynamic light scattering (DLS) measurements for nanoparticle dispersions with SBMIM[±] TFSI⁻ counterions in EMIM TFSI. Note that the shift of the curves is due to a change of viscosity due to different temperatures.

S3.2 Thermogravimetric analysis (TGA)

Isothermal TGA measurements are shown in Figure S5. After an initial heating of 20°C/min to 160°C and temperature stabilisation (together ten minutes) the consecutive weight loss for EMIM TfO after three hours at 160°C, three hours at 180°C and ten hours at 200°C is lower than 0.1%, showing that it is long-term stable at this temperature.¹

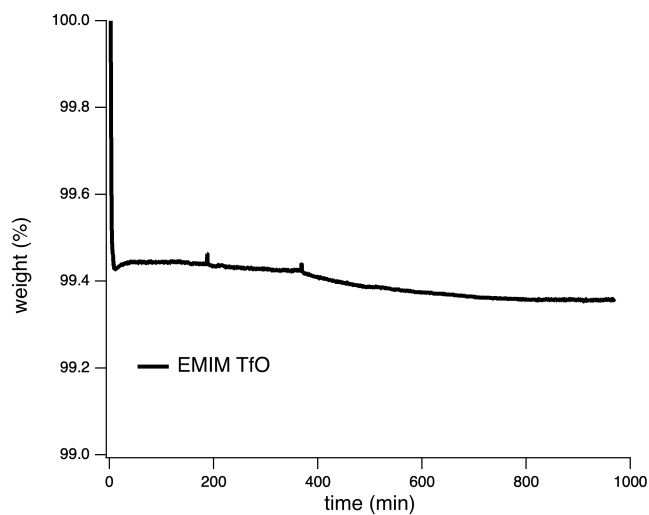


Figure S5. Isothermal thermogravimetric analysis (TGA) measurements for EMIM TfO for three hours at 160°C, three hours at 180°C and ten hours at 200°C.

References

¹The ferrofluids could not be measured yet due to the COVID related lock down.

4.3 | Conclusion

This chapter gives more information on the nanoparticle ionic liquid interface, here as an example for the ionic liquid EMIM TFSI which is one of the most promising for thermoelectric applications. The results indirectly prove that the zwitterions SBMIM[±] locate at the solid-liquid interface. This was possible by first increasing the surface charge density adding HTFSI or HTfO and adding SBMIM[±] in a second step. As already shown in chapter 3 long-term stable colloids can be obtained despite differences in interparticle interactions, being here slightly attractive for SBMIM[±] TfO⁻ and again repulsive for SBMIM[±] TFSI⁻ counterions. In addition, the colloidal stability in both systems is kept up to 200°C which is also the case for higher nanoparticle concentrations up to 12 vol% (only tested for SBMIM[±] TFSI⁻ counterions). Hence, these long-term stable ferrofluids are suited for the use in high temperature applications being one of the main advantages of using ionic liquids as solvents. Some TGA measurements are missing that could not be performed due to the COVID-19 lockdown. As soon as these measurements are performed and analysed, the article will be submitted.

Zwitterion-stabilised iron oxide nanoparticles in the ionic liquid EMIM TFSI: role of steric repulsion on colloidal stability up to 200°C

Contents

5.1	Introduction	69
5.2	Preparation of the nanoparticle dispersions	71
5.3	Results and discussion	72
5.3.1	First results at room temperature	72
5.3.2	Influence of temperature on colloidal stability	74
5.3.3	Discussion	77
5.4	Conclusion	79

5.1 | Introduction

Further modifications of the nanoparticle-ionic liquid interface with respect to colloidal and thermal stability are explored in this chapter. The equivalent of the zwitterion SBMIM[±] with a phosphonate group instead of a sulfonate group is analysed, called PAC_xMIM[±], x can be equal to 4, 6, and 12. Figure 5.1 depicts the structures of the ions that are analysed.

The principle of a zwitterion is hence kept. There are several reasons why the exchange of the sulfonate group with a phosphonate group is interesting. First, stable nanoparticle dispersions

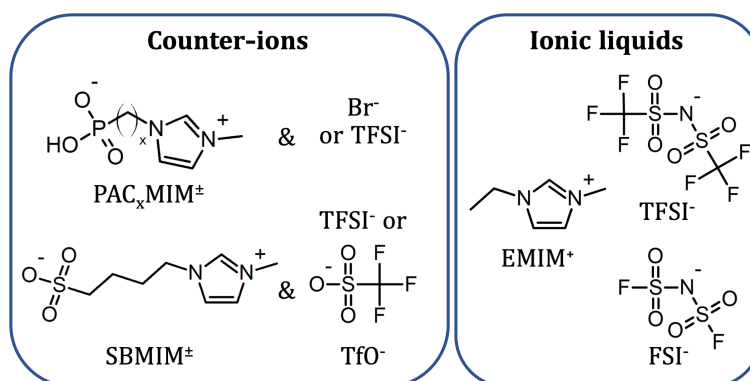


Figure 5.1 – Structures of the analysed counterions and ionic liquid. C_x represents the length of the alkyl chain length (=number of CH_2) connecting the phosphonate with the imidazolium group and is analysed here for 4,6, and 12. $\text{PAC}_4\text{MIM}^\pm$ is the equivalent to SBMIM^\pm with a phosphonate instead of a sulfonate group.

are reported, obtained by phase transfer from a molecular solvent to ionic liquids with this kind of coating. [62] Moreover, as the elements phosphor and bromine are not present in the ionic liquids EMIM TFSI and EMIM FSI, chemical titration of these elements in both transfer phases can give information about the localisation and condensation of the counterions $\text{PAC}_x\text{MIM}^\pm$ and Br^- and their transfer (or not) along with the particles. Second, changing the attaching group (phosphonate instead of sulfonate) could have implications on the stability of the ferrofluids as high surface affinity is reported for phosphonate groups. [76, 77] Third, phosphonic acids with imidazolium heads are commercially available with different chain lengths connecting these two groups. This is not the case for their sulfonic acid counterparts and our partners at SOLVIONIC were not able to synthesise them. Hence, the range of steric repulsion can be tuned in the case of phosphonic acids. The steric effect is analysed extending the alkyl chain length from 4 in $\text{PAC}_4\text{MIM}^\pm$ (and SBMIM^\pm) to 6 ($\text{PAC}_6\text{MIM Br}^-$) and 12 ($\text{PAC}_{12}\text{MIM Br}^-$).

However, the new zwitterion system is not completely analogue to SBMIM^\pm and also presents the following differences that we will keep in mind for the analysis. First, it is not possible to analyse the ions $\text{PAC}_x\text{MIM}^\pm$ and Br^- separately as pure $\text{PAC}_x\text{MIM}^\pm$ does not exist as a powder or liquid. It is only available in its cationic protonated form as phosphonic acid $\text{HPAC}_x\text{MIM}^\pm$ in combination with Br^- anions. Hence the new zwitterion system shows a change of the phosphonate group and the anion. Second, the pKa values of the two types of acids are different. Sulfonic acids are strong acids with pKa values ≈ -7 in contrast to phosphonic acids that are weak acids and have pKa values ≈ 2.2 and 7.5 . [78, 79] This could change the affinity of the anionic group for the surface of the particle and the nanoparticle surface charge density for the same concentration of added acids.

The nanoparticle dispersions are analysed in the same way as in the previous chapters and additionally chemical titrations (of P, Br and Fe) with inductively coupled plasma - mass spectrometry (ICP-MS) are used to determine the amounts of counterions that are transferred with the nanoparticles from water to the ionic liquids EMIM TFSI and EMIM FSI. After transfer, the dispersion in EMIM FSI was concentrated by ultra-centrifugation, leading to a concentrated nanoparticle dispersion on the bottom of the centrifugation tube and the dispersing liquid on the top. Both are analysed in order to determine the free and condensed counterion concentrations.

5.2 | Preparation of the nanoparticle dispersions

The nanoparticle surface is modified as explained in chapter 4 using the acids $\text{HPAC}_x\text{MIM}^+$ (with $x=4, 6, \text{ and } 12$) Br^- . Note that the acids $\text{HPAC}_4\text{MIM}^+ \text{Br}^-$, and $\text{HPAC}_6\text{MIM}^+ \text{Br}^-$ are soluble in water but not $\text{HPAC}_{12}\text{MIM}^+ \text{Br}^-$. Once deprotonated, these acids lead to an anionic entity, $\text{PAC}_x\text{MIM}^\pm \text{Br}^-$ that acts as counterion for the cationic particles. The exact role of each part (zwitterion $\text{PAC}_x\text{MIM}^\pm$ and Br^-) will be examined in the following. Around 200 μL of dispersion at $\phi_{NP} \approx 1 \text{ vol}\%$ are prepared in water with an acid concentration of 75 mmol/L leading to pH values around 2.2 and is mixed with the same amount of ionic liquid. A phase transfer of the nanoparticles to the ionic liquid EMIM TFSI occurs for $\text{HPAC}_x\text{MIM}^+$ ($x=4,6,12$) Br^- counterions. The density of the ionic liquid is bigger than that of water. Hence, a phase transfer of the nanoparticles leads to water rich supernatant on the top that contains no particles as is visually observed, with the nanoparticles dispersed in the ionic liquid rich phase on the bottom (see Figure 3b) and d) of chapter 3). However, it is more difficult to separate the two phases with a butyl instead of a dodecyl chain in $\text{HPAC}_x\text{MIM}^+$. Freeze-drying is used to remove the water. In some cases the uncoloured water rich upper phase was removed with a pipette before freeze-drying to accelerate the water removal and to analyse the partition of the ions between the two solvents.

In addition, concentrated nanoparticle dispersions with $\text{PAC}_6\text{MIM}^\pm \text{Br}^-$ counterions are prepared in EMIM FSI by ultra-centrifugation using an Optima 70 ultracentrifuge and a type 100 Ti fixed-angle rotor from the company Beckman Coulter, USA. The bottom ionic liquid phases containing the nanoparticles were centrifuged at 55 000 rpm (equals 243 000g) for 24 hours at 19°C. This leads to a concentrated nanoparticle dispersion on the bottom of the centrifugation

tube and the dispersing liquid on the top which are both analysed in order to determine the free and condensed counterion concentrations.

5.3 | Results and discussion

5.3.1 | First results at room temperature

Stable nanoparticle dispersions were obtained in water with $\text{PAC}_x\text{MIM}^\pm \text{Br}^-$ as counterions for all chain lengths ($x=4, 6,$ and 12) analysed here. This is in contrast to nanoparticles with $\text{SBMIM}^\pm \text{TFSI}^-$ counterions which agglomerate in water. Note however that $\text{SBMIM}^\pm \text{TfO}^-$ also leads to stable nanoparticle dispersions and hence the second anion (here Br^- , TfO^- or TFSI^-) is suggested to influence the colloidal stability in water.

After transfer of the nanoparticles to the ionic liquids EMIM TFSI and EMIM FSI, the uncoloured water rich phase were removed with a pipette and they are analysed by ICP-MS together with the nanoparticle dispersions in the ionic liquids after freeze-drying. Moreover, two concentrated nanoparticle dispersions with $\text{PAC}_6\text{MIM}^\pm \text{Br}^-$ counterions in EMIM FSI together with their corresponding dilute ionic liquid are analysed. The concentrations of P, Br and Fe (in the form of ϕ_{NP}) are given in Table 5.1.

Table 5.1 – ICP-MS measurements for nanoparticle dispersions in EMIM TFSI and EMIM FSI with $\text{PAC}_x\text{MIM}^\pm \text{Br}^-$ counterions. The corresponding uncoloured water rich phase after the phase transfer to the ionic liquid was removed with a pipette before freeze-drying for all samples, except if marked with* and is also analysed. n.m.= could not be measured yet.

sample	ϕ_{NP} in vol%	[P] in mmol/L	[Br] in mmol/L
in EMIM TFSI			
$\text{PAC}_4\text{MIM}^\pm \text{Br}^-$	0.92	57.5	24.2
corresp. water phase	n.m.	n.m.	n.m.
$\text{PAC}_6\text{MIM}^\pm \text{Br}^-$	0.85	50.1	2.6
corresp. water phase	0.00	18.8	60.3
$\text{PAC}_{12}\text{MIM}^\pm \text{Br}^- *$	0.84	0.8	97.4
in EMIM FSI			
$\text{PAC}_6\text{MIM}^\pm \text{Br}^-$	1.10	61.3	1.7
corresp. water phase	0.00	12.7	88.7
conc. $\text{PAC}_6\text{MIM}^\pm \text{Br}$	2.67	138.3	4.5
corresp. dilute IL	0.03	27.2	0.3
conc. $\text{PAC}_6\text{MIM}^\pm \text{Br}^-$	4.43	217.4	9.1
corresp. dilute IL	0.04	27.0	0.0

The following observations can be made. If the water-rich supernatant was removed with a pipette before freeze-drying, the Br^- anions are mainly in this water rich phase and only a small amount of Br^- anions are extracted with the nanoparticles into the ionic liquid-rich phase. The amount of phosphor (= amount of $\text{PAC}_x\text{MIM}^\pm$) shows the opposite behaviour, most of these counterions move with the nanoparticles. In the concentrated samples both P and Br concentrations increase with the nanoparticle volume fraction ϕ_{NP} . In order to specify the quantity of condensed (tightly bound) and free counterions, the dilute ionic liquid on the top of the centrifugation tube after ultra-centrifugation was chemically analysed, too. Under the assumption that the centrifugation does not disturb the equilibrium between free and condensed ions, the ion concentration in the supernatants equals the free ion concentration. The free ion concentration is determined in the solvent (ionic liquid EMIM FSI) separated of the nanoparticles in two concentrated samples by ultra-centrifugation. It is approximately 27 mmol/L for $\text{PAC}_6\text{MIM}^\pm$ and below 1 mmol/L for Br^- . Assuming this is valid for the samples in EMIM TFSI as well, the maximum amount of condensed phosphonate groups and Br^- in a compact monolayer is deduced, taking the available surface for nanoparticles with lognormal distribution ($d_0 = 8.7$ nm, $\sigma = 0.3$), $\phi_{NP} = 1$ vol%, and assuming ≈ 2 charges per nm^2 . In literature [80, 81] a mean phosphonate head group size of ≈ 0.5 nm^2 is observed in micelles, which equals approximately two charges per nm^2 . This leads to around 1.5 to 2.3 monolayers of $\text{PAC}_x\text{MIM}^\pm$ and below 0.2 monolayers of Br^- assuming that all these ions would locate at the nanoparticle interface.

The colloidal stability of the nanoparticle dispersions in EMIM TFSI with and without removing the water phase before freeze-drying was analysed in a multi-length-scale. No aggregates are detected in optical microscopy, and transmission electron microscopy (TEM) images show well dispersed nanoparticles (Figure 5.2). Only for nanoparticle dispersions with $\text{PAC}_{12}\text{MIM}^\pm$ Br^- counterions and a removed supernatant before freeze-drying some very small agglomerates are detected.

The TEM images were complemented with SAS and DLS measurements. Figure 5.3a) shows SAXS absolute intensities (normalised by the nanoparticle volume fraction Φ_{NP}). The results lead to the same conclusions as for the TEM images. Nanoparticle dispersions with $\text{PAC}_6\text{MIM}^\pm$ Br^- counterions give very similar results with or without the removal of the water supernatant before freeze-drying. Nanoparticle dispersions with $\text{PAC}_{12}\text{MIM}^\pm$ Br^- counterions are slightly better dispersed (more repulsive) if the supernatant is not removed before freeze-drying.

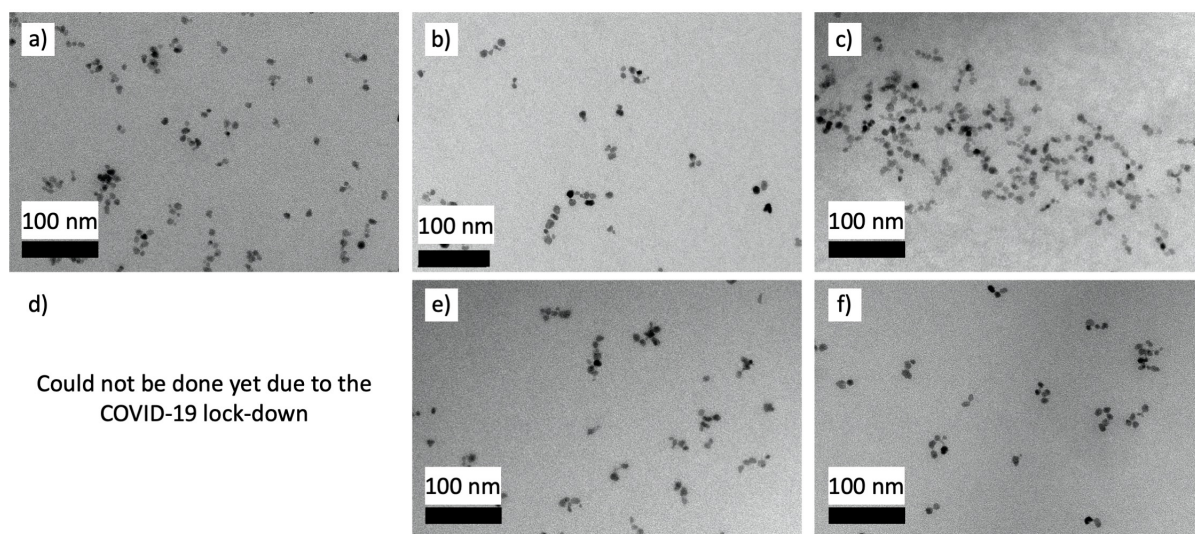


Figure 5.2 – TEM images of nanoparticle dispersions in EMIM TFSI with $\text{PAC}_x\text{MIM}^\pm \text{Br}^-$ counterions for a) and d) $x=4$, b) and e) $x=6$, and c) and f) $x=12$. For the dispersions displayed in a)-c) the supernatants were removed before freeze-drying and in d)-f) they were kept.

5.3.2 | Influence of temperature on colloidal stability

In a first step, Figure 5.3 b) gives information about the thermal stability, analysed with SAXS measurements before and after heating the ionic liquid-based nanoparticle dispersions up to 200°C with a heating rate of around $2^\circ\text{C}/\text{min}$ and staying at 200°C for around two hours. As a reference, the scattered intensity of nanoparticle dispersions with $\text{SBMIM}^\pm \text{TfO}^-$ counterions are shown. They are very similar to their equivalent, nanoparticle dispersions with $\text{PAC}_4\text{MIM}^\pm \text{Br}^-$ counterions before heating. However, the shape of the plotted curve differs at medium q values between 0.02 and 0.08 \AA^{-1} , being higher for $\text{SBMIM}^\pm \text{TfO}^-$ counterions.

The intensities at small q values decrease or stay the same after heating to 200°C , which suggests that these samples are all thermally stable. The change for $\text{PAC}_6\text{MIM}^\pm \text{Br}^-$ and $\text{PAC}_{12}\text{MIM}^\pm \text{Br}^-$ is in the limit of the error bars, however, the nanoparticle dispersion with $\text{PAC}_4\text{MIM}^\pm \text{Br}^-$ counterions reduce their attraction by more than a factor 2 when heated to 200°C . Structure factors are obtained (not shown) taking the same form factor as in the previous chapters. Here, all $S(Q \rightarrow 0)$ after heating are close to 1, meaning that the nanoparticle interactions are weak and the interactions are slightly more repulsive with a higher chain length.

In order to further explore the behaviour during the heating process itself, SANS coupled with

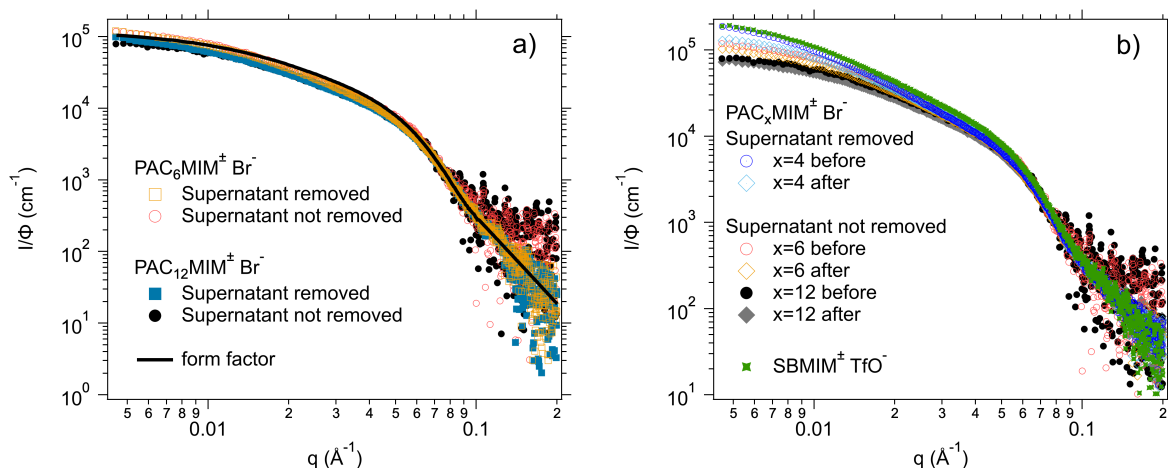


Figure 5.3 – SAXS absolute scattered intensities (normalised by the nanoparticle volume fraction $\Phi_{NP} \approx 1$ vol% for all nanoparticle dispersions) as a function of the scattering vector Q for nanoparticle dispersions in EMIM TFSI. a) nanoparticle dispersions with and without removing the uncoloured water rich phase after the phase transfer to the ionic liquid with a pipette before freeze-drying are analysed with $\text{PAC}_6\text{MIM}^{\pm} \text{Br}^-$ and $\text{PAC}_{12}\text{MIM}^{\pm} \text{Br}^-$ counterions. b) nanoparticle dispersions before and after heating to 200°C are given for $\text{PAC}_x\text{MIM}^{\pm}$ (with $x=4, 6,$ and 12) Br^- counterions. A curve for nanoparticle dispersions with $\text{SBMIM}^{\pm} \text{TfO}^-$ counterions are given as a reference.

DLS measurements were performed for $\text{PAC}_6\text{MIM}^{\pm} \text{Br}^-$ and $\text{PAC}_{12}\text{MIM}^{\pm} \text{Br}^-$ counterions for different temperatures (up to 200°C) (Figure 5.4). The initially elevated SANS intensity at low q values and apparent hydrodynamic diameter d_H for nanoparticles with $\text{PAC}_{12}\text{MIM}^{\pm} \text{Br}^-$ counterions between 27°C and 135°C appears as an accident as the corresponding SAXS measurements at room temperature before and after heating to 200°C show no evolution and match with the SANS measurement after the cycle. In addition, DLS measurements (not shown) performed with the same sample batch before and after the heating process, gives similar values as during the SANS measurements at higher temperatures and after heating. This discrepancy could be explained by trace pollution (initial solvent, water, dirt...) which is however disappearing reversibly when heated. Apart from this accident the samples seem thermally stable in the experimental time scale. However, the shape of the plotted curves for the nanoparticle dispersions with the two different counterions differs. The difference can be explained by the difference of the contrast that these counterions cause when located at the nanoparticle ionic liquid interface, proving that the $\text{PAC}_{12}\text{MIM}^{\pm}$ counterions are at the interface. However, the shape of the plotted curves is very different from the form factor used for all other SANS measurements (e.g. Figure S-1 in chapter 3). Hence, it was not possible yet to deduce nanoparticle interactions from SANS.

Thus, DLS measurements were carried out to determine the nanoparticle interactions. Figure

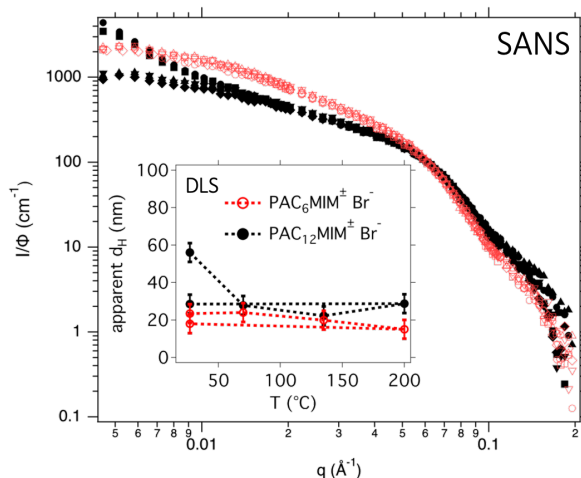


Figure 5.4 – SANS absolute scattered intensities (normalised by the nanoparticle volume fraction Φ_{NP}) at different temperatures (27°C (\circ), 70°C (\square), 135°C (\triangle), and 200°C (∇) and back at 27°C (\diamond)) as a function of the scattering vector Q for nanoparticle dispersions in EMIM TFSI. The uncoloured water rich phase after the phase transfer to the ionic liquid was not removed with a pipette before freeze-drying, meaning that all introduced ions are in the samples. Nanoparticle dispersions with $\text{PAC}_6\text{MIM}^\pm \text{Br}^-$ counterions at $\phi_{NP}=0.85$ vol% (in red) and with $\text{PAC}_{12}\text{MIM}^\pm \text{Br}^-$ counterions at $\phi_{NP}=0.84$ vol% (in black) are shown. The inset shows the corresponding apparent hydrodynamic diameter obtained by DLS measurements.

5.5 shows that the correlation functions G_1 for the nanoparticle dispersions slightly shift to longer times for all three counterions when diluted to lower nanoparticle volume fractions ϕ_{NP} . When diluted from 1 vol% to 0.1 vol%, the apparent hydrodynamic diameter increases by 2.8 nm, 1.5 nm, and 5.1 nm for $\text{PAC}_x\text{MIM}^\pm$ (with $x=4,6,12$) Br^- , respectively. This increase upon dilution indicates that the nanoparticle dispersions are all slightly repulsive. The determined apparent hydrodynamic diameter d_H is in the order $\text{PAC}_6\text{MIM}^\pm \text{Br}^- < \text{PAC}_{12}\text{MIM}^\pm \text{Br}^- \leq \text{PAC}_4\text{MIM}^\pm \text{Br}^-$.

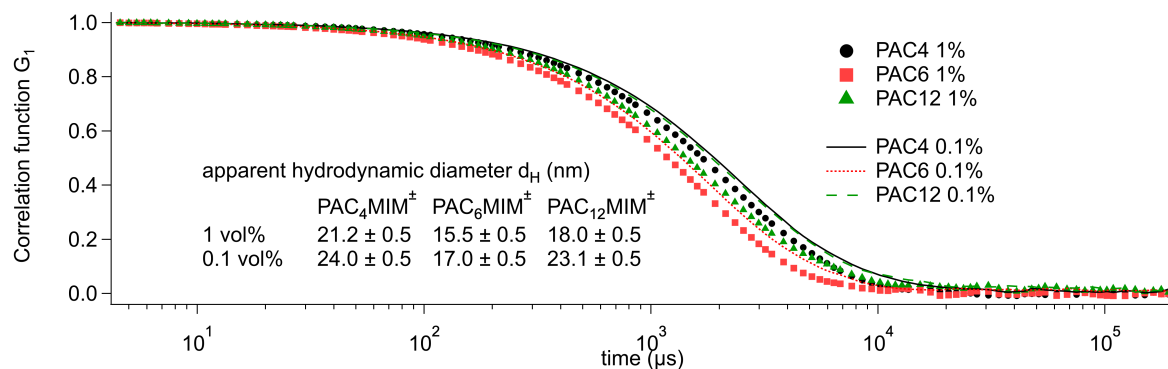


Figure 5.5 – Correlation functions G_1 obtained from DLS measurements for nanoparticle dispersions with PAC_xMIM ($x=4, 6$ and 12) Br^- counterions at $\phi_{NP} \approx 1$ and 0.1 vol%.

5.3.3 | Discussion

The colloidal stability of the nanoparticle dispersions was already discussed in detail in chapter 3 and 4, hence, only further findings about the mechanism influencing the layer efficiency are discussed here.

Assuming a similar behaviour for the nanoparticle charge for different counterions [3], σ is here approximately $25 \mu\text{C}/\text{cm}^2$ for the nanoparticle dispersions with $\text{PAC}_x\text{MIM}^\pm \text{Br}^-$ counterions as the pH value in water was approximately 2.2. Due to the slightly higher pH, this surface charge density is slightly lower than for the best nanoparticle dispersions with $\text{SBMIM}^\pm \text{TFSI}^-$ and $\text{SBMIM}^\pm \text{TfO}^-$ counterions ($\sigma \approx 30 \mu\text{C}/\text{cm}^2$). Assuming that a higher surface charge would also improve the colloidal stability for the phosphonate zwitterions, an increase of the surface charge density by an increased concentration of the acid could further improve the results.

The Θ_{ion}^{max} values of the additional analysed ions (compared to chapter 4) are $|\Theta_{\text{PAC}_4\text{MIM}^\pm}^{max}| \approx 35 \mu\text{C}/\text{cm}^2$ in analogy to SBMIM^\pm considering the size of the sulfonate and phosphonate group similar, $|\Theta_{\text{PAC}_6\text{MIM}^\pm}^{max}| \approx 30 \mu\text{C}/\text{cm}^2$, $|\Theta_{\text{PAC}_{12}\text{MIM}^\pm}^{max}| \approx 20 \mu\text{C}/\text{cm}^2$, and $|\Theta_{\text{Br}^-}^{max}| \approx 120 \mu\text{C}/\text{cm}^2$, [45]. All these values consider the ions as spheres and hence differences are observed for the different chain lengths. If the chain is however straight away from the nanoparticle surface, the Θ_{ion}^{max} values can depend only on the attaching phosphonate group and the Θ_{ion}^{max} values would hence be the same for all $\text{PAC}_x\text{MIM}^\pm$ zwitterions despite their chain length. A mean phosphonate head group size of $\approx 0.5 \text{ nm}^2$ is observed in micelles. This is equivalent to two charges per nm^2 which is assumed for the nanoparticles in this work. [80, 81] This is similar to values obtained for sulfonate groups. [82, 83]

Direct comparison of the attaching groups shows that nanoparticle dispersions with phosphonate ($\text{PAC}_4\text{MIM}^\pm$) lead to similar repulsive interparticle interactions than sulfonate (SBMIM^\pm) if the second counterion has a similar Θ_{ion}^{max} value ($|\Theta_{\text{Br}^-}^{max}| \approx 120 \mu\text{C}/\text{cm}^2$ and $|\Theta_{\text{TfO}^-}^{max}| \approx 100 \mu\text{C}/\text{cm}^2$). The nanoparticle - ionic liquid interface is hence imagined as in Figure 8b) of chapter 4, which is here shown again in Figure 5.6 a).

The zwitterions $\text{PAC}_x\text{MIM}^\pm$ must locate at the solid-liquid interface like SBMIM^\pm which is shown here by titrations and the difference of the shape of the plotted curve in SANS measurements. This is in accordance with the high surface affinity of phosphonate groups [76, 77] which is also reported for sulfonate groups [84, 85].

Higher chain length in the zwitterion $\text{PAC}_x\text{MIM}^\pm$ leads to slightly more repulsive systems in the SAXS measurements. This is assumed to be due to additional steric repulsion and is

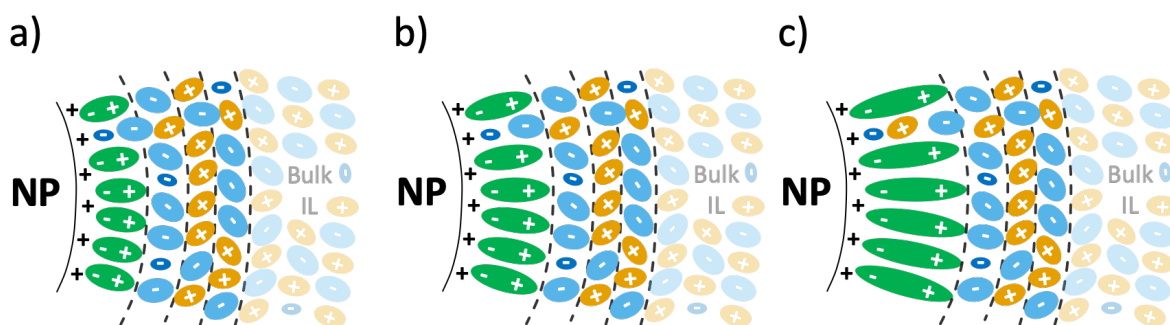


Figure 5.6 – Schemes of the nanoparticle (NP) ionic liquid (IL) interface for an imaginable case for a) $\text{PAC}_4\text{MIM}^\pm \text{Br}^-$ counterions in analogy to the scheme for $\text{SBMIM}^\pm \text{TfO}^-$ counterions shown in Figure 8b) of chapter 4, b) $\text{PAC}_6\text{MIM}^\pm \text{Br}^-$ counterions and c) $\text{PAC}_{12}\text{MIM}^\pm \text{Br}^-$ counterions. They are shown for a high surface charge density $\sigma \approx 25 \mu\text{C}/\text{cm}^2$ illustrated by several "+" on the nanoparticle surface. The ions are represented as ellipsoids, the zwitterion $\text{PAC}_x\text{MIM}^\pm$ in green, the cation EMIM^+ in yellow, and the anions TFSI^- and Br^- in light and dark blue, respectively.

illustrated in Figure 5.6 b) and c). The same behaviour is observed in DLS measurements when increasing the alkyl chain length from 4 to 6. However, increasing the alkyl chain length from 6 to 12 leads to bigger apparent hydrodynamic diameter. The acid with the maximum chain length $\text{HPAC}_{12}\text{MIM}^+ \text{Br}^-$ is not soluble in water in contrast to the two shorter analysed acids. In addition, it is not soluble in EMIM TFSI which could then lead to (partial) collapse of the dodecyl chain of the zwitterion, which would hence not contribute to steric repulsion. Additionally, a collapsing of the zwitterions on the surface could disturb the ion layering that is responsible for repulsion between the nanoparticles.

Although the amount of Br^- ions extracted with the particles as obtained with titrations is rather small, the amount staying with the nanoparticles stays at a constant amount compared to the available nanoparticle surface (around 20% of the available surface if all Br^- would locate in the first layer to the nanoparticle). Localisation of these ions would therefore disturb the first layer of $\text{PAC}_x\text{MIM}^\pm$ zwitterions due to their size difference and hence the multilayer structure formed behind. In addition, Br^- is a Lewis acid that can initiate degradation at higher temperatures. An exchange of the Br^- ion with another ion like TFSI^- could hence further improve the repulsion and thermal stability of the nanoparticle dispersions. The difference of the shape of the plotted curve in SANS measurements between $\text{PAC}_6\text{MIM}^\pm \text{Br}^-$ and $\text{PAC}_{12}\text{MIM}^\pm \text{Br}^-$ is considered to prove the localisation of the zwitterions $\text{PAC}_x\text{MIM}^\pm$ on the nanoparticle surface. The polydispersity of the core follows a Schultz distribution (parameters $d = 7 \text{ nm}$, $\sigma = 0.3$). The shell has a uniform thickness (values below, Table 5.2).

The curves were calculated as an example for a layer thickness of PAC_xMIM[±] corresponding to

Table 5.2 – SAXS and SANS SLD values for the calculated curves in Figure 5.7.

		SLD SANS	SLD SAXS
		in Å ⁻¹	in Å ⁻¹
Core	maghemite	6.85×10^{-6}	3.93×10^{-5}
Solvent	EMIM TFSI	2.41×10^{-6}	1.32×10^{-5}
Shell	PAC ₄ MIM [±]	1.85×10^{-6}	1.57×10^{-5}
	PAC ₆ MIM [±]	1.52×10^{-6}	1.52×10^{-5}
	PAC ₁₂ MIM [±]	0.92×10^{-6}	1.46×10^{-5}

half their stretched size (0.55 nm, 0.75 nm and 1.1 nm for x=4, 6, and 12, respectively). The calculated curves show the same trends as the measured scattered intensities. If the height of SAXS intensities are normalised at $q \approx 0.1 \text{ \AA}^{-1}$, almost no differences can be observed between the shape of the plotted curve of the intensity. However, SANS is already in absolute intensities and the calculated curves show the same difference of the shape of the plotted curve between PAC₆MIM[±] and PAC₁₂MIM[±] zwitterions as in Figure 5.4. This proves that the PAC_xMIM[±] zwitterions locate at the interface. Still, the calculated curves cannot fit the measured curves, The calculated intensity at low q values are below the measured ones. This can be due to an imperfect lognormal or Schultz size distribution, to an imperfect shape of nanoparticles which are not perfectly spherical as seen in the TEM images in Figure 5.2. Consequently, a fit was here not possible. A determination of a form factor in SANS measurements could help to determine the state of the nanoparticle interactions. On the contrary, the influence of the longer chain length on the contrast in SAXS measurements is below the error bars of the measurement and can here not be the reason for the differences.

5.4 | Conclusion

Long-term thermally stable nanoparticle dispersions can be obtained shown by a coupled DLS, SAXS and SANS analysis. A steric effect is analysed varying the chain length for PAC_xMIM[±] (x=4,6 and 12) Br⁻. The differences are subtle, however, the optimal alkyl chain length seems to be 6 followed by 4 and 12, being rather similar. Direct comparison of the attaching groups shows nanoparticle dispersions with phosphonate (PAC₄MIM[±]) lead to similar repulsive interparticle interactions than sulfonate (SBMIM[±]) if the second counterion has a similar Θ_{ion}^{max} value (Br⁻ and TfO⁻). However, when coupled with TFSI⁻ counterions, the SBMIM[±] leads to the most repulsive system.

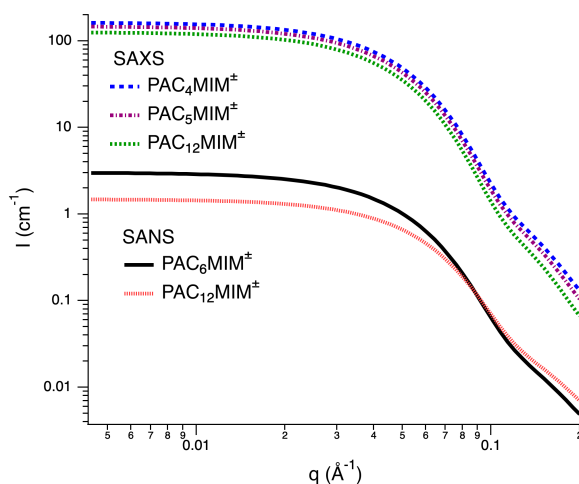


Figure 5.7 – Calculated SAXS and SANS scattered intensities for nanoparticles with $d=7$ nm and $\sigma=0.25$ at ϕ_{NP} 1 vol% for a layer thickness of PAC_xMIM^\pm corresponding to half their stretched size.

Removal of the water phase after the nanoparticle dispersion transferred to the ionic liquid EMIM TFSI has no crucial effect. Hence, the phase transfer can be used in applications to save time and energy.

Future experiments should focus on the steric effect in a wider range of ionic liquids. The influence of the different counterions on the thermoelectric properties were analysed by the MAGENTA project partners and first results show an effect which should be analysed more in detail.

Thermodiffusion in Molecular Solvents

Contents

6.1	Introduction	81
6.2	Article: “Inversion of thermodiffusive properties of ionic colloidal dispersions in water-DMSO mixtures probed by forced Rayleigh scattering”	82
6.3	Conclusion	99

6.1 | Introduction

After the chapters 3 to 5) described how to prepare colloidally and thermally stable magnetic nanoparticle dispersions in ionic liquids, the focus of this and the next chapter is on the analysis of thermodiffusion of the nanoparticle dispersions. Possible employment for thermoelectric applications rely on their thermodiffusive properties which are analysed by forced Rayleigh scattering (FRS) measurements mostly performed by colleagues of the laboratory. Thermodiffusion is quantified by a concentration gradient induced by a temperature gradient, through the Ludwig-Soret coefficient S_T . Former studies [7, 61, 86–88] showed that depending on several parameters (e.g. absolute temperature, nature of the solvent, nature of the surface charge and of the counterions), the nanoparticles move either towards cold (thermophobic, $S_T > 0$) or hot (thermophilic, $S_T < 0$) regions. In the beginning of this PhD ionic liquid-based nanoparticle dispersions were not developed yet. Hence, as a prove of concept of the functioning of the FRS setup, nanoparticle dispersions in molecular solvents were analysed first. In this chapter the effect of the solvent on the thermodiffusive properties are analysed for hydroxyl coated maghemite nanoparticles dispersed in water and dimethyl sulfoxide (DMSO) mixtures electrostatically

stabilised with ClO_4^- counterions. Mass diffusion coefficients and Soret coefficients as a function of the nanoparticle volume fraction are obtained using DLS, SANS and FRS.

The contribution of this PhD work to the article was in the synthesis and characterisation of the samples by SANS and DLS measurements, the determination of the χ parameter, contribution to the theoretical developments, and the preparation of the manuscript.

6.2 | Article: “Inversion of thermodiffusive properties of ionic colloidal dispersions in water-DMSO mixtures probed by forced Rayleigh scattering”

Inversion of thermodiffusive properties of ionic colloidal dispersions in water-DMSO mixtures probed by forced Rayleigh scattering^{***}

M. Sarkar¹, J.C. Riedl¹, G. Demouchy^{1,2}, F. Gélébart¹, G. Mériquet¹, V. Peyre¹, E. Dubois¹, and R. Perzynski^{1,a}

¹ Sorbonne Université, CNRS, PHysico-chimie des Electrolytes et Nanosystèmes Interfaciaux, F-75005 Paris, France

² Département de Physique, Univ. Cergy-Pontoise, 33 bd du port, 95011 Cergy-Pontoise, France

Received 22 January 2019 and Received in final form 20 April 2019

Published online: 11 June 2019

© EDP Sciences / Società Italiana di Fisica / Springer-Verlag GmbH Germany, part of Springer Nature, 2019

Abstract. Thermodiffusion properties at room temperature of colloidal dispersions of hydroxyl-coated nanoparticles (NPs) are probed in water, in dimethyl sulfoxide (DMSO) and in mixtures of water and DMSO at various proportions of water, x_W . In these polar solvents, the positive NPs superficial charge imparts the systems with a strong electrostatic interparticle repulsion, slightly decreasing from water to DMSO, which is here probed by Small Angle Neutron Scattering and Dynamic Light Scattering. However if submitted to a gradient of temperature, the NPs dispersed in water with ClO_4^- counterions present a thermophilic behavior, the same NPs dispersed in DMSO with the same counterions present a thermophobic behavior. Mass diffusion coefficient D_m and Ludwig-Soret coefficient S_T are measured as a function of NP volume fraction Φ at various x_W . The Φ -dependence of S_T is analyzed in terms of thermoelectric and thermophoretic contributions as a function of x_W . Using two different models for evaluating the Eastman entropy of transfer of the co- and counterions in the mixtures, the single-particle thermophoretic contribution (the NP's Eastman entropy of transfer) is deduced. It is found to evolve from negative in water to positive in DMSO. It is close to zero on a large range of x_W values, meaning that in this x_W -range S_T largely depends on the thermoelectric effect of free co- and counterions.

1 Introduction

When submitted to a gradient of temperature ∇T , ionic nanoparticles (NPs) dispersed in a polar solvent are subjected both to the Ludwig-Soret effect [1], which induces a gradient of volume fraction $\nabla\Phi$ and a Seebeck effect [2,3], which induces an electric field \mathbf{E} . This can be used for potential thermoelectric applications in terms of heat recovery [4–10]. In stationary conditions, both $\nabla\Phi$ and \mathbf{E} are proportional to ∇T and the NPs migrate either towards the cold region or towards the hot region depending on the sign of their Soret coefficient S_T , given (at high dilution) by $\nabla\Phi = -\Phi S_T \nabla T$. Their Seebeck coefficient S_e^{st} is given by $\mathbf{E} = S_e^{\text{st}} \nabla T$ and it is connected to S_T , through \hat{S}_{NP} ,

the Eastman entropy of transfer of the nanoparticles in the solvent¹ [2, 12–15]. This single-particle contribution \hat{S}_{NP} characterizes the affinity of the ionic NPs with the polar solvent in which they are dispersed [12, 15–17]. S_T depends on the interparticle interaction (thus on the NP's concentration and that of counterions), but also on the nature of these counterions and on the nature of the solvent [17–19].

In the present study, we focus on two polar solvents with a very different structural organization, namely dimethyl sulfoxide (DMSO, $\text{H}_3\text{C-SO-CH}_3$) and water. Water is a polar protic solvent strongly structured through a H-bond network [20], while DMSO is a less organized, aprotic and polar organic solvent, with a lower dielectric permittivity $\varepsilon_{\text{DMSO}} = 46$ [21] than water at room temperature. Mixtures of water and DMSO are chosen for this study as they are miscible in any proportions in these conditions. Using perchlorate (ClO_4^-) counterions, the same acidic magnetic nanoparticles can be dispersed in both solvents, with the same type of electrostatic

* Contribution to the Topical Issue “Thermal Non-Equilibrium Phenomena in Soft Matter”, edited by Fernando Bresme, Velisa Vesovic, Fabrizio Croccolo, Henri Bataller.

** Supplementary material in the form of a .pdf file available from the Journal web page at

<https://doi.org/10.1140/epje/i2019-11835-6>

^a e-mail: regine.perzynski@upmc.fr

¹ The entropy of transfer \hat{S}_i of ionic species i is defined as in [11] as Q_i^*/T with Q_i^* the heat of transport of ionic species i .

stabilization giving stable magnetic ferrofluids [18, 19]. Here the strong electrostatic interparticle repulsion imparts the two kinds of colloidal dispersions with similar properties. However in the presence of a temperature gradient, the same maghemite NPs present a thermophilic behaviour in water ($S_T < 0$) [16, 18, 19] while they present a thermophobic one ($S_T > 0$) in DMSO [6, 18, 19].

In order to follow progressively this change of thermodiffusive behaviour at room temperature, colloidal dispersions of maghemite NPs (9 nm in diameter) are dispersed in water and in DMSO at comparable $[H^+]$ concentration ($\sim 10^{-2} \text{ mol L}^{-1}$) with perchlorate counterions. Dispersions in water-DMSO mixtures are then prepared at various mole fractions of water x_W , various NP volume fraction Φ and same $[H^+]$. The colloidal structure of the dispersions and the interparticle electrostatic repulsion are determined by Small Angle Neutron Scattering and the electrophoretic charge of the NPs is determined (at low volume fraction) by electrophoretic measurements and Dynamic Light Scattering (DLS). We present here a Forced Rayleigh Scattering (FRS) study of these dispersions.

The samples probed here with the different techniques (SANS, DLS, FRS) have the same ionic concentration $[H^+] = 10^{-2} \text{ mol/L}$ for all the x_W solvent compositions studied.

After a presentation of the synthesis and characterization of the probed dispersions and that of the FRS experiment, we show and discuss the results obtained for the mass diffusion coefficient D_m of the NPs and the Soret coefficient S_T as a function of Φ and x_W . S_T is then analyzed with the model presented in [16] in terms of thermophoretic and thermoelectric contributions.

2 Preparation and characterization of the colloidal dispersions

2.1 Solvent characteristics

Like water, DMSO is a polar molecular solvent. It is a green grade solvent with low toxicity used in pharmaceutical applications, recyclable and biodegradable [22]. DMSO has amphiphilic properties with a strongly polar sulfoxide group and two hydrophobic methyl moieties. Being aprotic and H bond acceptor, it is miscible with water in any proportion above the DMSO melting point ($T > 18^\circ\text{C}$) in atmospheric conditions. Water-DMSO form an eutectic mixture 2 H₂O:1 DMSO at $x_W = 66\%$, liquid down to $T = -73^\circ\text{C}$ [23]. At room temperature the viscosity of DMSO is roughly twice that of water while their densities are very similar (see table S1 in the Electronic Supplementary Material (ESM)). The mixture viscosity, as well as its density present a non-ideal behavior with a maximum for molar-fractions of water $x_W \sim 66\%$ corresponding to the eutectic mixture [24–26]. Other physical characteristics such as the thermal conductivity k [27, 28], the static relative permittivity ϵ_r [29, 30] and the optical index n [24, 25] of water-DMSO mixtures

do not present such a pronounced non-ideal behaviour and are monotonous functions of x_W at room temperature; ϵ_r decreases (almost linearly) from 80 in water down to 46 in DMSO [29–32] and n increases from 1.33 in water up to 1.47 in DMSO [24, 25].

These macroscopic properties are connected to molecular scale interactions between water and DMSO, in particular through H-bonds and van der Waals forces. H-bond interactions are transient in nature, with ultrafast breaking and making processes and various kinds of H-bond associations are possible between water and DMSO molecules. A crossover is found in ref. [33] for the H-bond exchange rate at $x_W \sim 85\%$, which is associated to the fact that water-DMSO mixtures act as protein stabilizers and activators for $x_W > 85\%$, while for $x_W < 85\%$ they act as denaturators and inhibitors. In [34], hydrogen-bond population was numerically quantified on the whole range of x_W . Several structural studies, both experimental and numerical, have shown concentration-dependent organizations of water and DMSO molecules [35], structural microheterogeneities [36], the formation of chains of water molecules [37] or of network structures [38].

2.2 Chemical synthesis of the NP's dispersions

Ferrite NPs are synthesized following Massart's method [39, 40] by polycondensation of ferric and ferrous salts in strongly alkaline aqueous medium followed by a hydrothermal oxidation at 100°C under atmospheric pressure with nitric acid [41] leading to roughly spherical maghemite ($\gamma\text{-Fe}_2\text{O}_3$) nanoparticles, coated with hydroxyl groups. A size-sorting of the NPs as the one described in ref. [42] is performed. All the present dispersions are based on the same initial batch of NPs.

These NPs can be easily dispersed in water at $\text{pH} \sim 2$, where they are positively charged. They have a point of zero charge (PZC) $\sim 7\text{--}8$ in water, where they flocculate. The method described in [18, 19] is used here to tune the NP-solvent interface in water and in DMSO. Starting from a flocculated aqueous dispersion at PZC, all extra-ions and all the water molecules (that can be removed) are then eliminated by repeated washings. Then the NPs are charged in the chosen medium following a controlled and reproducible process to obtain NP's dispersions with perchlorate counterions (added in known quantity) at $[H^+] = 10^{-2} \text{ mol L}^{-1}$, either in water or in DMSO at a NP's volume fraction $\Phi \sim 2.5\%$. A portion of the obtained dispersions is ultracentrifugated at $2 \times 10^5 \text{ g}$. Providing that the ultracentrifugation does not perturb the local equilibria around NPs, concentrations of free co-ions H^+ and counterions ClO_4^- are determined in each dispersion by conductivity measurements in the supernatant. A solution similar to the supernatant is then used to obtain dilute dispersions at lower Φ in the same solvent. Dispersions in water-DMSO mixtures are obtained by mixing in the adapted proportion a dispersion in water and a dispersion in DMSO at the same Φ and the same ionic concentration.

Both in water and in DMSO, stable acidic dispersions with a long term stability (more than 15 years²) are obtained with positively charged NPs (hydroxyl groups - acidic medium).

2.3 Characterization of NPs and of their dispersions

The magnetization of a dilute aqueous dispersion (at $\Phi \sim 1\%$) up to 800 kA m^{-1} is determined at room temperature with a home-made Vibrating Sample Magnetometer (data not shown). The size distribution of the magnetic nanoparticles can then be deduced following the procedure of ref. [43]. It is adjusted with a log-normal distribution of diameter, of median diameter $d_0 = 7.5 \text{ nm}$ and polydispersity index 0.35, leading to a volume-averaged diameter $d_{\text{NP}} = \sqrt[3]{\langle d^3 \rangle} = 9.0 \text{ nm}$.

Dynamic Light Scattering measurements are performed in very dilute dispersions (at $\Phi \sim 0.2\%$) in water and in DMSO between $T = 22^\circ\text{C}$ and 40°C and in various mixtures at $T = 22^\circ\text{C}$ with a Vasco DLS particle analyzer from Cordouan Technologies dedicated to dark media. It allows to determine the NP's diffusion coefficient D^{DLS} .

The dynamic electrophoretic charge number ξ_0 of the NPs and its derivative $\partial\xi_0/\partial T$ are deduced (as in refs. [16,17]) in water and in DMSO from D^{DLS} and from measurements of the NP's electrophoretic mobility μ_{el} at $\Phi \sim 0.01\%$ with a NanoZS from Malvern (with a dip cell) for $25 \leq T \leq 40^\circ\text{C}$, using

$$\xi_0 = \frac{kT\mu_{\text{el}}}{eD^{\text{DLS}}} \quad \text{at } \Phi \rightarrow 0, \quad (1)$$

leading to $\xi_0 = 65 \pm 6$ and $\partial\xi_0/\partial T = 0.4 \pm 0.2 \text{ K}^{-1}$ in water; and $\xi_0 = 43 \pm 4$ and $\partial\xi_0/\partial T = 0.5 \pm 0.2 \text{ K}^{-1}$ in DMSO. The values of ξ_0 and $\partial\xi_0/\partial T$ for the various mixtures probed here are obtained by a linear interpolation of x_{W} between the values in pure water and in pure DMSO. As in [16,17], this effective charge ξ_0 is of the same sign but much smaller than the structural charge of the NPs, which is due the hydroxyl species H^+ present at the maghemite surface (~ 2 charges per nm^2 , leading to a structural charge number ~ 450). This difference has to be related here to a large amount of ClO_4^- species condensed on the surface.

Small Angle Neutron Scattering measurements are performed at PACE - LLB - Saclay - France in the range of scattering vectors Q ($2.4 \times 10^{-3} \text{ \AA} \leq Q \leq 4.3 \times 10^{-1} \text{ \AA}$) on various dispersions. The form factor of the nanoparticles is deduced in water as a function of the scattering vector Q by extrapolation at $\Phi = 0$ of the intensities of three dispersions at 0.3%, 1% and 2.5%. We follow the same procedure as in [19] to deduce the osmotic compressibility χ of the NP system from the scattered intensity at finite volume fraction. Figure 1(a) presents the evolution of χ in water as a function of the NP volume fraction Φ . As the interparticle repulsion is strong in these colloidal dispersions stabilized electrostatically, $\chi(\Phi)$ is here adjusted

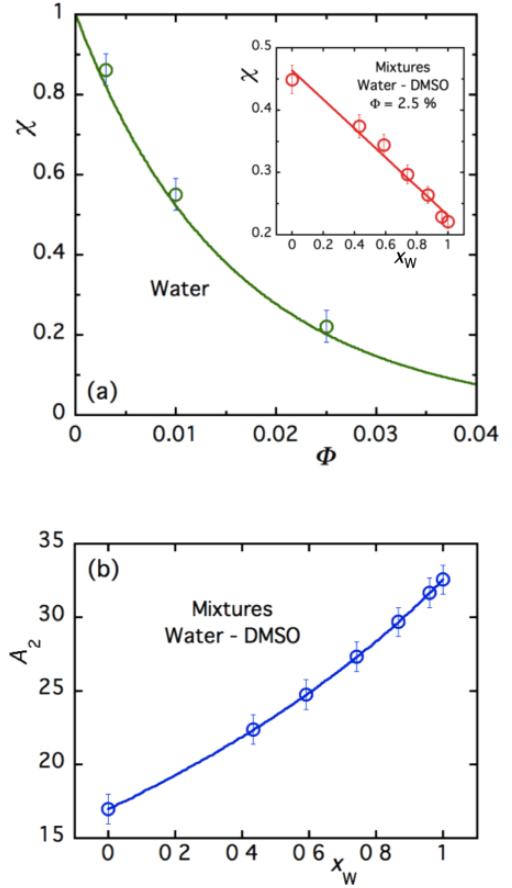


Fig. 1. (a) Osmotic compressibility χ as a function of the NP's volume fraction Φ in water; Open symbols: SANS results; Full line: χ_{CS} adjustment with eq. (2); inset: osmotic compressibility χ as a function of x_{W} in mixtures at $\Phi = 2.5\%$; open symbols: experimental SANS results; full line: linear adjustment; (b) A_2 as a function of x_{W} in mixtures as deduced from SANS determinations and eq. (3) (open symbols) and as interpolated with the Carnahan-starling model (full line).

(as in [16–19,44]) by the Carnahan-Starling expression for effective hard spheres [45,46] of volume fraction Φ_{eff} (and effective diameter taking in account the screening length κ^{-1}) as

$$\chi(\Phi) = \chi_{\text{CS}}(\Phi_{\text{eff}}) = \frac{(1 - \Phi_{\text{eff}})^4}{1 + 4\Phi_{\text{eff}} + 4\Phi_{\text{eff}}^2 - 4\Phi_{\text{eff}}^3 + \Phi_{\text{eff}}^4}. \quad (2)$$

The second virial coefficient A_2 of the osmotic pressure Π in the dispersion then writes

$$A_2 = A_2^{\text{HS}} \frac{\Phi_{\text{eff}}}{\Phi} = 4 \frac{\Phi_{\text{eff}}}{\Phi} \quad \text{with } \Phi_{\text{eff}} = \Phi \left(1 + \frac{2\kappa^{-1}}{d_{\text{NP}}} \right)^3, \quad (3)$$

with $A_2^{\text{HS}} = 4$, the hard sphere value of A_2 .

We obtain $A_2 = 33 \pm 3$ and $\kappa^{-1} = 4.6 \pm 0.4 \text{ nm}$ for the aqueous samples. The inset of fig. 1(a) shows the evolution of χ as a function of x_{W} obtained for the mixtures water-DMSO at constant $\Phi = 2.5\%$. For the analysis, the same NP's form factor as in water is kept to deduce χ . The

² As attested in DMSO by the DLS measurements presented in sect. S6 of the ESM.

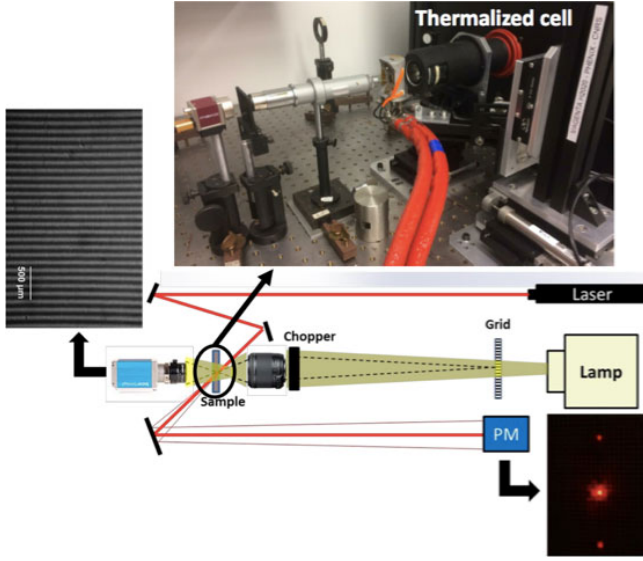


Fig. 2. Experimental device. The beam of a high-power Hg lamp is temporally modulated thanks to a chopper. It illuminates a grid, the image of which is made in the thermoregulated (optical) sample-cell, producing a thermal and a concentration gratings in the colloidal dispersion. Both gratings are probed by the diffraction of a non-absorbed He-Ne laser beam and a photo-multiplier (PM) records the first order diffraction as a function of time.

formalism of eqs. (2) and (3) then allows to obtain Φ_{eff} and A_2 as a function of x_W (see fig. 1(b)). It leads to $A_2 = 17 \pm 2$ and $\kappa^{-1} = 2.8 \pm 0.4$ nm in DMSO. These κ^{-1} values in water, DMSO and their mixtures are experimentally consistent with the values ϵ_r of the relative permittivity in these media [32] and they roughly scale as $\kappa^{-1} \sim 0.47 \sqrt{\epsilon_r}$ (in nm).

3 Forced Rayleigh Scattering experiment

The principle of the used Forced Rayleigh Scattering (FRS)³ setup (see fig. 2) has been extensively described in ref. [48]. Some improvements to the home-made device have been made. In particular, the modulation of the power lamp is decreased to a few Hz to probe more viscous systems than in ref. [48] and the sample environment is now thermo-regulated allowing to work between $T = -40^\circ\text{C}$ and 200°C . However only results at $T = 21 \pm 0.4^\circ\text{C}$ are presented here.

Using a high power lamp (6285 - 500W - Hg Arc Lamp - Spectra Physics) and thanks to the strong optical absorption of the maghemite NPs, a thermal grating (of period Λ ranging between 88 and $145 \mu\text{m}$) is created in the dispersion, contained in an optical cell of thickness 25 or $100 \mu\text{m}$. The Soret effect then induces a concentration grating in this dispersion. Both thermal and concentration gratings are here probed with the first order diffraction of

³ FRS implies forced inhomogeneities with respect to the spontaneous fluctuations observed in a classical Rayleigh scattering experiment [47].

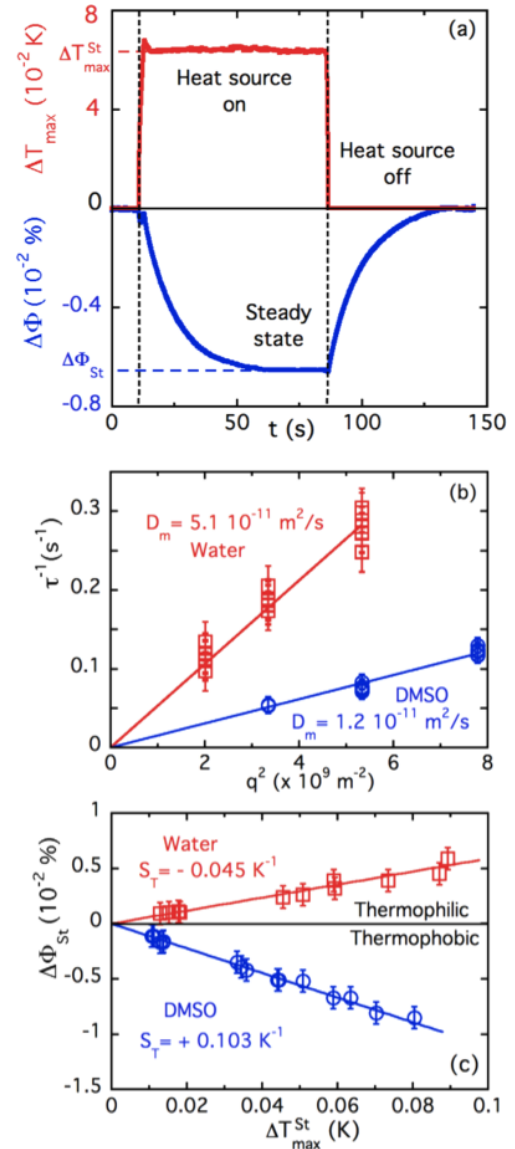


Fig. 3. (a) $\Delta\Phi$ and ΔT_{max} as a function of time for a dispersion at $\Phi = 2.5\%$ in DMSO at $q = 7.14 \times 10^4 \text{ m}^{-1}$. (b) Relaxation time τ^{-1} of $\Delta\Phi$ when the heat source is off as a function of q^2 and (c) $\Delta\Phi_{\text{St}} = f(\Delta T_{\text{max}}^{\text{St}})$ for dispersions at $\Phi = 2.5\%$ in water and in DMSO at various q and various powers of the lamp (in the linear regime).

a non-absorbing He-Ne laser. The Soret coefficient S_T is obtained in stationary conditions thanks to a few Hz modulation of the Hg lamp (the thermal response of the system being by orders of magnitude faster than the concentration one – see ESM, sects. S1 and S4). The relaxation of the concentration grating when the Hg lamp is off, allows to determine the mass diffusion coefficient D_m of the NPs.

With the heat source “on” (the Hg lamp heats the dispersion periodically at 8 Hz) the diffracted intensity, related to both the growing concentration grating and the corresponding thermal one, is recorded as a function of time until a stationary state is reached. This diffracted intensity is converted in i) temporal index-variations $\Delta n_\Phi(t)$

related to the temporal evolution of the concentration grating and ii) temporal index-variations Δn_T related to the temporal evolution of the thermal grating (see ESM, sect. S1 for more details). From the values of $\partial n/\partial T$ and $\partial n/\partial \Phi$ (see ESM, sect. S3), the temporal evolution⁴ of $\Delta \Phi$ associated to the concentration grating and of the envelope ΔT_{\max} of ΔT associated to the thermal grating are determined (see fig. 3(a) for a sample at $\Phi = 2.5\%$ and $q = 2\pi/\Lambda = 7.14 \times 10^4 \text{ m}^{-1}$ ($\Lambda = 88 \mu\text{m}$) in DMSO). When the heat source is switched off (see fig. 3(a)) $\Delta T_{\max} = 0$ and the diffracted intensity relaxes to zero as the concentration grating $\Delta \Phi$ relaxes exponentially to zero with a characteristic time τ . Figure 3(b) presents τ^{-1} as a function of q^2 in water and DMSO, at $\Phi = 2.5\%$, for different q values. These two quantities are proportional to each other, showing that the relaxation is a diffusion process, the (mass) diffusion coefficient D_m being the slope of these straight lines. We obtain $D_m = \tau^{-1}q^{-2} = 5.12 \times 10^{-11} \text{ m}^2 \text{ s}^{-1}$ for water and $D_m = 1.23 \times 10^{-11} \text{ m}^2 \text{ s}^{-1}$ for DMSO. Different powers of the lamp (ranging between 350 and 500 W) are used here to test that the response is linear and that the relaxation time τ^{-1} is independent of the power of the lamp.

Figure 3(c) presents the stationary value $\Delta \Phi_{\text{St}}$ of $\Delta \Phi$ as a function of $\Delta T_{\max}^{\text{St}}$, the value of ΔT_{\max} in the steady state, for water and DMSO, at $\Phi = 2.5\%$. They are obtained for different q values and different powers of the lamp (remaining in the range of linear response) to test that $\Delta \Phi_{\text{St}}$ and $\Delta T_{\max}^{\text{St}}$ remain proportional to each other, for a given sample independently of q and of the lamp-power. The slope of the straight lines in fig. 3(c) is proportional to the Soret coefficient S_T and as mentioned earlier they are of opposite sign in water and in DMSO. In the present experiment, the chopper, while operating, is equally open and closed. Thus the mean value of ΔT is $\langle \Delta T \rangle = \Delta T_{\max}/2$. The Soret coefficient is then given by

$$S_T = -\frac{2}{\Phi} \frac{\Delta \Phi_{\text{St}}}{\Delta T_{\max}^{\text{St}}}. \quad (4)$$

Figure 3(c) shows that at $\Phi = 2.5\%$, $|\Delta \Phi_{\text{St}}|$ is always smaller than $10^{-2}\%$ while $\Delta T_{\max}^{\text{St}} \leq 0.085 \text{ K}$ for both DMSO and water. We obtain here $S_T = -4.5 \times 10^{-2} \text{ K}^{-1}$ for water and $S_T = +0.10 \text{ K}^{-1}$ for DMSO.

4 Experimental results

FRS measurements are performed at several molar fractions of water x_W for different NP's volume fractions Φ ($0.5 \leq \Phi \leq 2.5\%$) at $[\text{H}^+] = 10^{-2} \text{ mol L}^{-1}$.

4.1 Diffusion coefficient

The mass diffusion coefficient D_m for several dispersions at different x_W is presented in fig. 4 as a function of the

⁴ By convention (see ESM, sect. S1) $\Delta \Phi$ is chosen here to be positive for $S_T < 0$ (particles moving towards hot regions) and to be negative for $S_T > 0$ (particles moving towards cold regions), with positive ΔT between bright and dark fringes.

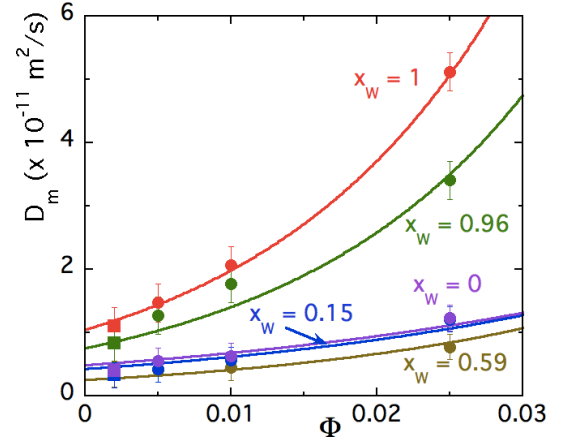


Fig. 4. Diffusion coefficient D_m as a function of the NP volume fraction Φ in mixtures of water and DMSO at different x_W – from top to bottom $x_W = 1, 0.96, 0, 0.15$ and 0.59 – as obtained from FRS measurements (circular symbols) and DLS measurements at $\Phi = 0.2\%$ (square symbols). Full lines corresponds to eq. (5) with $\chi(\Phi) = \chi_{\text{CS}}(\Phi_{\text{eff}})$ (see eq. (2)) obtained using the SANS measurement of fig. 1.

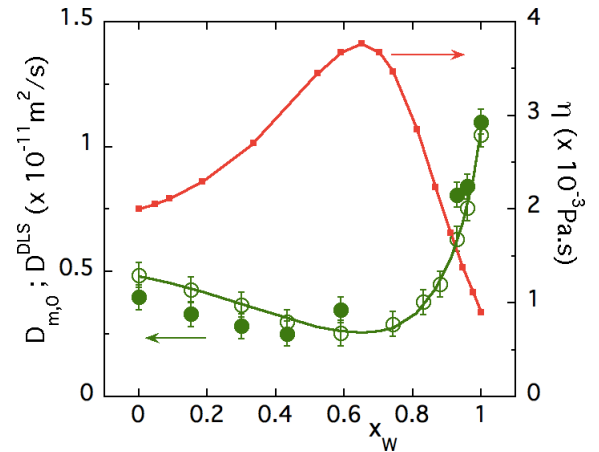


Fig. 5. Viscosity η of water-DMSO mixtures at 25°C as a function of the molar fraction of water x_W from ref. [24] (small squares/ full red line), Diffusion coefficient $D_{m,0}$ obtained at 21°C by FRS and extrapolated at $\Phi = 0$ (open circles) and D^{DLS} obtained at 22°C and $\Phi = 0.2\%$ (full circles) as a function of x_W . Full green line adjustment of $D_{m,0} = kT/\zeta_0$.

volume fraction Φ . For all solvent mixtures compositions, it is an increasing function of Φ , as expected for the strong interparticle repulsion inside the dispersions. In the low Φ regime, where both FRS and DLS are performed fig. 5 shows the good agreement between the two determinations of the diffusion coefficient. For all values of volume fraction, D_m is a non-monotonous function of x_W , with a minimum for $x_W \sim 0.6$, which corresponds to the maximum of the mixture viscosity given in fig. 5. Indeed D_m is related to the osmotic pressure Π and the local friction ζ of the NPs in the colloidal dispersion through the

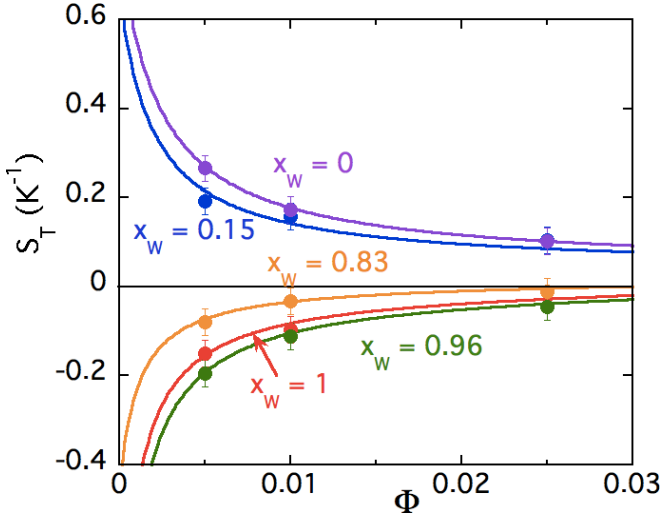


Fig. 6. Soret coefficient S_T as a function of the NP volume fraction Φ in mixtures of water and DMSO for several x_W values – from top to bottom $x_W = 0; 0.15; 0.83; 0.96$ and 1 – as obtained from FRS measurements (circular symbols). Full lines correspond to the adjustment of the results with eqs. (7) and (8), the entropy of transfer of ions (\hat{S}_{H^+}/kT and $\hat{S}_{ClO_4^-}/kT$) being deduced with the model of sect. 5.2.

following relations:

$$D_m = \frac{1}{\zeta} \frac{\partial \Pi}{\partial n_{NP}} = \frac{1}{\zeta} \frac{kT}{\chi} \quad \text{and} \quad \chi = \frac{kT}{\frac{\partial \Pi}{\partial n_{NP}}}, \quad (5)$$

where $n_{NP} = \Phi/V_{NP}$ is the number of NPs per unit volume (V_{NP} being the NP's volume), Π is the osmotic pressure of the NP system and χ is its osmotic compressibility written here in the framework of Carnahan-Starling formalism of effective hard spheres used in eqs. (2) and (3).

The full lines of fig. 4 corresponds to the adjustment $D_m(\Phi) = D_{m,0}/\chi_{CS}(\Phi_{\text{eff}})$ with $\Phi_{\text{eff}} = \Phi A_2/4$ and the A_2 values presented in fig. 1. Here it is assumed that the local friction ζ of the NPs in the colloidal dispersion equals ζ_0 the friction in the solvent, neglecting any influence of the interparticle interaction on the local friction.

The initial values $D_{m,0}$ at $\Phi = 0$ and $\chi = \chi_{CS} = 1$ deduced from FRS experiments are presented in fig. 5 as a function of x_W , for all the probed x_W . The good adjustment of $D_{m,0}(x_W)$ by kT/ζ_0 (deduced from the x_W -dependence of the viscosity), shows that it is the solvent viscosity which controls the variations of friction when x_W varies. This also attests the good NP's dispersion whatever the mixture as any aggregation of the NPs would lead to a significant decrease of the diffusion coefficient with respect to eq. (5) (shown by the full line in fig. 5). We see that the non-ideal behavior of the viscosity as a function of x_W in the water-DMSO mixtures is also observed in the experimental values of $D_{m,0}(x_W)$.

4.2 Soret coefficient

Figure 6 presents S_T as a function of Φ for several mixtures. As previously shown in fig. 3(c) the measured Soret

coefficient is found positive in DMSO (at $x_W = 0$) and negative in water (at $x_W = 1$). As expected from literature [6, 16] the Soret coefficient is a decreasing function of the volume fraction in DMSO, while it increases with Φ in water. These behaviors are also observed in mixtures at low and large x_W 's. In mixtures rich in water (large values of x_W) S_T is negative and increases with Φ while it is positive and decreases with Φ at low x_W in mixtures rich in DMSO. At intermediate values of x_W the situation is more complicated (data not shown). The measured Soret coefficient increases with Φ and remains negative, close to the one measured at $x_W = 0.83$ down to $x_W = 0.59$. At $x_W = 0.43$ and $x_W = 0.3$, S_T still increases with Φ but it becomes positive at large Φ 's. Let us analyze these dependences with the following modeling.

5 Theoretical background

5.1 Theoretical model

If the dispersions of ionic NPs are submitted to small gradients of volume fraction $\nabla\Phi$ and of temperature ∇T , the Ludwig-Soret coefficient S_T , being defined in stationary conditions by

$$\nabla\Phi = -\Phi S_T \nabla T, \quad (6)$$

can be rewritten [12, 13, 49, 50] following a model⁵ detailed in [6, 16, 17] as

$$S_T = \chi \left[\frac{\hat{S}_{NP}}{kT} - e\xi_0 \frac{S_e^{\text{st}}}{kT} \right]. \quad (7)$$

\hat{S}_{NP} is the NP Eastman entropy of transfer [11], defined as the ratio of the heat of transport of the NPs with the solvent. The stationary Seebeck coefficient S_e^{st} [13] equals for monovalent free ions:

$$eS_e^{\text{st}} = \frac{n_+ \hat{S}_+ - n_- \hat{S}_- + Z n_{NP} \chi \hat{S}_{NP}}{n_+ + n_- + Z n_{NP} \chi \xi_0}. \quad (8)$$

n_+ (respectively n_-) are the number of free H^+ (respectively ClO_4^-) ions per volume unit and \hat{S}_+ (respectively \hat{S}_-) their Eastman entropy of transfer. The (static) NP's effective charge Z is given by the electroneutrality of the dispersion (see refs. [6, 16, 17]). It is of the same order of magnitude as the (dynamic) NP's effective charges ξ_0 , determined experimentally (see sect. 2.3). For the sake of simplicity, we assimilate them to each other in the fits of $S_T(\Phi)$.

⁵ In a first approximation, we neglect here the term $\frac{1}{nkT} \frac{\partial \Pi}{\partial T}$ which is here always smaller than $9 \times 10^{-3} \text{ K}^{-1}$. As well the contribution of DMSO is not taken into account here because \hat{S}_{DMSO}/kT evolves from $-2.5 \times 10^{-3} \text{ K}^{-1}$ at $x_W = 0.1$ up to $+2.5 \times 10^{-3} \text{ K}^{-1}$ at $x_W = 0.9$ following the results of ref. [51]. Close to conditions where $S_T = 0$, these neglected terms could become slightly relevant.

In eqs. (7) and (8), the only unknown quantities are the three Eastman entropies of transfer, namely \hat{S}_{NP} , \hat{S}_+ and \hat{S}_- . The quantities \hat{S}_+ and \hat{S}_- are known in water, in the infinite dilution limit and at room temperature, from refs. [11, 52], $\hat{S}_{\text{H}^+}/kT = +0.018 \text{ K}^{-1}$ and $\hat{S}_{\text{ClO}_4^-}/kT = 0.000 \text{ K}^{-1}$. However they are not known in water-DMSO mixtures and in pure DMSO.

5.2 \hat{S}_{H^+} and $\hat{S}_{\text{ClO}_4^-}$ evaluation in water-DMSO mixtures

We propose here to evaluate \hat{S}_+ and \hat{S}_- from the enthalpy of transfer $\Delta_t H_{\text{ion}}^\circ$ of H^+ and ClO_4^- ions from water to water-DMSO mixtures, which are tabulated for several x_W values in refs. [53, 54]. Following the developments of the ESM, sect. S5, the Eastman entropy of transfer of the free ions $\hat{S}_\pm(x_W)$ can be expressed with the following expression:

$$\frac{\hat{S}_\pm}{kT}(x_W) = \frac{\hat{S}_\pm}{kT}(x_W = 1) - \frac{\Delta_t H_{\text{ion}}^\circ(x_W)}{RT^2}, \quad (9)$$

where $\Delta_t H_{\text{ion}}^\circ(x_W)$ is the enthalpy of transfer of (\pm) ions (H^+ and ClO_4^-) from water to the water-DMSO mixture at mole fraction of water x_W . Figure S4(a) of the ESM shows the values of \hat{S}_{H^+}/kT and $\hat{S}_{\text{ClO}_4^-}/kT$ as a function of x_W as deduced from refs. [53, 54] and eq. (9), together with the interpolations used here (in particular for H^+ for which we did not find any value of $\Delta_t H_{\text{ion}}^\circ(x_W)$ for $0 < x_W < 0.7$). Note that anyway \hat{S}_{H^+}/kT presents a non-ideal behavior, with a pronounced maximum in the vicinity of the eutectic proportion, while the variations of $\hat{S}_{\text{ClO}_4^-}/kT$ as a function of x_W are smoother.

The x_W -dependence of the NP's Eastman entropy of transfer \hat{S}_{NP} is then deduced from the measurements of S_T . The results obtained from eqs. (7), (8) and values of \hat{S}_{H^+}/kT and $\hat{S}_{\text{ClO}_4^-}/kT$ are presented in fig. 7(b). \hat{S}_{NP}/kT decreases from $\sim +1 \text{ K}^{-1}$ at $x_W = 0$ down to $\sim -0.5 \text{ K}^{-1}$ at $x_W = 1$, with a "plateau" close to 0 for $0.3 < x_W < 0.85$. In fig. S4(b) of the ESM, these results are compared to those obtained with a more basic evaluation of \hat{S}_\pm , obtained with the Born model which only takes into account electrostatic considerations. Both methods give very comparable results (see sect. S5 of the ESM for more details).

Using eq. (8) and the electroneutrality relation in the solution ($Zn_{\text{NP}} + n_+ + n_- = 0$), the thermoelectric contribution $-e\xi_0 S_e^{\text{st}}/kT$ in eq. (7) can be written as

$$-e\xi_0 \frac{S_e^{\text{st}}}{kT} = -\frac{\xi_0}{kT} \frac{Z \frac{n_{\text{NP}}}{n_+} (\chi(\Phi) \hat{S}_{\text{NP}} - \hat{S}_-) + (\hat{S}_+ - \hat{S}_-)}{2 + Z \frac{n_{\text{NP}}}{n_+} (1 + \chi(\Phi) \xi_0)}. \quad (10)$$

This thermoelectric contribution $-e\xi_0 \frac{S_e^{\text{st}}}{kT}$ is presented in fig. 7(a) as a function of Φ for the same x_W -values as in fig. 6.

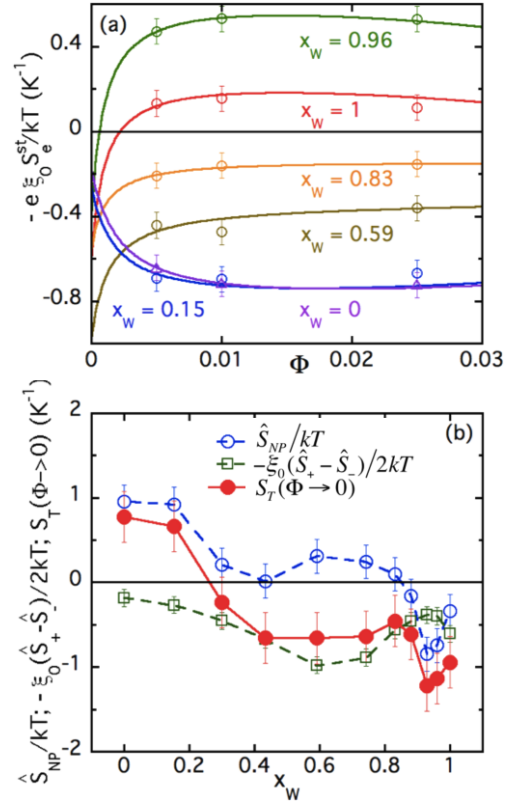


Fig. 7. (a) Thermoelectric contribution $-e\xi_0 \frac{S_e^{\text{st}}}{kT}$ as a function of Φ for $x_W = 1, 0.96, 0.83, 0.59, 0.15$ and 0 as obtained with the model of sect. 5.2. (b) Comparison between $S_T(\Phi \rightarrow 0)$ and its two contributions in eq. (11): $\frac{\hat{S}_{\text{NP}}}{kT}$ (the single-particle contribution to S_T) and $-\frac{\xi_0}{2}(\frac{\hat{S}_+}{kT} - \frac{\hat{S}_-}{kT})$ (the thermoelectric contribution of ions) obtained in the framework of the model of sect. 5.2 for \hat{S}_\pm . Full line and dashed lines are guides for the eye.

In the very dilute limit $\Phi \rightarrow 0$ and $\chi = 1$, the Soret coefficient reduces to

$$S_T(\Phi \rightarrow 0) = \frac{\hat{S}_{\text{NP}}}{kT} - \frac{\xi_0}{2} \left(\frac{\hat{S}_+}{kT} - \frac{\hat{S}_-}{kT} \right); \quad (11)$$

the first term coming from the NPs (single-particle thermophoretic contribution) and the second from the free ions (thermoelectric contribution of free ions at $\Phi = 0$). As an illustration of their relative importances, fig. 7(b) compares these two terms to $S_T(\Phi \rightarrow 0)$ as a function of x_W . In this very dilute limit ($\Phi \rightarrow 0$ and $\chi = 1$), the single-particle contribution \hat{S}_{NP} from the NPs is dominant in S_T for $x_W \leq 0.15$ (close to pure DMSO) and for $0.83 \leq x_W < 1$ (close to pure water), while on the contrary for $0.4 \leq x_W < 0.8$ it is the Seebeck contribution from the free ions, which dominates in the S_T -values (both contributions are close to each other at $x_W = 1$). Note that close to $x_W \sim 0.27$, where $S_T(\Phi \rightarrow 0) \sim 0$, the contributions neglected in footnote ⁵ may become slightly relevant.

Moreover we observe here that the single-particle thermophoretic contribution \hat{S}_{NP} changes its sign around x_W

~ 0.8 (being negative above). This corresponds to the value of x_W where the Soret coefficient of DMSO in water changes its sign in ref. [51] (being positive above). This “anti-correlation” could be related to the fact that whatever the solvent in which they are dispersed, these NPs always keep a layer of structural water at their surface leading to \hat{S}_{NP} of the same sign as the Soret coefficient of water in DMSO.

Let us note as well that, contrary to what we observe in fig. 4 for the dynamic quantity D_m , there is here no mark of non-ideality at $\Phi = 0$ for the Soret coefficient S_T in the neighborhood of the eutectic proportion $x_W \sim 0.66$, nor for any of its two components \hat{S}_{NP} and S_e^{st} . This could be related to the nature of the counter-ions condensed at the NP surface, which are here ClO_4^- and for which \hat{S}_- does not present any bump at the eutectic composition (see fig. S4(a) in the ESM).

At finite concentration, this simple description does not hold any longer since the interparticle interactions enter into play through the coefficient $\chi(\Phi)$ in eq. (7) and the NPs contribute to the thermoelectric term $-e\xi_0 \frac{S_e^{\text{st}}}{kT}$ (see eq. (8) and fig. 7(a)).

6 Discussion

The Eastman entropy of transfer \hat{S}_{NP} of the ionic NPs is the single-particle thermophoretic contribution (all the interparticle interaction and Seebeck contributions being already eliminated). It has been shown in [16–18] that \hat{S}_{NP} depends on all the details of the interface between the NPs and the solvent (NP’s coating, nature and concentration of free counterions, nature of the solvent).

This evolution of \hat{S}_{NP} correlates with the evolution of the structure and the dynamics of the pure water-DMSO mixtures [33,34]. Indeed, adding a few DMSO molecules in water induces huge changes in the molecular organization observed in the mixtures due to strong H bonds interactions between DMSO and water [34]. In the range $0.85 \leq x_W \leq 1$ where \hat{S}_{NP} is negative, the exchange rate of H bonds moreover slows down while adding DMSO due to these H bonds between the two solvent molecules which are for example at the origin of the cryoprotective role of DMSO for proteins in this range of x_W [33]. When increasing the DMSO content further ($x_W < 0.85$), the dynamics of the water/surface H bonds should change due to the increasing number of DMSO molecules, which can also solvate the NPs surfaces [33]. As well, adding some water molecules in DMSO ($0 \leq x_W \leq 0.1$) modifies its organization on the molecular scale, however this does not influence much \hat{S}_{NP} , which remains constant and positive. In the intermediate region ($0.1 < x_W \leq 0.65$) where the structure of DMSO does not evolve much [34], \hat{S}_{NP} does not change much either. We recall that no special behaviour is here detected in the region of the eutectic point close to $x_W = 0.66$.

Moreover, it has been shown in refs. [13,55–58] that two main mechanisms of ionic shielding contribute to \hat{S}_{NP} .

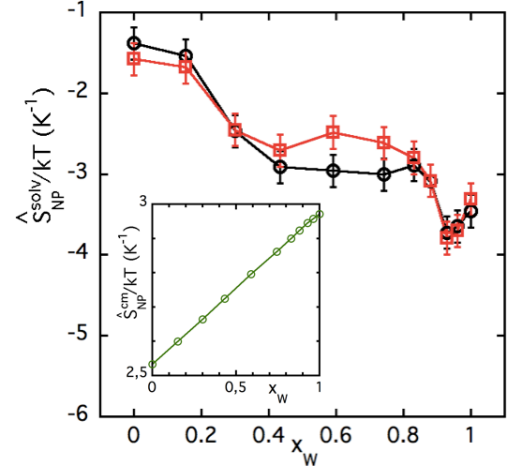


Fig. 8. $\hat{S}_{\text{NP}}^{\text{solv}}/kT$ (main figure) and $\hat{S}_{\text{NP}}^{\text{cm}}/kT$ (inset) as a function of x_W obtained using eqs. (12) and (13). Symbols of the main figure: $\hat{S}_{\text{NP}}^{\text{solv}}/kT$ deduced from fig. 7(b) in the framework of the model of sect. 5.2 (open squares); as deduced from the Born model for \hat{S}_{\pm} and fig. S4(b) of the ESM (open circles).

One is electrostatic. It is driven by the buildup of the NP’s charge and of the ionic shell. It is usually described [59–61] with the capacitor model $\hat{S}_{\text{NP}}^{\text{cm}}$. The second one $\hat{S}_{\text{NP}}^{\text{solv}}$ corresponds to the solvation of the NPs and of their ionic shell in the solvent [59]. \hat{S}_{NP} then expresses as

$$\hat{S}_{\text{NP}} = \hat{S}_{\text{NP}}^{\text{cm}} + \hat{S}_{\text{NP}}^{\text{solv}}. \quad (12)$$

The capacitor contribution can be written as

$$\hat{S}_{\text{NP}}^{\text{cm}} = \frac{\partial}{\partial T} \left[\frac{(eZ(x_W))^2}{2\pi\epsilon_0\epsilon(T, x_W)d_{\text{NP}}(2 + \kappa(T, x_W)d_{\text{NP}})} \right], \quad (13)$$

where $Z(x_W)$ is the static effective charge in the solution (taken here equal to $\xi_0(x_W)$), $\epsilon(T, x_W)$ is the relative permittivity of the aqueous dimethyl sulfoxide solution at x_W and where $\kappa^{-1}(T, x_W)$ is the screening length at x_W . $\epsilon(T, x_W)$ is obtained from ref. [30]; $\xi_0(x_W)$ and $d\xi_0(x_W)/dT$ are deduced by linear interpolation between their measured values in water and DMSO; $\kappa^{-1}(x_W)$ is deduced from eq. (3) and measurements of fig. 1.

$\hat{S}_{\text{NP}}^{\text{cm}}$ (see inset of fig. 8) then varies almost linearly from $\sim +2.5 \text{ K}^{-1}$ in pure DMSO to $\sim +3 \text{ K}^{-1}$ in pure water; It strongly depends on $d\xi_0/dT$.

$\hat{S}_{\text{NP}}^{\text{solv}}$, as obtained from eq. (12) is presented in fig. 8 in the framework of the model of sect. 5.2 for evaluating \hat{S}_{H^+}/kT and $\hat{S}_{\text{ClO}_4^-}/kT$ and compared to the values obtained with the Born model described in sect. S5.1 of the ESM. In both cases $\hat{S}_{\text{NP}}^{\text{solv}}$ is negative, as expected in water in ref. [59] and it stays negative whatever x_W , even in pure DMSO at $x_W = 0$.

It expresses a strong solvophilicity of the NPs on the whole range of x_W as $\hat{S}_{\text{NP}}^{\text{solv}}$ decreases from -1.5 K^{-1} in DMSO down to $\sim -3.5 \text{ K}^{-1}$ at large proportion of water ($x_W \geq 0.9$).

7 Summary: perspectives

The Soret coefficient of acidic NPs dispersed at $[H^+] = 10^{-2} \text{ mol L}^{-1}$ in water-dimethyl sulfoxide mixtures is measured at different mole fractions of water x_W . It is observed that at low fractions of water the NPs are thermophobic ($S_T > 0$) while at large fractions of water they are thermophilic ($S_T < 0$). This has to be ascribed both to the single-particle thermophoretic contribution (the so-called NP's entropy of transfer \hat{S}_{NP} which is linked to the particle/solvent interaction) and to the thermoelectric contribution (Seebeck term $-e\xi_0 \frac{S_e^{st}}{kT}$ in which all the charged species contribute).

It is shown here that the single-particle thermophoretic contribution of the NPs is dominant at low and large x_W values ($x_W \leq 0.15$ and ≥ 0.83) while it is the Seebeck term which dominates at intermediate x_W . Whatever x_W , the solvation contribution to \hat{S}_{NP} is negative, expressing a strong affinity of the ionic NPs with the mixtures of water and DMSO. However this solvation contribution is much stronger in absolute value at large water contents x_W , which implies a huge role of the hydrogen-bonds of water molecules with the NPs surface in this solvation contribution. The (negative) solvation contribution then dominates the (positive) electrostatic contribution and both \hat{S}_{NP} and S_T are negative. On the contrary at low values of x_W , the (positive) electrostatic contribution to \hat{S}_{NP} dominates the (negative) solvation term and gives a positive sign to \hat{S}_{NP} , as well as to the Soret coefficient S_T .

The interparticle interaction is here strongly repulsive. It imparts the systems with its colloidal stability and leads to higher NP's diffusion coefficients for larger NP's volume fractions Φ , whatever x_W . It is due to the strong decrease of the osmotic compressibility χ of the NP's system as Φ increases.

At low and large x_W values, whatever the S_T sign, the interparticle interaction reduces the Soret coefficient in absolute value as Φ increases, because of the decrease of χ . In the intermediate range of x_W , where the thermoelectric contribution becomes more important, the situation is more complicated.

Such colloidal dispersions of ionic NPs in mixtures of water and DMSO can be very useful for thermocell applications, as tuning the proportion of DMSO in the system allows to tune in sign and amplitude the Soret coefficient and the entropy of transfer of the NPs. However, they can also be useful to understand the temperature evolution of hydrogen bonding in these mixtures. Indeed in the present work, only room temperature measurements have been performed and it would be also important to explore the temperature evolution of the Soret coefficient (and of the NPs entropy of transfer) at higher temperatures, and also at lower temperatures in the eutectic vicinity, for molar fraction of water $x_W \sim 0.66$. The influence of the concentration of free ions $[H^+]$ and $[ClO_4^-]$ would be also important to examine, as it is a way to tune the Seebeck coefficient at finite concentration. As well it would be of paramount interest to study the influence of the nature of the counterion on the Soret coefficient. Unfortunately

up to now ClO_4^- is the only counterion that we know that leads to the colloidal stability of the dispersions of maghemite NPs in the whole range of x_W in water-DMSO mixtures.

We propose here a method to evaluate the ionic contributions \hat{S}_{H^+} and $\hat{S}_{ClO_4^-}$ using the ionic enthalpy of transfer of H^+ and ClO_4^- at room temperature. Direct experimental and/or numerical determinations of these quantities as a function of temperature would be extremely useful in the near future to analyze the Soret coefficient in these solutions of ionic NPs as a function of T .

We deeply thank Amandine Anfry for the ξ_0 determinations as a function of temperature, Sawako Nakamae for useful discussions, Fabrice Cousin for his help in the SANS measurements and Laboratoire Léon Brillouin for the beamtime allocation on PACE in ORPHEE. This work has been supported by European Union's Horizon 2020 research and innovation programme under the Grant No. 731976 (MAGENTA).

Author contribution statement

JCR synthesized and characterized all the samples, under the supervision of ED and VP. MS realized all the FRS measurements under the supervision of GD, GM and RP. The technical improvements of the FRS device were done by FG. The theoretical developments presented here were done in close collaboration among all the members of the team. All the authors were involved in the preparation of the manuscript. All the authors have read and approved the final manuscript.

Publisher's Note The EPJ Publishers remain neutral with regard to jurisdictional claims in published maps and institutional affiliations.

References

1. C. Soret, Arch. Sci. Phys. Nat. Genève **3**, 48 (1879).
2. S.A. Putnam, D.G. Cahill, Langmuir **21**, 5317 (2005).
3. C. Goupil, W. Seifert, K. Zabrocki, E. Müller, G. Snyder, Entropy **13**, 1481 (2011).
4. R. Hu, B. Cola, N. Haram, J. Barisci, S. Lee, S. Stoungton, G. Wallace, C. Too, M. Thomas, A. Gestos, M. dela Cruz, J. Ferraris, A. Zakhidov, R. Baughman, Nano Lett. **10**, 838 (2010).
5. V. Zinovyeva, S. Nakamae, M. Bonetti, M. Roger, Chem-ElectroChem **1**, 426 (2014).
6. B.T. Huang, M. Roger, M. Bonetti, T.J. Salez, C. Wiertel-Gasquet, E. Dubois, R.C. Gomes, G. Demouchy, G. Méridet, V. Peyre, M. Kouyaté, C.L. Filomeno, J. Depeyrot, F.A. Tourinho, R. Perzynski, S. Nakamae, J. Chem. Phys. **143**, 054902 (2015).
7. T.J. Salez, B.T. Huang, M. Rietjens, M. Bonetti, C. Wiertel-Gasquet, M. Roger, C.L. Filomeno, E. Dubois, R. Perzynski, S. Nakamae, Phys. Chem. Chem. Phys. **19**, 9409 (2017).
8. M. Dupont, D. MacFarlane, J. Pringle, Chem. Commun. **53**, 6288 (2017).

9. D. Al-Masri, M. Dupont, R. Yunis, D.R. MacFarlane, J.M. Pringle, *Electrochim. Acta* **269**, 714 (2018).
10. T.J. Salez, S. Nakamae, R. Perzynski, G. Mériduet, A. Cēbers, M. Roger, *Entropy* **20**, 405 (2018).
11. J.N. Agar, C.Y. Mou, J.L. Lin, *J. Phys. Chem.* **93**, 2079 (1989).
12. A. Würger, *Phys. Rev. Lett.* **101**, 108302 (2008).
13. A. Majee, A. Würger, *Phys. Rev. E* **83**, 061403 (2011).
14. A. Majee, *Effet thermoélectrique dans les dispersions colloïdale*, PhD Thesis, Université Bordeaux I (2012).
15. M. Reichl, M. Herzog, A. Gotz, D. Braun, *Phys. Rev. Lett.* **112**, 198101 (2014).
16. R. Cabreira-Gomes, A.F. da Silva, M. Kouyaté, G. Demouchy, G. Mériduet, R. Aquino, E. Dubois, S. Nakamae, M. Roger, J. Depeyrot, R. Perzynski, *Phys. Chem. Chem. Phys.* **20**, 16402 (2018).
17. M. Kouyaté, C. Filomeno, G. Demouchy, G. Mériduet, S. Nakamae, V. Peyre, M. Roger, A. Cēbers, J. Depeyrot, E. Dubois, R. Perzynski, *Phys. Chem. Chem. Phys.* **4**, 1895 (2019).
18. C.L. Filomeno, M. Kouyaté, F. Cousin, G. Demouchy, E. Dubois, L. Michot, G. Mériduet, R. Perzynski, V. Peyre, J. Sirieix-Plénet, F.A. Tourinho, *J. Magn. & Magn. Mater.* **431**, 2 (2017).
19. C.L. Filomeno, M. Kouyaté, V. Peyre, G. Demouchy, A.F.C. Campos, R. Perzynski, F.A. Tourinho, E. Dubois, *J. Phys. Chem. C* **121**, 5539 (2017).
20. Y. Marcus, *Chem. Rev.* **109**, 1346 (2009).
21. I. Plowas, J. Swiergiel, J. Jadzyn, *J. Chem. Eng. Data* **59**, 2360 (2014).
22. J. Kiefer, K. Noack, B. Kirchner, *Curr. Phys. Chem.* **1**, 340 (2011).
23. D. Rasmussen, A.M. Kenzie, *Nature* **220**, 1315 (1968).
24. J. Cowie, P. Toporowski, *Can. J. Chem.* **39**, 2240 (1961).
25. R. LeBel, D. Goring, *J. Chem. Eng. Data* **7**, 100 (1962).
26. C. Nieto-Draghi, J.B. Avalos, B. Rousseau, *J. Chem. Phys.* **119**, 4782 (2003).
27. H. Zhang, G. Zhao, H. Ye, X. Ge, S. Cheng, *Meas. Sci. Technol.* **16**, 1430 (2005).
28. J.-C. Zhou, Y.-Y. Che, K.-J. Wu, J. Shen, C.H. He, *J. Chem. Eng. Data* **58**, 663 (2013).
29. U. Kaatzte, R. Pottel, M. Schafer, *J. Phys. Chem.* **93**, 5623 (1989).
30. A. Luzar, *J. Mol. Liq.* **46**, 221 (1990).
31. Y. Doucet, F. Calmes-Perrault, M.-T. Durand, *C. R. Acad. Sci. Paris* **260**, 1878 (1965).
32. M. Skaf, *J. Phys. Chem. A* **103**, 10719 (1999).
33. S.M. Kashid, G.Y. Jin, S. Chakrabarty, Y.S. Kim, S. Bagchi, *J. Phys. Chem. Lett.* **8**, 1604 (2017).
34. K. Oh, K. Rajesh, J. Stanton, C. Baiz, *Angew. Chem. Int. Ed.* **56**, 11375 (2017).
35. A.K. Soper, A. Luzar, *J. Chem. Phys.* **97**, 1320 (1992).
36. A. Perera, R. Mazighi, *J. Chem. Phys.* **143**, 154502 (2015).
37. S. Banerjee, S. Roy, B. Bagchi, *J. Phys. Chem. B* **114**, 12875 (2010).
38. S. Roy, B. Bagchi, *J. Chem. Phys.* **139**, 034308 (2013).
39. R. Massart, *C. R. Acad. Sci. Paris, Ser. C* **291**, 1 (1980).
40. R. Massart, *IEEE Trans. Magn.* **17**, 1247 (1981).
41. J.A. Gomes, M.H. Sousa, F.A. Tourinho, R. Aquino, G.J. da Silva, J. Depeyrot, E. Dubois, R. Perzynski, *J. Phys. Chem. C* **112**, 6220 (2008).
42. R. Massart, E. Dubois, V. Cabuil, E. Hasmonay, *J. Magn. & Magn. Mater.* **149**, 1 (1995).
43. B. Berkovski (Editor), *Magnetic Fluids and Applications Handbook* (Begell House Inc. Publ., New York, 1996).
44. E. Wandersman, A. Cēbers, E. Dubois, G. Mériduet, A. Robert, R. Perzynski, *Soft Matter* **9**, 11480 (2013).
45. N.F. Carnahan, K.E. Starling, *J. Chem. Phys.* **53**, 600 (1970).
46. J.A. Barker, D. Henderson, *J. Chem. Phys.* **47**, 4714 (1967).
47. Y. Nagasaka, T. Hatakeyama, M. Osuka, A. Nagashima, *Rev. Sci. Instrum.* **59**, 1156 (1988).
48. G. Demouchy, A. Mezulis, A. Bée, D. Talbot, J.-C. Bacri, A. Bourdon, *J. Phys. D: Appl. Phys.* **37**, 1417 (2004).
49. R. Piazza, A. Parola, *J. Phys.: Condens. Matter* **20**, 153102 (2008).
50. J. Burelbach, D. Frenkel, I. Pagonabarraga, E. Eiser, *Eur. Phys. J. E* **41**, 7 (2017).
51. H. Ning, S. Wiegand, *J. Chem. Phys.* **125**, 221102 (2006).
52. N. Takeyama, K. Nakashima, *J. Solut. Chem.* **17**, 305 (1988).
53. G. Hefter, Y. Marcus, W. Waghme, *Chem. Rev.* **102**, 2773 (2002).
54. Y. Marcus, *Ion Properties* (Marcel Dekker, New York, 1997).
55. J.K.G. Dhont, W.J. Briels, *Eur. Phys. J. E* **25**, 61 (2008).
56. D. Vigolo, S. Buzzaccaro, R. Piazza, *Langmuir* **26**, 7792 (2010).
57. M. Yang, M. Ripoll, *Soft Matter* **9**, 4661 (2013).
58. K.A. Eslahian, A. Majee, M. Maskos, A. Würger, *Soft Matter* **10**, 1931 (2014).
59. S. Duhr, D. Braun, *Proc. Natl. Acad. Sci. USA* **103**, 19678 (2006).
60. J.K.G. Dhont, S. Wiegand, S. Duhr, D. Braun, *Langmuir* **23**, 1674 (2007).
61. H. Ning, J.K.G. Dhont, S. Wiegand, *Langmuir* **24**, 2426 (2008).

Inversion of thermodiffusive properties of ionic colloidal dispersions based on DMSO-water mixtures probed by forced Rayleigh scattering

Electronic Supporting Information

by

M. Sarkar, J. Riedl, G. Demouchy, F. Gélébart,
G. Mériguet, V. Peyre, E. Dubois, R. Perzynski

S1 Diffraction by a refractive index modulation

The two timescale model used in the analysis of our experiment have been studied in detail in Ref. [1], together with the diffracted intensity of the probing laser-beam. High orders of diffraction are observed in the experiment, which is performed in the Raman-Nath regime (thin grating) with a very small Klein factor Q_{Klein} [2, 3, 4]:

$$Q_{\text{Klein}} = \frac{2\pi\lambda d}{n\Lambda^2} \ll 1. \quad (\text{S1})$$

It can be checked that this relation is fulfilled in the experiment with wavelength $\lambda = 632$ nm, largest sample thickness $d = 100$ μm , lowest refractive index $n = 1.33$ and smallest grating-period $\Lambda = 88$ μm .

Figure S1 shows the temporal evolution of the (first order) diffracted intensity for a system - first at the concentration steady-state with the chopper alternatively on and off, and - then relaxing to zero after switching off the heat source (chopper off). Left (resp. right) part of the figure is an illustration for a dispersion with a positive (resp. negative) Soret coefficient. The two time-scale model is based on the fact that the thermal diffusion of the system (thermal diffusion coefficient $D_{\text{th}} = k/\rho c_p$ with k the conductivity, ρ the density and c_p the specific heat capacity) is a rapid process compared to the nanoparticle diffusion (mass diffusion coefficient D_m) (see section 3 of main text and section S4 of E.S.I.). Then, if the concentration is at steady state, the contribution of the thermal grating to the diffracted signal exhibits the same periodicity as the heating light (given by the chopper characteristics: frequency 8Hz with a duty cycle of 50%).

Looking at the first order of diffraction of the (1D) spatial grating along the Ox direction, the temperature and the volume fraction of particles can be assimilated to:

$$\Phi(x, t) = \Phi_0 + \frac{\Delta\Phi(t)}{2} \sin\left(2\pi\frac{x}{\Lambda}\right). \quad (\text{S2})$$

$$T(x, t) = T_0 + \frac{\Delta T(t)}{2} \sin\left(2\pi\frac{x}{\Lambda}\right); \quad (\text{S3})$$

Here Φ_0 and T_0 are respectively the mean value of the volume fraction and of the temperature along the x-axis during the experiment, $\Delta\Phi$ and ΔT being their spatial-modulations. By convention ΔT is always taken positive;

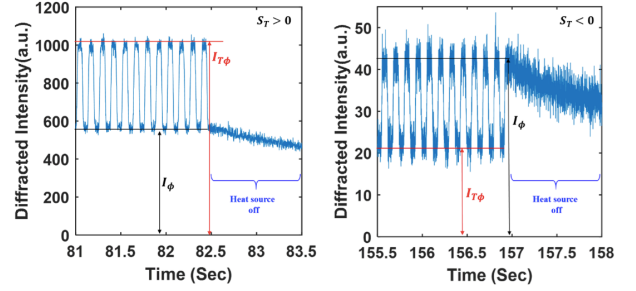


Figure S1. Temporal evolution of the diffracted intensity, first oscillating at concentration steady-state between $I_{T\Phi}$ (chopper on and system at the upper temperature steady-state) and I_Φ (chopper off system at the lower temperature steady-state) and relaxing to zero after switching off the heat source (chopper off); Left figure, example for a dispersion with a positive Soret coefficient; Right figure, example for a dispersion with a negative Soret coefficient.

$\Delta\Phi$ is positive if the NPs go towards hot regions (meaning $S_T < 0$) and $\Delta\Phi$ is negative if the NPs go towards cold regions (meaning $S_T > 0$). The stationary value of $\Delta\Phi$ is denoted $\Delta\Phi_{\text{St}}$ and ΔT oscillates at 8 Hz between 0 when the heat source is off and ΔT_{max} when the heat source is on.

The spatial modulations of temperature and of volume fraction induce spatial modulations of the refractive index, which can be written as :

$$n = n_0 + \frac{\Delta n}{2} \sin\left(2\pi\frac{x}{\Lambda}\right) \quad (\text{S4})$$

For a probe beam of intensity I_0 , with an angle of incidence θ (assuming that the modulation is weak ($n_0 \gg \Delta n$) and that the dielectric medium is lossless ($n'' \sim 0$)), the modulation Δn is related to the first-order diffracted intensity I_d in the conditions of Eq. S1 through:

$$\Delta n = \pm \frac{\lambda \cos \theta}{\pi d} \sqrt{\frac{I_d}{I_0}}, \quad (\text{S5})$$

here $\theta = 38^\circ$.

Let us denote $\Delta n_{T\Phi}$ the contributions of T and Φ modulations together. We can assume that the total refractive index modulation $\Delta n_{T\Phi}$ is a linear sum of two contributions to the refractive index modulation, namely one (Δn_T) owing to the temperature gradient and the second one (Δn_Φ) owing to the concentration gradient, written as:

$$\Delta n_{T\Phi} = \Delta n_\Phi + \Delta n_T. \quad (\text{S6})$$

Experimentally, we have access to the first-order diffracted intensity $I_{T\Phi}$, associated to $\Delta n_{T\Phi}$ when the chopper is on (and the system at steady state with respect to both Φ and T). When the chopper is off, at the steady state of Φ and T , the diffracted intensity is I_Φ (see Fig. S1). Depending on the sign of the Soret coefficient, $I_{T\Phi}$ is either larger or lower than I_Φ . For positive Soret coefficients (when particles move to regions with lower temperatures) the temperature and volume fraction modulations are in

antiphase while for negative Soret coefficients (particles move to higher temperatures) they are in phase. As the variation of refractive index with temperature ($\partial n/\partial T$) is usually negative while $\partial n/\partial \Phi$ is positive, the contributions of the temperature and concentration gradients to the total refractive index are additive for positive Soret coefficients while for negative Soret coefficients they oppose each other (see Fig.S1). We then deduce [1]:

$$|\Delta\Phi| = \frac{|\Delta n_\phi|}{\partial n/\partial \Phi} = \frac{\lambda \cos \theta}{\pi d} \frac{\partial n/\partial \Phi}{\partial n/\partial \Phi} \sqrt{I_\phi/I_0} \quad (\text{S7})$$

$$\begin{aligned} \Delta T_{\max} &= \frac{|\Delta n_T|}{|\partial n/\partial T|} = \frac{|\Delta n_{T\phi} - \Delta n_\phi|}{|\partial n/\partial T|} \\ &= \frac{\lambda \cos \theta}{\pi d} \left| \sqrt{I_{T\phi}/I_0} - \sqrt{I_\phi/I_0} \right|, \end{aligned} \quad (\text{S8})$$

$\Delta\Phi$ being here of the same sign of $I_\phi - I_{T\phi}$.

Fig. 3a of the main paper illustrates the time evolution of $\Delta\Phi$ and ΔT_{\max} as obtained for a dispersion at $\Phi = 2.5\%$ in DMSO at a given Λ . In that particular case, $\Delta\Phi$ reaches its stationary value $\Delta\Phi_{\text{st}}$ in ~ 60 s while ΔT_{\max} reaches a roughly constant value $\Delta T_{\max}^{\text{St}}$ in a few seconds. The experimental values of I_ϕ and $I_{T\phi}$ are obtained thanks to a filtering processing of the signal, at the chopper frequency. As illustrated by Fig. 3c of the main paper, the conditions $\Delta T_{\max}^{\text{St}} \ll T_0$ and $|\Delta\Phi_{\text{st}}| \ll \Phi_0$ are always fulfilled.

S2 Theoretical modeling

When a temperature gradient is applied to the sample, the particle current owing to its volume fraction flow can be written as:

$$\mathbf{j}_{\text{NP}} = -D_m \nabla \Phi - \Phi_0 S_T D_m \nabla T. \quad (\text{S9})$$

Here we neglect the electric drift of the particles in the presence of an external electric field [1,5]. D_m is the diffusion coefficient related to Fick's diffusion while S_T is the Soret coefficient which is a measure of the volume fraction gradient induced by the temperature gradient. In steady state without particle flow ($\mathbf{j}_{\text{NP}} = \mathbf{0}$) the Soret coefficient is given by

$$\Phi_0 S_T \nabla T = -\nabla \Phi \quad (\text{S10})$$

Using the continuity equation for the volume fraction flow $\partial \Phi/\partial t = -\nabla \mathbf{j}_{\text{NP}}$ the temporal variation of the volume fraction can be written using Eq. S9 as

$$\frac{\partial \Phi}{\partial t} = D_m \nabla^2 \Phi + \Phi_0 S_T D_m \nabla^2 T. \quad (\text{S11})$$

Using Eq. S2, it reduces to:

$$\frac{\partial \Delta\Phi}{\partial t} = -D_m q^2 \Delta\Phi - \Phi_0 S_T D_m q^2 \Delta T. \quad (\text{S12})$$

When the heat-source is switched off, $\Delta T = 0$ almost immediately (see Fig. 4a of the main paper in the condition of heat source off) and the relaxation of the volume fraction modulation $\Delta\Phi(t)$ is given by:

$$\Delta\Phi_{\text{off}}(t) = \Delta\Phi_{\text{st}} \exp(-q^2 D_m t) \quad (\text{S13})$$

The volume fraction gradient undergoes an exponential decay, with a time constant $\tau = q^{-2} D_m^{-1}$ and the diffusion coefficient D_m can be determined. In the main text we present some results obtained for the heat-source off (see Fig. 3b of the main paper showing τ^{-1} as a function of q^2 for two samples at the same volume fraction $\Phi_0 = 2.5\%$). The slope of the straight lines gives the value of D_m .

It is important to note that the rate on/off of the chopper when the heat-source is on, is an important parameter in the measurements. Here we use a chopper with a duty cycle of 50% and then during the heating process $\langle \Delta T \rangle = \Delta T_{\max}/2$. We thus deduce the Soret coefficient in the steady state with the following expression:

$$\Phi_0 S_T = -\frac{2\Delta\Phi_{\text{st}}}{\Delta T_{\max}^{\text{St}}}. \quad (\text{S14})$$

Fig. 3c of the main paper shows $\Delta\Phi_{\text{st}}$ as a function of $\Delta T_{\max}^{\text{St}}$ for two samples at the same volume fraction Φ_0 . The slope of the straight lines gives the value of S_T . Note that to deduce S_T , it is important to check that the measurements performed at different powers of the heating lamp remain within the range of linear response where $\Delta T \ll T_0$. It is also important to check that S_T remains constant while varying q (or equivalently the period Λ of the grid) to check that the frequency of the chopper allows the thermal modulation to relax completely during one of its "off" time-period.

S3 Values of $\partial n/\partial T$ and $\partial n/\partial \Phi$ of NP dispersions in water-DMSO mixtures

For the analysis of the S_T measurements, it is necessary to know the values of $\partial n/\partial T$ and $\partial n/\partial \Phi$ of the colloidal dispersions as a function of Φ and of their molar fraction of water x_W .

In E.S.I. of Ref. [6], it has been shown that in water, the quantity $\partial n/\partial \Phi$ is well described by the formalism of Bruggeman [7] up to $\Phi = 2.5\%$. We assume here that it is also true in the mixtures of water and DMSO. It is also shown that at low volume fractions and to the first order, the quantity $\partial n/\partial T$ in the dispersions equals that of the pure solvent. Fig. S2 shows, as a function of x_W the values of $\partial n/\partial T$ used in the analysis of the main paper. They are interpolated from experimental measurements of index variations of the solvent mixtures as a function of T at given x_W , using the ARAGO apparatus from Cordouan Technologies.

Table S1. Characteristics of water and DMSO at room temperature. η is the viscosity from [8], ρ the density from [8], c_p the specific heat capacity, k the thermal conductivity from [9] and D_{th} calculated with Eq. S16.

Solvent	η 10^{-3} Pa s	ρ 10^3 kg m $^{-3}$	c_p J g $^{-1}$ K $^{-1}$	k W m $^{-1}$ K $^{-1}$	D_{th} 10^{-7} m 2 s $^{-1}$
H $_2$ O	0.90	1.00	4.18	0.60	1.4
DMSO	2.00	1.10	1.94	0.19	0.9

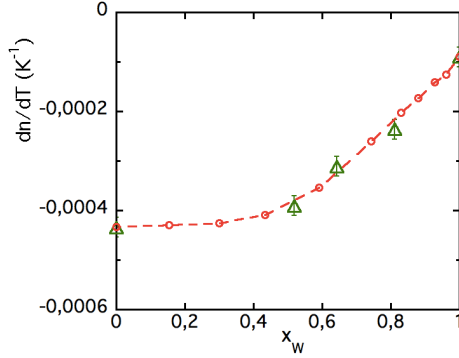


Figure S2. Values of $\partial n/\partial T$ in the water/DMSO mixtures used in the main paper; Symbols : (Open triangles) experimental determinations obtained in mixtures with the ARAGO-Cordouan apparatus; (open circles and dashed line) interpolation used for the S_T analysis.

S4 Thermal conductivity of NP dispersions in water-DMSO mixtures

At the NP's concentration steady state, the process of thermal diffusion is driven by the following continuity equation :

$$\rho c_p \frac{\partial T}{\partial t} - k \nabla \cdot \mathbf{j}_{th} = \dot{Q}_{vol} - \dot{Q}_{loss} \quad (S15)$$

where, as partly seen previously, ρ is the density, c_p the specific heat capacity, k the thermal conductivity, \mathbf{j}_{th} the heat flow and $\dot{Q}_{vol} - \dot{Q}_{loss}$ the averaged heat input (\dot{Q}_{vol}) per time and volume unit in the sample minus the various losses of power per volume unit (\dot{Q}_{loss}).

The process of temperature evolution is then a diffusion process ruled by the solvent thermal diffusion coefficient D_{th} :

$$D_{th} = \frac{k}{\rho c_p}, \quad (S16)$$

with typical values at room temperature given in Table S1 of E.S.I. for water and DMSO. Measurements from Ref. [9] and simulation results from Ref. [10] in water-DMSO mixtures are presented in Fig. S3.

The associated relaxation time τ_{th}

$$\tau_{th} = D_{th}^{-1} q^{-2} \quad (S17)$$

is then ~ 1.4 ms in water and ~ 2.2 ms in DMSO, for $q = 7.14 \times 10^4$ m $^{-1}$ ($\Lambda = 88$ μ m) as in Fig. 3a of the main paper.

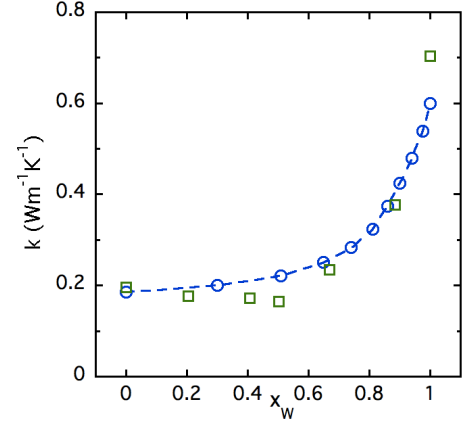


Figure S3. Thermal conductivity k of mixtures water-DMSO as a function of (x_W) - Symbols: (o) experimental data from [9]; (\square) simulation data from [10].

S5 Evaluation of \hat{S}_{\pm} in water-DMSO mixtures

We propose here two methods to evaluate \hat{S}_{+} and \hat{S}_{-} .

S5.1 Born model

A first minimal approach (I) has been proposed in Refs. [11, 12] based on the Born model. Using the stick boundary condition in the friction of ion i , $\hat{S}_i = Q_i^{*o}/T$ can be evaluated as¹:

$$\hat{S}_i = \frac{Q_i^{*o}}{T} = -\frac{e^2 Z_i^2}{4\epsilon^2 R_i} \frac{\partial \epsilon}{\partial T} \quad (S18)$$

where Z_i and R_i are the valence and the radius of ion i , in the medium of dielectric constant ϵ . However, this rough calculation, based on a continuous dielectric description does not take into account the specificities of the ion solvation. Fig. S4a shows in dotted lines the values of \hat{S}_{H^+}/kT and $\hat{S}_{ClO_4^-}/kT$ as a function of x_W deduced from Eq. S18.

S5.2 Enthalpy of transfer

Another method (II) (developed in Section 5.2 of the main paper) is used to deduce \hat{S}_{+} and \hat{S}_{-} from the enthalpy of transfer $\Delta_t H_{ion}^o$ of H $^+$ and ClO $_4^-$ ions from water to water-DMSO mixtures. They are tabulated for several x_W values in Refs. [13, 14].

¹ Q_i^{*o} is the heat of transport of ion i .

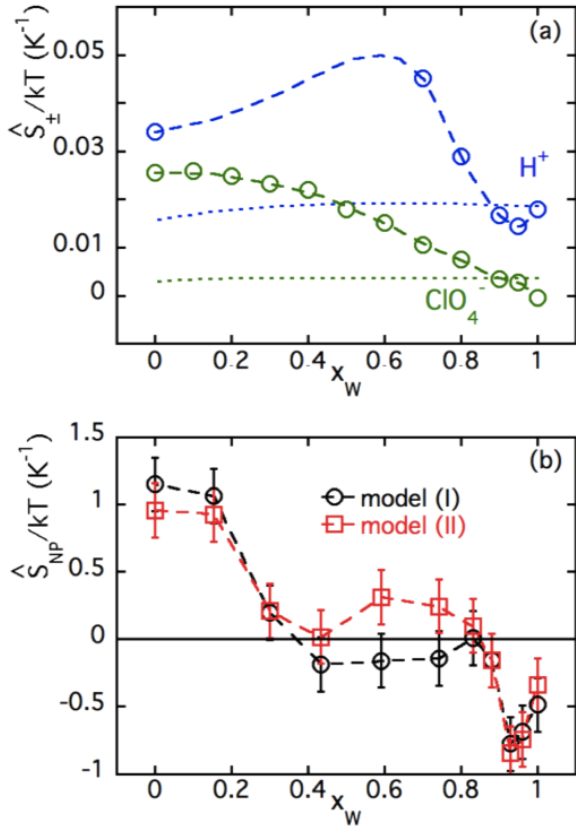


Figure S4. (a) Values of \hat{S}_{H^+}/kT and $\hat{S}_{ClO_4^-}/kT$ as a function of x_W as deduced for model (I) from Eq. S18 (dotted lines) and for model (II) from Eq. 9 of the main paper and Refs [13,14] (open symbols : computed from the experimental values of [13, 14] and dashed lines interpolations used here); (b) Values of \hat{S}_{NP}/kT as a function of x_W as deduced from Eqs. 7 and 8 of the main paper, and values of \hat{S}_{H^+}/kT and $\hat{S}_{ClO_4^-}/kT$ from (a) [Open circles: from Eq. S18 (model (I)); Open squares: from Eq. 9 of the main paper (model (II)) and Ref. [13,14]].

S5.2.1 Evaluation of the change of S_T with the change of solvent

In a solvent or a mixture of solvents φ , the steady state in a temperature gradient yields for one type of ions (denoted \pm) and neglecting other couplings:

$$\nabla n_{\pm} = -S_T^{\varphi} n_{\pm} \nabla T, \quad (S19)$$

which leads to the following operational definition of the Soret coefficient

$$S_T^{\varphi} = -\frac{d \ln n_{\pm}^{\varphi}}{dT} \quad (S20)$$

If another mixture ψ is considered, the concentrations of the ions in the mixtures φ and ψ are related at equilibrium by the partition constant

$$K^{\circ} = n_{\pm}^{\psi} / n_{\pm}^{\varphi} \quad (S21)$$

and the Gibbs free energy of transfer

$$\Delta_t G_{\varphi \rightarrow \psi}^{\circ} = -RT \ln K^{\circ} \quad (S22)$$

Using eq. S20 in the mixture ψ and introducing the partition constant

$$S_T^{\psi} = -\frac{d \ln n_{\pm}^{\psi}}{dT} = S_T^{\varphi} - \frac{d \ln K^{\circ}}{dT} \quad (S23)$$

which yields finally with the use of van't Hoff equation:

$$S_T^{\psi} = S_T^{\varphi} - \frac{\Delta_t H_{\varphi \rightarrow \psi}^{\circ}}{RT^2} \quad (S24)$$

In these conditions, the Soret coefficient of an ion, S_T^{ψ} , in a mixture of solvents ψ can be derived from the Soret coefficient of this ion, S_T^{φ} , in another mixture of solvents φ and the heat of transfer of the ion under consideration from the mixture φ to the mixture ψ .

S5.2.2 \hat{S}_{H^+} and $\hat{S}_{ClO_4^-}$ in water-DMSO mixtures

We apply Eq. S24 to water-DMSO mixtures. The obtained values of \hat{S}_{H^+} and $\hat{S}_{ClO_4^-}$ are presented in Fig. S4a (open symbols - model (II)). They are deduced from their respective values in water at 298 K (obtained in the dilute limit in Ref.[11,15]) and the enthalpy of transfer $\Delta_t H^{\circ}$, from water to water-DMSO mixtures, of H^+ and ClO_4^- ions, tabulated in Refs. [13,14]. Fig. S4a shows also, as dashed lines, the interpolations used here (in particular for H^+ for which we did not find any value of $\Delta_t H_{ion}^{\circ}(x_W)$ for $0 < x_W < 0.7$).

S5.2.3 \hat{S}_{NP} in water-DMSO mixtures deduced from the two models of \hat{S}_{H^+} and $\hat{S}_{ClO_4^-}$

The x_W -dependence of the NP's Eastman entropy of transfer \hat{S}_{NP} is then deduced by the two methods from the measurements of S_T . The results, obtained from Eqs. 7 and 8 of the main paper and values of \hat{S}_{H^+}/kT and $\hat{S}_{ClO_4^-}/kT$ from Fig. S4a, are presented in Fig. S4b. \hat{S}_{NP}/kT decreases from $\sim +1 K^{-1}$ at $x_W = 0$ down to $\sim -0.5 K^{-1}$ at $x_W = 1$, with a "plateau" close to 0 for $0.3 < x_W < 0.85$.

Fig. S4b shows globally a rather weak influence of the model used for the evaluation of \hat{S}_{\pm} , on the obtained value of $\hat{S}_{NP}(x_W)$. It is because the main contribution from ions in the thermoelectric term of S_T comes from the difference $\hat{S}_{+} - \hat{S}_{-}$, which has rather close values in models (I) and (II) (except for $0.4 < x_W < 0.8$, where it becomes more influent).

S6 NP's dispersions in DMSO - Comparison between samples of different ages

Dispersions of magnetic particles in DMSO with ClO_4^- counterions at $[H^+] = 10^{-2}$ mole/L, kept in a closed bottle, remains stable during years. Fig. S5 illustrates this

Table S2. Characteristics of the three NP's dispersions in DMSO (with ClO_4^- counterions at $[\text{H}^+] = 10^{-2}$ mole/L) probed with DLS in Fig. S5; Magnetic characteristics deduced from magnetization measurements : d_0 median diameter, σ polydispersity index, $\sqrt[3]{\langle d^3 \rangle}$ volume-averaged diameter; age of the sample since chemical preparation, expressed in years

Sample name	d_0 (nm)	σ	$\sqrt[3]{\langle d^3 \rangle}$ (nm)	age (years)
A	8.0	0.45	10.8	15
B	9.0	0.3	9.7	0
C	7.0	0.35	8.4	0

point by comparing field autocorrelation functions G_1 obtained as in [16] by Diffusion Light Scattering (DLS)² as a function of the autocorrelation time t , for the three samples of Table S2. Two samples (samples B and C) are freshly prepared ones, while sample A is 15 years old.

Fig. S5-top compares the DLS autocorrelation functions $G_1(t)$ for sample A at different concentrations. When the concentration increases the relaxation time at half-maximum $\tau_{1/2}$ which scales as $D_m^{-1} \propto \chi$ becomes shorter, expressing that the NPs are in repulsive interaction ($A_2 > 0$ and χ decreasing when Φ increases) and not agglomerated, after 15 years.

Fig. S5-bottom compares the DLS autocorrelation functions $G_1(t)$ of the three samples A, B and C, based on different NPs, at very dilute volume fractions (at which $\chi = 1$). The three DLS relaxations are close to each other with no sign of aggregation, which would lead to a tail at long autocorrelation times. The hierarchy of the three relaxation times at half-maximum $\tau_{1/2}$ is comparable to the hierarchy of the NP's volume-averaged diameters of the different samples (see Table S2).

References

1. G. Demouchy, A. Mezulis, A. Bée, D. Talbot, J.-C. Bacri, and A. Bourdon, Diffusion and thermodiffusion studies in ferrofluids with a new two-dimensional forced Rayleigh-scattering technique, *J. Phys. D: Appl. Phys.* **37**, 1417 (2004).
2. W. Klein, C. Tipnis, and E. Hiedemann, Experimental study of fraunhofer lighth diffraction by ultrasonic beams of moderately high frequency at oblique incidence, *J. Acoust. Soc. Amer.* **38**, 229 (1965).
3. W. Klein, Theoretical efficiency of bragg devices, *Proc. I.E.E.E.* **54**, 803 (1966).
4. H. Kogelnik, Couple wave theory for thick hologram gratings, *Bell Syst. Tech. J.* **48**, 2909 (1969).
5. J. Lenglet, A. Bourdon, J.-C. Bacri, and G. Demouchy, Thermodiffusion in magnetic colloids evidenced and studied by forced rayleigh scattering experiments, *Phys. Rev. E* **65**, 031408 pp. 1 (2002).

² with a Vasco DLS particle analyzer from Cordouan technologies adapted for dark and absorbing media which operates at a scattering vector $2.6 \cdot 10^{-3} \text{Å}^{-1}$ in DMSO.

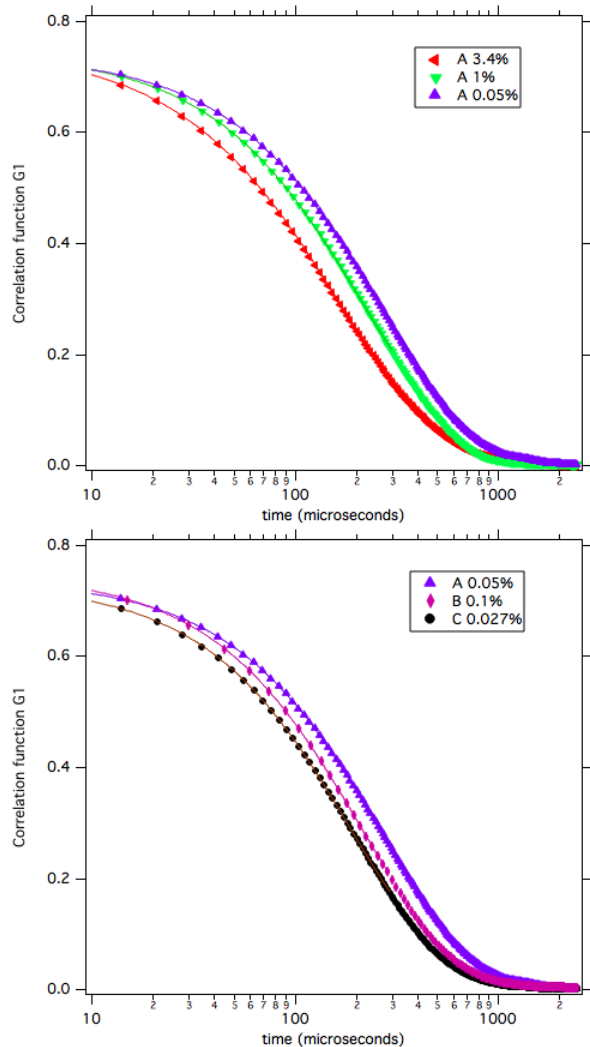


Figure S5. (Top) DLS autocorrelation functions $G_1(t)$, as a function of the autocorrelation time t , for a 15-years-old sample in DMSO (Sample A from Table S2) at three different volume fractions Φ , showing that the interparticle interaction is still repulsive; (Bottom) DLS autocorrelation functions $G_1(t)$ of three different samples in DMSO at very low volume fractions with negligible interparticle interaction ($\chi \sim 1$) and different distributions of NP's diameter (see Table S2). The three autocorrelation functions are close to each other, that of Sample A being the slowest, as its volume-averaged diameter is the largest and that of Sample C being the quickest, as its volume-averaged diameter is the smallest.

6. R. Cabreira-Gomes, A. F. da Silva, M. Kouyaté, G. Demouchy, G. Méridet, R. Aquino, E. Dubois, S. Nakamae, M. Roger, J. Depeyrot, and R. Perzynski, Thermodiffusion of repulsive charged nanoparticles - the interplay between single-particle and thermoelectric contributions, *Phys. Chem. Chem. Phys.* **20**, 16402 (2018).
7. D. A. G. Bruggeman, Berechnung verschiedener physikalischer Konstanten von heterogenen Substanzen. I. Dielektrizitätskonstanten und Leitfähigkeiten der Mischkörper aus isotropen Substanzen, *Ann. Phys., ser. 5* **24**, 636 (1935).

8. J. Cowie and P. Toporowski, Association in the binary liquid system dimethyl sulphoxide - water, *Can. J. Chem.* **39**, 2240 (1961).
9. J.-C. Zhou, Y.-Y. Che, K.-J. Wu, J. Shen, and C.H.He, Thermal conductivity of DMSO + C₂H₅OH, DMSO + H₂O, and DMSO + C₂H₅OH + H₂O mixtures at $T = (278.15 \text{ to } 338.15 \text{ K})$, *J. Chem. Eng. Data* **58**, 663 (2013).
10. C. Nieto-Draghi, J. B. Avalos, and B. Rousseau, Transport properties of dimethyl sulfoxide aqueous solutions, *J. Chem. Phys.* **119**, 4782 (2003).
11. J. N. Agar, C. Y. Mou, and J. L. Lin, Single ion heat of transport in electrolyte solutions, *J. Phys. Chem.* **93**, 2079 (1989).
12. M. Born, Volumen und hydrationswärme der ionen, *Zeitschrift für Physik* **1**, 45 (1920).
13. G. Hefter, Y. Marcus, and W. Waghome, Enthalpies and entropies of transfer of electrolytes and ions from water to mixed aqueous organic solvents, *Chem. Rev.* **102**, 2773 (2002).
14. Y. Marcus, *Ion properties* (Marcel Dekker, New York 1997).
15. N. Takeyama and K. Nakashima, Proportionality of intrinsic heat of transport to standard entropy of hydration for aqueous ions, *J. Solution Chem.* **17**, 305 (1988).
16. C. L. Filomeno, M. Kouyaté, V. Peyre, G. Demouchy, A. F. C. Campos, R. Perzynski, F. A. Tourinho, and E. Dubois, Tuning the solid/liquid interface in ionic colloidal dispersions: Influence on their structure and thermodynamic properties, *J. Phys. Chem. C* **121**, 5539 (2017).

6.3 | Conclusion

The article shows that the nature of the solvent, under otherwise similar conditions, influences the thermophoretic response. While the nanoparticles in pure DMSO move towards the cold side, the thermophoretic behaviour of the nanoparticles becomes thermophilic with increasing water content, the two extremes being shown in Figure 6.1 for several nanoparticle volume fractions ϕ_{NP} . The Soret coefficient changes sign at a mole fraction of water of roughly 25%. This influence of the solvent on the thermophoretic response is hence analysed in several ionic liquids in order to analyse if a change is also observed.

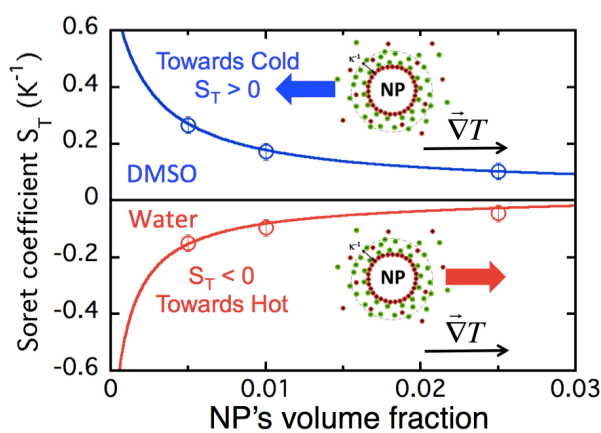


Figure 6.1 – Scheme for electrostatically stabilised nanoparticle dispersions with ClO_4^- counterions behaving thermophilic in water and thermophobic in DMSO. Taken from [5]

Thermodiffusion in an ionic liquid and effect of magnetic fields

Contents

7.1 Introduction	100
7.2 Article: “Thermodiffusion anisotropy under magnetic field in ionic liquid-based ferrofluids”	101
7.3 Conclusion	113

7.1 | Introduction

After the previous chapter showed a proof of concept of the functioning of the FRS setup at room temperature, this chapter uses the developments of the thermodiffusion measurement setup during this project (hermetically sealed FRS cells, temperature control, varying applied magnetic fields) to analyse the thermodiffusive properties of ionic liquid-based nanoparticle dispersions. It is shown here for one of the most promising sample, a positive maghemite nanoparticles with SBMIM[±] TFSI⁻ counterions in EMIM TFSI (studied in chapter 4 regarding its colloidal and thermal stabilities). The thermodiffusion is analysed in a broad range of temperatures (20 to 200°C) and at an elevated nanoparticle concentration $\phi_{NP} = 5.95$ vol% in order to analyse the effect of varying magnetic fields (up to 100 kA/m), applied perpendicular and parallel to the temperature gradient.

The contribution of this PhD work to the article was the synthesis and characterisation of the sample by SAXS, SANS and DLS measurements, contribution to the theoretical developments, and the preparation of the manuscript. It will be soon submitted to RSC Soft Matter.

7.2 | Article: “Thermodiffusion anisotropy under magnetic field in ionic liquid-based ferrofluids”

Cite this: DOI: 00.0000/xxxxxxxxxx

Thermodiffusion anisotropy under magnetic field in ionic liquid-based ferrofluids

T. Fiuza,^{a,b} M. Sarkar,^a J.C. Riedl,^a A. Cēbers,^c F. Cousin,^d G. Demouchy,^{a,e} J. Depeyrot,^b E. Dubois,^a F. Gélébart,^a G. Mériquet,^a R. Perzynski,^{a,*} and V. Peyre^a

Received Date

Accepted Date

DOI: 00.0000/xxxxxxxxxx

Ferrofluids based on maghemite nanoparticles, typically 10 nm in diameter, are dispersed in an ionic liquid (1-ethyl 3-methylimidazolium bistriflimide - EMIM-TFSI). The average interparticle interaction is found repulsive by small angle scattering of X-rays and of neutrons, with a second virial coefficient $A_2 = 7.3$. A moderately concentrated sample at $\Phi = 5.95$ vol% is probed by forced Rayleigh scattering under an applied magnetic field (up to $H = 100$ kA m⁻¹) from room temperature up to $T = 460$ K. The in-field anisotropy of the mass diffusion coefficient D_m and that of the (always positive) Soret coefficient S_T are well described by the presented model in the whole range of H and T . The main origin of the anisotropy is the spatial inhomogeneities of concentration in the ferrofluid along the direction of applied field. Since this effect is related to the magnetic dipolar interparticle interaction, the anisotropy of thermodiffusion progressively vanishes when temperature increases and thermal motion rises.

1 Introduction

Ferrofluids^{1–4} based on Ionic Liquids (FF-ILs) are new colloidal materials, developed for improving thermoelectric low-grade energy harvesting^{5–9}. In classical ionic ferrofluids based on polar solvents, it has been recently shown that the application of a magnetic field is able to improve the thermoelectric properties of the material¹⁰. The use here of an Ionic Liquid (IL) as solvent brings new properties, among which the access to a wider range of temperatures T ¹¹. In ionic liquids, which are molten salts at low T 's only composed of anions and cations, the colloidal dispersions of nanoparticles (NPs) has been shown to be possible despite the totally different internal structure of ILs from that of molecular solvents. NPs either coated by polymers,^{12–17} or coated with shorter surfactant chains, or even bare charged NPs^{17–23} have been dispersed in ILs. Among the extreme variety of room temperature ionic liquids^{24–26}, 1-Ethyl-3-methylimidazolium bistriflimide (EMIM-TFSI), which is a widely used IL in applications^{27–29}, can be considered as an important model system, since it is not too viscous at room temperature and is stable in a large range of T ^{11,26,30,31}. Hydroxyl-coated maghemite NPs, synthesized in wa-

ter (diameter ~ 10 nm) are modified in order to adapt the NP/solvent interface, i.e. the charge and the nature of the counterions, both shown to be crucial^{17,20,21}. After a liquid-liquid transfer from water to the IL, stable dispersions are obtained, that can be concentrated up to ~ 12 vol% in EMIM-TFSI^{17,32}, these dispersions remaining stable (from both a chemical and a colloidal point of view) at least up to 473 K³².

Our aim is here to probe the under-field anisotropy of the NP's thermodiffusive properties at various temperatures, in terms of Soret coefficient S_T and diffusion coefficient D_m ³³. A Forced Rayleigh scattering experiment^{34–41} is undertaken, in the presence of an applied magnetic field and in a wide range of temperatures T (from room temperature up to ~ 460 K), using a moderately concentrated dispersion ($\Phi = 5.95$ vol%) in order to render easier the under-field anisotropy measurement. As in³³ for aqueous ferrofluids at room temperature, the results are here analysed according to the model developed in⁴². To perform these adjustments, it is of paramount importance to probe independently the interparticle interaction in the colloidal dispersion. Small Angle Neutron Scattering (SANS) and Small Angle X-ray Scattering (SAXS) experiments are thus also undertaken to determine the osmotic compressibility χ of the NP's system and the corresponding second virial coefficient in the colloidal dispersion^{23,43}.

In the next section we present the colloidal system, briefly recalling how it is prepared and the proposed origin of its stability, together with the probing by SAXS and SANS measurements of the interparticle repulsion. The third section is devoted to the forced Rayleigh scattering experiments and the obtained results.

^a Sorbonne Université, CNRS, Lab. PHENIX, 4 Place Jussieu, F-75005 Paris, France.

^b Grupo de Fluidos Complexos, Inst. de Física, Univ. de Brasília, Brasília (DF), Brazil.

^c MMML Lab, Faculty of Physics and Mathematics, University of Latvia, Zellu-8, LV-1002 Riga, Latvia.

^d Lab. Léon Brillouin - UMR 12 CNRS-CEA CEA-Saclay, 91191 Gif-sur-Yvette, France.

^e Dpt de physique, Univ. de Cergy Pontoise, 33 Bd du Port, 95011 Cergy-Pontoise, France.

* corresponding author, regine.perzynskit@sorbonne-universite.fr

The fourth section recalls the theoretical model used here to interpret the measurements. The last section presents a global discussion of the whole study.

2 Magnetic Fluid samples

2.1 Synthesis

The magnetic nanoparticles used here are chemically synthesized using a well-known aqueous coprecipitation method^{44,45}. From the analysis of magnetic measurements (Vibrating Sample Magnetometer), their size distribution can be described by a log-normal distribution of median diameter 8.9 nm and a polydispersity index 0.23, leading to a volume-averaged diameter² $d_{NP} = 9.6$ nm. The details of the preparation of their dispersions in EMIM-TFSI are given extensively in¹⁷. Here is a short summary of the process. Firstly, the interface of the NPs is modified in water: a structural charge $Z \sim +400 \pm 100$ is introduced. The species compensating their charge are deprotonated 1-(4-sulfobutyl)-3-methylimidazolium bistriflimide (SMIM[±]-TFSI⁻), which has been shown to be close to the interface¹⁷. Secondly, the ionic liquid is added and the water removed by freeze-drying, leading to NPs in pure EMIM-TFSI. All the process is performed with a volume fraction of NPs around 1%.

EMIM-TFSI is a room-temperature ionic liquid, here supplied by Solvionic, with a viscosity ranging from 4×10^{-2} Pa s at 294 K down to 3×10^{-3} Pa s at 460 K (following²⁶). It presents a low vapor pressure, a low flammability, a high ionic conductivity and a wide electro-chemical window^{11,26,31}. It is also chemically stable up to high temperature (long-term ~ 500 K and up to ~ 700 K for shorter times¹¹), making it a good candidate for thermoelectrical applications⁴⁶. The colloidal dispersions of the used maghemite NPs have been reported as being stable at room temperature in¹⁷ with a repulsive interparticle interaction.

A series of samples at various volume fractions Φ have been produced by ultracentrifugation of the initial dispersion at $\Phi \sim 1\%$, following the method described in³².

2.2 Colloidal stability - Interparticle interaction

Small Angle X-ray Scattering (SAXS) experiments were carried out with the XEUSS 2.0 (Xenocs) of LLB-Saclay at room temperature on dispersions at several volume fractions Φ 's between 0.2 % and 12 %. Complementary Small Angle Neutron Scattering (SANS) experiments were performed at PAXY spectrometer in Orphée - LLB - Saclay at various T 's ranging between 293 K and 473 K. All these experiments were performed without applied magnetic field. The scattered intensity $I(q)$, analyzed as in^{47,48}, shows that the interparticle interaction is repulsive indeed. The determination of the intensity at low scattering vector ($q \rightarrow 0$) leads to the osmotic compressibility χ of the NP's system, which is related to the osmotic pressure Π of the NP's system by the following relation:

$$\chi = \frac{kT}{\left(\frac{\partial \Pi_{v_{NP}}}{\partial \Phi}\right)_T}, \quad (1)$$

where v_{NP} is the NP's volume. The experimental results at room temperature and zero magnetic field are shown in Fig. 1. Moreover it has been observed that χ does not present any significant temperature dependence in the experimental T -range. As shown by Fig. 1, the Φ -dependence of χ can be described by the Carnahan-Starling formalism^{43,49} with effective hard spheres of volume fraction $\Phi_{eff} = 1.82 \Phi$ and a second virial coefficient $A_2 = 7.3$.

The colloidal stability of the samples under-field up to $H = 716$ kA m⁻¹ ($= 9000$ Oe) has been checked optically, looking at the scattering pattern of a non-absorbing laser beam, as described in^{17,50}.

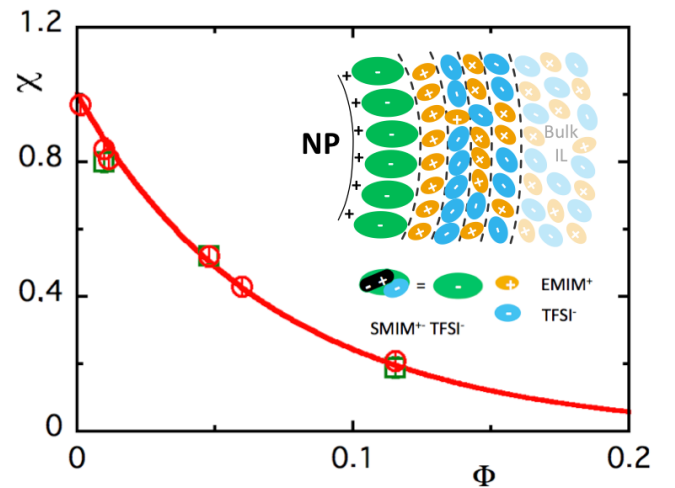


Fig. 1 Main figure: Osmotic compressibility χ of the NPs in the colloidal dispersions as a function of their volume fraction Φ - Open symbols: Experimental determinations at room temperature by SAXS (open circles) and SANS (open squares) - Full line: Carnahan-Starling adjustment with effective hard spheres^{43,49} of volume fraction $\Phi_{eff} = 1.82 \Phi$ leading to $A_2 = 7.3$; Inset: Sketch of the ionic layering around the NPs responsible for the colloidal stability of the dispersion. The NP's surface, which is positive due to the hydroxyls groups, is compensated by a first layer of condensed SMIM[±]-TFSI⁻ counterions, layer which initiates the long range IL-layering.

The colloidal stability of these samples, both in zero field and under-field, proves that a strong interparticle repulsion exists, which dominates the two kinds of interparticle attractions that are present here, van der Waals attraction (which is isotropic and is present in any colloid) and magnetic dipolar interaction (which is anisotropic and attractive on average, which is present in magnetic colloids such as those studied in the present work).

It has been proven both experimentally⁵¹⁻⁵³ and by numerical simulations⁵⁴⁻⁵⁸ that along a flat and charged interface, Ionic Liquids can organize themselves as layers of ions, of alternating sign. Along a curved interface such as that of the present charged NPs^{22,59}, long-range charge-density oscillations can be also formed, for given geometrical and charged conditions of the IL anions and cations^{17,57,60}. If the number of organized layers is large enough, they are able to overcome attractive component of the interparticle interaction (usually van der Waals attraction) and stable colloidal dispersions can be ob-

tained^{17,20,22,60}. The colloidal stability of the present NPs in EMIM-TFSA is thus proposed to come here from the "effective" interparticle repulsion, due to the regular layering of ions, of alternate sign, around the NPs (see the sketch in the inset of Fig. 1), which dominates both van der Waals and magnetic dipolar interparticle attractions. Here the resultant screening κ^{-1} of the repulsive (on average) interparticle interaction can be extracted from the Carnahan-Starling adjustment of $\chi(\Phi)$, writing²³ Φ_{eff}/Φ as $[(d_{\text{NP}} + 2\kappa^{-1})/d_{\text{NP}}]^3$. It leads to $\kappa^{-1} \sim 1.1$ nm. The structure of the liquid being modified on few κ^{-1} , typically up to 5 κ^{-1} , it corresponds to 6-7 layers of anions and cations from the IL²⁸.

3 Forced Rayleigh scattering experiment

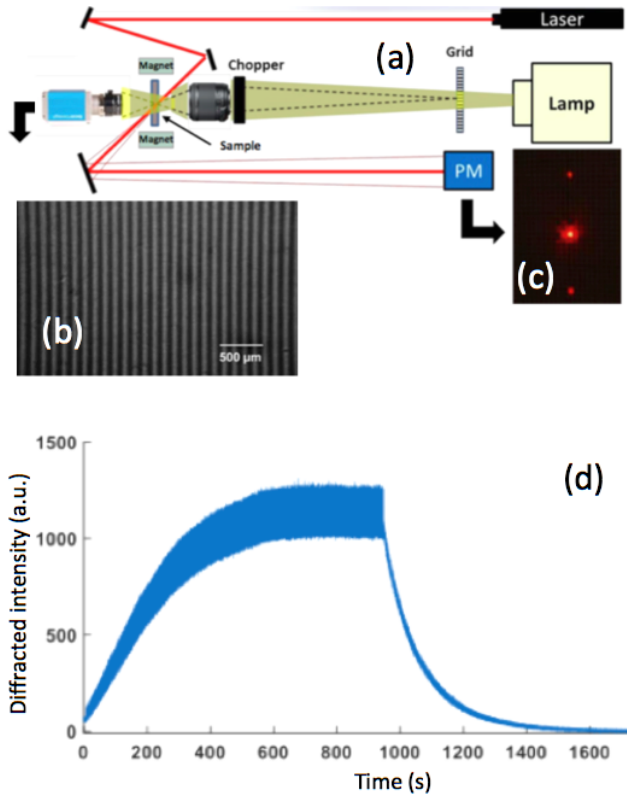


Fig. 2 Forced Rayleigh scattering device: (a) Experimental set-up, seen from above; The Hg-lamp illuminates a grid, the image of which is made, periodically at a few Hz, in the thermalized sample, eventually submitted to an horizontal magnetic field \vec{H} ; Both a thermal and a concentration arrays are induced in the sample (for more details see text); Their temporal evolution is observed by the diffraction of a He-Ne laser beam; (b) Direct observation of the image of the grid in the sample; (c) Diffracted pattern of the He-Ne laser beam by the temperature and concentration arrays; (d) Recorded intensity of the first order diffraction at $\Phi = 5.95\%$ as a function of time; When the heating beam is cut, the recorded intensity relaxes towards zero.

3.1 Experimental device

The setup we use for these forced Rayleigh scattering* (FRS) measurements (see Fig. 2) has been initially presented in ref.³⁸. A high power lamp (Oriel 6285 - 500 W - Hg Arc Lamp) illuminates a grid, the image of which is made in the liquid sample, put in a thin and thermalized optical cell (of thickness $e = 25$ μm). Because of the strong optical absorption of the maghemite NPs a thermal grating of time-dependent amplitude $\Delta T(t)$ and of spatial period Λ ranging between 88 and 145 μm , is created in the NP dispersion. A concentration grating of amplitude $\Delta\Phi(t)$ with the same spatial period Λ is then induced thanks to the Ludwig-Soret effect^{61,62}. Both the thermal and the concentration gratings are here probed with the first order diffraction of a He-Ne laser beam, which is poorly absorbed by these dispersions. The Soret coefficient S_T links the applied temperature gradient $\vec{\nabla}T$ and the induced volume-fraction gradient $\vec{\nabla}\Phi$, in the following way:

$$\vec{\nabla}\Phi = -\Phi S_T \vec{\nabla}T. \quad (2)$$

S_T is obtained here by means of a modulation at 4 Hz of the Hg lamp intensity (the thermal response of the system being by orders of magnitude faster than the concentration one) and thanks to the knowledge of $\partial n/\partial T$ and $\partial n/\partial\Phi$ † (for details see⁴¹ and its E.S.I.). If $\Delta\Phi_{\text{St}}$ is the spatial modulation of volume fraction in stationary conditions, we obtain:

$$S_T = -\frac{\Delta\Phi_{\text{St}}}{\Phi\langle\Delta T\rangle}, \quad (3)$$

$\Delta\Phi_{\text{St}}$ being negative with the convention of⁴¹ and $\langle\Delta T\rangle$ being the time-averaged spatial modulation of temperature. As an example, at $\Phi = 5.95\%$, we obtain here $|\Delta\Phi_{\text{St}}|/\Phi \leq 10^{-2}$ and $\langle\Delta T\rangle \leq 0.1$ K whatever the amplitude and the direction of the applied field \vec{H} and whatever T in the experimental range.

Switching off the Hg lamp makes the concentration grating relax as well as the modulation of the optical index related to $\Delta\Phi(t)$ and thus also the intensity of the diffracted beam (see Fig. 2(d)), allowing a determination of the mass diffusion coefficient D_m of the NPs.

$$\Delta\Phi(t) = \Delta\Phi_{\text{St}} e^{-q^2 D_m t} \quad (4)$$

with $q = 2\pi/\Lambda$.

The sample environment is thermo-regulated (here temperature T may vary from room temperature up to 460 K). It is also possible to apply an horizontal magnetic field \vec{H} , homogeneous at the scale of the sample, thanks to movable magnetic polar pieces (here H may vary from 0 up to 100 kA m⁻¹), making possible to

* Forced Rayleigh scattering implies forced inhomogeneities with respect to the spontaneous fluctuations observed in a classical Rayleigh scattering experiment³⁴.

† The derivative $\partial n/\partial T$ is taken equal⁶⁰ -2.82×10^{-4} K⁻¹ and independent of T in our range of T from the optical index measurement of⁶³ (even if only measured up to 353 K) and $\partial n/\partial\Phi = 0.97$ as calculated from⁶⁴.

determine both $S_T(H, T)$ and $D_m(H, T)$ in a large range of temperature and magnetic field. The under-field anisotropy of $S_T(H, T)$ and $D_m(H, T)$ is probed by orienting the temperature gradient (and thus also the concentration gradient) either horizontally or vertically, optical cell and grating being both in the vertical plane. All problems of gravity such as convection and instabilities do not occur here because of the small values of $\Delta\Phi$ and of the sample thickness. In-field measurements are performed at ratios sample thickness e over spatial period Λ , such that $0.17 < e/\Lambda < 0.28$, thus in the 2D-array conditions. The experiments are also performed at magnetic fields \vec{H} below the threshold of 2D magnetoconvection^{66,67}.

It is checked that the measured S_T is independent of Λ and of the power of the Hg lamp (the experimental range is limited to the power linear regime⁶⁵).

3.2 Experimental results in zero field

Fig. 3 presents the values of D_m (main figure) and S_T (inset) obtained experimentally in zero magnetic field at various temperatures T and volume fractions Φ .

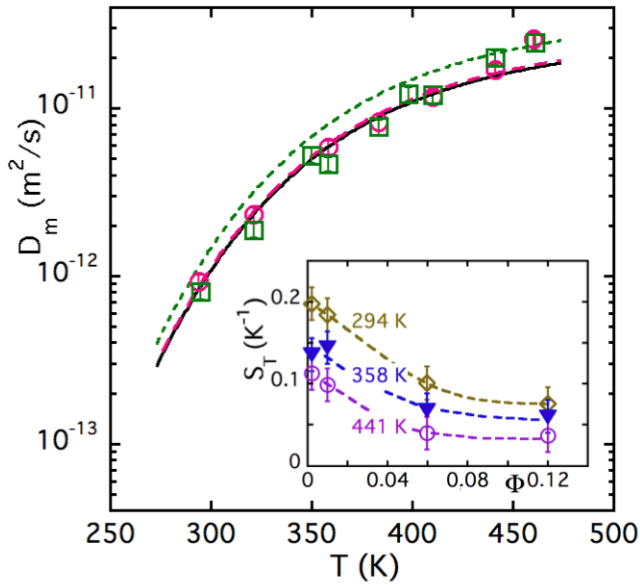


Fig. 3 *Main figure*: Diffusion coefficient D_m at various Φ as a function of T . The symbols are experimental determinations at 5.95% (open squares) and $\Phi = 1\%$ (open circles). The full line corresponds to the ideal case $D_m(\Phi \rightarrow 0, T)$ given by Eq. 7. The green dashed line corresponds to the general case of Eq. 5 for $\Phi = 5.95\%$ and the pink long dashed for 1%, taking into account the interparticle correlations with $\chi = 0.86$ at $\Phi = 5.95\%$ and 0.43 at $\Phi = 1\%$, $\zeta(\Phi, T)$ being given by Eq. 8 with the hard sphere volume fraction equal to $\Phi_{\text{eff}} = 1.82 \Phi$. *Inset*: Soret coefficient S_T at various T 's as a function of Φ . Dashed lines are guide for the eye.

3.2.1 Diffusion coefficient in zero field

In zero applied magnetic field, the mass diffusion coefficient D_m is isotropic and equals:

$$D_m(\Phi, T) = \frac{1}{\zeta} \frac{\partial \Pi_{V, \text{NP}}}{\partial \Phi} = \frac{1}{\zeta(\Phi, T)} \frac{kT}{\chi(\Phi)} \quad (5)$$

where the compressibility $\chi(\Phi)$ is given by Eq. 1 and Fig. 1; χ has been shown experimentally to be T -independent. Oppositely the friction term ζ is Φ and T -dependent.

In the absence of interparticle correlations ($\Phi \rightarrow 0$), $\chi = 1$ and the friction $\zeta(T)$ writes as:

$$\zeta(\Phi \rightarrow 0, T) = \zeta_0(T) = 3\pi\eta_0(T)d_H \quad (6)$$

where $\eta_0(T)$ is the solvent viscosity and d_H the NP's hydrodynamic diameter. The mass diffusion coefficient $D_m(\Phi \rightarrow 0, T)$ can then be written as :

$$D_m(\Phi \rightarrow 0, T) = \frac{kT}{\zeta_0(T)} = \frac{kT}{3\pi\eta_0(T)d_H} \quad (7)$$

In the presence of interparticle correlations $\chi \neq 1$ and $\zeta(T) \neq \zeta_0(T)$, these correlations modify D_m . An expression for the friction experienced by hard spheres in hydrodynamic interaction at a volume fraction Φ has been proposed in⁶⁸ for $\Phi \ll 1$:

$$\zeta(\Phi, T) = \zeta_0(T)(1 + k_F\Phi) \quad \text{with } k_F = 6.55 \quad (8)$$

The evolution of $D_m(\Phi, T)$ as a function of T is plotted in main Fig. 3. The full line is the computation of $D_m(\Phi \rightarrow 0, T)$ as a function of T taking $\eta_0(T)$ as given by²⁶ and $d_H = 13.6$ nm. As shown by this figure and Eq. 7, the strong temperature dependence of $D_m(\Phi \rightarrow 0, T)$ can be ascribed to the large decrease of the solvent viscosity $\eta_0(T)$ as T increases.

However, note that here, the NPs present strong interparticle repulsion (as shown by Fig. 1, $\chi = 0.43$ at $\Phi = 5.95\%$). These interparticle correlations cannot be forgotten in the expression of $D_m(\Phi, T)$. Fig. 3 thus also presents $D_m(\Phi, T)$ as obtained from the general expression of Eq. 5 for $\Phi = 5.95\%$ (dashed line) and $\Phi = 1\%$ (long dashed line), using SAXS and SANS experimental χ values and Eq. 8 with $\Phi_{\text{eff}} (= 1.82 \Phi)$ as hard sphere volume fraction. It matches correctly the experimental results at $\Phi = 1\%$, which are close to the ideal case $D_m(\Phi \rightarrow 0, T)$ due to a compensation between $\chi(\Phi = 1\%)$ and $\zeta(T, \Phi = 1\%)/\zeta_0(T)$ – except at $T \geq 420$ K, but it should be necessary to check that the viscosity values deduced from the calculations of Paduszynski and Domanska²⁶ are completely reliable in this range of T . On the contrary, a systematic discrepancy (by a factor ranging from 1.4 at room temperature down to 1.2 at 420 K) is found at $\Phi = 5.95\%$, meaning that the friction ζ is 40% to 20% larger than what is given by the development of Eq. 8 at this volume fraction in this temperature-range.

3.2.2 Soret coefficient in zero field

Inset of Fig. 3 shows the evolution of the Soret coefficient S_T as a function of the volume fraction Φ at three different temperatures. Let us note first that whatever Φ and T , the measured S_T is

here always positive, contrary to what is sometimes observed for ferrofluids in water^{33,37} and similarly to what is observed with ferrofluids in another very different ionic liquid (ethylammonium nitrate, EAN)²³. EAN is indeed hydrophilic and totally miscible with water, whereas EMIM-TFSI is hydrophobic[‡].

Moreover the Soret coefficient S_T is a decreasing function of Φ , which is expected as it has been shown in⁴³ that

$$|S_T| \propto \chi, \quad (9)$$

which is here a decreasing function of Φ – see Fig. 1. S_T also decreases as a function of T , as observed in EAN²³. For a deeper analysis of the behaviour of $S_T(\Phi, T)$ (as in²³ for example), a larger number of samples at various volume fractions Φ should be investigated. It will be done in a forthcoming paper, we focus hereafter on the under-field behavior of only one sample ($\Phi = 5.95\%$) in the whole accessible T -range of the experiment.

3.3 Under-field experimental results

An anisotropy of both the diffusion coefficient D_m (see Fig. 4) and of the Soret coefficient S_T (see Fig. 5) is observed whatever T ranging between 295 K and 460 K, if an external magnetic field \vec{H} is applied to the sample during the FRS measurement ($0 \leq H \leq 100 \text{ kA m}^{-1}$). D_m and S_T both depend on the amplitude of the applied field and on its direction, as it has been previously observed for D_m and/or S_T in non-ionic magnetic fluids^{69–71} and in aqueous ferrofluids^{33,35,72,73} at room temperature.

We recall that we limit ourselves here to gradients of temperature ($\vec{\nabla}T$) and of concentration ($\vec{\nabla}\Phi$) either horizontal (and thus parallel (\parallel) to the applied field – this direction is here denoted \vec{H}_{\parallel}) or vertical (and thus perpendicular (\perp) to the field – this direction is here denoted \vec{H}_{\perp}).

Fig. 4 and 5 show typical in-field anisotropies of D_m and of S_T observed at $\Phi = 5.95\%$ and $0 \leq H \leq 100 \text{ kA m}^{-1}$, for both \vec{H}_{\parallel} and \vec{H}_{\perp} . As previously shown in main Fig. 3, the zero field value of D_m increases with T . Under-field D_m is anisotropic with $D_m(H_{\perp}) < D_m(H=0) < D_m(H_{\parallel})$ and this anisotropy decreases with T . In an opposite manner (as also previously shown in inset of Fig. 3), the zero field value of S_T decreases with T with an under-field anisotropy of S_T , with $S_T(H_{\parallel}) < S_T(H=0) < S_T(H_{\perp})$. Let us note that, in the experimental range, whatever the amplitude of \vec{H} and whatever its direction with respect to $\vec{\nabla}\Phi$ and $\vec{\nabla}T$, $S_T(H)$ remains always positive, as $S_T(H=0)$.

4 Under-field model and adjustment of the experimental results

4.1 Under-field model of diffusion coefficient

At room temperature, the in-field anisotropy of D_m in aqueous samples, measured in the absence of temperature gradient, has been extensively described with a mean-field framework in^{35,72,73}. In this framework, the effective Langevin parameter ξ_e in the ferrofluid, based on NPs of magnetization m_S with a volume

v_{NP} and a magnetic moment $\mu_{\text{NP}} = m_S v_{\text{NP}}$, is defined as :

$$\xi_e = \xi(H, T) + \lambda \gamma L(\xi_e) \quad \text{with} \quad \xi(H, T) = \frac{\mu_0 \mu_{\text{NP}} H}{kT} \quad (10)$$

$\xi(H, T)$ is the Langevin parameter, λ the mean-field parameter, γ the magnetic dipolar interaction parameter

$$\gamma(\Phi, T) = \frac{\mu_0 m_S \mu_{\text{NP}} \Phi}{kT} \quad (11)$$

and $L(\xi) = \cotan(\xi) - 1/\xi$ the Langevin function. Here we use $\lambda = 0.22$ as in^{35,72,74}, value confirmed by the numerical simulations in water of ref.⁷³ §.

The in-field diffusion coefficient D_m then writes with $\vec{\nabla}T \parallel \vec{\nabla}\Phi$, either perpendicular to the applied field \vec{H} (\vec{H}_{\perp}) or parallel (\vec{H}_{\parallel}):

$$D_m^{\vec{H}_{\perp}} = \frac{kT}{\zeta} \left(\frac{1}{\chi} - \alpha_{\lambda} \right) = D_m^* [1 - \chi \alpha_{\lambda}] \quad (12)$$

and

$$D_m^{\vec{H}_{\parallel}} = \frac{kT}{\zeta} \left(\frac{1}{\chi} + \beta_{\lambda} - \alpha_{\lambda} \right) = D_m^* [1 + \chi (\beta_{\lambda} - \alpha_{\lambda})] \quad (13)$$

where $D_m^*(\Phi, T) = D_m(H \rightarrow 0, \Phi, T)$, the parameters α_{λ} and β_{λ} being given by :

$$\alpha_{\lambda} = \frac{\lambda \gamma L^2(\xi_e)}{1 - \lambda \gamma L'(\xi_e)} \quad (14)$$

and

$$\beta_{\lambda} = \frac{\gamma L^2(\xi_e)}{[1 - \lambda \gamma L'(\xi_e)][1 + (1 - \lambda) \gamma L'(\xi_e)]}. \quad (15)$$

α_{λ} is associated with the mean-field-averaged dipolar interaction, which is here isotropic and attractive. The term β_{λ} is anisotropic and due to the discontinuity of \vec{H}_{\parallel} in Maxwell equations along the spatial inhomogeneities[¶] of concentration^{3,35,42,72}. β_{λ} is maximum in the field direction parallel to $\vec{\nabla}\Phi$ and null perpendicularly. The higher is the volume fraction Φ , the larger are magnetic dipolar parameter γ and coefficient β_{λ} , and thus the larger is the anisotropy of D_m .

The adjustments of $D_m^{\vec{H}_{\perp}}$ and $D_m^{\vec{H}_{\parallel}}$ at room temperature are both presented in Fig. 4. They are made, assuming as in refs.^{35,72,74} that χ and ζ keep under-field their zero field value. Using $\chi = 0.43$ and $m_S = 3.2 \times 10^5 \text{ A m}^{-1}$, and letting in the fit d_{NP} and D_m^* as free parameters. D_m^* is found within the experimental error bar of $D_m(H=0)$ and we obtain $d_{\text{NP}} = 13.2 \text{ nm}$, leading to $\gamma = 2.3$ at room temperature. In the monodisperse model used here for the adjustment, the polydispersity in NP's diameter is not taken in account and the value of d_{NP} obtained is 30% larger than the volume average diameter obtained from magnetization measurements. It is anyway reasonable as it corresponds

§ The validity of the simple mean-field model of Eq. 10 with $\lambda = 0.22$ has been tested up to $\gamma \sim 5$. It has been shown (at room temperature) in ref.^{75,76} that this model gives same initial magnetic susceptibility as the second order perturbation model of Ivanov and Kuznetsova⁷⁷ with $\lambda = 1/3$ and as the mean-spherical model of Morozov and Lebedev⁷⁸, all the three being in good agreement with experiments.

¶ Such under-field inhomogeneities of concentration are also present at the local scale as attested by small angle scattering^{74,79}.

‡ Note that the NP/ liquid interface is not constituted of the same species and H-bonds can occur with EAN while only weaker ones can exist with EMIM-TFSI.

to a reduced dipolar parameter $\Psi_{dd} = \gamma/\Phi = 39$, quite comparable to those previously obtained experimentally for aqueous samples based on maghemite NPs similar in diameter^{75,76}.

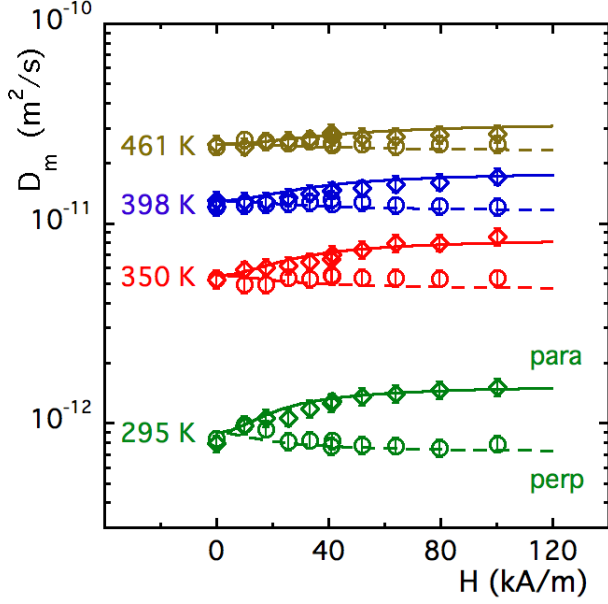


Fig. 4 Under-field diffusion coefficient D_m as a function of the applied field for different temperatures T (from bottom to top: 295, 350, 398 and 461 K); The label perp (resp. para) and open discs (resp. open diamonds) mean measurements in H_{\perp} direction (resp. H_{\parallel}); Symbols correspond to FRS measurements, dashed lines (resp. full lines) correspond to adjustment of the data in H_{\perp} direction with Eq. 12 (resp. in H_{\parallel} direction with Eq. 13). See the text for the detailed values of the parameters used.

At higher temperatures than 295 K, the osmotic compressibility χ , as determined by SANS measurements at $H=0$, is observed to be independent of T ³². The temperature dependence of $\zeta(T)$ enters inside the fitting parameter $D_m^*(T)$, still kept within the experimental error bar of $D_m(H=0)$ at the given T .

However two other parameters have to be modified in the model because of their T -dependence and that of the NP's magnetization $m_S(T)$. Namely these two parameters are the Langevin parameter

$$\xi(H, T) \propto \frac{\mu_{NP}}{T} \propto \frac{m_S(T)}{T} \quad (16)$$

and the dipolar parameter

$$\gamma(\Phi, T) \propto \frac{m_S \mu_{NP}}{T} \propto \frac{m_S^2(T)}{T} \quad (17)$$

In a first approximation, it is here proposed to approximate the temperature dependence of m_S with the following Bloch law of bulk maghemite^{80–83} as finite-size effects and interface effects on the magnetization are small for the present size of NPs^{84–87}:

$$m_S(T) = 390 \left(1 - 3.3 \times 10^{-5} T^{\frac{3}{2}} \right), \quad (18)$$

where m_S is expressed in kA m^{-1} , T in K. Note that Eq. 18 is only valid up to 723 K, temperature above which maghemite transforms in hematite^{80,81}.

Fig. 4 presents the adjustment of the in-field anisotropy of D_m at $\Phi = 5.95\%$ and various T 's, with χ kept independent of \vec{H} and T as said above, $d_{NP} = 13.2$ nm and D_m^* being the only T -dependent fitting parameter. At each T , the shape of the anisotropy of D_m is well adjusted with the model of Eqs. 12, 13, 14 and 15 with a dipolar interaction parameter $\gamma(T)$ derived from Eqs. 11 and 18 given in Table 1. The model quite nicely reproduces the anisotropy of D_m in the experimental range of T and \vec{H} .

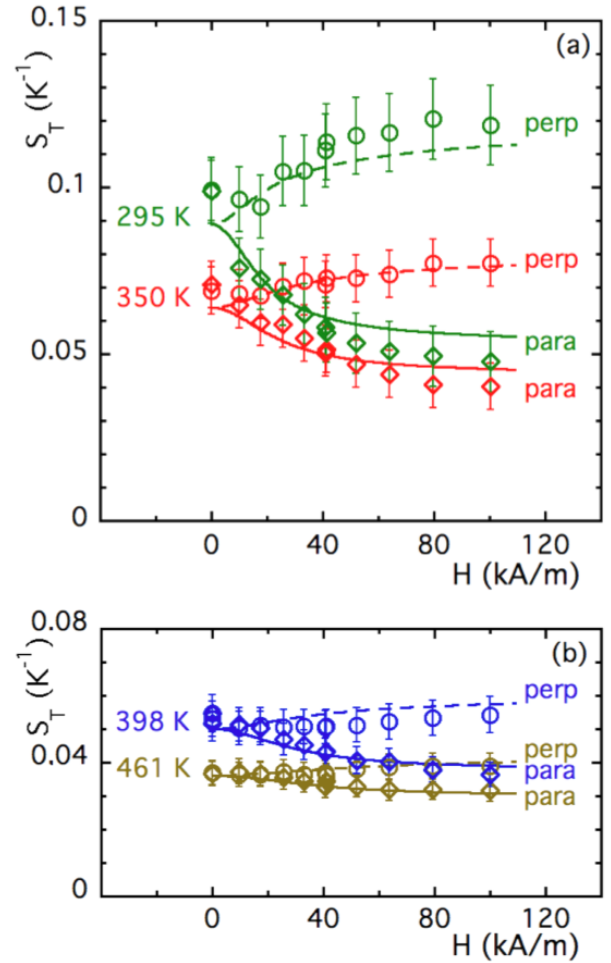


Fig. 5 Under-field Soret coefficient S_T as a function of the applied field for different temperatures T (Fig. 5a at 295 and 350 K, Fig. 5b at 398 and 461 K); The label perp (resp. para) and open discs (resp. open diamonds) mean measurements in H_{\perp} direction (resp. H_{\parallel}); Symbols correspond to FRS measurements, dashed lines (resp. full lines) correspond to adjustment of the data in H_{\perp} direction with Eq. 19 (resp. in H_{\parallel} direction with Eq. 20). See the text for the detailed values of the parameters used in the adjustments.

Table 1 Evolution of some fit parameters as a function of T (see text).

T (K)	γ	$D_m(H=0)$ (m ² /s)	D_m^* (m ² /s)	$\frac{D_m^* - D_m(H=0)}{D_m^*}$	$S_T(H=0)$ (K ⁻¹)	S_T^* (K ⁻¹)	$\frac{S_T^* - S_T(H=0)}{S_T^*}$
295	2.3	$8.06 \cdot 10^{-13}$	$9.0 \cdot 10^{-13}$	+ 10 %	0.099	0.089	- 11 %
350	1.7	$5.24 \cdot 10^{-12}$	$5.7 \cdot 10^{-12}$	+ 8 %	0.070	0.064	- 9 %
398	1.3	$1.21 \cdot 10^{-11}$	$1.3 \cdot 10^{-11}$	+ 7 %	0.054	0.05	- 8 %
461	0.92	$2.45 \cdot 10^{-11}$	$2.5 \cdot 10^{-11}$	+ 2 %	0.037	0.036	- 3 %

4.2 Under-field model of Soret coefficient

The in-field anisotropy of the Soret coefficient $S_T(\vec{H})$ can be expressed in the same framework as that of Eqs. 12 and 13 for $D_m(\vec{H})$ but including derivatives of the NP's chemical potential with respect to temperature^{33,42}:

$$S_T^{\vec{H}_\perp} = \frac{1}{1 - \chi \alpha_\lambda} \left[S_T^* + \chi \frac{S_1}{T} \right] \quad (19)$$

and

$$S_T^{\vec{H}_\parallel} = \frac{1}{1 + \chi(\beta_\lambda - \alpha_\lambda)} \left[S_T^* + \chi \frac{S_1 - S_2}{T} \right], \quad (20)$$

where $S_T^* = S_T(H \rightarrow 0, \Phi, T)$, the parameters S_1 and S_2 being given by :

$$S_1 = \frac{\xi_e L(\xi_e)}{1 - \lambda \gamma L'(\xi_e)} - \ln \frac{\sinh \xi_e}{\xi_e} \quad (21)$$

and

$$S_2 = \beta_\lambda \frac{\xi_e L'(\xi_e)}{L(\xi_e)}. \quad (22)$$

These equations involve the same parameters as Eqs. 12 and 13, in particular ξ_e (effective Langevin parameter given by Eq. 10), λ (mean field parameter, here fixed to 0.22), $\gamma(T)$ (dipolar interaction parameter deduced from Eqs. 11 and 18), α_λ and β_λ given by Eqs. 14 and 15. We use in Fig. 5 the same values of all these parameters as in Fig. 4 and only keep free S_T^* as a T -dependent parameter, adjusted within the experimental error bar of $S_T(H=0)$ at the given temperature. A quite reasonable agreement with the experimental variation of in-field anisotropy of the Soret coefficient $S_T(\vec{H})$ is obtained in the whole range of T and \vec{H} .

$D_m^*(T)$ and $S_T^*(T)$, which have been left free because of the substantial experimental error bars on the direct experimental determinations of D_m and S_T in zero field at T , presents however a systematic small shift with respect to these values (see Table 1). This shift, which remains within the experimental error bar, is positive for D_m^* and negative for S_T^* .

5 Discussion

Let us go deeper in the analysis of each of the terms entering in the adjustments, to try to separate their respective influences.

In the under-field analysis the two main contributions to $D_m(\vec{H})$ and $S_T(\vec{H})$ come from the two parameters α_λ and β_λ , which equal zero at zero magnetic field. The term α_λ is related to the under-field dipolar interaction, modeled in the framework of a mean field approximation. It decreases as T increases. In this framework, it is isotropic and thus exists in both directions \vec{H}_\perp and \vec{H}_\parallel . In the model, the under-field anisotropic contribution to

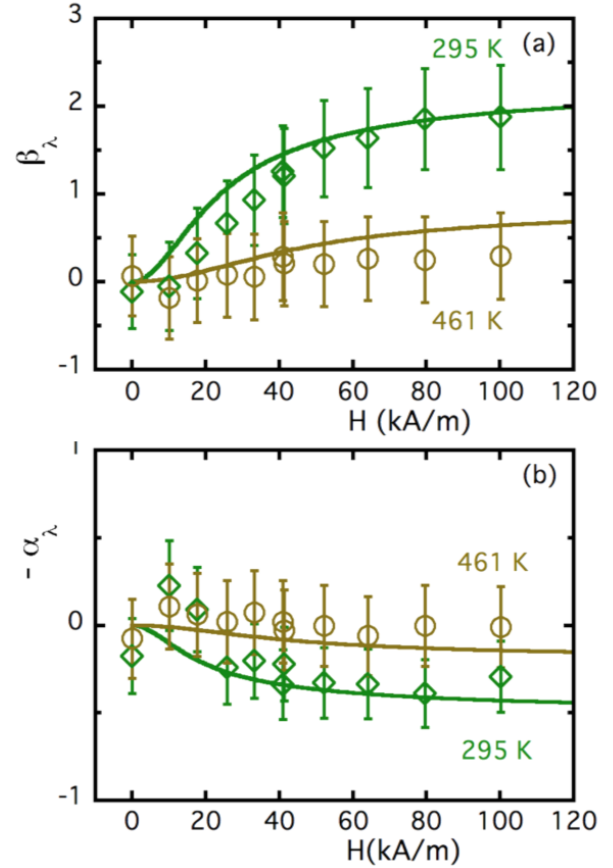


Fig. 6 Field-dependence of parameters $-\alpha_\lambda$ (b) and β_λ (a) at $T=295$ K and 461 K. Experimental values (see text for details) are obtained from Eqs. 23 and 24 (open diamonds at $T=295$ K; open discs at $T=461$ K). Theoretical adjustments (full lines) are deduced from Eqs. 14 and 15, using the same parameters values as in Fig. 4.

$D_m(H)$ comes from the under-field inhomogeneities of concentration, modeled by β_λ . This anisotropic term, which is also proportional to the magnetic dipolar parameter $\gamma(T)$, becomes weaker as T increases. Let us first briefly have a deeper look on these two terms α_λ and β_λ , and on their influence on the under-field variations of $D_m(\vec{H})$ and $S_T(\vec{H})$. We then will focus on the two terms S_1 and S_2 .

It is possible to compare the theoretical expressions of α_λ and β_λ given by Eqs. 14 and 15 to direct experimental determinations,

namely^{||}:

$$-\alpha_\lambda = \frac{1}{\chi} \frac{D_m^{\vec{H}_\perp} - D_m^*}{D_m^*} \quad (23)$$

as in \vec{H}_\perp direction α_λ solely appears in D_m and

$$\beta_\lambda = \frac{1}{\chi} \frac{D_m^{\vec{H}_\parallel} - D_m^*}{D_m^*}. \quad (24)$$

as the anisotropy of D_m is solely influenced by β_λ .

Fig. 6 presents at $T = 295$ K and 461 K the experimental values of $-\alpha_\lambda$ and β_λ deduced from Eqs. 23 and 24 using $\chi = 0.43$ and D_m^* values obtained in Fig. 4 adjustments (see Table 1). Fig. 6 also compares these experimental determinations to the theoretical expressions of $-\alpha_\lambda$ and β_λ deduced from Eqs. 14 and 15, using the same parameters values as in Fig. 4. As expected, there is a very good agreement between the theoretical and the experimental expressions of $-\alpha_\lambda$ and β_λ as a function of H and T , within the error bar of the experiment.

For its part, the anisotropy of the Soret coefficient S_T is also mainly related to the terms α_λ and β_λ , which bring large contributions, larger than S_1 and $S_1 - S_2$. In order to probe more precisely the influence of the terms S_1 and $S_1 - S_2$, we can remark that when looking at the product $S_T D_m$ both α_λ and β_λ contributions vanish. We obtain^{**}:

$$\frac{S_T^{\vec{H}_\perp} D_m^{\vec{H}_\perp}}{D_m^*} = S_T^* + \chi \frac{S_1}{T} \quad (25)$$

and

$$\frac{S_T^{\vec{H}_\parallel} D_m^{\vec{H}_\parallel}}{D_m^*} = S_T^* + \chi \frac{S_1 - S_2}{T}. \quad (26)$$

Fig. 7 presents, at the various T 's, the experimental values of $S_T^{\vec{H}_\perp} D_m^{\vec{H}_\perp} / D_m^*$ (open discs) and $S_T^{\vec{H}_\parallel} D_m^{\vec{H}_\parallel} / D_m^*$ (open diamonds), using D_m^* values obtained in Fig. 4 adjustments (see Table 1). Fig. 7 also presents the expressions $S_T^* + \chi S_1 / T$ (full lines) and $S_T^* + \chi (S_1 - S_2) / T$ (dotted lines), using S_T^* values obtained in Fig. 5 adjustments (see Table 1), $\chi = 0.43$ and theoretical expressions of S_1 and S_2 , given by Eqs. 27 and 28.

The first conclusions from this representation are that here:

$$\chi \frac{S_1(H, T)}{T} \ll S_T^*(T) \quad (27)$$

$$\chi \frac{[S_1(H, T) - S_2(H, T)]}{T} \ll S_T^*(T), \quad (28)$$

which means that almost no under-field anisotropy is predicted in Eqs. 25 and 26 from a theoretical point of view, as well as a very weak field dependence of $S_T D_m / D_m^*$, weaker than the experimental error bar.

From an experimental point of view, similar conclusions are obtained. If a subsidiary field anisotropy of $S_T D_m / D_m^*$ is observed

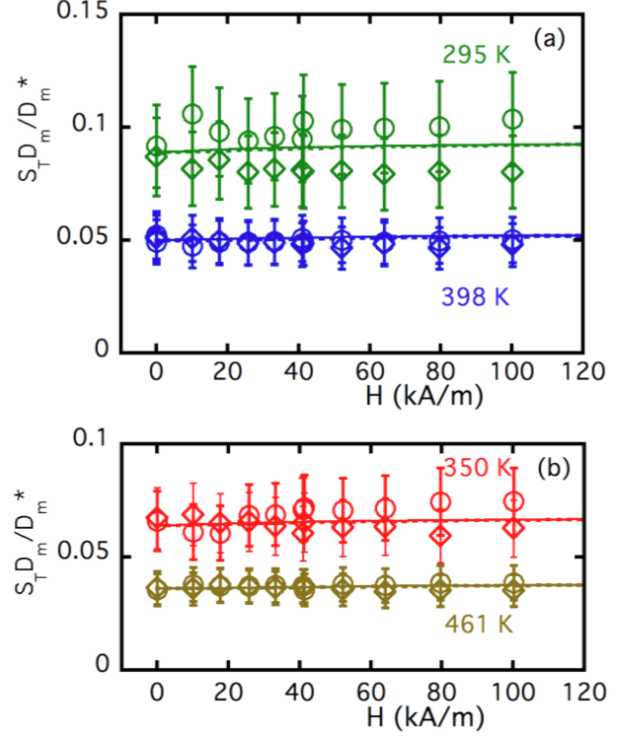


Fig. 7 Under-field anisotropy of $S_T D_m / D_m^*$ at various T 's; Experimental determinations (open discs symbols correspond to measurements in H_\perp direction and open diamonds to measurements in H_\parallel direction) are compared with theoretical expressions of Eqs. 25 (full line) and 26 (dotted line) - for details see text.

(mainly at 295 K and 350 K), it however always remains smaller than the error bar. So within the error bar, which is here much larger than $\chi S_1 / T$ and $\chi (S_1 - S_2) / T$ variations, experimental values of $S_T D_m / D_m^*$ can thus be adjusted by Eqs. 25 and 26. Then the main contribution to the under-field anisotropy of S_T is coming, as for D_m , from the term β_λ , which is associated to the under-field inhomogeneities of concentration.

Note that the small shift at $H=0$ between experimental and adjusted values of D_m and S_T , almost completely compensate in $D_m S_T$ representation of Fig. 7. It is also true for β_λ in Fig. 6a. On the contrary the term α_λ in Fig. 6b, present small distortions at very low fields. This isotropic term α_λ , associated to the under-field modeling of the mean-field averaged magnetic dipolar interaction, is in fact responsible for the small, but systematic, positive shift obtained between D_m^* and the direct experimental value of D_m in zero field at the same temperature. It is as well responsible for the negative shift obtained between S_T^* and the direct experimental value of S_T in zero field at the same temperature.

We propose the following explanation; In Eq. 12, contributions of magnetic dipolar interparticle interaction appear in two places, i) inside the compressibility χ measured in zero field by SAXS and SANS, through a contribution χ_{dip} (here supposed additive) and also ii) in the mean-field expression α_λ , which equals zero in zero field. The approximation of Eq. 12 is in fact very rough in very low fields as the zero-field contribution χ_{dip} should vanish in the

^{||} We use here the adjusted value of D_m^* and not the corresponding experimental value $D_m(H=0)$ to reduce the error bar in Fig. 6

^{**} We use here the adjusted values of S_T^* and D_m^* , and not the corresponding experimental values $S_T(H=0)$ and $D_m(H=0)$ to reduce the error bar in Fig. 7

presence of field. Eq. 12 is thus strictly valid only in the limit of $\chi_{\text{dip}} \ll \chi$ (condition which is here verified see ahead).

At the first order, in zero field, D_m^* can be seen as the extrapolation of $D_m(\vec{H})$ at $H = 0$ in the absence of zero-field magnetic dipolar interaction, $D_m^* \sim kT/[\zeta(\chi - \chi_{\text{dip}})]$ while experimentally we measure $D_m(H=0) = kT/\zeta\chi$. The conclusion is equivalent for S_T^* ; following Eq. 9, $S_T^* \propto (\chi - \chi_{\text{dip}})$ and $S_T(H=0) \propto \chi$.

We can then roughly evaluate here at $T = 295$ K the contribution χ_{dip} in zero field of the magnetic dipolar interaction to the total compressibility χ of the NPs' system to $\sim 10\%$ of χ , as $(D_m^* - D_m(H=0))/D_m^* \sim (S_T(H=0) - S_T^*)/S_T^* \sim 10\%$: $\chi_{\text{dip}} \sim +0.04$, which is of the order of magnitude of the error bar on χ measurements at 295 K. This contribution would be smaller than the error bar at higher T s.

6 Conclusions

Due to an efficient long-range ionic layering of the EMIM-TFSI anions and cations around the maghemite NPs, the present synthesized ferrofluids are stable colloids in a large domain of temperatures T and applied magnetic fields \vec{H} , at least up to 460 K and 100 kA m⁻¹. This stability will be very useful for their future thermoelectric applications. In zero applied field, the average interparticle repulsion is associated to a large second virial coefficient $A_2 = 7.3$, found experimentally independent of T . In FRS measurements performed with a fluid sample of thickness 25 μm in gradients of temperature $\vec{\nabla}T$ such as $\Delta T \ll T$ over ~ 100 μm , the NPs always presents a positive Soret coefficient S_T . The NPs are thus always migrating to the cold, whatever the mean temperature T . Increasing T lowers S_T , and it also increases D_m , as the EMIM-TFSI viscosity decreases.

Under-field S_T and D_m coefficients are anisotropic. S_T is larger when $\vec{\nabla}T$ and $\vec{\nabla}\Phi$ are perpendicular to \vec{H} , while D_m reduces in this configuration, which is promising for thermoelectric applications¹⁰. The main cause of thermodiffusion anisotropy is attributed to under-field spatial inhomogeneities of NP's concentration, associated here to β_λ coefficient in the model. When T increases, the NP's magnetization m_S as well as the magnetic dipolar interaction parameter and β_λ coefficient decrease, the under-field anisotropy of both S_T and D_m coefficients then drastically reduces, as it is observed in the experiment. The under-field anisotropy of S_T and D_m is well described, at the first order, by the model from^{33,42} applied here in the whole range of T and \vec{H} , using the same values of the different parameters for the adjustment of both S_T and D_m at same \vec{H} and T .

Conflicts of interest

There are no conflicts of interest to declare.

Acknowledgements

We acknowledge funding from the Brazilian agency CNPq, the bilateral programs PHC OSMOSE 2018 No. 40033S and CAPES-COFECUB No. Ph 959/20 and the European Union's Horizon 2020 research and innovation programme under grant agreement No. 731976 (MAGENTA). We acknowledge the Laboratoire Léon Brillouin, CEA-Saclay, France for neutron beamtime at PAXY spec-

trometer and especially Arnaud Hélyary for technical assistance on the SANS-DLS setup.

Notes and references

- 1 R. Rosensweig, *Ferrohydrodynamics.*, Cambridge University Press, Cambridge, 1985.
- 2 *Magnetic Fluids and Applications Handbook*, ed. B. Berkovsky, Begell House Inc. Publ., New-York, 1996.
- 3 E. Blums, A. Cēbers and M. Maiorov, *Magnetic Liquids*, W. de G. Gruyter, New York, 1997.
- 4 *Ferofluids : Magnetically Controllable Fluids and Their Applications*, ed. S. Odenbach, Springer Verlag, Berlin, 2003.
- 5 B. Huang, M. Roger, M. Bonetti, T. J. Salez, C. Wiertel-Gasquet, E. Dubois, R. C. Gomes, G. Demouchy, G. Mériquet, V. Peyre, M. Kouyaté, C. L. Filomeno, J. Depeyrot, F. A. Tourinho, R. Perzynski and S. Nakamae, *J. Chem. Phys.*, 2015, **143**, 054902.
- 6 M. Bonetti, N. Nakamae, B. Huang, T. J. Salez, C. Wiertel-Gasquet and M. Roger, *J. Chem. Phys.*, 2015, **142**, 244708.
- 7 M. Dupont, D. MacFarlane and J. Pringle, *Chem. Commun.*, 2017, **53**, 6288–6302.
- 8 Z. He and P. Alexandridis, *Adv. Colloid Interface Sci.*, 2017, **244**, 54–70.
- 9 T. J. Salez, B. T. Huang, M. Rietjens, M. Bonetti, C. Wiertel-Gasquet, M. Roger, C. L. Filomeno, E. Dubois, R. Perzynski and S. Nakamae, *Phys. Chem. Chem. Phys.*, 2017, **19**, 9409–9416.
- 10 T. Salez, M. Kouyaté, C. L. Filomeno, M. Bonetti, M. Roger, G. Demouchy, E. Dubois, R. Perzynski, A. Cēbers and S. Nakamae, *Nanoscale Adv.*, 2019, **1**, 2979–2989.
- 11 Y. Cao and T. Mu, *Ind. Eng. Chem. Res.*, 2014, **53**, 8651–8664.
- 12 D. Zhao, Z. Fei, W. H. Ang and P. J. Dyson, *Small*, 2006, **2**, 879–883.
- 13 L. Rodríguez-Arco, M. T. López-López, F. González-Caballero and J. D. Durán, *Journal of Colloid and Interface Science*, 2011, **357**, 252–254.
- 14 N. Jain, X. Zhang, B. S. Hawkett and G. G. Warr, *ACS Applied Materials & Interfaces*, 2011, **3**, 662–667.
- 15 C. Guibert, V. Dupuis, J. Fresnais and V. Peyre, *J. Colloid Interface Sci.*, 2015, **453**, 105–111.
- 16 X. Shi, W. Huang and X. Wang, *Lubr. Sci.*, 2018, **30**, 73–82.
- 17 J. C. Riedl, M. A. Akhavan Kazemi, F. Cousin, E. Dubois, S. Fantini, S. Loïs, R. Perzynski and V. Peyre, *Nanoscale Adv.*, 2020, **2**, 1560–1572.
- 18 G.-T. Wei, Z. Yang, C.-Y. Lee, H.-Y. Yang and C. R. C. Wang, *J. Am. Chem. Soc.*, 2004, **126**, 5036–5037.
- 19 K. Ueno, A. Inaba, M. Kondoh and M. Watanabe, *Langmuir*, 2008, **24**, 5253–5259.
- 20 M. Mamusa, J. Siriex-Plénet, F. Cousin, E. Dubois and V. Peyre, *Soft Matter*, 2013, **10**, 1097–1101.
- 21 M. Mamusa, J. Siriex-Plénet, F. Cousin, R. Perzynski, E. Dubois and V. Peyre, *J. Phys.: Condens. Matter*, 2014, **26**, 284113.
- 22 H. Zhang, K. Dasbiswas, N. B. Ludwig, G. Han, B. Lee,

- S. Vaikuntanathan and D. V. Talapin, *Nature*, 2017, **542**, 328–331.
- 23 K. Bhattacharya, M. Sarkar, T. J. Salez, S. Nakamae, G. Demouchy, F. Cousin, E. Dubois, L. Michot, R. Perzynski and V. Peyre, *ChemEngineering*, 2020, **4**, 5.
- 24 K. N. Marsh, J. Boxall and R. Lichtenthaler, *Fluid Phase Equilibria*, 2004, **219**, 93–98.
- 25 M. D. Fayer, *Chem. Phys. Lett.*, 2014, **616-617**, 259–274.
- 26 K. Paduszynski and U. Domanska, *J. Chem. Inf. Model.*, 2014, **54**, 1311–1324.
- 27 Y. Wakizaka, *PhD thesis*, University of Southampton - UK, 2007.
- 28 C. Largeot, C. Portet, J. Chmiolat, P. Taberna, Y. Gogotsi and P. Simon, *J. Am. Chem. Soc.*, 2008, **130**, 2730–2731.
- 29 R. Bhandary, J. G. Alauzun, P. Hesemann, A. Stocco, M. In and P. H. Mutin, *Soft Matter*, 2017, **13**, 8023–8026.
- 30 *Products | Solvionic*, 2020, <http://en.solvionic.com/products/>, Accessed: 2020-04-07.
- 31 *Ionic Liquids in Synthesis*, ed. P. Wasserscheid and T. Welton, Wiley-VCH Verlag GmbH & Co. KGaA, Weinheim, FRG, 2002.
- 32 J. C. Riedl and et al, *a voir*.
- 33 M. Kouyaté, C. Filomeno, G. Demouchy, G. Mériquet, S. Nakamae, V. Peyre, M. Roger, A. Cēbers, J. Depeyrot, E. Dubois and R. Perzynski, *Phys. Chem. Chem. Phys.*, 2019, **21**, 1895–1903.
- 34 Y. Nagasaka, T. Hatakeyama, M. Osuka and A. Nagashima, *Rev. Sci. Instrum.*, 1988, **59**, 1156–1168.
- 35 J.-C. Bacri, A. Cēbers, A. Bourdon, G. Demouchy, B. M. Heegaard and R. Perzynski, *Phys. Rev. Lett.*, 1995, **74**, 5032–5035.
- 36 A. Mezulis, M. Maiorov and E. Blums, *J. Magn. Magn. Mat.*, 2002, **252**, 221–223.
- 37 S. Alves, G. Demouchy, A. Bée, D. Talbot, A. Bourdon and A. M. Figueiredo Neto, *Philosophical Magazine*, 2003, **83**, 2059–2066.
- 38 G. Demouchy, A. Mezulis, A. Bée, D. Talbot, J. Bacri and A. Bourdon, *J. Phys. D: Appl. Phys.*, 2004, **37**, 1417–1428.
- 39 H. Ning and S. Wiegand, *J. Chem. Phys.*, 2006, **125**, 221102 1–4.
- 40 H. Ning, J. Dhont and S. Wiegand, *Langmuir*, 2008, **24**, 2426–2432.
- 41 M. Sarkar, J. C. Riedl, G. Demouchy, F. Gélébart, G. Mériquet, V. Peyre, E. Dubois and R. Perzynski, *Eur. Phys. J. E*, 2019, **42**, 979–2989.
- 42 T. Salez, S. Nakamae, R. Perzynski, G. Mériquet, A. Cēbers and M. Roger, *Entropy*, 2018, **20**, 405.
- 43 R. Cabreira-Gomes, A. da Silva, M. Kouyaté, G. Demouchy, G. Mériquet, R. Aquino, E. Dubois, S. Nakamae, M. Roger, J. Depeyrot and R. Perzynski, *Phys. Chem. Chem. Phys.*, 2018, **20**, 16402–16413.
- 44 R. Massart, *C. R. Acad. Sci. Paris*, 1980, **291**, 1–3.
- 45 R. Massart, *I.E.E.E., Trans. on Magn.*, 1981, **2**, 1247–1248.
- 46 E. Laux, L. Jeandupeux, S. Uhl, H. Keppner, P. P. López, P. Sanglard, E. Vanoli and R. Marti, *Mater. Today Proc.*, 2019, **8**, 672–679.
- 47 C. Filomeno, M. Kouyaté, V. Peyre, G. Demouchy, A. Campos, R. Perzynski, F. Tourinho and E. Dubois, *J. Phys. Chem. C*, 2017, **121**, 5539–5550.
- 48 C. Filomeno, M. Kouyaté, F. Cousin, G. Demouchy, E. Dubois, L. Michot, G. Mériquet, R. Perzynski, V. Peyre, J. Sirieix-Plénet and F. Tourinho, *J. Magn. Magn. Mat.*, 2017, **431**, 2–7.
- 49 N. Carnahan and K. Starling, *J. Chem. Phys.*, 1970, **53**, 600.
- 50 J.-C. Bacri, R. Perzynski, D. Salin, V. Cabuil and R. Massart, *J. Magn. Magn. Mat.*, 1990, **85**, 27–32.
- 51 R. G. Horn, D. F. Evans and B. W. Ninham, *Journal of Physical Chemistry*, 1988, **92**, 3531–3537.
- 52 R. Hayes, G. G. Warr and R. Atkina, *Phys. Chem. Chem. Phys.*, 2010, **12**, 1709–1723.
- 53 H.-W. Cheng, P. Stock, B. Moeremans, T. Baimpos, X. Banquy, F. U. Renner and M. Valtiner, *Adv. Mater. Interfaces*, 2015, 1500159.
- 54 M. Mezger, H. Schröder, H. Reichert, S. Schramm, J. S. Okasinski, S. Schöder, V. Honkimäki, M. Deutsch, B. M. Ocko, J. Ralston, M. Rohwerder, M. Stratmann and H. Dosch, *Science*, 2008, **322**, 424–428.
- 55 J. Vatamanu, O. Borodin and G. D. Smith, *J. Am. Chem. Soc.*, 2010, **132**, 14825–14833.
- 56 C. Merlet, B. Rotenberg, P. A. Madden and M. Salanne, *Phys. Chem. Chem. Phys.*, 2013, **15**, 15781.
- 57 V. Ivaništšev, S. O'Connor and M. Fedorov, *Interface Mag.*, 2014, **23**, 65–69.
- 58 S. W. Coles, A. M. Smith, M. V. Fedorov, F. Hausen and S. Perkin, *Faraday Discuss.*, 2018, **206**, 427–442.
- 59 G. Feng, R. Qiao, J. Huang, S. Dai, B. G. Sumpter and V. Meunier, *Phys. Chem. Chem. Phys.*, 2011, **13**, 1152–1161.
- 60 V. Kamysbayev, V. Srivastava, N. B. Ludwig, O. J. Borkiewicz, H. Zhang, J. Ilavsky, B. Lee, K. W. Chapman, S. Vaikuntanathan and D. V. Talapin, *ACS Nano*, 2019, **13**, 5760–5770.
- 61 C. F. W. Ludwig, *Sitzungsberichte der Akad. der Wissenschaften Math. Klasse*, 1856, **20**, 539.
- 62 C. Soret, *Arch. Sci. Phys. Nat. Genève*, 1879, **3**, 48.
- 63 S. Seki, S. Tsuzuki, K. Hayamizu, Y. Umebayashi, N. Serizawa, K. Takei and H. Miyashiro, *J. Chem. Eng. Data*, 2012, **57**, 221–2216.
- 64 D. A. G. Bruggeman, *Ann. Phys.*, 1935, **416**, 636–664.
- 65 W. Luo, T. Du and J. Huang, *Phys. Rev. Lett.*, 1999, **82**, 4134–4137.
- 66 D. Zablotzky, *PhD thesis*, Faculty of Physics and Mathematics - Univ. of Latvia, Riga - Latvia, 2012.
- 67 D. Zablotzky, A. Mezulis and E. Blums, *C. R. Mec.*, 2013, **341**, 449–454.
- 68 G. K. Batchelor, *J. Fluid Mech.*, 1982, **119**, 379–408.
- 69 E. Blums, S. Odenbach, A. Mezulis and M. Maiorov, *Phys. Fluids*, 1998, **10**, 2155–2163.
- 70 E. Blums, *J. Magn. Magn. Mat.*, 2005, **289**, 246–249.
- 71 L. Sprenger, A. Lange and S. Odenbach, *Phys. Fluids*, 2014, **26**, 022001.
- 72 J. C. Bacri, A. Cēbers, A. Bourdon, G. Demouchy, B. M. Heegaard, B. Kashevsky and R. Perzynski, *Phys. Rev. E*, 1995, **52**,

- 3936–3942.
- 73 G. Mériguet, E. Dubois, M. Jardat, A. Bourdon, G. Demouchy, V. Dupuis, B. Farago, R. Perzynski and P. Turq, *J. Phys. Cond. Matter*, 2006, **18**, S2685–S2696.
- 74 G. Mériguet, F. Cousin, E. Dubois, F. Boué, A. Cēbers, B. Farago and R. Perzynski, *J. Phys. Chem. B*, 2006, **110**, 4378–4386.
- 75 F. Gazeau, F. Boué, E. Dubois and R. Perzynski, *J. Phys. Cond. Matt*, 2003, **15**, S1305–S1334.
- 76 G. Mériguet, E. Wandersman, E. Dubois, A. Cēbers, J. de Andrade Gomes, G. Demouchy, J. Depeyrot, A. Robert and R. Perzynski, *Magneto-hydrodynamic*, 2012, **48**, 415–426.
- 77 A. O. Ivanov and O. B. Kuznetsova, *Phys. Rev. E*, 2001, **64**, 041405.
- 78 K. I. Morozov and A. V. Lebedev, *J. Magn. Magn. Mat.*, 1990, **85**, 51.
- 79 E. Wandersman, E. Dubois, F. Cousin, V. Dupuis, G. Mériguet, R. Perzynski and A. Cēbers, *Europhysics Lett.*, 2009, **86**, 10005 1–5.
- 80 *Magnetic oxides in geomagnetism* by K.M. Creer and I.G. Hedley and W. O'Reilly p.649-688 in "Magnetic oxides", ed. D. Craik, J. Wiley, London, 1975.
- 81 *Properties and behaviour of iron oxides as determined by Mössbauer spectroscopy* by E. Murad p. 309-350 in "The Geobiochemical Cycle of Iron in Iron in Soils and Clay Minerals", ed. J. Stucki, B. Goodman and U. Schwertmann, D. Reidel Publishing Company, Dordrecht, Holland, 1988.
- 82 E. Tronc, D. Fiorani, M. Nogues, A. M. Testa, F. Lucari, F. D'Orazio, J. M. Greneche, W. Wernsdorfer, N. Galvez, C. Chaneac, D. Maily and J. P. Jolivet, *J. Magn. Magn. Mat.*, 2003, **262**, 6.
- 83 B. Cullity and C. Graham, *Introduction to Magnetic Materials*, John Wiley and sons, Inc. - IEEE Press, Hoboken, New Jersey, USA, 2nd edn, 2009.
- 84 R. Kodama, *J. Magn. Magn. Mat.*, 1999, **200**, 359–272.
- 85 X. Battle and A. Labarta, *J. Phys. D: Appl. Phys.*, 2002, **35**, R15–R42.
- 86 R. Aquino, J. Depeyrot, M. H. Sousa, F. A. Tourinho, E. Dubois and R. Perzynski, *Phys. Rev. B*, 2005, **72**, 184435 1–10.
- 87 F. G. da Silva, J. Depeyrot, A. Campos, R. Aquino, D. Fiorani and D. Peddis, *J. of Nanosci. Nanotechnol.*, 2019, **19**, 4888–4902.

7.3 | Conclusion

The analysed ionic liquid-based nanoparticle dispersions with SBMIM[±] TFSI⁻ counterions in EMIM TFSI is thermophobic for all analysed magnetic fields (up to 100 kA/m) and temperatures (up to 200°C). The Soret coefficient S_T can be enhanced by applying a magnetic field perpendicular to the temperature and nanoparticle concentration gradients (ΔT and $\Delta\phi_{NP}$) making them suitable for thermoelectric applications.

Conclusions and Perspectives

Key parameters to obtain colloidally stable dispersions in a broad range of ionic liquids, temperatures (up to 200°C), magnetic fields (up to ≈ 700 kA/m), and nanoparticle concentrations (up to ≈ 12.5 vol%) were identified.

This was achieved studying various parameters for the dispersion of nanomagnets in more than 20 ionic liquids that include control of the nanoparticle surface charge, the nature of their charged surface groups and molecules producing this superficial charge, the nature of the counterions compensating this charge, and the route of transfer from water (the synthesis medium for the nanoparticles) to the ionic liquid.

Since the target thermoelectric applications require charged nanoparticles, the focus of this work is on such systems and the possibility of solely steric repulsion is not explored.

When nanoparticle surfaces are charged, they can be dispersed in ionic liquids thanks to an ion multilayer structure formed by alternating cation-rich and anion-rich layers leading to repulsion exceeding attractive contributions to the interparticle interaction. These layers can be composed of the ionic liquid ions and/or other ions coming from the nanoparticle surface modification. The repulsion efficiency depends on the nanoparticle surface charge density and the nature and size of the ions that locate at the interface as follows:

First, an affinity of the ion for the analysed surface is required for it to localise at the interface. If they do, the induced ion layering is controlled by the ratio $\kappa_{ion} = |\sigma / \Theta_{ion}^{max}|$ with σ being the solid's surface charge density and Θ_{ion}^{max} being the maximum charge density of a densely packed counterion monolayer. A multilayered structure of ions with alternating charges is formed close to the solid surface if the ratio $\kappa_{ion} = |\sigma / \Theta_{ion}^{max}|$ is close to 0.5. Experimentally, the nanoparticle surface charge density and thus κ_{ion} can only be changed within given limits, but introducing additional ions to the ionic liquid can also alter the ratio κ_{ion} by changing Θ_{ion}^{max} , if they localise at the solid liquid interface. This localisation at the interface of some counterions is evidenced by the results for colloidal stability, decoupling the increase of the surface charge and the addition of zwitterions. In addition, chemical titrations and the study of the nanostructure with small angle scattering also show the localisation of some of the counterions at the nanoparticle-ionic

liquid interface. Attention needs to be paid to other species that can locate at the interface like residual water molecules which can alter the nanostructure. All these modifications can change the balance of interparticle interaction from attractive to repulsive, switching from a structure of (small) aggregates to individually dispersed nanoparticles and need to be controlled tediously. Interestingly, in the case of small attraction leading to small aggregates, systems can be colloidally and thermally stable in the long term. Indeed, samples prepared longer than a year ago are still colloidally stable.

The effect of steric contribution on the interparticle interactions was also analysed with charged polymer coatings and ions with different chain lengths. Although stable dispersions can be obtained with a steric repulsive contribution, the repulsion induced by polyelectrolytes is weaker than the one induced by a multilayer ion organisation on bare charged nanoparticle surfaces. In addition, longer alkyl chains have poorer temperature stability and are hence not the desired choice for high temperature applications.

Improvements in the methodology for of analysing the nanoparticle dispersions were developed. First, small angle scattering (SAS) coupled with dynamic light scattering (DLS) was necessary to simultaneously analyse colloidal and thermal stabilities of the nanoparticle dispersions. However, SAS measurement setups are not available at the PHENIX laboratory and before this PhD work, DLS measurements were only possible up to 70°C. Thermal and colloidal stability, and nanoparticle interactions were obtained prior and used as pre-requisite to perform and analyse thermodiffusion measurements. However, during the PhD project this process was inverted. Thermodiffusion measurements are used first in order to predict stabilities necessary for SANS and SAXS measurements. Hence, smaller volumes of new samples are necessary to obtain first information about their properties.

Concluding, the findings during this PhD study suggest that conditions allowing long-term colloidally and thermally stable nanoparticle dispersions can be obtained in the vast majority of ionic liquids despite their diversity. This is reached by the right choice out of the nanoparticle surface modifications proposed here for more than 20 ionic liquids. The upper temperature stability is limited by the chemical stability of pure ionic liquids and the introduced ions and polymers, not by a disruption of the colloidal stabilisation. Compact ions with low Lewis acidity are reported to have higher temperature stabilities and should be therefore preferred if colloidal stability shows no difference.

This new understanding yields materials with properties of both the magnetic nanoparticles and the pure ionic liquids which is extremely useful for a number of applications. The work feeds into

the increasingly active area of ionic liquid-based materials and provides a set of methods that can be readily applied to a variety of colloidal ionic liquid systems, allowing it to be adopted by a sizeable community and have a widespread and lasting impact.

Hence, these long term stable ferrofluids are suitable for employment for thermoelectric applications which is explored together with the MAGENTA project partners. The results are promising and further research will be performed. For instance, it would be interesting to investigate mixtures between ionic liquids and molecular solvents to better understand the role of uncharged molecules for colloidal and thermal stability as well as concerning thermoelectric properties and also to limit the viscosity.

Several collaborations were started aiming at a fine understanding of the thermodiffusive and thermoelectric behaviour of the ionic liquid-based ferrofluids developed in this work. In particular, adsorption of nanoparticles in thermoelectric cells is currently analysed in a combined X-Ray reflectivity, ICP-MS and Quartz Crystal Microbalance (QCM). Though this pioneering work are not reported in this thesis, their very encouraging results are currently under redaction for soon publication.

Bibliography

- [1] M. Armand, F. Endres, D. R. MacFarlane, H. Ohno, and B. Scrosati, “Ionic-liquid materials for the electrochemical challenges of the future,” *Materials For Sustainable Energy: A Collection of Peer-Reviewed Research and Review Articles from Nature Publishing Group*, vol. 8, p. 9, 2010.
- [2] H. Zhang, K. Dasbiswas, N. B. Ludwig, G. Han, B. Lee, S. Vaikuntanathan, and D. V. Talapin, “Stable colloids in molten inorganic salts,” *Nature*, vol. 542, no. 7641, pp. 328–331, 2017.
- [3] I. T. Lucas, S. Durand-Vidal, E. Dubois, J. Chevalet, and P. Turq, “Surface Charge Density of Maghemite Nanoparticles: Role of Electrostatics in the Proton Exchange,” *J. Phys. Chem. C*, vol. 111, no. 50, pp. 18568–18576, 2007.
- [4] C. P. Fredlake, J. M. Crosthwaite, D. G. Hert, S. N. V. K. Aki, and J. F. Brennecke, “Thermophysical Properties of Imidazolium-Based Ionic Liquids,” *J. Chem. Eng. Data*, vol. 49, no. 4, pp. 954–964, 2004.
- [5] M. Sarkar, J. C. Riedl, G. Demouchy, F. Gelebart, G. Meriguet, V. Peyre, E. Dubois, and R. Perzynski, “Inversion of thermodiffusive properties of ionic colloidal dispersions in water-DMSO mixtures probed by forced Rayleigh scattering,” *Eur. Phys. J. E*, vol. 42, no. 6, p. 72, 2019.
- [6] M. F. Dupont, D. R. MacFarlane, and J. M. Pringle, “Thermo-electrochemical cells for waste heat harvesting – progress and perspectives,” *Chemical Communications*, vol. 53, no. 47, pp. 6288–6302, 2017.
- [7] B. T. Huang, M. Roger, M. Bonetti, T. J. Salez, C. Wiertel-Gasquet, E. Dubois, R. Cabreira Gomes, G. Demouchy, G. Mériquet, V. Peyre, M. Kouyaté, C. L. Filomeno, J. Depeyrot, F. A. Tourinho, R. Perzynski, and S. Nakamae, “Thermoelectricity and thermodiffusion in charged colloids,” *The Journal of Chemical Physics*, vol. 143, no. 5, p. 054902, 2015.

-
- [8] T. J. Salez, B. T. Huang, M. Rietjens, M. Bonetti, C. Wiertel-Gasquet, M. Roger, C. L. Filomeno, E. Dubois, R. Perzynski, and S. Nakamae, “Can charged colloidal particles increase the thermoelectric energy conversion efficiency?,” *Physical Chemistry Chemical Physics*, vol. 19, no. 14, pp. 9409–9416, 2017.
- [9] J. N. Israelachvili, *Intermolecular and Surface Forces*. Academic Press, 2011.
- [10] R. E. Rosensweig, *Ferrohydrodynamics*. Courier Corporation, 2013.
- [11] B. M. Berkovskiĭ, V. G. Bashtovoĭ, and Unesco, eds., *Magnetic fluids and applications handbook*. New York: Begell House, Inc, 1996.
- [12] K. Raj, B. Moskowitz, and R. Casciari, “Advances in ferrofluid technology,” *Journal of Magnetism and Magnetic Materials*, vol. 149, no. 1-2, pp. 174–180, 1995.
- [13] A. S. Teja and P.-Y. Koh, “Synthesis, properties, and applications of magnetic iron oxide nanoparticles,” *Progress in Crystal Growth and Characterization of Materials*, vol. 55, no. 1-2, pp. 22–45, 2009.
- [14] X. Zhang, L. Sun, Y. Yu, and Y. Zhao, “Flexible Ferrofluids: Design and Applications,” *Adv. Mater.*, vol. 31, no. 51, p. 1903497, 2019.
- [15] R.-J. Yang, H.-H. Hou, Y.-N. Wang, and L.-M. Fu, “Micro-magnetofluidics in microfluidic systems: A review,” *Sensors and Actuators B: Chemical*, vol. 224, pp. 1–15, 2016.
- [16] M. Wang and Y. Yin, “Magnetically Responsive Nanostructures with Tunable Optical Properties,” *J. Am. Chem. Soc.*, vol. 138, no. 20, pp. 6315–6323, 2016.
- [17] T. I. Volkova, V. Böhm, V. A. Naletova, T. Kaufhold, F. Becker, I. Zeidis, and K. Zimmermann, “A ferrofluid based artificial tactile sensor with magnetic field control,” *Journal of Magnetism and Magnetic Materials*, vol. 431, pp. 277–280, 2017.
- [18] K. Ulbrich, K. Holá, V. Šubr, A. Bakandritsos, J. Tuček, and R. Zbořil, “Targeted Drug Delivery with Polymers and Magnetic Nanoparticles: Covalent and Noncovalent Approaches, Release Control, and Clinical Studies,” *Chem. Rev.*, vol. 116, no. 9, pp. 5338–5431, 2016.
- [19] N.-T. Nguyen, M. Hejazian, C. H. Ooi, and N. Kashaninejad, “Recent Advances and Future Perspectives on Microfluidic Liquid Handling,” *Micromachines*, vol. 8, no. 6, p. 186, 2017.

- [20] R. Namgung, K. Singha, M. K. Yu, S. Jon, Y. S. Kim, Y. Ahn, I.-K. Park, and W. J. Kim, “Hybrid superparamagnetic iron oxide nanoparticle-branched polyethylenimine magnetoplexes for gene transfection of vascular endothelial cells,” *Biomaterials*, vol. 31, no. 14, pp. 4204–4213, 2010.
- [21] M. A. Khairul, E. Doroodchi, R. Azizian, and B. Moghtaderi, “Advanced applications of tunable ferrofluids in energy systems and energy harvesters: A critical review,” *Energy Conversion and Management*, vol. 149, pp. 660–674, 2017.
- [22] M. Colombo, S. Carregal-Romero, M. F. Casula, L. Gutiérrez, M. P. Morales, I. B. Böhm, J. T. Heverhagen, D. Prosperi, and W. J. Parak, “Biological applications of magnetic nanoparticles,” *Chem. Soc. Rev.*, vol. 41, no. 11, p. 4306, 2012.
- [23] L. Mestrom, J. J. M. Lenders, R. de Groot, T. Hooghoudt, N. A. J. M. Sommerdijk, and M. V. Artigas, “Stable ferrofluids of magnetite nanoparticles in hydrophobic ionic liquids,” *Nanotechnology*, vol. 26, no. 28, p. 285602, 2015.
- [24] T. Welton, “Room-Temperature Ionic Liquids. Solvents for Synthesis and Catalysis,” *Chemical Reviews*, vol. 99, no. 8, pp. 2071–2084, 1999.
- [25] T. L. Greaves and C. J. Drummond, “Protic Ionic Liquids: Properties and Applications,” *Chem. Rev.*, vol. 108, no. 1, pp. 206–237, 2008.
- [26] S. Werner, M. Haumann, and P. Wasserscheid, “Ionic Liquids in Chemical Engineering,” *Annu. Rev. Chem. Biomol. Eng.*, vol. 1, no. 1, pp. 203–230, 2010.
- [27] Y. Cao and T. Mu, “Comprehensive Investigation on the Thermal Stability of 66 Ionic Liquids by Thermogravimetric Analysis,” *Ind. Eng. Chem. Res.*, vol. 53, no. 20, pp. 8651–8664, 2014.
- [28] C. Maton, N. De Vos, and C. V. Stevens, “Ionic liquid thermal stabilities: decomposition mechanisms and analysis tools,” *Chem. Soc. Rev.*, vol. 42, no. 13, p. 5963, 2013.
- [29] M. V. Fedorov and A. A. Kornyshev, “Ionic Liquids at Electrified Interfaces,” *Chem. Rev.*, vol. 114, no. 5, pp. 2978–3036, 2014.
- [30] J. G. Huddleston, A. E. Visser, W. M. Reichert, H. D. Willauer, G. A. Broker, and R. D. Rogers, “Characterization and comparison of hydrophilic and hydrophobic room

-
- temperature ionic liquids incorporating the imidazolium cation,” *Green Chem.*, vol. 3, no. 4, pp. 156–164, 2001.
- [31] R. Hayes, G. G. Warr, and R. Atkin, “Structure and Nanostructure in Ionic Liquids,” *Chem. Rev.*, vol. 115, no. 13, pp. 6357–6426, 2015.
- [32] D. R. MacFarlane, N. Tachikawa, M. Forsyth, J. M. Pringle, P. C. Howlett, G. D. Elliott, J. H. Davis, M. Watanabe, P. Simon, and C. A. Angell, “Energy applications of ionic liquids,” *Energy Environ. Sci.*, vol. 7, no. 1, pp. 232–250, 2014.
- [33] M. Bonetti, S. Nakamae, B. T. Huang, T. J. Salez, C. Wiertel-Gasquet, and M. Roger, “Thermoelectric energy recovery at ionic-liquid/electrode interface,” *The Journal of Chemical Physics*, vol. 142, no. 24, p. 244708, 2015.
- [34] E. Laux, S. Uhl, L. Jeandupeux, P. P. López, P. Sanglard, E. Vanoli, R. Marti, and H. Keppner, “Thermoelectric Generators Based on Ionic Liquids,” *Journal of Elec Materi*, vol. 47, no. 6, pp. 3193–3197, 2018.
- [35] A. M. Smith, A. A. Lee, and S. Perkin, “Switching the Structural Force in Ionic Liquid-Solvent Mixtures by Varying Composition,” *Physical Review Letters*, vol. 118, no. 9, 2017.
- [36] A. M. Smith, A. A. Lee, and S. Perkin, “The Electrostatic Screening Length in Concentrated Electrolytes Increases with Concentration,” *The Journal of Physical Chemistry Letters*, vol. 7, no. 12, pp. 2157–2163, 2016.
- [37] R. Hayes, N. Borisenko, M. K. Tam, P. C. Howlett, F. Endres, and R. Atkin, “Double Layer Structure of Ionic Liquids at the Au(111) Electrode Interface: An Atomic Force Microscopy Investigation,” *J. Phys. Chem. C*, vol. 115, no. 14, pp. 6855–6863, 2011.
- [38] A. Elbourne, S. McDonald, K. Voïchovsky, F. Endres, G. G. Warr, and R. Atkin, “Nanostructure of the Ionic Liquid–Graphite Stern Layer,” *ACS Nano*, vol. 9, no. 7, pp. 7608–7620, 2015.
- [39] R. Hayes, N. Borisenko, B. Corr, G. B. Webber, F. Endres, and R. Atkin, “Effect of dissolved LiCl on the ionic liquid–Au(111) electrical double layer structure,” *Chemical Communications*, vol. 48, no. 82, p. 10246, 2012.
- [40] H.-W. Cheng, P. Stock, B. Moeremans, T. Baimpos, X. Banquy, F. U. Renner, and M. Valtiner, “Characterizing the Influence of Water on Charging and Layering at Electrified
-

- Ionic-Liquid/Solid Interfaces,” *Advanced Materials Interfaces*, vol. 2, no. 12, p. 1500159, 2015.
- [41] M. Mezger, H. Schroder, H. Reichert, S. Schramm, J. S. Okasinski, S. Schoder, V. Honkimaki, M. Deutsch, B. M. Ocko, J. Ralston, M. Rohwerder, M. Stratmann, and H. Dosch, “Molecular Layering of Fluorinated Ionic Liquids at a Charged Sapphire (0001) Surface,” *Science*, vol. 322, no. 5900, pp. 424–428, 2008.
- [42] M. Chu, M. Miller, and P. Dutta, “Crowding and Anomalous Capacitance at an Electrode–Ionic Liquid Interface Observed Using Operando X-ray Scattering,” *ACS Central Science*, vol. 2, no. 3, pp. 175–180, 2016.
- [43] N. Hjalmarrsson, D. Wallinder, S. Glavatskih, R. Atkin, T. Aastrup, and M. W. Rutland, “Weighing the surface charge of an ionic liquid,” *Nanoscale*, vol. 7, no. 38, pp. 16039–16045, 2015.
- [44] S. Coles, A. M. Smith, M. V. Fedorov, F. Hausen, and S. Perkin, “Interfacial structure and structural forces in mixtures of ionic liquid with a polar solvent,” *Faraday Discuss.*, vol. 206, pp. 427–442, 2018.
- [45] V. Ivaništšev and M. Fedorov, “Interfaces between Charged Surfaces and Ionic Liquids: Insights from Molecular Simulations,” *Interface magazine*, vol. 23, no. 1, pp. 65–69, 2014.
- [46] V. Ivaništšev, S. O’Connor, and M. Fedorov, “Poly(a)morphic portrait of the electrical double layer in ionic liquids,” *Electrochemistry Communications*, vol. 48, pp. 61–64, 2014.
- [47] M. Z. Bazant, B. D. Storey, and A. A. Kornyshev, “Double Layer in Ionic Liquids: Over-screening versus Crowding,” *Physical Review Letters*, vol. 106, no. 4, p. 046102, 2011.
- [48] S. A. Kislenco, Y. O. Moroz, K. Karu, V. B. Ivaništšev, and M. V. Fedorov, “Calculating the Maximum Density of the Surface Packing of Ions in Ionic Liquids,” *Russian Journal of Physical Chemistry A*, vol. 92, no. 5, pp. 999–1005, 2018.
- [49] Z. He and P. Alexandridis, “Nanoparticles in ionic liquids: interactions and organization,” *Physical Chemistry Chemical Physics*, vol. 17, no. 28, pp. 18238–18261, 2015.
- [50] N. Jain, X. Zhang, B. S. Hawkett, and G. G. Warr, “Stable and Water-Tolerant Ionic Liquid Ferrofluids,” *ACS Applied Materials & Interfaces*, vol. 3, no. 3, pp. 662–667, 2011.

-
- [51] C. Guibert, V. Dupuis, J. Fresnais, and V. Peyre, “Controlling nanoparticles dispersion in ionic liquids by tuning the pH,” *Journal of Colloid and Interface Science*, vol. 454, pp. 105–111, 2015.
- [52] L. Rodríguez-Arco, M. T. López-López, F. González-Caballero, and J. D. Durán, “Steric repulsion as a way to achieve the required stability for the preparation of ionic liquid-based ferrofluids,” *Journal of Colloid and Interface Science*, vol. 357, no. 1, pp. 252–254, 2011.
- [53] K. Ueno, A. Inaba, M. Kondoh, and M. Watanabe, “Colloidal Stability of Bare and Polymer-Grafted Silica Nanoparticles in Ionic Liquids,” *Langmuir*, vol. 24, no. 10, pp. 5253–5259, 2008.
- [54] V. Kamysbayev, V. Srivastava, N. B. Ludwig, O. J. Borkiewicz, H. Zhang, J. Ilavsky, B. Lee, K. W. Chapman, S. Vaikuntanathan, and D. V. Talapin, “Nanocrystals in Molten Salts and Ionic Liquids: Experimental Observation of Ionic Correlations Extending beyond the Debye Length,” *ACS Nano*, vol. 13, no. 5, pp. 5760–5770, 2019.
- [55] F. C. C. Oliveira, L. M. Rossi, R. F. Jardim, and J. C. Rubim, “Magnetic Fluids Based on γ -Fe₂O₃ and CoFe₂O₄ Nanoparticles Dispersed in Ionic Liquids,” *The Journal of Physical Chemistry C*, vol. 113, pp. 8566–8572, May 2009.
- [56] M. Mamusa, J. Siriex-Plénet, F. Cousin, E. Dubois, and V. Peyre, “Tuning the colloidal stability in ionic liquids by controlling the nanoparticles/liquid interface,” *Soft Matter*, vol. 10, no. 8, p. 1097, 2014.
- [57] M. Mamusa, J. Siriex-Plénet, F. Cousin, R. Perzynski, E. Dubois, and V. Peyre, “Microstructure of colloidal dispersions in the ionic liquid ethylammonium nitrate: influence of the nature of the nanoparticles’ counterion,” *Journal of Physics: Condensed Matter*, vol. 26, no. 28, p. 284113, 2014.
- [58] J. C. Riedl, M. A. Akhavan Kazemi, F. Cousin, E. Dubois, S. Fantini, S. Loïs, R. Perzynski, and V. Peyre, “Colloidal dispersions of oxide nanoparticles in ionic liquids: elucidating the key parameters,” *Nanoscale Adv.*, vol. 2, no. 4, pp. 1560–1572, 2020.
- [59] K. Ueno, S. Imaizumi, K. Hata, and M. Watanabe, “Colloidal Interaction in Ionic Liquids: Effects of Ionic Structures and Surface Chemistry on Rheology of Silica Colloidal Dispersions,” *Langmuir*, vol. 25, no. 2, pp. 825–831, 2009.
-

- [60] M. Mamusa, J. Sirieix-Plénet, R. Perzynski, F. Cousin, E. Dubois, and V. Peyre, “Concentrated assemblies of magnetic nanoparticles in ionic liquids,” *Faraday Discussions*, vol. 181, pp. 193–209, 2015.
- [61] K. Bhattacharya, M. Sarkar, T. J. Salez, S. Nakamae, G. Demouchy, F. Cousin, E. Dubois, L. Michot, R. Perzynski, and V. Peyre, “Structural, Thermomodiffusive and Thermoelectric Properties of Maghemite Nanoparticles Dispersed in Ethylammonium Nitrate,” *ChemEngineering*, vol. 4, no. 1, p. 5, 2020.
- [62] R. Bhandary, J. G. Alauzun, P. Hesemann, A. Stocco, M. In, and P. H. Mutin, “Phase transfer of TiO₂ nanoparticles from water to ionic liquid triggered by phosphonic acid grafting,” *Soft Matter*, vol. 13, no. 44, pp. 8023–8026, 2017.
- [63] A. M. M. S. Medeiros, A. L. Parize, V. M. Oliveira, B. A. Neto, A. F. Bakuzis, M. H. Sousa, L. M. Rossi, and J. C. Rubim, “Magnetic Ionic Liquids Produced by the Dispersion of Magnetic Nanoparticles in 1-*n*-Butyl-3-methylimidazolium bis(trifluoromethanesulfonyl)imide (BMI.NTf₂),” *ACS Applied Materials & Interfaces*, vol. 4, no. 10, pp. 5458–5465, 2012.
- [64] J. Gao, R. S. Ndong, M. B. Shiflett, and N. J. Wagner, “Creating Nanoparticle Stability in Ionic Liquid [C₄mim][BF₄] by Inducing Solvation Layering,” *ACS Nano*, vol. 9, no. 3, pp. 3243–3253, 2015.
- [65] X. Shi, W. Huang, and X. Wang, “Ionic liquids-based magnetic nanofluids as lubricants,” *Lubrication Science*, vol. 30, no. 2, pp. 73–82, 2018.
- [66] J. Nordström, L. Aguilera, and A. Matic, “Effect of Lithium Salt on the Stability of Dispersions of Fumed Silica in the Ionic Liquid BMImBF₄,” *Langmuir*, vol. 28, no. 9, pp. 4080–4085, 2012.
- [67] J. Sirieix-Plénet, L. Gaillon, and P. Letellier, “Behaviour of a binary solvent mixture constituted by an amphiphilic ionic liquid, 1-decyl-3-methylimidazolium bromide and water,” *Talanta*, vol. 63, no. 4, pp. 979–986, 2004.
- [68] R. Massart, “Preparation of aqueous magnetic liquids in alkaline and acidic media,” *IEEE Transactions on Magnetism*, vol. 17, no. 2, pp. 1247–1248, 1981.
- [69] J.-P. Jolivet and E. Tronc, “Interfacial electron transfer in colloidal spinel iron oxide. Conversion of Fe₃O₄- γ -Fe₂O₃ in aqueous medium,” *Journal of Colloid and Interface Science*, vol. 125, pp. 688–701, Oct. 1988.

-
- [70] R. Massart, E. Dubois, V. Cabuil, and E. Hasmonay, "Preparation and properties of monodisperse magnetic fluids," *Journal of Magnetism and Magnetic Materials*, vol. 149, no. 1-2, pp. 1-5, 1995.
- [71] J.-C. Bacri, R. Perzynski, D. Salin, V. Cabuil, and R. Massart, "Ionic ferrofluids: A crossing of chemistry and physics," *Journal of Magnetism and Magnetic Materials*, vol. 85, no. 1-3, pp. 27-32, 1990.
- [72] D. Frot, P. Patin, B. Woodley, and F. Pinier, "Décteur d'Intensité Lumineuse Diffusée par des Films de Milieux Colloidaux," 1994.
- [73] K. Padiuszyński and U. Domańska, "Viscosity of Ionic Liquids: An Extensive Database and a New Group Contribution Model Based on a Feed-Forward Artificial Neural Network," *Journal of Chemical Information and Modeling*, vol. 54, no. 5, pp. 1311-1324, 2014.
- [74] U. Schwertmann and R. M. Cornell, *Iron Oxides in the Laboratory: Preparation and Characterization*. John Wiley & Sons, 2008.
- [75] A. Brûlet, D. Lairez, A. Lapp, and J.-P. Cotton, "Improvement of data treatment in small-angle neutron scattering," *Journal of Applied Crystallography*, vol. 40, no. 1, pp. 165-177, 2007.
- [76] K. Turcheniuk, A. V. Tarasevych, V. P. Kukhar, R. Boukherroub, and S. Szunerits, "Recent advances in surface chemistry strategies for the fabrication of functional iron oxide based magnetic nanoparticles," *Nanoscale*, vol. 5, no. 22, p. 10729, 2013.
- [77] P. H. Mutin, G. Guerrero, and A. Vioux, "Hybrid materials from organophosphorus coupling molecules," *J. Mater. Chem.*, vol. 15, no. 35-36, p. 3761, 2005.
- [78] K. Popov, H. Rönkkömäki, and L. H. J. Lajunen, "Critical evaluation of stability constants of phosphonic acids (IUPAC Technical Report)," *Pure and Applied Chemistry*, vol. 73, no. 10, pp. 1641-1677, 2001.
- [79] G. Guerrero, J. G. Alauzun, M. Granier, D. Laurencin, and P. H. Mutin, "Phosphonate coupling molecules for the control of surface/interface properties and the synthesis of nanomaterials," *Dalton Trans.*, vol. 42, no. 35, p. 12569, 2013.

- [80] P. Walde, M. Wessicken, U. Rädler, N. Berclaz, K. Conde-Frieboes, and P. L. Luisi, "Preparation and Characterization of Vesicles from Mono-*n*-alkyl Phosphates and Phosphonates," *J. Phys. Chem. B*, vol. 101, no. 38, pp. 7390–7397, 1997.
- [81] R. Demel, C. Yin, B. Lin, and H. Hauser, "Monolayer characteristics and thermal behaviour of phosphatidic acids," *Chemistry and Physics of Lipids*, vol. 60, no. 3, pp. 209–223, 1992.
- [82] J.-G. Ma, B. J. Boyd, and C. J. Drummond, "Positional Isomers of Linear Sodium Dodecyl Benzene Sulfonate: Solubility, Self-Assembly, and Air/Water Interfacial Activity," *Langmuir*, vol. 22, no. 21, pp. 8646–8654, 2006.
- [83] A. K. Sood and M. Aggarwal, "Evaluation of micellar properties of sodium dodecylbenzene sulphonate in the presence of some salts," *J Chem Sci*, vol. 130, no. 4, p. 39, 2018.
- [84] X. Lu, S. Deng, B. Wang, J. Huang, Y. Wang, and G. Yu, "Adsorption behavior and mechanism of perfluorooctane sulfonate on nanosized inorganic oxides," *Journal of Colloid and Interface Science*, vol. 474, pp. 199–205, 2016.
- [85] E. Potapova, R. Jolsterå, A. Holmgren, and M. Grahn, "The Effect of Inorganic Ions on Dodecylbenzenesulfonate Adsorption onto Hematite: an ATR-FTIR Study," *Journal of Surfactants and Detergents*, vol. 17, no. 5, pp. 1027–1034, 2014.
- [86] M. Kouyaté, C. L. Filomeno, G. Demouchy, G. Mériguet, S. Nakamae, V. Peyre, M. Roger, A. Cēbers, J. Depeyrot, E. Dubois, and R. Perzynski, "Thermodiffusion of citrate-coated γ -Fe₂O₃ nanoparticles in aqueous dispersions with tuned counter-ions – anisotropy of the Soret coefficient under a magnetic field," *Phys. Chem. Chem. Phys.*, vol. 21, no. 4, pp. 1895–1903, 2019.
- [87] T. Salez, S. Nakamae, R. Perzynski, G. Mériguet, A. Cebers, and M. Roger, "Thermoelectricity and Thermodiffusion in Magnetic Nanofluids: Entropic Analysis," *Entropy*, vol. 20, no. 6, p. 405, 2018.
- [88] C. L. Filomeno, M. Kouyaté, V. Peyre, G. Demouchy, A. F. C. Campos, R. Perzynski, F. A. Tourinho, and E. Dubois, "Tuning the Solid/Liquid Interface in Ionic Colloidal Dispersions: Influence on Their Structure and Thermodiffusive Properties," *J. Phys. Chem. C*, vol. 121, no. 10, pp. 5539–5550, 2017.

Appendix

Table 7.1 gives an overview of colloidal stability at the micrometre scale observed with optical microscopy. Different surface modifications of the nanoparticles and several ionic liquids are analysed.

DISPERSIONS OF NANOMAGNETS IN IONIC LIQUIDS FOR THERMOELECTRIC APPLICATIONS

Thermoelectricity allows for the conversion of heat to electricity providing one possible methodology for the recycling of low-grade waste heat. Despite improvements, present thermoelectric solid materials have several limitations. Therefore, investigations in complex liquids (e.g. ionic liquids or nanofluids) have been proposed in recent years. This work presents the application of novel ionic-liquid based magnetic complex fluids to this problem. Ionic liquids are a broad class of liquids, that consist solely of ions, and can be liquid at room temperature; with many properties ideal for thermoelectric materials. In addition, recent studies on aqueous nanoparticle dispersions have demonstrated that the addition of magnetic nanoparticles (nanomagnets) can influence the thermoelectric coefficient and enhance the liquid's thermoelectric efficiency. It is here thus proposed to combine the two avenues by using dispersions of nanomagnets in ionic liquids for thermoelectric applications. In former studies, using EAN as an ionic liquid, it was shown that colloidal stability was controlled by the solid-liquid interface this finding was here extended on a broad range of ionic liquids with different sets of cations and anions, defining general trends and principles for colloidal stability in ionic liquids at room temperature. To obtain ionic liquid-based colloids, it was necessary to control the surface charge of the nanoparticles, the nature of charged surface groups and molecules producing this superficial charge, the nature of the counterions compensating this charge, and the route of transfer. In a second step the temperature dependent colloidal stability of ionic-liquid based colloids in the temperature range of future TE devices (here 20-200°C) was studied for different counterions (analysing a steric effect) and nanoparticle concentrations. Even if the temperature stability of ionic liquids is one of their advantages over molecular liquids this has not been in the focus of studies yet. The measurements showed that some of the samples keep their properties up to 200°C and thermodiffusion properties were obtained. Optical microscopy, transmission electron microscopy (TEM), magnetic measurements, FAAS and ICP-MS were only performed at room temperature whereas Dynamic Light Scattering (DLS), forced Rayleigh scattering (FRS) and small angle x-ray/neutron scattering (SAXS/SANS) together with thermogravimetric analysis (TGA) were performed to analyse the ionic liquid-based nanoparticle dispersions.

Keywords : IONIC LIQUID, COLLOID, FERROFLUID, NANOPARTICLE, IRON OXIDE, STABILITY, INTERFACE.

Etablissement : Sorbonne Université
Laboratoire PHENIX (UMR 8234)
4 place Jussieu
75252 Paris Cedex 05, FRANCE

